

See discussions, stats, and author profiles for this publication at: <https://www.researchgate.net/publication/274318080>

Electron Microscopy of Solid Catalysts—Transforming from a Challenge to a Toolbox

ARTICLE *in* CHEMICAL REVIEWS · MARCH 2015

Impact Factor: 46.57 · DOI: 10.1021/cr500084c · Source: PubMed

CITATIONS

6

READS

164

3 AUTHORS, INCLUDING:



Dangsheng Su

Chinese Academy of Sciences

643 PUBLICATIONS 12,960 CITATIONS

[SEE PROFILE](#)



Bingsen Zhang

Chinese Academy of Sciences

105 PUBLICATIONS 1,221 CITATIONS

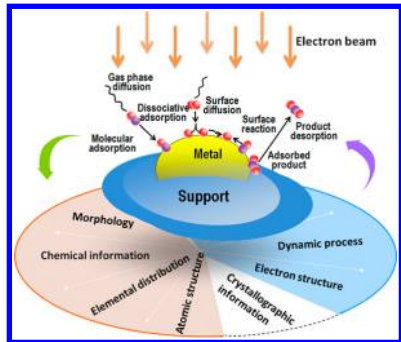
[SEE PROFILE](#)

Electron Microscopy of Solid Catalysts—Transforming from a Challenge to a Toolbox

Dang Sheng Su,*†‡ Bingsen Zhang,† and Robert Schlögl,‡

†Shenyang National Laboratory for Materials Science, Institute of Metal Research, Chinese Academy of Sciences, 72 Wenhua Road, Shenyang 110016, China

‡Department of Inorganic Chemistry, Fritz Haber Institute of the Max Planck Society, Faradayweg 4–6, 14195 Berlin, Germany



CONTENTS

| | |
|---|------|
| 1. Introduction | 2819 |
| 2. General Characteristics of Solid Catalysts | 2819 |
| 2.1. Structural Properties | 2819 |
| 2.2. Additional Challenges for the Structural Characterization of Catalysts | 2819 |
| 3. Role of Electron Microscopy for the Characterization of Solid Catalysts | 2821 |
| 3.1. Basic Information That a Modern TEM/STEM Can Provide | 2821 |
| Morphological Information | 2821 |
| Crystallographic Information | 2822 |
| Structural Information | 2822 |
| Compositional Information | 2822 |
| Electronic Information | 2823 |
| 3.2. Advanced Information that a Modern TEM/STEM can Provide | 2823 |
| Nanoporosity | 2823 |
| Charge Transfer | 2823 |
| Active Site | 2823 |
| Surface Adsorption | 2823 |
| Information Similar to That from Synchrotron Radiation | 2823 |
| Dynamic Behaviors and Catalytic Data | 2823 |
| 4. Selected Developments in Electron Microscopy | 2823 |
| 4.1. Aberration Corrected TEM/STEM | 2823 |
| Image-Corrected TEM | 2823 |
| Probe-Corrected and High Brightness STEM | 2824 |
| 4.2. Correction of Chromatic Aberration | 2824 |
| 4.3. High-Resolution EELS | 2824 |
| 4.4. New and Efficient X-ray Detectors | 2824 |
| 4.5. Electron Tomography | 2824 |
| 4.6. Electron Holography | 2825 |
| 4.7. Ultrafast or 4D Electron Microscopy | 2825 |
| 4.8. <i>In-situ</i> Environmental TEM | 2825 |
| 4.9. Environmental SEM | 2826 |
| 4.10. Identical Location TEM | 2827 |
| 4.11. Low-Voltage Electron Microscopy | 2828 |
| 4.12. Precession Electron Diffraction | 2828 |
| 4.13. Some Specific Techniques for Catalysis Research | 2828 |
| 5. Image Interpretation | 2830 |
| 6. Electron Microscopy Investigation of Solid Catalyst | 2830 |
| 6.1. Identification of Active Sites | 2830 |
| Identification of Single Metal Atoms and Clusters | 2831 |
| 6.2. Atomic Structure of Metal Nanoparticles | 2834 |
| 6.3. Determining Size Distribution and Dynamics of Small Particles with TEM/STEM | 2836 |
| 6.4. Location of Nanoparticles on Support | 2838 |
| 6.5. Metal–Support Interaction | 2839 |
| Imaging of Metal–Support Interaction | 2839 |
| Metal–Support Interaction of Nonequilibrium Particles | 2839 |
| Size-Dependent Metal–Support Interaction | 2840 |
| Charge-Transfer between Metal and Support | 2840 |
| 6.6. Structure and Dynamics of Bimetallic Particles | 2841 |
| Structure of Bimetallic Particles | 2841 |
| Dynamics of Bimetallic Particles | 2843 |
| 6.7. Atomic Structure of Surface of Performance Catalyst | 2845 |
| Surface Oxygen in Ag Catalyst | 2845 |
| Surface Structure of Oxides | 2847 |
| 6.8. Structure of Complex Oxide Catalyst | 2849 |
| 6.9. Defects and Nonstoichiometry of Graphene and CNT | 2850 |
| 6.10. Real Structure of Molecular Sieve | 2851 |
| 7. <i>In Situ</i> and Environmental Electron Microscopy | 2852 |
| 7.1. <i>In Situ</i> Electron Microscopy of Catalysts | 2852 |
| 7.2. Environmental Electron Microscopy of Catalytic Reactions | 2854 |
| 8. Electron Microscopy for Catalysis: Electron-Beam Damage and Other Side-Effects | 2858 |
| 8.1. Electron-Beam Damage | 2858 |
| Electron-Beam Damage in Conventional TEM | 2859 |
| Electron-Beam Damage in Environmental TEM | 2860 |
| 8.2. Other Side-Effects | 2861 |
| 9. A Worked Example: Cu/ZnO | 2862 |
| 10. Concluding Remarks and Perspectives | 2863 |

Received: February 13, 2014

Published: March 31, 2015

| | |
|----------------------|------|
| Author Information | 2866 |
| Corresponding Author | 2866 |
| Notes | 2866 |
| Biographies | 2866 |
| Acknowledgments | 2866 |
| Abbreviations | 2867 |
| References | 2867 |

1. INTRODUCTION

Nanoscience is a cross-sectional interdisciplinary field of research that can hardly be overestimated in its enabling character for technologies in many application areas. A centerpiece of nanoscience is the ability to determine the structure and composition of nanoscopic objects ranging from mesoscopic dimensions in the range of about 100 nm down to individual atoms and clusters. Any rational science in this size domain has to rely on such analytical capabilities. The enormous driving force of semiconductor metrology but also the need to understand catalysts and other areas of functional material science where dynamical phenomena are part of the desired function have driven the development of electron microscopy (EM) into dimensions that were hardly imaginable still about 10 years ago.^{1,2} The implementation of aberration correction on commercial transmission electron microscopy (TEM)/scanning TEM (STEM), thanks to the faster computers that make online automatic aberration diagnosis and autotuning possible, renders atomic resolution imaging and spectroscopy an accessible technique for many laboratories. Resolution of less than 1 Å and probe size of 0.5 Å have been achieved,^{3,4} which may be nearing the highest possible resolution due to thermal magnetic field noise.^{5,6} Imaging of single atom and energy dispersion X-ray spectroscopy (EDX)/electron energy loss spectroscopy (EELS) on a single atomic column has been demonstrated.^{7–12} A single atom, dimers, or trimers of metallic atoms have been identified as possible active centers on supports that have never been observed before.^{13–18} The delimitation of Frensel fringes on the perimeter of the specimens allows the determination of the surface structure of industrial catalyst.^{19–21} EELS using a monochromatized beam allows the measurement of core-level near edge structure in loss spectra with an energy resolution that is comparable to that measured with synchrotron microscopy,²² but with an atomic resolution that could never be achieved with other photon sources. Parallel to this development, electron tomography (ET) and electron holography have been well established as common laboratory techniques.^{23–27} *In-situ* and environmental TEM (ETEM) is another benchmark in the rapid development of electron microscopy that promotes TEM/STEM from a diagnostic tool to research equipment.^{28–35}

In this century, human society is facing the challenge of an energy shortage and climate changes.³⁶ The emission of corresponding carbon dioxides is the major contributor to the green-house gases causing climate changes, with the accompanying catastrophes we experience nowadays in every corner of the world. Catalysis is considered as a key factor for energy conversion,³⁷ both to cope with the energy crisis by synthesis of solar fuels and to minimize the green-house effect. Developing new catalysts with high activity, high selectivity, and high stability is a grand challenge we face.³⁷ This is, however, only realizable under a sustainable condition: the main constituents of new catalysts must be abundant in nature and cheaper, and their production process must be environmentally friendly. In

addition, new catalysts must be developed for processes not possible today, such as artificial photosynthesis or hydrogen production from water.

These new challenges for materials science and catalysis are seen as one of the major driving forces for the current revolution in electron microscopy. From the first TEM built by Ernst Ruska and Max Knoll (with a magnification of only 70!) to spherical aberration correction (point resolution of 0.5 Å!) with various analytic modes and associated detectors, such as for X-rays, backscattered electrons, and energy-lost electrons (Figure 1), the electron microscope has advanced from a simple piece of imaging equipment to a comprehensive research toolbox indispensable for many science and technology disciplines. Apart from nanoscience and nanotechnology, catalysis is one of the most important areas, where EM, particularly TEM and STEM, has found applications.^{39–42} It can be said that the evolution of catalysis science is based on the ability to cope with the structural complexity of solid catalysts, which is largely made possible by the advancement of electron microscopy.^{40,43} Figure 2 shows the huge increase of the number of research papers on solid catalysts investigated by TEM annually from 1991 to 2014 in the ISI Web of Science, evidencing the significant contributions of TEM and its associated techniques to the study and development of solid catalysts. Numerous reviews have been published on the application of (S)TEM in heterogamous catalysis.^{21,25,26,28,44–61}

This paper reviews the significant developments using TEM/STEM and associated spectroscopic techniques to characterize solid state catalysts and to study some catalytic processes or phenomena. We focus on the progress made in the last ten years and on the contribution of TEM/STEM to the understanding of catalysis and the reaction mechanism at the atomic lever rather than on the development of the techniques itself. We start with the summary of the major characteristics of solid catalysts, their challenges to instrumental developments, and the major advancement of TEM/STEM in this decade. We then continue the review with selected case studies illustrating the new possibilities of electron microscopy in catalysis science for understanding the reaction mechanisms, on one hand, and for the knowledge-based development of new catalysts on the other hand. We end the paper with a critical conclusion and perspectives.

2. GENERAL CHARACTERISTICS OF SOLID CATALYSTS

2.1. Structural Properties

Catalysts are complex solids. The structural complexity is associated with their ability to undergo in every catalytic cycle structural changes of their active sites that are reverted into a metastable initial state of activity.⁴⁷ It is obvious that such nonequilibrium processes can only occur at low temperatures with respect to the characteristic transformation temperatures of the base material of the catalyst. In order to be effective under such conditions, the dimension of the active part of a catalyst must be very small and should be well within the nanosize range. For instance, a catalyst could be a mixed metal oxide with a surface termination different from its average bulk structure, or a very small metal particle supported on high surface support.

Fundamental information about such a catalyst is size, its morphology, and chemical composition. Additional critical data relating to its nanosize are the number and the nature of local

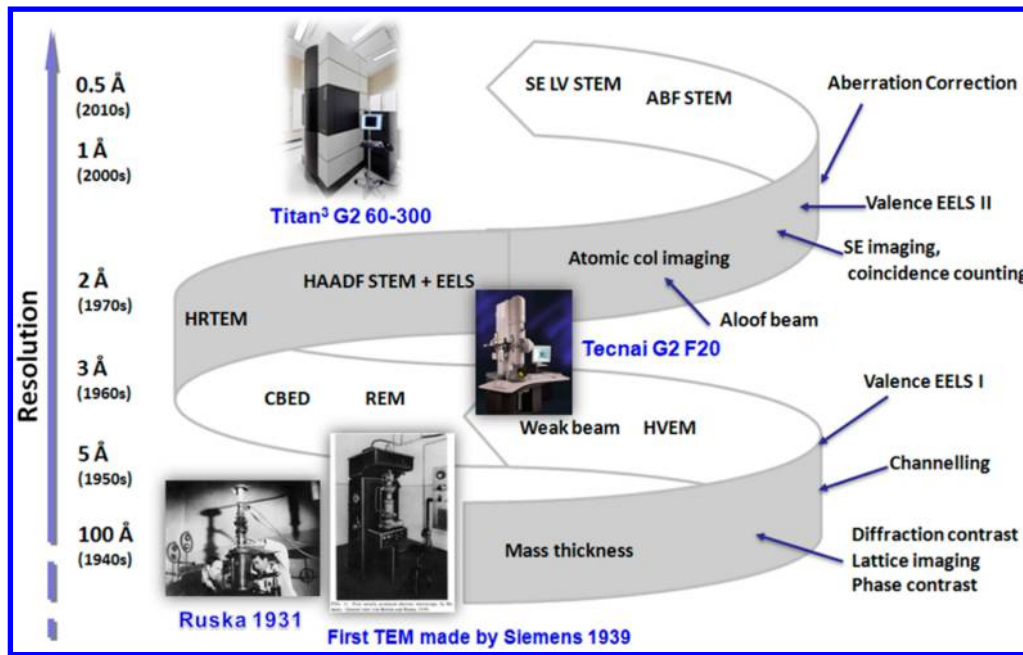


Figure 1. Milestones of transmission electron microscopy, summarizing the development of TEM (from the first one designed and built by Ernst Ruska and Max Knoll to the modern aberration-corrected TEM with sub-angstrom resolution) and the tendency of spatial resolution achieved (left side). Reprinted with permission from ref 38. Copyright 2014 WILEY-VCH Verlag GmbH & Co. KGaA, Weinheim.

crystallographic phases, the size distribution and dispersion of supported catalysts, the atomic structure of nanoparticles, and their locations on the support. More advanced data concern the surface termination. A quite different set of information available from electron microscopy of catalysts deals with the defect structure, both of its bulk (number and types of point, linear or planar defects) and of imperfect termination of its surface (edges, kinks, terraces). Such information is critical for describing the bulk and structural dynamics of the catalyst. In most cases where we know about the active structure of a catalyst, we find that the as-synthesized form of a catalyst is the precursor state to the active phase. Under the influence of the reaction conditions, numerous processes of restructuring occur and bring about the active form of the catalyst. Such equilibration processes can be of complex nature and may last for weeks after the initial start-up of a catalytic reaction. They require thus our utmost attention and are usually difficult to detect with integral techniques:⁶² modification of the defect structure of a solid is a first and strong sign of such restructuring processes^{63–65} even if their result cannot be observed directly due to reversible transformations upon shutting down the catalyst from its reaction conditions. This structural complex and dynamics are special characteristics of solid catalyst that challenge its investigation and characterization.

A comprehensive understanding of a catalyst thus requires a characterization in three stages:

- (1) Precursor of active phase, or the starting materials, that undergoes in every catalytic cycle structural changes of the active sites;
- (2) Working state with the active sites of a catalyst under reaction conditions at equilibrium process;
- (3) Spent catalyst upon shutting down from the reaction conditions.

To give a full description of a catalyst, all the general information at these three stages is necessary. A completed

structural characterization of the catalyst precursor (stage 1) is not only a proof of a synthetic strategy or concept of preparation of nanostructured catalysts consisting of, for instance, multielements, wanted size distribution, or a zeolite with designed pore structure. The information obtained at stage 1 is also of fundamental importance for the understanding of structural dynamics in a chemical reaction. The study under reaction conditions may give a detailed data set of the active sites, which is of essential importance for an understanding of catalytic mechanism, but the structural dynamics of a working catalyst cannot be reasonably understood without the information on precursor. The study of working catalysts under real reaction condition (85% of all industrial chemical process operate usually at high temperature and in the pressure range of 5–100 bar (1Bar = 100 KPa)) is still a challenge, despite the recent rapid development of operando spectroscopy⁶⁶ or *in situ* methods, including the *in situ* synchrotron radiation technique⁶⁷ and environmental TEM (ETEM) that will be discussed in the following.

The critic or reservation in accessing the role of electron microscopy (but also of all the other methods such X-ray or vibration spectroscopy) for the study of catalysts as being at best of secondary importance is thus erroneous.⁶⁰

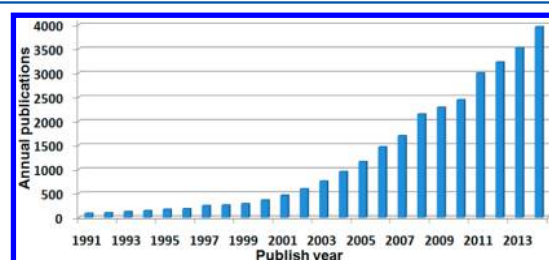


Figure 2. Number of papers on catalyst investigated by TEM published annually, from 1991 to 2014 (Data from ISI Web of Science on Dec. 31, 2014).

2.2. Additional Challenges for the Structural Characterization of Catalysts

Catalysts perform their function under transport of mass and energy. In contrast to many other functional materials, catalysts are continuously confronted with environmental conditions that require making and breaking of chemical bonds that belong to the catalyst structure; a “protection” of the functional material is not possible. This unique situation requires the design of chemical reactivity in addition to the design of electronic structure. The operation of transport phenomena requires further design of supermolecular structures in several dimensions of space to account for conductance of gases and fluids and for the transport of heat liberated or required during the reaction. This is done through controlling micro- and mesopores, through generation of granular morphologies, and through formulation of primary powder particles into aggregates with pores in the micron scale range.

Such hierarchical structures require morphological information being typical for the whole material on scales ranging from atomic resolution to the $10\text{ }\mu\text{m}$ level covered by light optical microscopy. Selection and preparation of specimen for examination on this large span of length scales from one sample is a particular challenge. The usual practice of “dusting” fines from a catalytic material onto sample holders for TEM and STEM is most unreliable for a concise catalyst characterization. In multiphase systems it may well be that small fines exhibit different structures and compositions than larger particles,^{68–71} being “black” for the selected microscopic analysis and thus remaining unaccounted for structural analysis. The alternative of preparing a well-defined specimen by suitable thinning of compacted material creates additional structural defects in particular for nonmetallic materials and thus hampers the description of the most relevant real structure of the sample. The necessary verification of analyzing the relevant part of a catalyst has thus to come from a comparison of diffraction information and of compositional information between bulk average data (from X-ray diffraction (XRD) and from X-ray fluorescence (XRF)/ICP) and the local information from microscopy. This verification of the relevance of local information for a macroscopic amount of a catalyst is all too often missing and can thus lead to controversial views about the nature of active phases. Origins of such discrepancies are the microheterogeneity of nonequilibrium materials on one side and the possible beam modifications⁷² of such structures^{73–75} in the microscope on the other side. The direct verification of the relevance of microscopic information for catalytic function by performing an *in situ* experiment is still impossible as it has not been possible to observe catalytic activity of sample amounts typical of microscopic examination. The use of external microreactors verifying the catalytic performance of sample amounts deposited on TEM grids is a most useful approximation to the ultimate *in situ* TEM investigation.^{31,47}

3. ROLE OF ELECTRON MICROSCOPY FOR THE CHARACTERIZATION OF SOLID CATALYSTS

There are many physical tools that are widely used to characterize the catalysts.⁷⁶ It is obviously that XRD⁶² is the first choice for the crystallographic investigation of a solid catalyst determining lattice parameters, unit cell, and space symmetry. It is also widely used for phase analysis of a multiple-components catalyst and to estimate the averaged size of nanoparticles. Vibrational spectroscopy and, in particular,

Raman spectroscopy^{77,78} provide useful information on a catalyst that is mostly related to molecular bonding and the structure⁷⁹ of active sites, as they can be performed *in situ* and combined with complementary techniques. *In-situ* X-ray photoelectron spectroscopy (XPS) and near edge X-ray absorption fine structure (NEXAFS) give information on surface species and on electronic structures^{80–83} of working catalysts.

But all these powerful tools do not exhibit high spatial resolution. Scanning probe microscopy (scanning tunneling microscopy (STM) and atomic force microscopy (AFM)) can provide images of a flat surface with comparable resolution to that of TEM/STEM. They require in many cases the special treatment (cleaning, for instance) of the surface, and sometimes the application is limited (for instance, STM cannot image the surface of an insulator). TEM/STEM is not simply the complementary tool of the above-mentioned methods. As we will see below, they have become quite robust tools for catalysis research, providing essential information, both static and dynamic, on solid catalysts that cannot be obtained with any other methods.

The most important feature of TEM/STEM characterization of a catalyst, differing from all the other methods mentioned above, is that TEM/STEM provides an image or visualization of a catalyst in real space. The method further provides a full account of geometric and morphological complexity to the extent that the information content of a single electron micrograph can barely be analyzed. It is thus most adequate to document not only a single image but rather galleries of images showing, to a certain extent, the distribution of structural information. The often-referred to “typical” electron micrograph barely exists for catalytic materials.

Nowadays, a modern TEM instrument gives, in addition to imaging and diffraction information, spectroscopic, tomographic, and holographic information and microscopic information on the highest point resolution. A modern TEM instrument features numerous attachments and detectors that allow the recording or analysis of photons/electrons emitted or scattered by the specimen, respectively. The most outstanding feature of a modern TEM/STEM system is the aberration corrector and monochromator. Modified goniometers and charge-coupled device (CCD) recording systems are the prerequisite for the high performance of a modern TEM/STEM system. When an *in situ* specimen holder or environmental cell is used, the TEM/STEM moves from the conventional characterization tool to a research “nanolaboratory” to provide addition to the “static” information, also the dynamic information about the activation, equilibrium, and deactivation process, and the catalytic performance when the reactant/product are *in situ* analyzed by gas chromatography–mass spectrometry (GC-MS).

We see clearly that a modern TEM/STEM is extending its function from a *characterization* tool to a pool of nano- and catalytic researches. In the following, we categorize the function of a TEM/STEM in catalytic research as *basic* and *advanced* to illustrate the role of TEM/STEM for a knowledge-based development of catalysis. We start with the most basic information that a standard TEM/STEM can provide.

3.1. Basic Information That a Modern TEM/STEM Can Provide

Morphological Information. The trial use of a TEM/STEM is to get images of the studied catalyst. Derived from

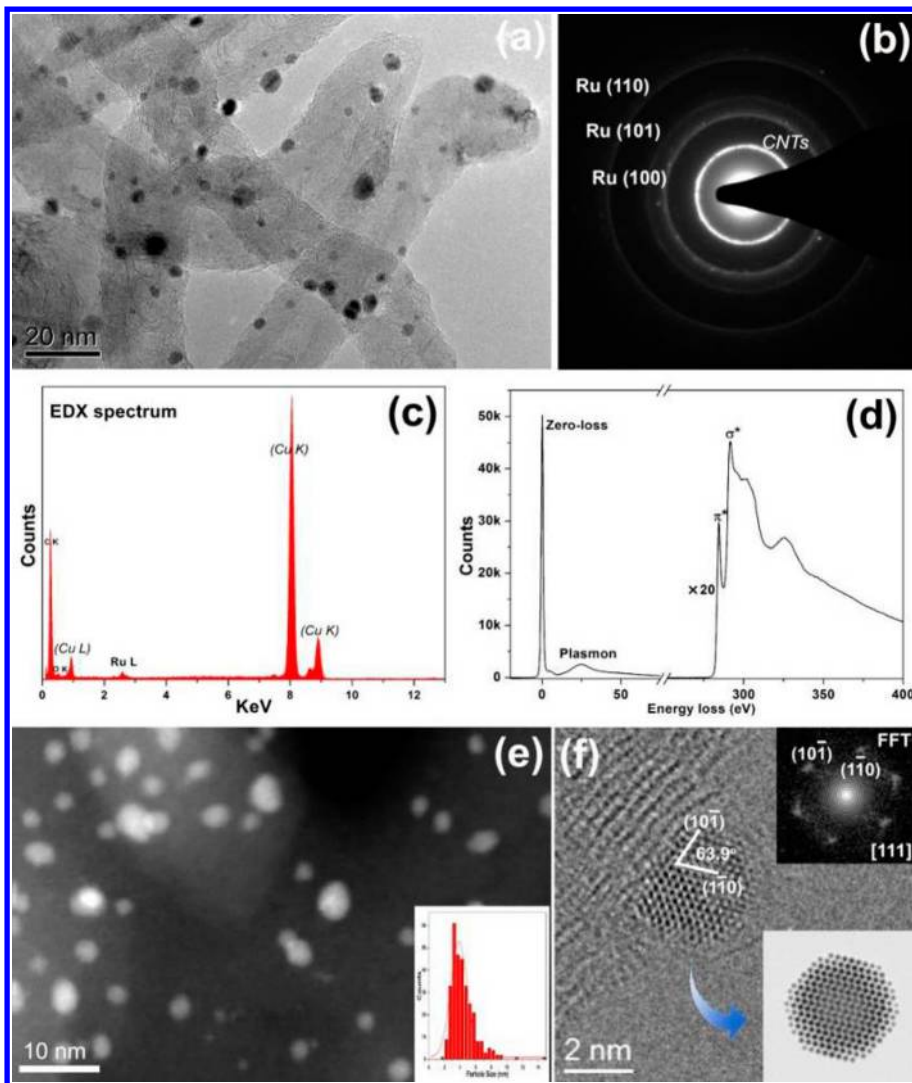


Figure 3. Examples of various basic TEM/STEM techniques applied to catalyst study, shown on a Ru/CNT catalyst: (a) bright-field image of Ru nanoparticles supported on CNTs showing the general morphology of the catalyst; (b) SAED of part a containing structural information on the catalyst; (c) EDX spectrum of Ru/CNTs catalyst showing the chemical composition. (d) EELS taken from CNT support showing plasmon excitation and carbon K ELNES; (e) STEM of Ru/CNTs catalyst and (f) a high-resolution image of Ru particle with atomic structure.¹⁴¹ The size distribution of Ru nanoparticles is given in part e. The power spectrum of the Fourier transformation of the Ru particle in part f and a simulated HRTEM image are inserted in part f. Adapted from ref 141. Copyright 2011 Royal Society of Chemistry.

such images, the size and shape of particles and their distribution can be obtained.^{84–91} For nanoparticles, high resolution imaging,^{92,93} assisted by image simulation,⁹⁴ and the weak-beam contrast technique^{95,96} allow the determination of the atomic structure and the three-dimensional (3D) shape of the particles.^{85,97}

Crystallographic Information. Electron diffraction can determine the symmetry and space group of a specimen, local and global. Selected area electron diffraction (SAED) in a TEM can determine the crystallographic structure of a volume phase of interest. Electron nanodiffraction provides information on the crystal structure, defects, or shapes of nanoparticles by forming a very narrow electron beam to obtain the diffraction pattern.⁹⁸ Convergent-beam electron diffraction (CBED) of a very small volume of the specimen allows the direct observation of the reciprocal lattice, permitting the measurement of local variation of the lattice parameter, and identifies the symmetry of the crystal structure.⁹⁹

Structural Information. High-resolution TEM (HR-TEM) and HR-STEM are two different imaging modes that allow for direct imaging of the atomic structure of samples. The image theories for these two modes are difference: HR-TEM is by phase contrast while HR-STEM is by atom scattering (Z-contrast). Both are powerful tools to study solid catalysts on the atomic scale.^{100–110} HR-STEM is essentially a high-angle annular dark-field (HAADF) technique in which the heavy atoms are the strongest scatterers and appear bright.^{57,59}

Compositional Information. EDX is a standard technique on a modern TEM for qualitative and quantitative element analysis. This technique is especially suitable for heavy elements with high fluorescence yield.^{111–116} For light elements (e.g., B, C, N, O, and P), the use of core-level EELS is recommended.^{117–120} EDX or EELS could be carried out with very high lateral resolution, allowing chemical analysis of individual nanoparticles or across a surface or interface.^{121–125} Element mapping of an energy-filtered TEM (EFTEM) becomes more popular to give two-dimensional images of the

light element distribution.^{123,126} EELS has a relatively higher geometrical signal collection efficiency than EDX.¹²⁷

Electronic Information. The chemical bonding in an active phase and the oxidation state of ions in compounds are of particular interests for catalysis. In a TEM, this kind of information can be obtained by analyzing the energy distribution of transmitted electrons that have interacted with core electrons by means of EELS. In general, valence state, bond distance, and composition can be retrieved from the core-level energy-loss spectrum.^{127–138} The collective behaviors of valence electrons and surface plasmon excited by incident electron at relatively low energy area can be studied by plasmon-spectroscopy.^{127,139,140}

Figure 3 summarizes the most frequent applications of electron microscopy for catalyst investigation. It can be used in one or more of its numerous modern variants: overview image (Figure 3a), high-resolution image (Figure 3f), or as a means of effecting electron diffraction (Figure 3b), or as a powerful scanning probe instrument (Figure 3e), or as an EELS/EDX tool (Figure 3c and 3d).¹⁴¹ The morphology, composition, particle size distribution (PSD), crystallographic structure, and electronic information on Ru/CNTs catalyst can be obtained. The combined information available from one spot within a single grain of catalytic material is of unrivaled value for understanding and verifying design concepts. No other single instrument yields such a wealth of diverse information concerning solid catalysts and their surfaces.

3.2. Advanced Information that a Modern TEM/STEM can Provide

Nanoporosity. TEM/STEM or HR-TEM/HAADF-STEM can generate only a two-dimensional (2D) projection of a three-dimensional (3D) structure. The information on the real 3D structure (e.g., inner structure, nanoporosity, 3D shape of a nanoparticle, etc.) is missing in a 2D TEM/STEM image. The advanced electron microscopy–electron tomography can yield invaluable information about the local features of nanoporous solids in 3D at nano- or atomic scale.^{26,142,143}

Charge Transfer. In heterogeneous catalysis, perturbations of electronic structure by charge transfer across the interfaces between nanoparticles and supports can significantly affect the chemisorption of gas molecules and the energy of catalytic reactions. Modern electron microscopy techniques (e.g., EELS or electron holography) give the opportunity to explore the charge-transfer in metal–support systems and thus to explain the catalytic behavior.⁵⁶

Active Site. The active sites of heterogeneous catalysts are often single atoms, clusters, or steps, kinks, or defects on particles.^{144,145} The high resolution TEM/STEM with aberration corrector can be used to identify the active sites on the extended surface of solid catalyst and their role in reactions.^{15,16,20,146}

Surface Adsorption. Catalyst surfaces are frequently covered intentionally or unintentionally with atoms or molecules derived in the gaseous/liquid environment or via segregation of impurities. This can modify the surface structure, composition, or even morphology of catalysts and thus affect the catalytic performance. Aberration-corrected (S)TEM is now capable of imaging the adsorbents and the possible structure modification at the atomic level; its interpretation needs, however, image simulation and support of DFT calculations.¹⁴⁴

Information Similar to That from Synchrotron Radiation. Synchrotron radiation-based methods are able to

explore the fine chemical and structural variation within solid catalysts, also under reaction conditions.^{67,147} The advanced electron microscope equipped with aberration corrector and monochromator can provide some equivalent information. This solely relies on the improvement of energy-resolution (Figure 4), which now can be achieved on an advanced EM.¹⁴⁸ The *in situ* TEM can also reveal some dynamic structural information on catalysts in gas or liquid environments.^{149,150}

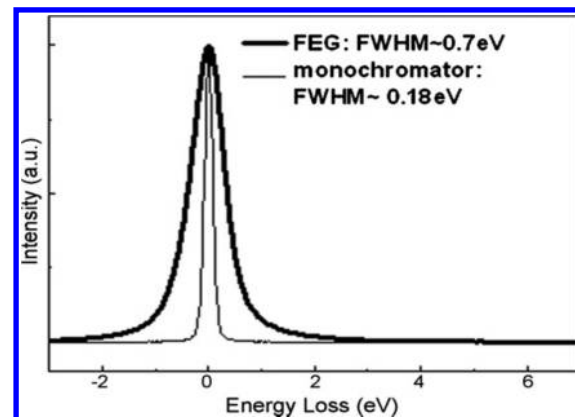


Figure 4. Zero loss peaks acquired in vacuum using conventional FEG (Schottky source) and with a monochromator. Reprinted with permission from ref 148. Copyright 2008 Elsevier.

Dynamic Behaviors and Catalytic Data. Visualizing dynamic catalysts under working conditions at the atomic scale is critical to understand their action and the development of improved catalysts and processes, but this is only valuable and useful if the catalytic activity can be detected, being sure that the observed dynamic is associated with the intended product instead of with the side-reaction. The recently developed “operando TEM” technique with online EELS sensitive to a trace amount of reactants/product can be used to detect and quantify catalytic products with the simultaneous observation of the structural dynamics of catalysts.⁶⁶

4. SELECTED DEVELOPMENTS IN ELECTRON MICROSCOPY

Before we summarize in the following briefly the major technical advancement of TEM/STEM, it should be mentioned here that it is the computer-controlled goniometers, the ultrasensitive CCD, and most importantly, the advanced software and hardware control in computer that made the implementation of many techniques reviewed or discussed below possible.

4.1. Aberration Corrected TEM/STEM

Image-Corrected TEM. The point resolution of a TEM is limited by the wavelength λ and by the coefficient of spherical aberration C_s of the objective lens, given by the formula $\sim C_s^{1/4} \lambda^{3/4}$. The spherical aberration is inherent for cylindrical electron lenses for which C_s cannot be made zero,¹⁵¹ but can be corrected by introducing multipole-based spherical aberration correctors.^{152,153} Aberration-correction improves not only the point resolution down to the subnanometer region, but also the image quality by eliminating the blurring and delocalization effects. It should be mentioned here that the aberration-correction technique brings new imaging possibility to an advanced TEM. The spherical aberration is now tunable: by assigning C_s a certain small positive or negative residual

value,^{154,155} some specific light element in a solid, for instance, Li atoms^{156–160} or oxygen atoms,^{161–163} can be imaged. The position of atoms in a solid can be determined in aberration-corrected micrographs with a precision of a few picometers.¹⁶⁴

Probe-Corrected and High Brightness STEM. A high performance STEM requires a very narrow electron beam with sufficient current density. The advances in the correction of lens aberrations^{165,166} enable sub-angstrom beam sizes,^{3,152} and a Schottky cold field emission gun as a high brightness electron source guarantees the fine probe a high current density. All these allow rapid atomic-resolution Z-contrast imaging of single atoms or clusters^{7,167,168} as well as the chemical and bonding information along the individual atomic column, or even on a single atom.⁸

4.2. Correction of Chromatic Aberration

When spherical aberration is corrected, the performance of a TEM/STEM, especially the information limit at high spatial frequency, is determined by chromatic aberration and other factors (the stability of high tension tank and the stability of objective lens current).^{169,170} Chromatic aberration causes electrons of different energies to be focused with different strengths, but can be corrected partly by introducing a Wien monochromator to the field emission electron gun (FEG)¹⁷¹ or by adding a C_c (chromatic aberration coefficient) corrector.¹⁷² With the correction of chromatic aberration, the information limit of a TEM can be pushed below 0.5 Å.^{168,173}

4.3. High-Resolution EELS

For conventional FEG TEM, the energy resolution is typically between 0.75 and 1 eV. This is insufficient to explore the details of the chemical bonding and electronic structure.²² Such data are invaluable additions to crystallographic information when it comes to phase analysis of similar compounds such as oxides with different oxidation states of the same ion¹⁷⁴ or when the coordination of light elements such as nitrogen in carbon is interrogated.^{175–177} High energy resolution EELS can be obtained by using a Wien monochromator to reduce the energy spread of a Schottky field emitter and by using ultrastable high tension tanks and by improving the electron optics of the spectrometers. An energy resolution of EELS on a modern TEM/STEM of about 0.18 eV or below is now realistic, as shown in Figure 4. This energy resolution is comparable with that of synchrotron radiation for XAS.

The lack of surface sensitivity of this transmission technique is favorably used in combination with NEXAFS that can be obtained as truly surface-sensitive information. If spectra from both techniques are acquired with the same level of resolution, it is possible by direct comparison to decide over segregation and termination phenomena in complex catalytic solids. The study of complex V_xO_y systems^{73,178–180} used in selective oxidation is an instructive example of this technique.

4.4. New and Efficient X-ray Detectors

There are also technical developments for the detection of X-ray that significantly improve the ease of the composition analysis and element mapping, especially when this is collected in 3D. Among them are the X-ray detector without liquid nitrogen cooling (EDAX company), and the silicon drift detectors (SDDs). Advanced technology integrates 4 SDDs very close to the sample area (Figure 5).¹⁸¹ This combination significantly improves the X-ray collection efficiency. The time needed for 3D element mapping can be reduced from hours to minutes.

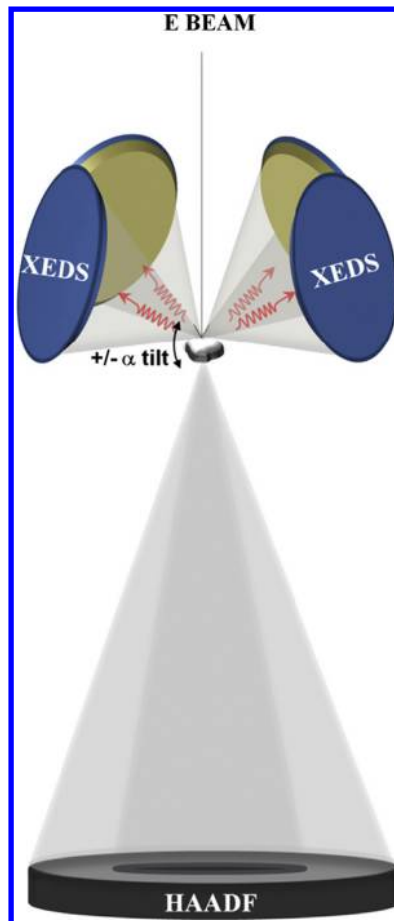


Figure 5. Schematic illustration of a highly efficient X-ray detection system combining 4 SDD detectors arranged symmetrically around the sample and the objective lens pole pieces. Reprinted with permission from ref 181. Copyright 2013 Elsevier.

4.5. Electron Tomography

Already in the 1960s, efforts to “retrieve” 3D information from 2D TEM projections have been pioneered,^{182–184} but it remained mainly a research field of structural biology. Its wide spreading into materials science and catalysis started in this century.^{28,185–188} The rapid development of electron tomography relies on the availability of large-area CCD cameras, automation of microscopy, and advances in computational methods.²⁶ The principle of electron tomography is illustrated in Figure 6. The significance of this method in exploring the 3D structure of mesoporous materials and the space distribution of supported material partially has been demonstrated in numerous publications.^{23,26,48,189–192}

In catalysis, particles are mostly of equilibrated sizes and mesoporous materials are usually unstable under the electron beam. As tomographic studies require the acquisition of a large number of micrographs from exactly the same specimen volume, it is of great relevance that the sample under study is stable and, in particular, does not equilibrate under extensive beam irradiation. Erroneous distributions and particle shapes or sizes would result from such a study if the sample was not stable in its reactive form under the electron beam. Irradiation effects can lead to destructive dehydration and to chemical reduction, which both would affect the metal–support interactions of typical particulate catalysts. Some relief lies in the fact that tomographic reconstructions focus on the

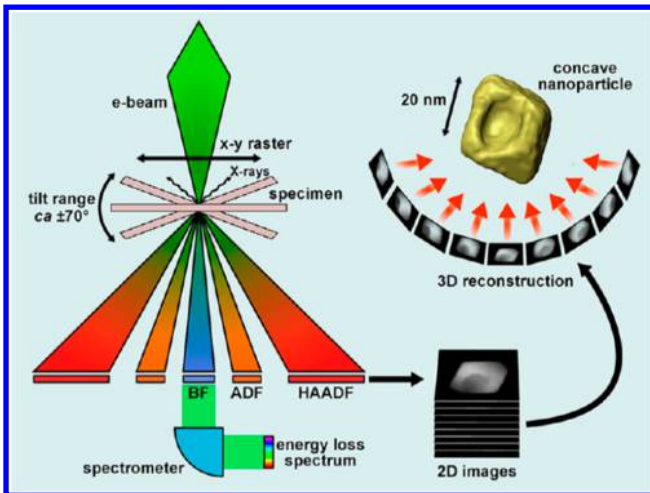


Figure 6. Schematic illustration of electron tomography showing the acquisition of a “tilt series” of 2D images of an object in HAADF-STEM mode (left), and the reconstruction of the 3D object through the 2D images (right). Reprinted with permission from ref 26. Copyright 2012 American Chemical Society.

representation of matter and pores in space and usually do not show atomic details, thus rendering over minor phenomena of beam modification.

It should be mentioned here that Bethge et al. pioneered in 1968 an effective gold-decoration technique to reveal the detailed 3D information about the surface topography of graphite or some multilayered materials with electron microscopy.^{193,194} It proved invaluable in tracing catalytic channeling at graphite surfaces, such as identifying the screw dislocations and 5- and 7-membered rings, and recording the kinetics of single layer graphene-oxidation.¹⁹⁵

4.6. Electron Holography

In 1948 Dennis Gabor proposed electron holography with the intention to improve the resolution of electron microscopy.¹⁹⁶ The basic principle is the interference of electron waves without distortions introduced by imperfect lenses. Nowadays it is possible to obtain electron holograms in a modern TEM/STEM with high-brightness and high-coherent FEG guns when an electron biprism is mounted onto the conjugate image plane (Figure 7).^{24,197} Electron holography can provide, after corresponding posteriori treatment of holograms, an image of the electrostatic field and charge distribution, magnetic domains, and flux line and other information depending on the type of materials studied.^{23,198,199}

4.7. Ultrafast or 4D Electron Microscopy

Catalysis, chemical reaction, and excited structure have fast dynamic nature and require time-resolved investigation. The recent development of ultrafast or four-dimension (4D) EM by Zewail et al. introduces time scale as the fourth domain to complete the information on real, reciprocal, and energy space provided by a conventional EM. This allows the study of many fast chemical or physical phenomena of a solid, for instance, charge transfer or bond breaking.^{200–206} The basic principle of an ultrafast or 4D EM is using coherent and timed single-electron packets to form an image otherwise obtained by using N-electrons in traditional microscopes. Femtosecond laser systems were integrated onto a redesigned electron microscope, as is illustrated in Figure 8. Laser pulses with a well-defined delay excite the sample and generate an electron, respectively

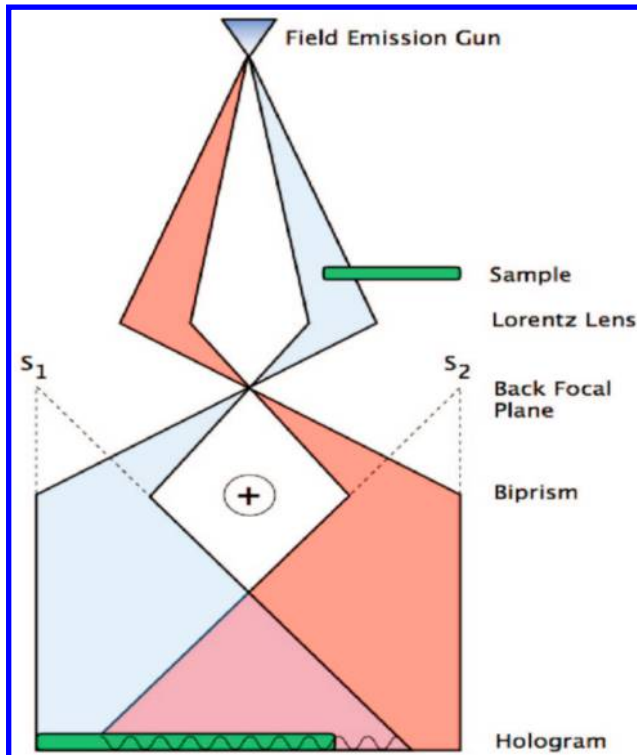


Figure 7. Schematic illustration of electron holography in a TEM by introducing an electron biprism close to a conjugate image plane. A “reference” electron wave propagating through vacuum interferes with the electron wave that has interacted with the specimen, forming an off-axis electron hologram. Reprinted with permission from ref 24. Copyright 2008 American Chemical Society.

(see Figure 8). This is the fundamental difference from a conventional EM where a continuous flow of electrons is generated to illustrate the sample. An ultrafast or 4D EM can have a time resolution on the order of picoseconds but maintaining all the other advantages of conventional EM. Study of atomic-scale dynamics with high temporal resolution is possible.²⁰⁷ When the temporal resolution is applied to the electron tomogram, the dynamics of nano-objects such as CNTs is visualized in real-space and real-time.^{201,202}

4.8. *In-situ* Environmental TEM

Heterogeneous catalysis is a dynamic process at the atomic level. Many efforts have been made to develop *in situ* environmental TEM (ETEM) for a direct, real time probing of the dynamic catalyst–gas molecule reactions at elevated temperatures.^{66,208–218} The pioneering works by Gai contribute essentially to this technical development. In an ETEM, the specimen stage can be devised to cope with *in situ* studies. A gas reaction cell can be fitted inside an electron microscope column (Figure 9). Additional differential pumping system and aperture are needed to avoid interference of gas molecules with the electron beam in the long beam path of an electron microscope.^{30,219–221} A schematic cross-sectional view is shown in Figure 9. The gas pressure around the specimen stage can range from 10^{-3} Pa up to 2500 Pa (for N₂).^{28,30} The samples can be heated up to 1000 °C depending on the differently designed specimen holders. Atomic resolution of 0.12 nm can be obtained at 200 kV in gases with pressures above 1000 Pa.

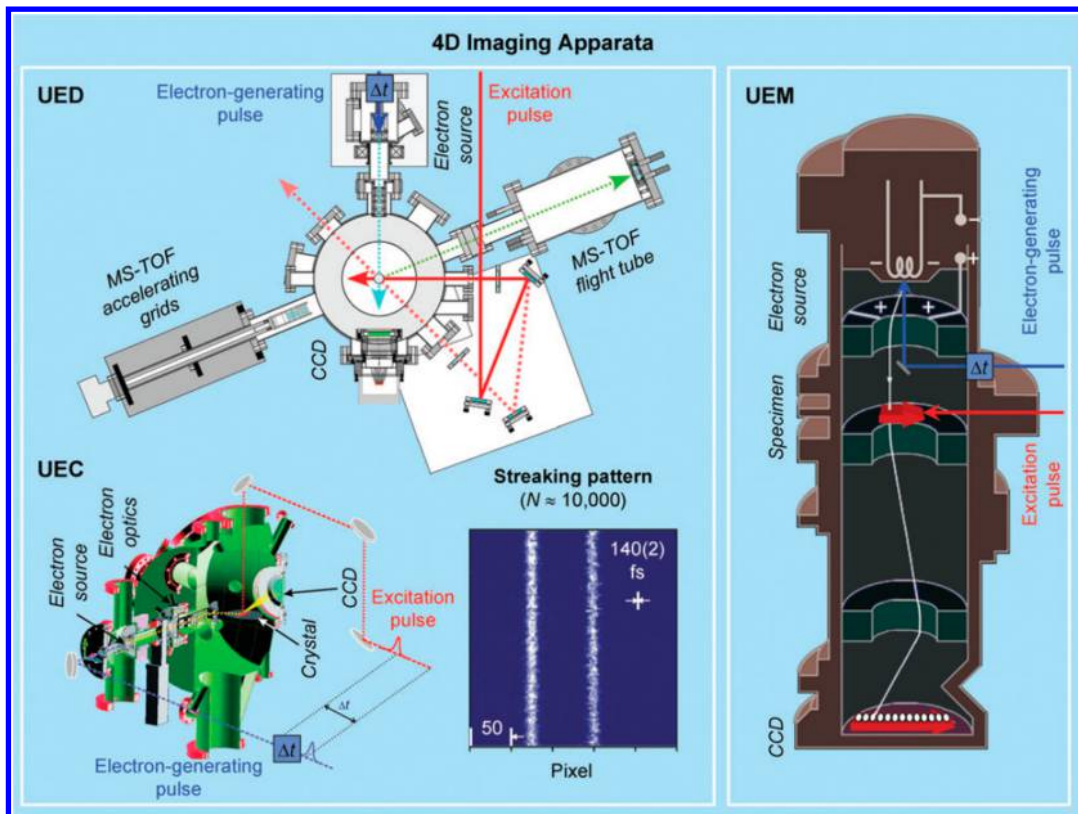


Figure 8. Schematic illustration of Zewail's 4D apparatus for ultrafast electron diffraction (UED), crystallography (UEC), and microscopy (UEM) with a streaking pattern for pulses of about 10000 electrons in UEC (insert). Reprinted with permission from ref 205. Copyright 2008 Royal Society of Chemistry.

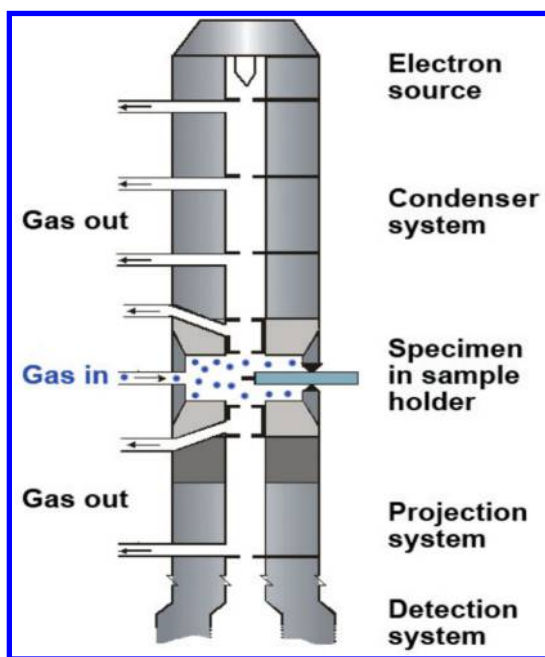


Figure 9. Schematic drawing of microscope column and differential pumping scheme. Reprinted with permission from ref 30. Copyright 2012 Elsevier.

ETEM is useful for revealing the dynamic structure of catalysis in gases and at elevated temperatures, but the relatively low gas and low temperature around and at the samples may provide only a mechanism of a model reaction (under the

conditions that the influence of the electron beam is excluded) and could not simply be scaled-up to a technical process.²⁸

Another way to study solid catalysts in a chemical environment is to use a specimen holder modified to an environmental cell, in which (high-pressure) gases are confined between two membranes that are thin enough for electron transmission; one example, is shown in Figure 10. This technique is suitable for any laboratories, since a change of TEM column is not necessary.²²³ The setup, called also a nanoreactor, is composed of two Si chips with a very thin SiN membrane about 20 nm thick, a Pt heater, and an inlet and outlet for the gases. The SiN membrane allows a gas pressure up to 10 bar in the nanoreactor.^{222,224}

Recently, the *in situ* fluid stage was designed using a similar principle to that shown in Figure 10, but the chamber between SiN windows is fully enclosed, containing liquid solution. The fluid path length of the stages in the direction of the electron beam can be varied from 50 up to 1000 nm, depending on the liquid used to obtain images with reasonable resolution and contrast.^{225,226} This provides the possibility to study colloidal chemistry, liquid phase reaction, and electrochemistry/electrocatalysis if a potential can be applied.

4.9. Environmental SEM

The technical development of environmental SEM (ESEM) is originally aimed to study biological objects or isolating materials. A gaseous environment in an SEM chamber allows the image of such a specimen in its native state.^{227–232} For instance, biological or hydrated samples at a pressure of ~10 Torr water vapor will keep their morphology without being dehydrated or dried. Coating an insulator with a metallic layer

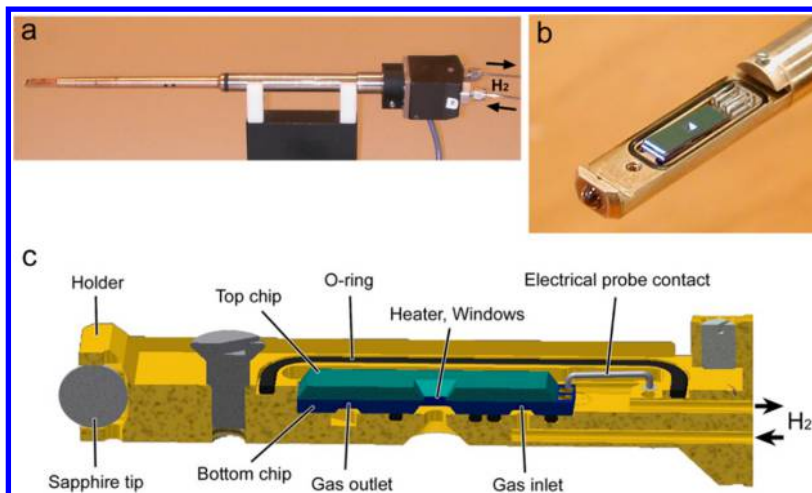


Figure 10. (a) A TEM specimen holder. (b) Nanoreactor integrated in the specimen holder. (c) A cross-sectional illustration of the construction of a nanoreactor integrated in the specimen holder. Reprinted with permission from ref 222. Copyright 2012 Elsevier.

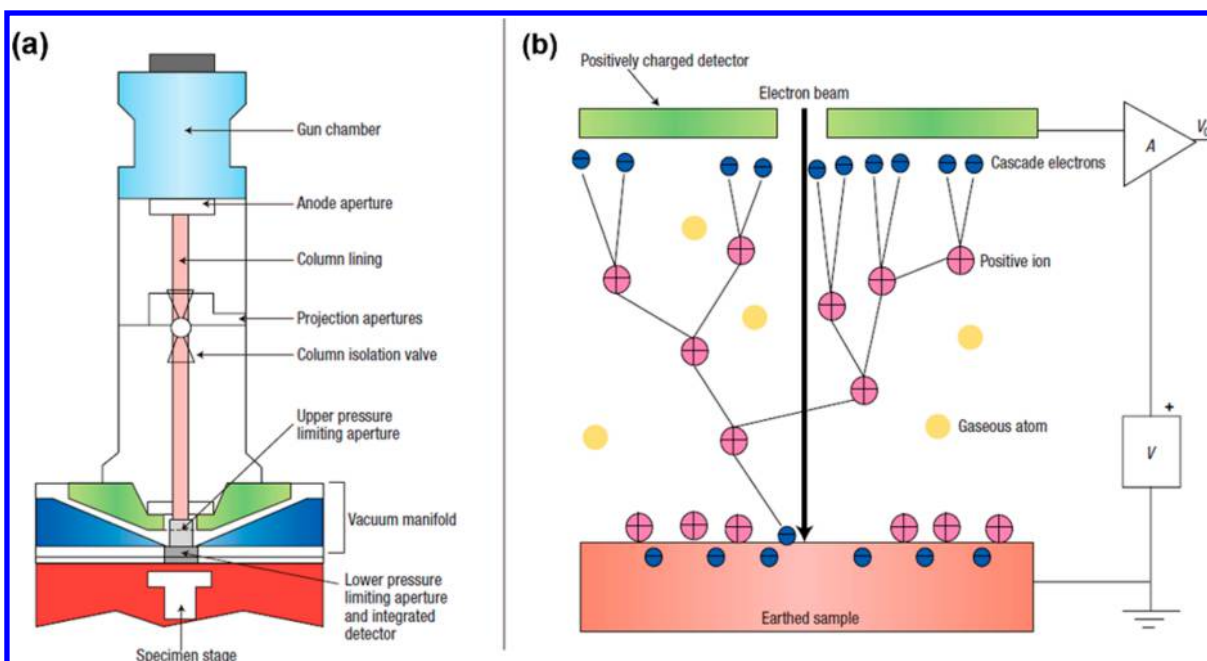


Figure 11. (a) ESEM configuration with different pressure zone. A system of differential pumping- and pressure-limiting apertures allows the chamber to be maintained at a pressure of a few torr, but the gun maintains at high vacuum. (b) Schematic illustration of electron beam–sample–gas molecular interactions in an ESEM chamber. The electrons emitted from the sample ionize the gas molecules. Each ionizing collision gives rise to a daughter electron, which, like the original electron, is accelerated toward the positively charged detector, and further collisions can occur en route to the detector. The positive ions drift back toward the sample surface. Reprinted with permission from ref 227. Copyright 2003 Nature Publishing Group.

before imaging is longer more necessary in ESEM. In this sense, the earlier ESEM is still a “static” technique not aimed to study dynamic processes but to avoid sophisticated specimen preparation. An ESEM needs special electron detectors and differential pumping systems that allow for the transfer of probing electrons from the gun (10^{-6} to 10^{-7} Torr) to the high pressure sample chamber (up to ~ 10 Torr, Figure 11a). Accumulation of charge on an isolator can be avoided by the mechanism illustrated in Figure 11b.²²⁷

Recently, ESEM is demonstrated to be an effective tool to study catalytic reactions in a chemical environment at high temperature (see the following section 7.2). Modified ESEM

enables the imaging of the molecular salvation dynamics at materials surfaces.²²⁸

4.10. Identical Location TEM

Identical location TEM (IL-TEM) uses a grid of inert metal (usually gold) on which fine catalyst particles are dispersed. The grid is marked by letters and numbers in perpendicular directions, respectively, allowing an identification of the same location of the catalyst before and after (electro)chemical treatment or catalytic reaction. Any dynamic changes of a catalyst can be studied both prior to and *a posteriori*.^{233–237} There are no changes on TEM, but a microreactor should be constructed in which the very low amount of catalysts on the grid acts as an active phase; one example is shown in Figure

12A. A vacuum transfer holder is needed to avoid any contact of the used catalyst with air. This method is simple,

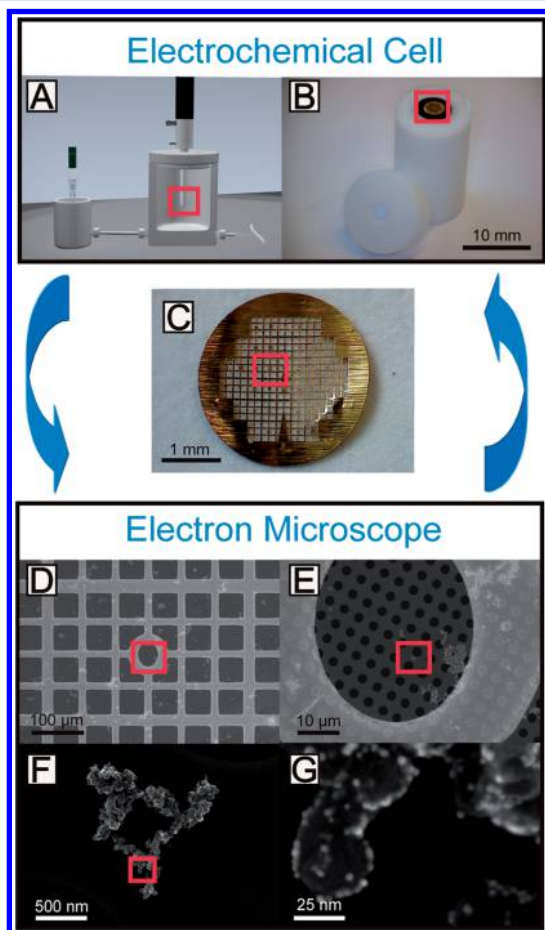


Figure 12. (A) Electrochemical cell in which the working electrode tip includes a TEM finder grid (B), magnified in (C). (D–G) Tracking process of the identical location of particles by the letters and numbers on the grid in a TEM. Reprinted with permission from ref 233. Copyright 2012 Royal Society of Chemistry.

nondestructive, and very useful for reactions where the conditions or chemical potential can never be mimicked in ETEM or using an E-cell, at least not at the current stage of technology. IL-TEM has been successfully used to investigate identical locations on a catalyst before and after electrochemical treatments.^{233–239} Figure 12 shows the detailed process of the IL-TEM method in electrocatalysis. This method can be extended to gas- or liquid-phase reactions when a microreactor is used with an online GC-MS spectrometer.

4.11. Low-Voltage Electron Microscopy

Most commercial TEMs operate at 200–300 kV. The high energy electrons can cause knock-on effects²⁴⁰ in low Z materials such as carbon and thus radiation damage. The theoretically estimated knock-on threshold for carbon, below which only minor damage occurs, is around 80 kV.²⁴¹ Operating below this threshold is thus desired for carbon materials. Modern TEM instruments offer the option to operate at such medium voltage. Recently efforts have been made to develop low-voltage TEM/STEM (20–80 kV).^{242,243} The loss in resolution (lower energy electrons have a larger wavelength) is compensated by a smaller C_s through aberration corrections. In STEM mode, probe sizes close to 1 Å at 60 kV

could be reached.²⁴⁴ Low-voltage EM is especially important for identification of individual light atoms,²⁴⁵ such as carbon, nitrogen, boron, and oxygen, which are of relevance for catalysis. They either constitute reactant molecules or are used as intentional or unintentional dopants. Their identification is essential for the understanding of chemical dynamics in catalysis where constituents of the reactants intercalate into the catalyst and bring about important changes in reactivity.^{246,247}

4.12. Precession Electron Diffraction

The strong interaction between electron and matter leads in many cases to complications in data analysis and interpretation. One example is the dynamical diffraction when electron beams transmit a thick specimen or a complex bulk structure. In 1990s, Vincent and Midgley suggested a precession electron diffraction (PED) technique to obtain diffraction patterns from bulk crystal with recorded intensities close to that obtained under kinematic diffraction conditions.²⁴⁸ The principle of the PED technique is that nonsystematic dynamical effects such as Kikuchi lines or dynamical diffraction (which could be strong when a bulk crystal is exactly at Bragg conditions) are avoided or reduced by using off-axis electron beam illumination. This needs a hollow cone illumination of the specimen that is obtained by serially tilting/deflecting the incident electron beam (precession). After transmitting the specimen, the diffracted beams are complementarily deflected back, forming a diffraction pattern at the back focal plane.²⁴⁹ One important feature of PED is that not only reflections of the zeroth Laue zone but also those from the first Laue zone can be excited and recorded. The acquisition of an increased number of intensities close to kinematical conditions is very useful for structural solution of complex bulk systems.^{249,250} Using the PED method, the fine structure of bulk catalyst supports and the geometry of the metal and supports, such as zeolites^{251,252} and metal–organic framework structures (MOFs),^{253,254} can be well investigated.

We have summarized here very briefly the major advances and technical improvements of TEM/STEM achieved in past decade that have been commercialized. Their applications in materials science and nanoscience with revolutionary results are exemplified in Figure 13, displaying a collection of images/spectra from examples of investigation using the new generation TEM/STEM. A similar collection could be found in ref 207.

4.13. Some Specific Techniques for Catalysis Research

The techniques discussed above are generally developed innovations applicable to many fields of material science in addition to our topic of heterogeneous catalysis. They are based upon modifications of the TEM instrument with additional features and in addition by a rigorous digitization of the TEM operation reaching the point of complete remote control and automatic alignment.

These augmented instruments allow for problem-oriented analysis and data evaluation treatments. Among the many options there, we mention a few characteristic examples illustrating the innovative application of TEM to problems of catalyst characterization. In Table 1 some examples are collected. This is neither a review of modern methods nor a representation of particularly important individual papers. The examples rather serve as illustration for the present-day possibilities of TEM applications. It is noted here that the average depth of TEM in catalysis is way behind these

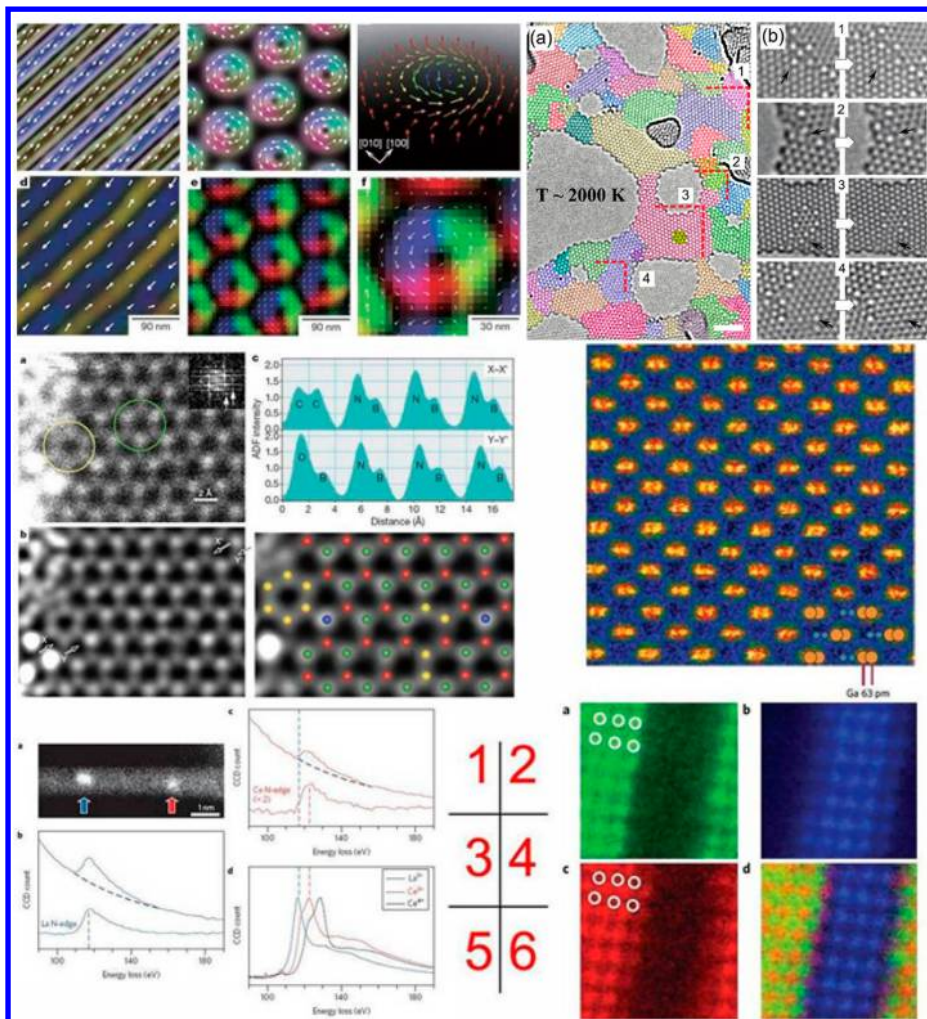


Figure 13. Some representative examples of images and spectra obtained on the new generation of advanced TEM/STEM. 1: Topological spin textures in a helical magnet $\text{Fe}_{0.5}\text{Co}_{0.5}\text{Si}$.²⁵⁵ 2: Dynamic rearrangements of carbon bonds.²⁵⁶ 3: ADF-STEM image of monolayer BN showing the identification of individual light atoms.²⁵⁷ 4: HAADF-STEM image of the wurtzite GaN [211] crystal structure with a Ga dumbbell spacing of 63 pm.³ 5: Single-atom spectroscopy for La and Ce.¹⁰ 6: Spectroscopic imaging of a $\text{La}_{0.7}\text{Sr}_{0.3}\text{MnO}_3/\text{SrTiO}_3$ multilayer, showing the different chemical sublattices. More details about each example can be found in the given literature. Adapted with permission from refs 3, 7, 10, and 255–257. (Ref 3: Copyright 2008 Cambridge University Press. Ref 7: Copyright 2008 The American Association for the Advancement of Science. Ref 10: Copyright 2012 Elsevier. Ref 255: Copyright 2010 Nature Publishing Group. Ref 256: Copyright 2011 American Chemical Society. Ref 257: Copyright 2010 Nature Publishing Group.)

Table 1. Selected Examples of TEM Techniques or Methods That Specially Useful for Investigation of Solid Catalyst

| Title | Authors | Topics | ref |
|---|-----------------|--|-----|
| Lattice measurement and alloy compositions in metal and bimetallic nanoparticles | Tsen et al. | A reliable method for determining the lattice spacings of metallic and bimetallic nanoparticles in phase contrast HREM images | 258 |
| Quantitative energy dispersive X-ray microanalysis of electron beam-sensitive alloyed nanoparticles | Braudy et al. | A method to evaluate the composition of bi- or multimetallic particles in which one element can be preferentially removed by electron beam irradiation in TEM. | 259 |
| Robust atomic resolution imaging of light elements using scanning transmission electron microscopy | Findlay et al. | Method that allows direct imaging of light elements in crystals with STEM. | 260 |
| Atom-by-atom structural and chemical analysis by annular dark-field electron microscopy | Krivanek et al. | Optimized low-voltage operation of aberration-corrected STEM to detect and identify atoms in noncrystalline material consisting of several atomic species | 257 |
| Time-resolved annular dark field imaging of catalyst nanoparticles | Masel et al. | Method that allows dynamic transmission electron microscopy of catalyst nanoparticle with 15 ns pulsed electron images | 261 |

examples. The average bright-field TEM followed by a feature analysis and some qualitative interpretation of the images can be much enhanced in its value when some of the techniques mentioned in Table 1 are added to the analytical approach. Even if some of the techniques require special additions or modifications to standard instruments, they may serve as ideas how existing instrumentation may be adapted to the challenges

presented by catalysts. It is finally noted here that it is not the most advanced figures of merit in resolution or probe size that are the drivers to enhanced catalysts science but rather the adequate combination of the many imaging techniques available to more standard modern instruments. Smart modifications of instruments are then of high additional value.

5. IMAGE INTERPRETATION

While electron diffraction and the associated spectroscopic techniques on a modern TEM/STEM provide important and complementary information on a studied catalyst in the form of diffraction pattern and spectra, the most important advantage to use TEM/STEM over all the other techniques in catalysis science (but also in other materials science) is imaging the specimen as a direct “viewing” of the catalyst globally (low magnification) or locally (high resolution). As important as it is to obtain an image, its correct interpretation is equally important. This is especially important for study of catalysts, since the “active site” is only a minority of an imaged nanocatalyst and, in most cases, they do not have translation symmetry.

Three image contrasts are mostly used in electron microscopic study of catalysts: mass–thickness contrast, phase contrast, and Z-contrast.

The mass–thickness contrast is the first contrast we see when we operate any TEM. It is used to get a global impression of how the investigated catalyst looks, serving as proof of synthesis or checking the used catalyst. Mass–thickness contrast, as it is called, is the intensity difference in an image, depending on the local mass or density, the thickness of a specimen, and the atomic number Z of its constituter, that causes a difference in the incoherent (Rutherford) elastic scattering of electrons.^{262,263} The interpretation of a carefully recorded low and medium magnification image of a mass–thickness contrast image is straightforward. Mass–thickness contrast is used not only for the screening of preparations or for checking the general morphology of the catalyst (Figure 3a) but also, for instance, for the determination of the size distribution of nanoparticles (Figure 22).

Phase contrast is the contrast that produces a high-resolution image in a TEM. When electrons pass through atoms in materials, the relative phase of the electron wave changes. The interference of transmitted and diffracted electron waves produces the so-called phase contrast. Phase contrast gives, ideally, the image of individual atom columns and is nowadays the most used technique on a modern TEM to get so-called high-resolution or atomic resolution images (although in fact only the electrostatic potential of a column of atoms that causes the phase change of the electron wave is imaged). The interpretation of the high resolution image of a TEM is, unfortunately, not straightforward.²⁶⁴ Aberrations, defocus, or astigmatism of the imaging lenses can introduce additional phase changes of the exit wave, making the interpretation of the contrast is not necessarily intuitive, apart from the fact that the image is also influenced by the thickness of the irradiated area. While the atom columns in a metal could be either a bright or dark spot in a high resolution image (it should be black at Scherzer defocus, that makes the interpretation somehow easier), the phase-contrast image of a metal oxide or other multielement specimen is too complicated to be deconvoluted by the human eye for retrieval of the real structure. This is illustrated in Figure 14: the phase contrast of $(\text{VO})_2\text{P}_2\text{O}_7$, a catalyst for selective oxidation of *n*-butane to maleic anhydride, changes drastically when only the defocus value changes. The only way to match the phase contrast of a high resolution image to a real structure model is the image simulation for which the simulation programs are commercially available.^{265,266}

This phase problem is overcome by the technique of Z-contrast STEM, providing incoherent images of specimens at

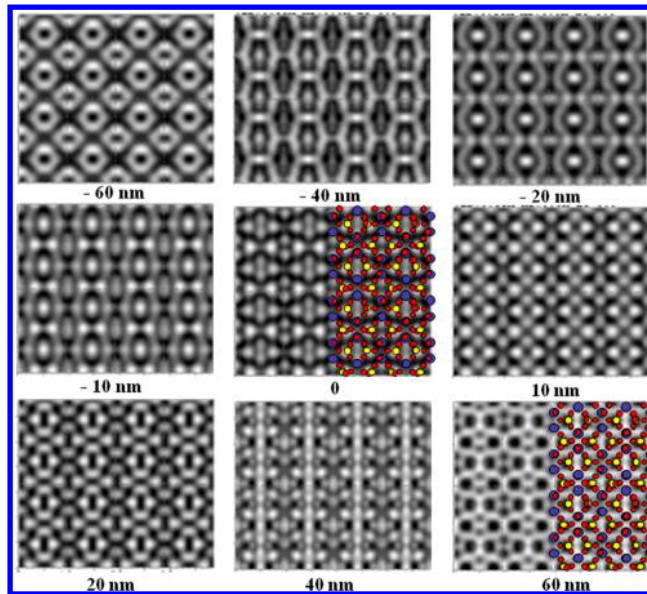


Figure 14. Simulated high resolution images of $(\text{VO})_2\text{P}_2\text{O}_7$ with different focus from -60 nm to 60 nm . The insets are the corresponding structural models of $(\text{VO})_2\text{P}_2\text{O}_7$. This image is simulated with the program developed originally by Stadelmann.²⁶⁶

atomic resolution.²⁶⁷ Z-contrast images stem from the intensity difference of high-angle incoherent (Rutherford) scattered electrons. This intensity is proportional to the atomic number (Z) of the scattering atoms. The recorded image is not the results of interference of electron beams and thus there is no phase involved. The interpretation of Z-contrast image is therefore greatly simplified. One feature of Z-contrast STEM is that it can image single atom, not only atom columns. In catalysis, the active sites of a catalyst are mostly the sites that do not have translation symmetry or periodic structure. When the electron beam aberration is corrected and high brightness FEG is used, Z-contrast STEM is very appealing and successful for the investigation of solid catalysts: image of single metal, dimmer, trimmer or clusters on a support with a lowered averaged Z , as discussed in the following, can be obtained. This has been proven to be the most important achievement made by STEM to study the active sites of a catalyst, as shown by the mostly analyzed examples in this review. For ETEM, images with directly interpretable contrast are the prerequisite for the *in situ* observation of reaction dynamics at atomic level.^{150,268}

6. ELECTRON MICROSCOPY INVESTIGATION OF SOLID CATALYST

The following section discusses selected case studies illustrating the possibilities in catalysis science of electron microscopy. We note that none of these examples are “cookbook” recipes for solving analytical challenges. They do, however, indicate for specific cases the questions to be posed and the answers possible by modern instrumentation. The discussion does not critically analyze the results and conclusion of the authors quoted. It rather tries to extract the generic value of the original analysis. The present authors do not necessarily agree with the conclusions presented by the original authors.

6.1. Identification of Active Sites

One of the most important achievements obtained in catalysis by means of electron microscopy is the identification of individual atoms, metal complexes, or oligomers on supported

catalyst as possible active sites and the assignment of their possible role in catalysis.^{15,18,145,269,270} For a long time, HR-TEM of particulate catalysts has mainly focused on the identification of integrity and orientation of well-developed facets. The identification of Wulff-shaped metal particles^{141,219,271–273} is frequently used as confirmation of the single crystal²⁷⁴ approach. The alternative approach of assigning catalytic function to single sites²⁷⁵ and ensembles of high energetic structures without lattice periodicity²⁷⁶ is often discussed but was difficult to verify by experimental observation.

Although single atoms have been imaged occasionally on dedicated STEM nearly 20 years ago,^{278,279} the microscopic techniques of the past decades did lack the resolution to determine the nuclearity of small metal-containing clusters. But the situation changes drastically now. The aberration-correction of FEG STEM makes it possible to form electron probes of 0.1 nm diameter or smaller.¹⁵² FEG allows a fine focused probe with enough density so that the contrast of large Z single atoms on a support with a lower averaged (if the support consists of more than two elements) Z value can be recorded (Figure 15).

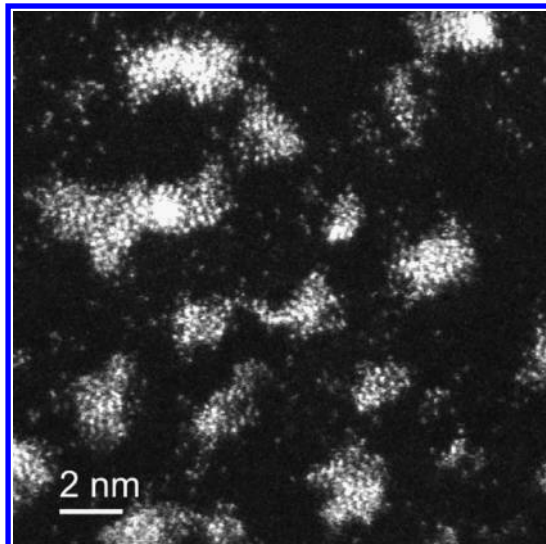


Figure 15. Aberration-corrected HAADF-STEM image of Pt catalyst supported on carbon. Small Pt clusters and single Pt atoms distributed among Pt nanoparticles are imaged. Reprinted with permission from ref 277. Copyright 2013 WILEY-VCH Verlag GmbH & Co. KGaA, Weinheim.

Apart from single atoms, images of clusters of a few atoms,¹³ single atomic layer “rafts” of atoms on a carbon substrate,¹⁸ are reported. It is also possible to obtain an STEM image when the atomic number difference is small.^{43,152,189}

Identification of Single Metal Atoms and Clusters.

Single-Atoms and Small Clusters. Single-site heterogeneous catalysts are ion-exchanged zeolites, metal organic frameworks, or organometallic complexes anchored on supports.^{280,281} Recently, the phrase “single-atom catalyst” is used to describe single metal atoms dispersed on metal, metal oxide, or graphene.¹⁴⁵ They are reported to be active in oxidation (for instance single Pt atoms dispersed on FeO_x), water-gas shift, and hydrogenation (for instance Au atoms supported on ZrO_2) reactions. The most direct and important evidence for single-atom catalyst is the aberration-corrected HAADF-STEM images showing bright spots interpreted as from single heavy

atoms, such as the one shown in Figure 15. The observed single atoms are correlated to unusual catalytic performance of the catalyst. However, there is still no correlation made *in situ* and care must be taken that the single atoms observed in (S)TEM are not derived from nanoparticles migrating to the support when the catalyst is irradiated by a high energetic electron beam.

Single Pt, Au, Ir, and Pd atoms are identified by means of (S)TEM as single atom catalysts.^{15,18,145,146,282,283} Gold nanoparticles on reducible metal oxides belong to one of the most studied catalysts in the past few years. Gold, one of the most inert metals, becomes active when the size is in the few nanometers range. The most studied reaction that gold nanoparticle can catalyze is the oxidation of carbon monoxide, even at very low temperatures.^{284–286} Hutchings and co-workers prepared a series of iron oxide-supported gold nanocatalyst samples ranging from with little or no activity to with high activities toward CO oxidation. Using aberration-corrected STEM they could correlate high catalytic activity for CO oxidation with the presence of bilayer clusters of 0.5 nm in diameter consisting of only 10 Au atoms (Figure 16). In this study, the presence of individual Au atoms or planar monolayer gold clusters of 3–4 atoms (illustrated in Figure 16F) could not be correlated to any high CO oxidation. The activity of gold bilayer clusters is in good agreement with previous findings obtained using model catalyst systems.¹⁸

Single-Site Metal Complexes. A single-site metal complex has a single metal center and an open-side where it binds substrates (Figure 17a). It has well-defined structure and features an isolated site. Supported single-site metal complexes are catalysts exemplified by the metallocenes for alkene hydrogenation or polymerization.²⁸⁷ Iridium complexes on the dehydroxylated MgO (Figure 17a) or on zeolite are one of such catalysts. Catalysts of supported single-site metal complexes have been industrially used, but it is not clear whether the metal complexes are really site-isolated or have coalesced to metal clusters. Although spectroscopic methods such as IR or EXAFS can provide clues for the site isolation, it is the HAADF-STEM that provides direct image evidence of well-dispersed single iridium atom complexes on a dehydroxylated MgO powder.^{269,288,289} No coalesced iridium clusters are detectable. Figure 17b displays a typical HAADF-STEM image of the catalyst. The high atomic number of Ir compared with that of support produces bright contrast of single Ir atoms, indicating that the complex is site-isolated. This used to be the first image evidence of site-isolation of mononuclear metal complexes bonded to a high-area support.²⁶⁹ The single-site Ir complexes are stable during ethene hydrogenation. *In-situ* EXAFS during the reaction could not confirm that Ir–Ir bonds are formed, indicating no aggregation occurs, but *in situ* XANES reveals the changes in the ligand environment of the iridium as the complexes interact with the reactant molecules.

Care must be taken when determine single-site metal complexes by means of electron microscopy: (i) it is a good practice to use IR and EXAFS to confirm or verify the electron microscopic finding; (ii) single-site metal complexes could be very electron beam sensitive, forming metal clusters upon prolonged exposure to high energetic electrons. Only the first images that were taken in any region of the sample can be used to draw conclusions; subsequent images could show already the migration of metal atoms and the formation of metal clusters—the catalyst is already damaged by the electron beam.²⁶⁹

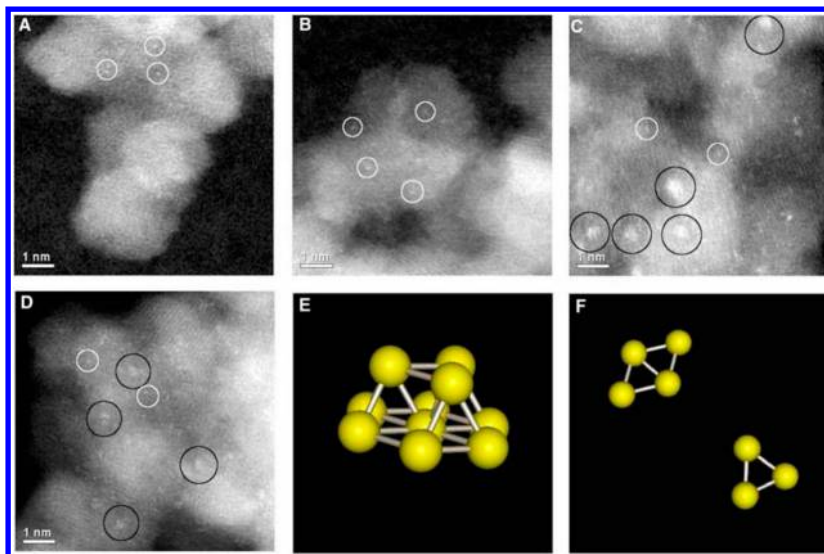


Figure 16. Aberration-corrected HAADF-STEM images of inactive (A and B) and active (C and D) Au/FeO_x catalysts. Individual Au atoms are indicated with white circles, whereas subnanometer Au clusters consisting of only a few atoms are marked by black circles. Schematic diagrams of 0.5 nm bilayer clusters containing 10 atoms and 0.2–0.3 nm planar monolayer clusters of only 3 or 4 atoms are given in E and F, respectively. Reprinted with permission from ref 18. Copyright 2008 The American Association for the Advancement of Science.

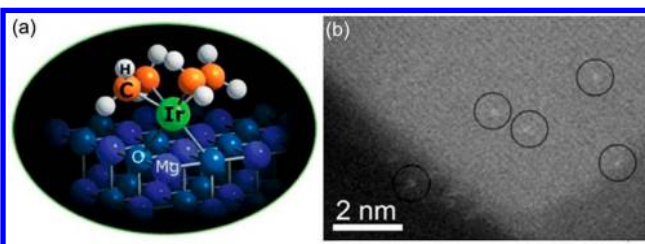


Figure 17. (a) Structural model of a single-site Ir complex on MgO powder. (b) HAADF-STEM image of the supported complex catalyst showing individual Ir atoms in bright contrast (indicated by black circles) on MgO support. Adapted with permission from ref 269. Copyright 2009 Royal Society of Chemistry.

Isolated Promoter Atoms. The ability to image single atoms also has a significant role in the evolution of promoted catalysts. Promotion of a catalyst with a third kind of atom is a way either to increase the selectivity by site-isolating or to improve the long time stability of the catalyst. The effect of promotion is

well-known, but the state (isolated or cluster), locations of the promoting atoms (on or in the active phase or present on the support), and their dynamic response to the reactive environment are objects of many intensive studies. Theoretically, with aberration-correction STEM techniques, it is possible to elucidate promoter atoms of high atomic number Z in catalyst formulations by direct HAADF-STEM imaging. However, it is far from easy to image promoter atoms in an industrial catalyst.

Platinum group metals (Pt, Ru, Re, Ir) are often used as promoters, for instance, to promote Fischer–Tropsch catalysts either to lower the reduction temperature of the oxide catalyst, preserving the high surface area, or to alter the surface configuration.²⁹⁰ Shannon et al. promoted 20%Co-alumina catalysts by postimpregnation with Pt, Ru, Re, and Ir promoter precursors respectively and tried to localize the promoter atoms on catalyst after reduction in a nitrogen stream with 5% hydrogen followed by a surface passivation using 1% O₂ in nitrogen at 35 °C for 16 h.²⁹¹ Some promoter atoms could be imaged by Cs-corrected HAADF-STEM. The imaged Re, Pt, and Ir promoters are mostly isolated atoms; Ru atoms are

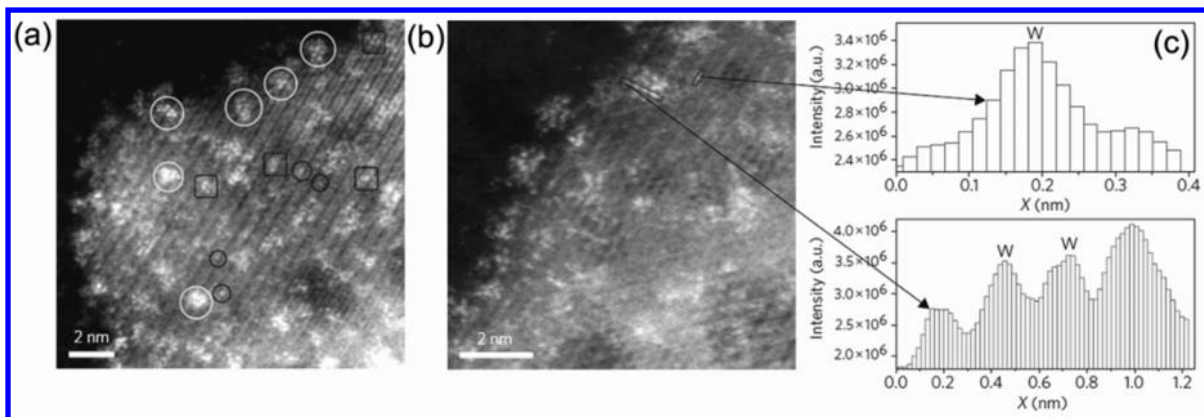


Figure 18. HAADF-STEM images of a postimpregnated WO_x/ZrO₂ catalyst (a, b). Black squares indicate surface poly-tungstate species with several tungsten atoms. White circles indicate WO_x clusters with diameters of ~0.8–1.0 nm. Line intensity profile (c) from a single tungsten atom and across a WO_x cluster as indicated in b. Reprinted with permission from ref 17. Copyright 2009 Nature Publishing Group.

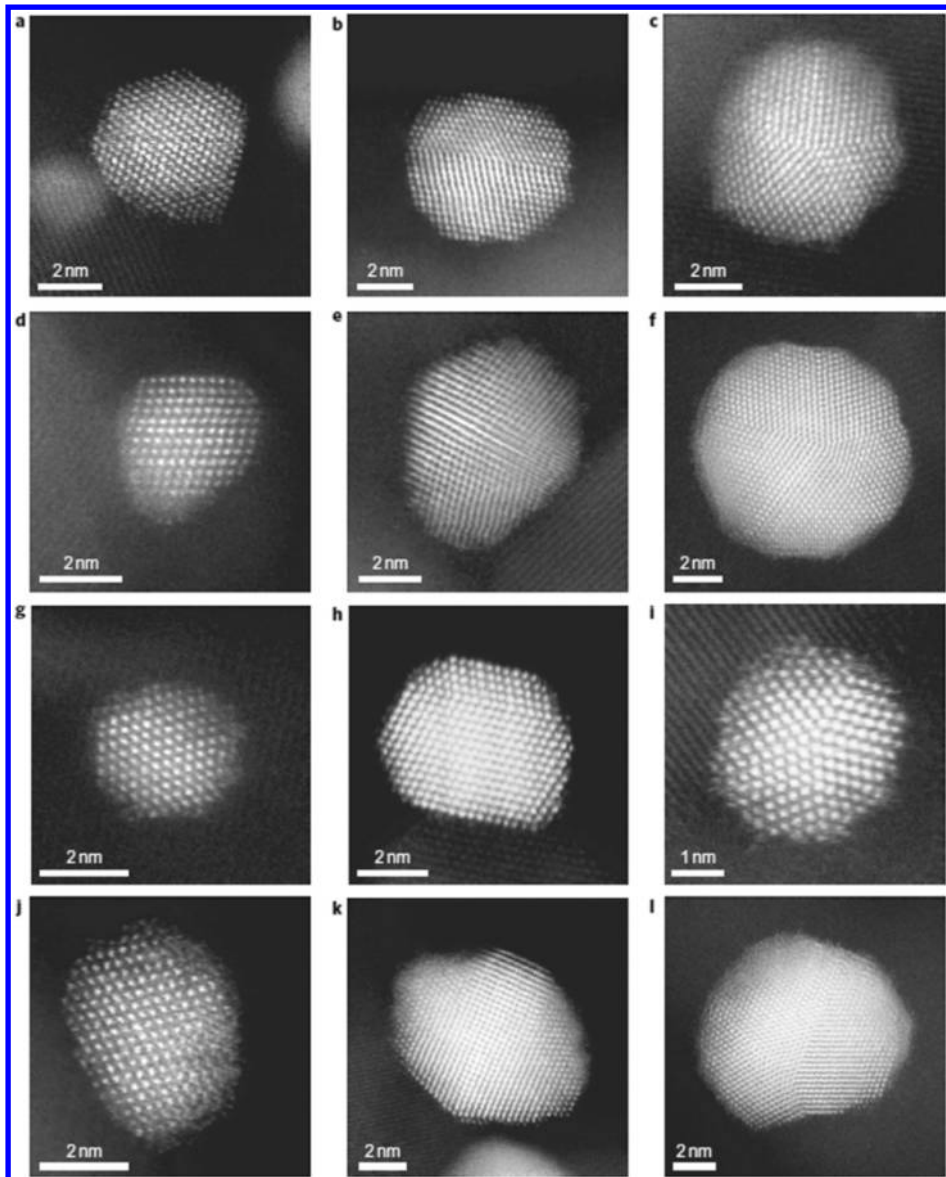


Figure 19. Representative HAADF STEM images of supported gold nanoparticles on TiO_2 with increasing particle size. Panels a, d, g, and j show sub-octahedral particles, panels b, c, e, f, h, i, k, and l show characteristic singly twinned or decahedral-type particles. Reprinted with permission from ref 311. Copyright 2011 Nature Publishing Group.

mostly in cluster form within Co particles. However, not all promoter atoms can be imaged or detected by EELS. Their in-depth analysis and simulation show that the visibility of dopant atoms depends on the location of atoms in the catalyst with respect to the electron beam. Re, Ir, and Pt promoter atoms located near the exit surface or in the lattice of the specimen produce stronger contrast than atoms on or near the up-surface of the sample where electrons incidence. For Ru atoms, the contrast is very low regardless of their locations.²⁹⁰

In the literature, the variation of Z-contrast with depth parallel to the incident electron beam was proposed as a method to determine the depth position of dopant atoms in a specimen, but it is obvious that this is only applicable to specimens with uniform thickness. It should also be kept in mind that the observed bright contrast in a HAADF-STEM image may not be necessarily from the dopant atoms. Also, contamination of any heavy atoms can produce bright contrast in such an image. EELS measurements, if available, on the

localized bright spot should be used to check the nature of the observed atom.

The questions how the promoter atoms behave under reaction conditions, for instance, whether they migrate together to clusters or they diffuse deeper into the catalyst particles, or from the bulk to the surface, remain to be answered.

Identification of Oxide Clusters. The power of HAADF-STEM imaging is also demonstrated to identify the active $\text{Zr}-\text{WO}_x$ clusters supported on a ZrO_2 crystallite for light alkane ($\text{C}4-\text{C}8$) isomerization at low temperature.¹⁷ Due to its high thermal stability and resistance in hydrogen, oxygen, and water atmospheres, WO_x/ZrO_2 is considered as an alternative to sulfated zirconia catalyst,^{292,293} Despite the many characterization studies and catalytic tests applied to this system,^{17,294} the size and the atomic structure of WO_x clusters, when bonded to a ZrO_2 -support, were under discussion for a long time. Kiely and co-workers touched this issue by means of aberration-corrected STEM.¹⁷ Using HAADF-STEM imaging, they could

identify the coexistence of mono- and poly-tungstate clusters supported on ZrO_2 (Figure 18). The line scan in Figure 18 revealed that the atom at the periphery of a cluster has a lower intensity—an indication of the successful inclusion of a zirconium atom within the WO_x cluster.¹⁷ With the development of aberration-corrected STEM, it is now possible to probe sub-nanometer V–Ti, V–Zr, and Cr–Zr clusters on TiO_2 or ZrO_2 supports, respectively.⁵⁷

The advent of an increasing number of observations of single atoms dispersed on supports seems to shine new light on our understanding of dispersed systems. It was always assumed that in heterogeneous catalysts particles or nanostructures of active metals form the reactive part of a catalyst, whereas in molecular catalysts single atoms surrounded by a ligand shell are active. If we consider the support as a large ligand, then we conceptually see vanishing the distinction between molecular and heterogeneous catalysis. At practically relevant metal support systems with low loadings (below 0.5%), the metal component was often found to be “invisible” to conventional TEM. The active phase was thus assumed to be located in pores or buried into the support. These unsatisfactory hypotheses find now a simple and convincing explanation: the “old” TEM instruments were simply inadequate to detect very small nanoparticles. The development in (S)TEM instrumentation, especially Cs-corrected HAADF-STEM, has thus opened the door to a new world of active sites consisting of ultrasmall particles or individual atoms²⁹⁵ that we possibly used for a long time already without knowing about their existence.

A critical question occurs in this context: We mostly see the individual atoms in combination with larger conventional particles. Assuming that the metallic properties of a catalyst are of critical importance for its catalytic function (through e.g. donating electrons from the pool of a conduction band with a well-defined energy), it may be questioned that individual atoms are really the active phase. The reduced electron exchange capacity of individual atoms of single atoms on a support stems from the necessity to form a strong bond between the individual atom and the support. If these bonds would not be strong, then coagulation both under the electron beam of the TEM and during operation would quickly remove these atoms.²⁹⁵ The fact that we see little or no beam damage clearly evidences that a stable electronic structure exists shared between the atom of observation and the support. In this instance the missing beam damage is a diagnostic tool for the unobservable chemical bond of the objects of interest.

6.2. Atomic Structure of Metal Nanoparticles

Electron microscopy is the unique tool through which the atomic structure of individual nanoparticles was explored and resolved.^{92,296–304} Microbeam electron diffraction (micro-diffraction) and special imaging techniques (bright- and dark-field imaging, weak-beam imaging) can be applied to single particles for the determination of structure and morphology.^{305,306} With the user-friendly interface of a modern TEM and the development of the CCD technique, these valuable and power methods are, unfortunately, replaced by direct imaging at high magnification. For small particles (<15 nm in size), high-resolution imaging has been developed into a routine tool for elucidating the particle structure with atomic resolution.^{93,307}

The mostly reported structures of small metal particles are multiply twinned or single crystalline structure with a relaxed lattice. The structural model of multiply twinned particles (MTP) was first introduced by Ino^{305,306} to interpret the

abnormal (111) spots in electron diffraction pattern and image contrast of small gold particles. Thanks to the high-resolution TEMs, the MTP structures of nanoparticles and derivations from them have been well resolved since 1980; the most representative of them are decohedron and icosahedron. Other common structures of metal nanoparticles are cuboctahedron, and these with spherical shape minimizing the surface energy. Since high-resolution image is, from nature, phase contrast, image simulation is necessary for a correct interpretation of the obtained lattice fringes.^{308–310} Details can be found in numerous comprehensive reviews referenced above and therein.

Since the contrast in a HAADF-STEM is due to high-angle Rutherford scattered electrons and the intensity is proportional to Z^2 , there is a tendency to use the HAADF-STEM technique to obtain a lattice-resolved image of nanoparticles.⁴³ The contribution due to diffraction contrast in such images is at a minimum level, so its interpretation is more intuitive and straightforward. A particularly elegant example of an HAADF-STEM image of gold nanoparticles is presented by Lopez-Sanchez et al.,³¹¹ shown in Figure 19. The gallery of Figure 19 summarizes the most representative morphology and microstructure of metal particles, including these of cuboctahedral, singly twinned, and multiply twinned. Also the lattice fringes of relatively large gold particles (Figure 19f, k, l) can be imaged with HAADF-STEM.

Multiply twinned or spherical metal particles are terminated with low index facets, mostly the (111) or (100) planes in the case of face-centered-cubic metals. S.G. Sun et al. studied a series of Pt-group (Pt, Pd, Au, Rh, Ir, Ru, and Os) nanocrystals with high-index faces (e.g., Pt{730}, Pd{730}, and Au{711}) and found that those particles are high-performance electrocatalysts.^{312–318} Such high-index surface particles are large in size and are single-crystalline but cannot be prepared with colloidal or deposition methods rather than electrochemically.

High-resolution TEM and HAADF-STEM give only the 2D projection of 3D nanoparticles. As mentioned above, image simulation constructing a model with preknowledge of the structure or Wulff-construction is needed to get the possible morphology from a single projection. But the fine inner structure of such nanoparticles may be lost in 2D projection. The recent progresses in 3D electron tomography of atomic resolution^{319–323} revealed detailed 3D structure of nanoparticles (Figure 20b–f) that otherwise cannot be accessed in conventional 2D projections (Figure 20a).³¹⁹ Atomic steps at 3D twin boundaries, the 3D core structure of the edge, and screw dislocations can be obtained.^{319,320}

The shape of a small particle depends on the preparation parameters and its interaction with the environment. Nanoparticles on strongly interacting supports, such as the ones often used in catalysis, have single crystallite structure terminated with low index surface planes. The shape of a small particle is a function of chemical potential and can change at high temperature, especially due to strong metal–support interaction under reducing/oxidizing atmosphere. Many efforts have been made to observe the shape and dynamics of nanoparticles in catalysis to understand reaction mechanisms.^{223,324,325} The Cu/ZnO system is a catalyst for methanol synthesis. The surface termination of Cu can be different when Cu nanoparticles are exposed to reducing–oxidizing gases. Changes of adsorbed gases on the surface of Cu particles result in changes in specific surface energy and such reconstructing. This surface reconstructing and dynamics of morphology

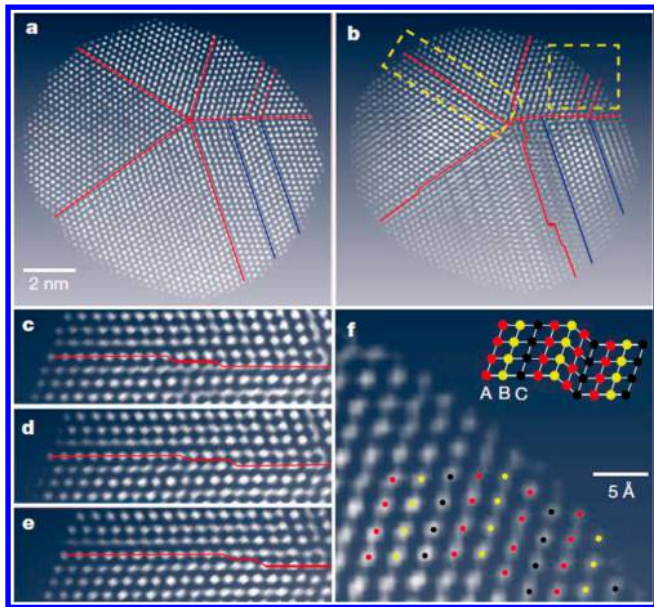


Figure 20. Example showing the advantage of 3D atomic resolution electron tomography in evaluation of the inner structure of nanoparticles. The 2D projection image in (a) suggests that the imaged particle is a multiply twinned decahedron with additional grain boundaries (red- and blue-colored). The internal slice from the tomographical series reveals atomic steps at the grain boundary (in yellow-marked regions); the distance between the blue-colored boundaries is larger than that in (a). (c) is the enlarged view of a grain boundary in (b). (d) and (e) are sliced above and below the slice of (c). (f) shows a stacking fault in an internal slice and the corresponding structure model. Reprinted with permission from ref 319. Copyright 2013 Nature Publishing Group.

(wetting) of Cu particles on ZrO play an important role in methanol synthesis from CO/CO₂/H mixture.²¹⁹ In addition to surface termination and shape reconstructing, lattice stress has also to be identified to influence the catalytic performance of a catalyst. By means of a combined TEM-XRD approach, a direct correlation between the activity of the catalyst and the planar defects and lattice strain in Cu particles in Cu/ZnO/Al₂O₃ catalyst for methanol synthesis was established.³²⁵

In addition to the impressive contrast of the beautiful particles imaged along a main crystallographic zone axis that were preferentially shown in many publications,^{311,326} the

majority of particles are not imaged (the deduced question is how representative is an TEM study if only selected particles, usually with high symmetry, are imaged). Not all preparations of a catalyst or reactions occur under equilibrium condition so that a large number of particles may have complex shapes and unknown internal structures.⁴⁴ Such metastable particles may exhibit interesting surface chemical properties and may behave differently from the nanoparticles with relaxed structure when irradiated with an electron beam.²⁷² Unfortunately, such particles are mostly screened off for imaging by operators aiming to get impressive lattice-resolved contrast of “representative” particles. Figure 21 shows that both the shape and the inner structure of a raft-like Au particle of irregular form supported on active carbon behave in a dynamic way under an electron beam. The observed fluctuation in shape and inner structure cannot be explained by a disorder–order transition, but rather by the energy transfer from incident electrons to the small particle. More detailed discussion about the electron-beam induced damage or structure modification of small particles is given in section 8.

The previous example has shown an application of TEM in catalysis that is not frequently discussed in explicit form. As it is still difficult to observe catalyst nanoparticles in operation with atomic resolution, the electron beam in the TEM may be used as stimulus to observe in a given system with high resolution the potential of structural dynamics. If we observe an object being fully stable in TEM, both in its inner structure and at its surface, then we may conclude that this object has a low propensity toward structural dynamics under catalytic conditions. This type of dynamics does of course not include reactant-induced dynamics, meaning structural transformations requiring a reactant in addition to an energetic stimulus, as provided by the electron beam. If the object under study does, however, respond to the stimulus either at its surface (only safely observable with aberration-corrected microscopes) or in its internal structure, then we may safely assume that under catalytic conditions the object will exhibit structural dynamics. An extension of this application of TEM is the observation of spectroscopic changes of a catalyst system under the electron beam, as can be provided by recording a time series of EELS spectra.³²⁷

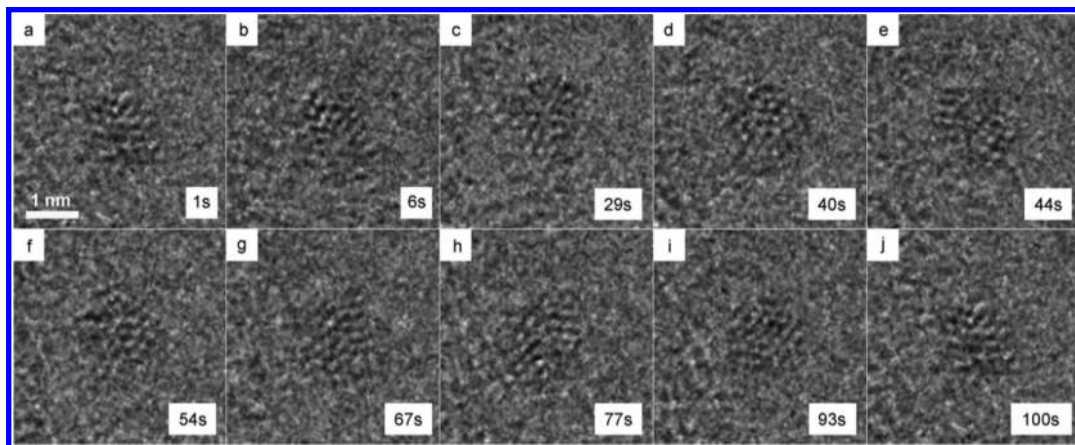


Figure 21. Dynamic changes of a small Au particle supported on activated carbon under electron beam irradiation at various observation times. Reprinted with permission from ref 272. Copyright 2011 WILEY-VCH Verlag GmbH & Co. KGaA, Weinheim.

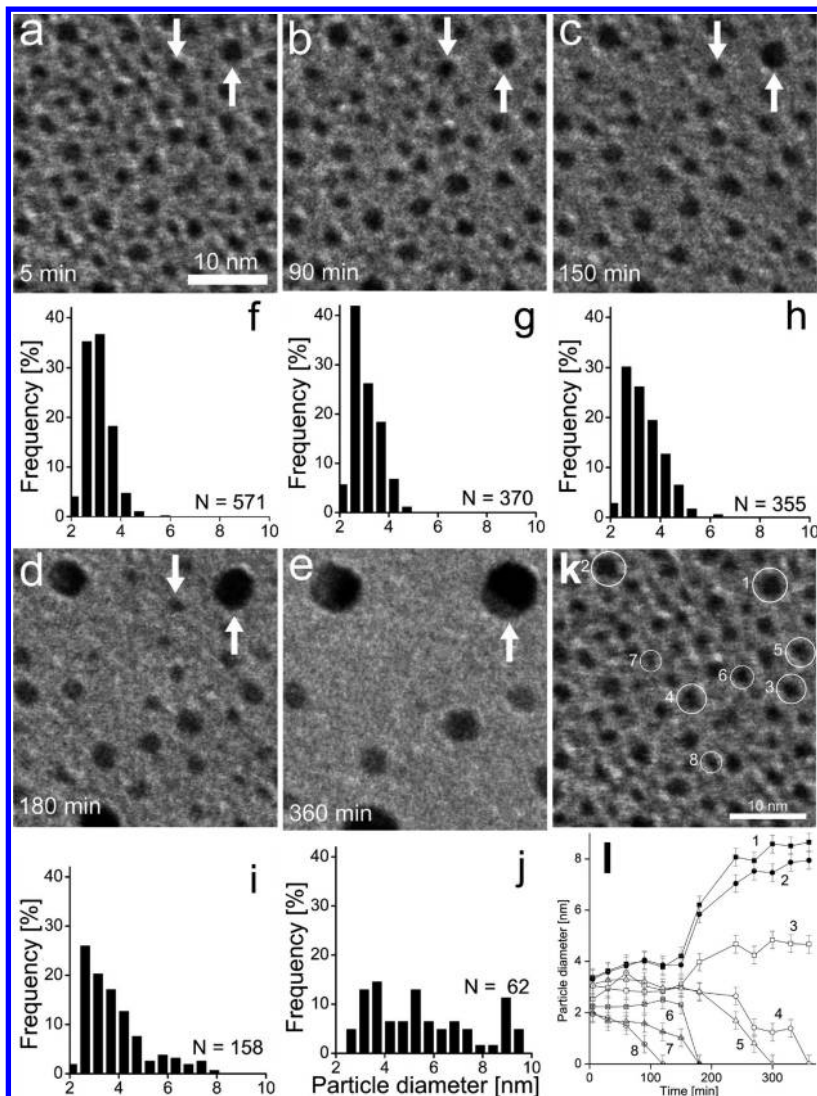


Figure 22. *In-situ* TEM images (the $40 \times 40 \text{ nm}^2$ part selected from $130 \times 130 \text{ nm}^2$ area) of Pt supported on Al_2O_3 catalyst in 10 mbar at 650°C (a–e), the histogram of the particle size distribution measured from the full images ($130 \times 130 \text{ nm}^2$) (f–j), eight circled particles in part a for time-resolved analysis (k), and the diameter of circled nanoparticles as a function of time (l). Adapted with permission from ref 328. Copyright 2010 American Chemical Society.

6.3. Determining Size Distribution and Dynamics of Small Particles with TEM/STEM

One of the most important applications of TEM in catalysis is the determination of the particle size distribution (PSD) of supported nanoparticles. The PSD can then be used to calculate the dispersion of an active phase (the percentage of atoms on the surface) and the specific surface area of an active phase. One example of the dynamic PSD study of platinum nanoparticles determined with TEM under 10 mbar air at 650°C is given in Figure 22.³²⁸ The Pt particles undergoes an Oswald ripening process, and the diameters increase with the increase of sintering time (see Figures 22a–e). The PSDs change correspondingly as a function of sintering time, as shown in Figures 22f–j. Focusing on the dynamic changes of Pt nanoparticles, eight selected particles were tracked (circled in Figures 22k–l). Detailed analysis reveals that the sintering mechanism of Pt nanoparticles supported on Al_2O_3 mainly is correlated to the size and the distance of the adjacent nanoparticles.³²⁸

Since the sizes of catalytic particles are usually in the nanometer range, high-magnification or even high-resolution TEM experiments are needed for this purpose.^{44,329–332} However, the prerequisite for a useful PSD is that all particles, at least as much as possible, are imaged and counted to give a statistically meaningful result. Especially particles smaller than 2 nm or larger than 20 nm must be included in the statistics. In practice, however, the smaller ones are often lost in the statistic due to the too weak contrast, and the large ones are intentionally ignored as singularity of the preparation. The PSD obtained in this manner is an artificially “averaged” one and cannot represent the true size distribution of a catalyst system. In the case that ultrasmall particles are counted, the diameter of the particles must be precisely measured on the digital images. One should always keep in mind that the TEM image represents only a projection of the sample in the beam direction.³³³ Parts of supported nanoparticles may be not visitable due to the geometry, thickness, and orientation of supports in the TEM with respect to the electron beam. Also imaging conditions may have an influence on the final PSD, as

discussed below. It is more than just taking images and accounting particles to get reliable PSD.⁴⁴

Already in the 1980s, Heinemann and Soria have pointed out that the visibility of small particles depends very strongly on the imaging conditions of the microscope.³³⁴ For instance, when amorphous carbon is used as support, the contrast of small particles of 1 nm or smaller cannot be distinguished from the phase contrast background of the support. Any analysis of the size distribution of such small metal particles is inconclusive or fails if the focus, astigmatism of the lens, and drift of the specimen are not optimally controlled.³³⁴ In the case that the supporting materials are crystallite oxides, depending which space frequency is transferred by the objective lens, either only the lattice fringes of the oxide support are sharply produced, obscuring any contrast from very small particles and thus the presence of them (Figure 23a), or the very weak mass contrast

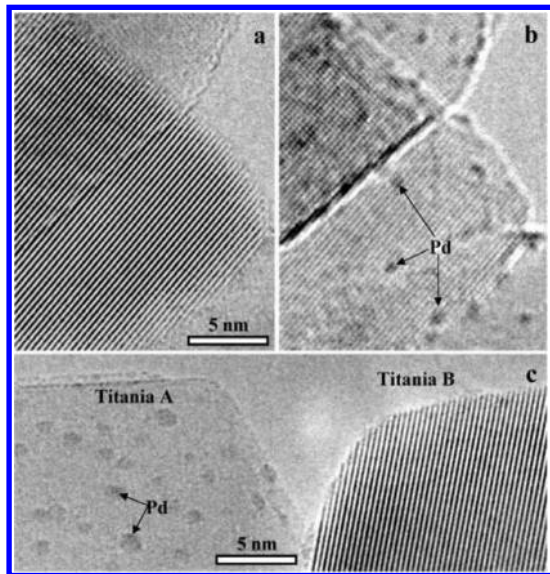


Figure 23. HRTEM images of a titania-supported palladium catalyst illustrating the variations of the visibility of small particles when the defocus changes (a and b). In (c), the electron micrograph shows two titania supports with (Titania A) and without (Titania B) palladium nanoparticles, respectively. The palladium clusters supported on Titania B are visible when changing the objective lens focus. Reprinted with permission from ref 44. Copyright 2004 Cambridge University Press.

of the particle (smaller than 2 nm) vanishes in or is overshadowed by the defocused lattice fringes of the oxide support (Figure 23b), making any accurate measurement of the particle size rather difficult.⁴⁴ Also, different heights of oxide crystallite on the sample grid can give false appearance of the catalyst if the image is taken with a unique focus value. The micrograph in Figure 23c may give the impression that palladium nanoclusters supported on titania are preferentially dispersed onto the left crystallite (Titania A) but not on the right one (Titania B). But this is wrong, and the image is misleading, since Titania A and Titania B are two pieces of the catalyst that are only located on the TEM grid at different heights along the direction of the electron beam.⁴⁴ Several micrographs must be taken from the same specimen area at different imaging conditions to differentiate the particles from the background.³³⁴

Until a few years ago bright-field imaging of a TEM was the most used mode for the determination of particle size distribution. Now with the widespread of field emission STEM, HAADF-STEM imaging is becoming the choice for the study of tiny clusters and small particles of high Z atoms, as discussed in previous section. It is much easier to image ultrasmall metallic nanoparticles supported on amorphous carbon film, graphene, activated carbon or on metal oxides, as it is very often used in heterogeneous catalysts.^{84,336–338} The advantage to use HAADF-STEM than HR-TEM to determine PSDs is demonstrated on Ru&Pd nanoparticles supported on carbon and on iron oxide (Figures 24). Numerous small Ru/Pd

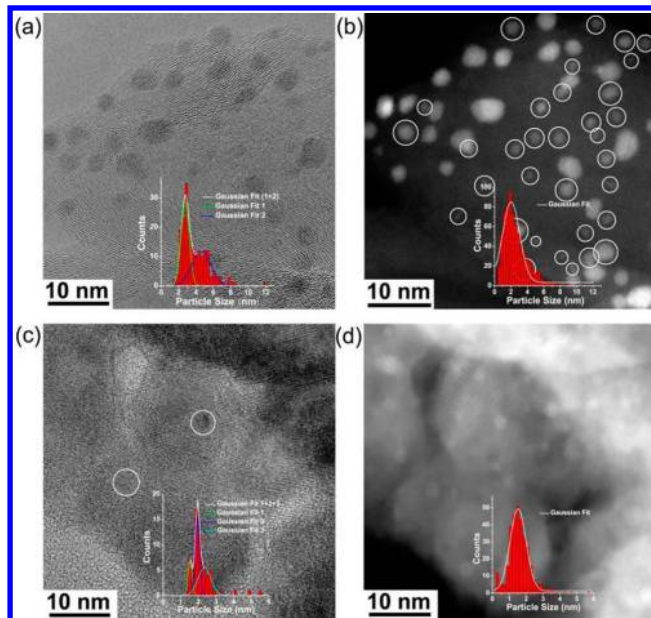


Figure 24. HRTEM (a) and HAADF-STEM (b) images of Ru/CNTs, and HRTEM (c) and STEM (d) images of Pd/FeO_x catalyst, respectively, showing different visibilities of small particles when imaged with these two methods. The insets are the corresponding PSDs. Some small particles (circled in part (b)) are not visible in (a). Most of the Pd nanoparticles in part (d) are invisible in part (c), except for the circled two particles. Adapted with permission from ref 335. Copyright 2011 WILEY-VCH Verlag GmbH & Co. KGaA, Weinheim.

particles are only visible in HAADF-STEM image, but not in HR-TEM. The total number of particles accounted and the calculated PSD differs therefore significantly, both for carbon and oxide support.³³⁵ HAADF-STEM is strongly recommended for the determination of PSD when the support is oxide.

For the small clusters imaged in STEM with low signal-noise ratio (for instance those in Figures 17 and 18), a direct measurement of the cluster size from the raw image could be inaccurate. In addition to the noise in the image, the obtained intensity profile across the clusters can be further modified by any blurring effect in the STEM image—initial probe size, beam broadening, and cluster orientation.³³⁹ A Gaussian blur function can be used to smooth the noise in the images: each pixel is convoluted with a Gaussian normal distribution function with a standard deviation so that a clearly recognizable contour of the particle can be obtained.³⁴⁰ Care must be taken not to oversmooth the profiles and thus enlarge the size of the clusters artificially. Some other techniques, for instance,

plasmon imaging,³⁴¹ have been tested to get images in which the particles are distinguishable from the support.

The size distribution is only meaningful if the acquired TEM or STEM images are not selected or zoomed from the catalyst and the number of subsequent digitally processed particles should be no less than a few hundreds. Although efforts are continuously made to develop a reliable algorithm for measuring PSD from TEM/STEM images,³⁴² it remains still a rather difficult task to get statistically meaningful PSD of supported catalyst.⁴⁴ The determination of the mean particle size, PSD, and dispersion of nanoparticles should always be complementarily performed with XRD and gas chemisorption experiments.³⁴³

6.4. Location of Nanoparticles on Support

In addition to the size distribution and the dispersion of the nanoparticles/clusters, their spatial distribution is of importance for understanding the catalytic performance of a supported catalyst. Mesoporous materials (silica, titania, and carbon) or nanotubular materials (CNTs) are newly developed materials and frequently tested as catalyst support,³⁴⁴ among many other reasons also due to the so-called confinement effect.^{345,346} Care must be taken when using TEM to determine the location of nanoparticles on porous or tubular support—keeping in mind that TEM gives only a 2D projection of a 3D structure. Nanoparticles supported on CNTs could be either inside or outside the tube, but this information is lost due to the 2D projection. Sometimes, simple tricks such as tilting the specimen in TEM or using SEM can help to give a correct answer.^{347–349} Haller et al. developed an elegant method to calculate the fraction of nanoparticles inside/outside a CNT by simply measuring the inside and outside diameters of the CNT in a 2D projection.³⁵⁰

The development of the 3D electron tomography technique on standard (S)TEM renders possible, without “tricks”, the determination of the spatial distribution of catalyst particles in porous^{26,351,353} and in tubular structures.^{347,354} One typical example of a reconstructed electron tomogram of bimetallic Pt–Ru particles supported on and within a disordered mesoporous silica catalyst is displayed in Figure 25a.^{26,351} Such a tomogram gives a general impression of what the surface morphology of the support looks like and where the observed particles are anchored. By making the reconstructed 3D image of the support partially transparent, a better illustration of the locations of nanoparticles throughout the silica support, also inside the pore or in the concave, can be obtained describing the 3D distribution of the particles.^{26,351} Quantification could be made giving the statistics of particles supported on or within the support, respectively. In addition, electron tomograms allow also the analysis of the nature of the pore network and the concave/convex surface, enable the determination of the local surrounding of the anchored particles, and establish the relationship between the local morphology (for instance the curvature) of the support and the location of adsorbed nanoparticles.

The new possibility of (S)TEM to determine the space distribution of supported catalyst and the 3D morphology of the support brings some interesting aspects in catalysis. For instance, it is found that nanoparticles have the propensity to preferentially locate on the grain boundaries, on the stepped site of the oxide support,¹⁸⁹ or in crevices between the individual titania grains,³⁵² as shown in Figure 25b,c. The location of nanoparticles on different sites renders them with

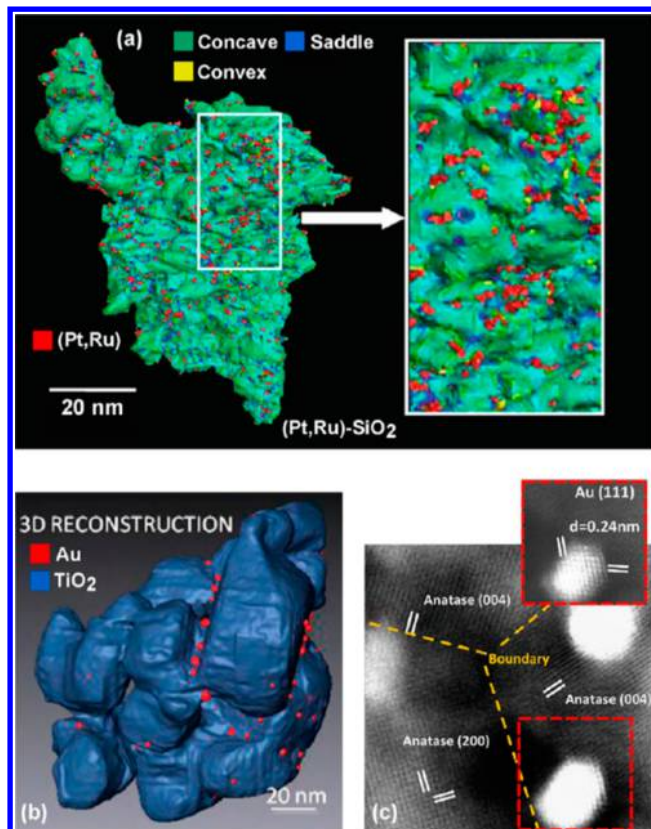


Figure 25. (a) Electron tomographic reconstruction of (Pt, Ru) nanocatalysts supported on a disordered mesoporous silica. The nanocatalysts (red) are preferentially anchored at the (blue) saddle-points.³⁵¹ (b) Surface visualization of Au nanocatalysts (red) supported on titania (blue) shows that most nanocatalysts are located in the crevices between titania crystallites; confirmed by the aberration-corrected STEM image in panel (c).³⁵² Reprinted with permission from ref 26. Copyright 2012 American Chemical Society.

different properties, for instance, the sintering resistance at high temperature.³⁵⁵

As impressive as such 3D and transparent views into the mesostructure of a catalyst are, as careful one has to be with its general applicability. The acquisition of tomographic data requires many images to be taken (about 50 images from exactly the same location of a catalyst). It is obvious that a strong stimulus for particle transformation or motion to the equilibrium location is given as well as structural dynamics within the particles may be turned on (see discussion in section 8). In addition the support can be damaged by the electron beam and get reduced, maybe only through the help of spillover processes at the locations of the metal particles. During the complex image contrast transformations needed to correct any possible drift and to reconstruct the information as shown in Figure 25, it may be quite difficult to detect signs of such transformations. In severe cases the reconstruction will fail, but in gradual cases or during rapid transformations the image may not reproduce the actual state of the catalyst.

To ensure the validity of the TEM information in general, it is highly recommended to verify the extractable information by complementary techniques, not only due to the reasons in the previous paragraph but also due to the frequently confronted question how is the zoomed (S)TEM information representative. X-ray diffraction and gas adsorption are useful but also routine quantitative methods that can be applied without

limitations to objects amenable to electron tomography. Failure to use such comparisons may give an incorrect impression about the active state of a catalyst, as the tomographic reproduction may describe a nonactive or damaged state of the active system.

6.5. Metal–Support Interaction

In catalysis, the role of the supports is not only the function to hold the active phase dispersively on a compared large object being accessible by reactant molecules. The metal–support interaction can be a function of chemical potential, which may positively or negatively influence the performance of the active phase, especially the lifetime of the catalyst. The phrase Strong Metal–Support Interaction (SMSI)^{356–358} is explicitly used for catalyst systems consisting of active metal particles on reducible support. The interaction under reducing conditions can induce an electronic effect (charge transfer between support and metal particles), changing the chemisorption capacity of the active phase, with passivation of metal particles with a surface layer preventing the interaction between the gas molecules and the metal surface, or the formation of alloy with the element of support. All these effects can change the performance of the catalyst and in the worse case deactivate it rapidly. The SMSI can be well studied by means of S(TEM) with its ability of imaging, diffraction, and spectroscopy being a perfect tool to study nanoobject with atomic resolution.^{310,359,360} However, it is recommended that any conclusion of (S)TEM study should be proved or supported by other techniques (for instance, adsorption). The topic has been comprehensively reviewed by many publications.^{49,361–363}

Imaging of Metal–Support Interaction. There are two modes in (S)TEM to study the metal–support interaction: profile imaging and plan-view imaging. In profile imaging mode, the specimen is tilted with the interface between the support and particle parallel to the electron beam.^{114,304,333,364,365} The advantage of profile-imaging is the possibility to study the interface structure and perimeter of the particle. An excellent example how to use profile imaging HRTEM to study SMSI of Rh- or Pt-containing catalysts supported ceria- or ceria-containing mixed oxides is illustrated in Figure 26.^{49,366–369}

In plan-view mode, the specimen is aligned with the electron beam perpendicular to the interface. The interface is not visible in this mode if the particles are large, but the shape of the particles and its change during activation or in reaction, the alloying between elements of particles and support, and the coalescence of particles can be observed by imaging and studied by diffraction and spectroscopy. Figure 27 displays a plan-view HRTEM study of Pt–Si intermetallic alloy formations and coalescence of Pt particles caused by metal–support interaction.^{370,371} Another example to study metal–support interaction of small particles in plan-view mode with atomic resolution is given in Figure 30.

A clear picture of the existence of metal–support interactions can be reached through the application of rigorous model systems.³⁷² The example shown in Figure 28 occurred from collaboration between a surface-science group³⁷³ and an electron microscopy group. We applied cross-sectional preparation of a model system consisting of a single-crystalline iron oxide layer grown as a multilayer film on a Pt single crystal support with Pt nanoparticles on top of the magnetite oxide layer. Under suitable preparation conditions, the iron oxide is capable of creeping from one edge of the Pt nanoparticle on top of its (111) termination, forming an overlayer of exactly

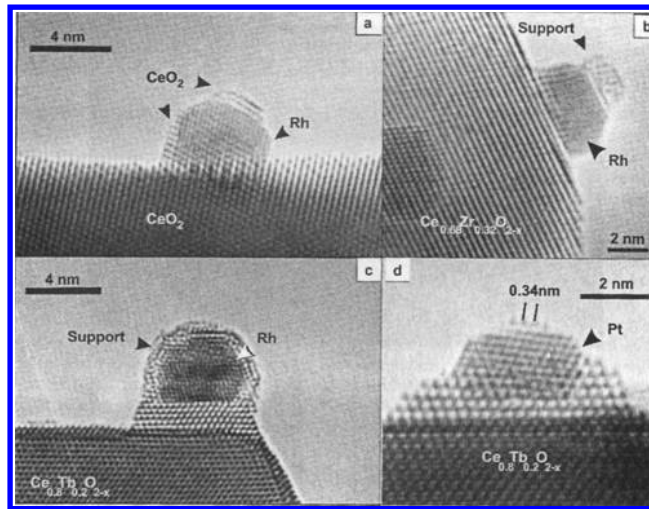


Figure 26. Profile imaging of metal–support interaction revealing the decoration of Rh or Pt particles by support material (a, b, c): the presence of thin surface layers (a) in 2.4 wt % Rh/CeO₂ reduced at 900 °C,³⁶⁹ thicker layer (b) in 0.78 wt % Rh/Ce_{0.68}Zr_{0.32}O_{2-x} reduced at 900 °C,³⁶⁸ and the formation of a “pedestal” (c) in 0.5 wt % Rh/Ce_{0.8}Tb_{0.2}O_{2-x} reduced at 900 °C. Note the growth between the support and the particle. Part (d) shows a Pt particle in 5 wt % Pt/Ce_{0.8}Tb_{0.2}O_{2-x} reduced at 700 °C being in the process of encapsulation.⁴⁹ Adapted with permission from refs 49, 368, and 369. (Ref 49: Copyright 2000 John Wiley & Sons, Ltd. Ref 368: Copyright 2000 American Chemical Society. Ref 369: Copyright 1995 Elsevier.)

one sandwich Fe–O with a complex relation to the supporting metal atoms. This composite is highly active in the model reaction of CO oxidation,²⁸⁶ as the overlayer prevents poisoning of the Pt by strongly adsorbed CO. Extensive use as catalyst destroys irreversibly the SMSI overlayer as it oxidizes the iron oxide. The example reveals the importance of complementary use of a scanning probe and electron microscopy to study such complex model systems. Without the surface science information it would be difficult to identify the nature of the overlayer species in Figure 28. Without the electron microscopic information the exact structural details and the origin of the overlayer would be difficult to describe.

Metal–Support Interaction of Nonequilibrium Particles. The particles in the previous model system are often in an equilibrium state terminated with a low index plane. Such a model system is an oversimplified catalyst but provides a clear picture of SMSI. However, it is rather difficult to apply the results obtained from a perfect single-crystal model directly to a real catalyst system, since the latter often contains particles of different sizes, structures, orientation, and morphologies that are not necessarily in equilibrium shape. One example is the well-developed Cu/ZnO high performance catalyst for methanol synthesis. For such a real catalyst, only qualitative TEM study on a selected individual particle may not give a full description of the existed SMSI.^{374,375}

The contact angle between the metal particle and the support is a measure of the equilibrium stage of the SMSI (the definition of a contact angle is illustrated in Figure 29n). As shown, for example, on Cu particles supported on ZnO or ZrO₂ for methanol synthesis, contact angles between particles and support (wetting effect) are measured based on electron micrographs (Figure 29a–m).^{325,376} On both supports, the contact angles depend on the Cu particle size, but not linearly.

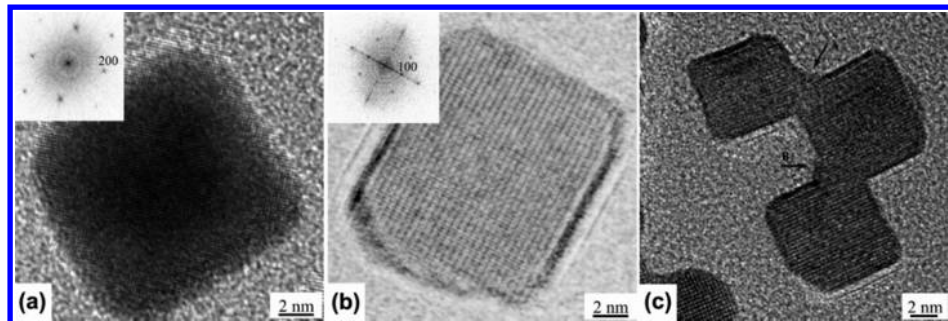


Figure 27. (a) HR-TEM of an as-grown Pt particle, (b) Pt₃Si intermetallic alloy formed during the reduction of Pt/SiO₂ in H₂ at 873 K. The corresponding Fourier transforms are inserted. (c) Coalescence of three particles caused by reduction. Adapted with permission from ref 371. Copyright 2003 Elsevier.

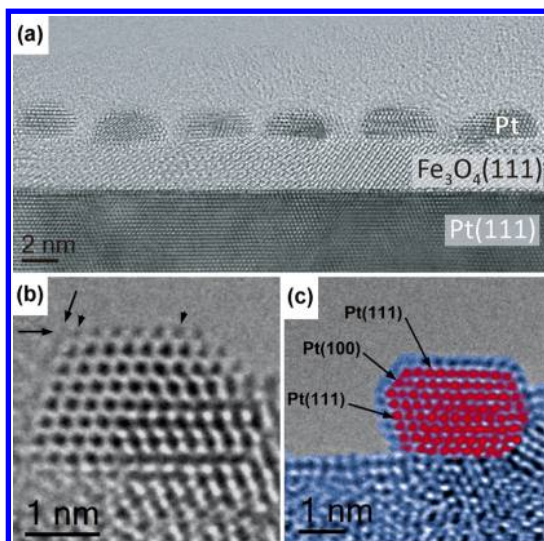


Figure 28. Model catalyst for the identification of SMSI of iron oxide over Pt nanoparticles. The sample was prepared on a Pt(111) single crystal by depositing first magnetite Fe₃O₄ as a single crystalline layer on top of it and subsequently depositing Pt on the iron oxide (a). The cross-sectional preparation of the system reveals the Pt nanoparticles on the surface of the iron oxide. One can see a layer of iron oxide covering as a nonepitaxial overlayer the Pt. In (b, c) an enlargement reveals the complex ordering relationship between Pt and iron oxide as well as showing that the iron oxide creeps on top of the Pt particle from one of the side facets and stops once it reaches the edge of the particle. Adapted with permission from ref 372. Copyright 2014 WILEY-VCH Verlag GmbH & Co. KGaA, Weinheim.

They reach a stable value around 120° at the Cu equivalent diameter of about 6 nm (Figure 29o). Smaller particles have smaller contact angle with the support. On average, the contact angles on ZnO are smaller than on ZrO₂. From the measured contact angle, the apparent work of adhesion can be calculated. The calculated apparent work of adhesion of Cu on ZnO is larger than on ZrO₂. This is the indication that ZnO support could provide a stronger interaction with small-sized Cu particles that could induce stronger epitaxial strain in Cu particles and thus increases their catalytic activity. Compared to the standard Wulff analysis typically applied in this field, this kind of analysis has an advantage of being applicable in the case of nonequilibrium particle morphology, which is typical for industrial catalysts.^{325,376}

This example shows how valuable information can be obtained for an in-depth understanding of a studied catalyst system with respect either to the structure–performance

correlation or the explanation of a possible reaction mechanism if (semi)quantitative analysis can be made on the recorded electron micrographs.

Size-Dependent Metal–Support Interaction. The performance of supported catalysts depends on the size of catalytic particles: the well-known example is the supported cobalt particles for Fischer–Troppe reaction, where the size of cobalt determines the selectivity of alkane, or the gold particles supported on metal oxide, where the activity depends strongly on the size of gold particles and the used supports. The study of the size dependent metal–support interaction is therefore interesting for the understanding of the size-dependent catalytic performance. The advances in TEM/STEM technique, especially the aberration correction, have revealed some new aspects in metal–support interactions.

Shibata et al. studied the atomic structure of gold nanoparticles on a TiO₂ (110) surface in plan-view mode (Figure 30) using aberration-corrected HAADF STEM.³⁷⁷ The big difference in the atomic numbers between gold (77) and titanium (21) or oxygen (8) allows the imaging of gold atoms in this observation mode. When the gold particles are smaller than 2 nm (Figure 30a and b), the gold atoms are preferentially anchored on Ti–O-column sites and on O-column sites of the TiO₂ surface, leading to the formation of an epitaxial and coherent interface (illustrated in the enlarged image in Figure 30f with colored atoms and arrowed lattice fringes). When the size of gold particles becomes larger than 3 nm (Figure 30c–e), the accommodation of the big lattice mismatch becomes a dominate driving force so that the gold–TiO₂ interface loses lattice coherency,³⁷⁷ and an incoherent interface and twinned gold nanoparticles with planar defects are formed. The histogram in Figure 30g shows that an interface transition with corresponding structure transition of gold particles occurs when the particle size increases. The DFT calculations reveal that a charge transfer occurs from TiO₂ to gold particles, but is only significant to two-layer gold clusters. For a large gold particle, the weak transfer is only constrained to a few atom layers at the interface and the electronic structure of the part far away from the interface is more like that of bulk gold.³⁷⁷ Experimental determination of charge transfer in the Au/TiO₂ system is discussed below.

Charge-Transfer between Metal and Support. Charge transfer is an important metal–support interaction and can be studied by spectroscopic methods such as X-ray absorption near edge structure (XANES) spectroscopy. There are also reports to use an electron microscopy associated technique to study the charge transfer between metal and support. Ichikawa et al. made an electron holographic analysis at the Au–TiO₂

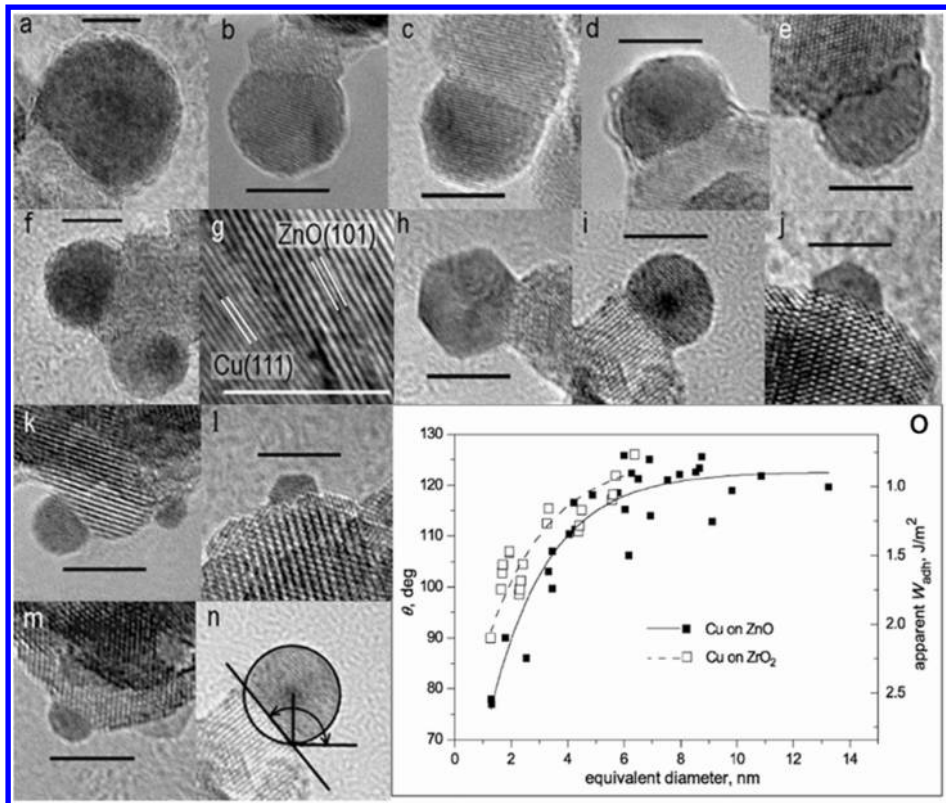


Figure 29. Typical morphologies of Cu nanoparticles supported on ZnO (a–g) and on ZrO_2 (h–n). Scale bars: 5 nm. The definition of contact angle between Cu nanoparticle and support is given in (n). (o) measured contact angle θ as a function of nanoparticles size. The right axis shows the calculated apparent work of adhesion $W_{adh} = \gamma_{Cu}(1 + \cos \theta)$. Adapted with permission from ref 376. Copyright 2006 Royal Society of Chemistry.

catalyst interface and found that there was interaction between gold particles and TiO_2 support at the interface additionally to the above-mentioned lattice matching.³⁷⁸ A detailed analysis of the mean inner potential based on electron holographic data suggests a charge transfer from gold particles to TiO_2 at the Au/ TiO_2 interface. (This observation of charge transfer from gold to TiO_2 support differs from the above-mentioned DFT calculation reported in ref 377). This electron transfer changes the electronic structure of gold particle to an electronic structure like Pt or Ir.^{379,380} Platinum-like catalytic behavior of Au⁺ species supported on titanosilicate was also reported for propylene epoxidation reaction with H_2/O_2 mixture.³⁸¹

In addition to electron holography, the charge transfer can also be studied by means of a combination of aberration-corrected STEM and EELS.⁵⁶ Sanchez et al. analyzed Ti L-edge EELS of TiO_2 substrate of a Au/ TiO_2 catalyst (Figure 31a) recorded on an area without and an area with a supported Au nanocluster (arrows A, C, and B, respectively in Figure 31b). In EELS of the Ti L edge without a gold cluster on the surface (Figure 31c), an energy shift in the Ti L-edge (<1 eV) of the free TiO_2 substrate compared with that bulk TiO_2 indicates the presence of not a small number of Ti^{3+} at the surface. The Ti L-edge spectrum at the interface of Au/ TiO_2 (Figure 31d) indicates a restoration of the electronic state of Ti atoms at the interface resembling the bulk TiO_2 (Ti^{4+}), as indicated by arrows in Figure 31d. This sophisticated experiment and analysis suggest a charge transfer from the substrate to the Au atoms at the Au/ TiO_2 interface.⁵⁶

The charge transfer determined by EELS (from TiO_2 support to Au atoms) is in the opposite direction as determined by electron holography. This is a typical example that electron

microscopy can provide very important information on a catalytic system, but the final conclusion must be made in correlation to the results of other techniques, to the prehistory of the catalyst (preparation and activation), and to the specific reaction. For Au catalyst, it is well-known that the active sites may involve Au⁺, whose presence results from the catalyst preparation (for instance precursor used) or from the catalyst treatment (for instance calcinations),^{382,383} or the active sites could be an anionic gold (Au⁻) species as a consequence of the interaction with a F center defect in the underlying oxide support.^{384–386} The TEM technique now can access these two kinds of gold catalyst.

6.6. Structure and Dynamics of Bimetallic Particles

Structure of Bimetallic Particles. It is known that the properties of metallic systems can be greatly extended by mixing elements to generate intermetallic compounds and alloys.^{387,388} Bimetallic particles can be prepared by coreduction, thermal decomposition, seeded-growth, galvanic replacement reaction, and noble-metal-induced-reduction.^{389,390} Some representative examples of bimetallic nanoparticles are depicted in Figure 32.³⁷² The structure and composition of bimetallic systems are rich, and the chemical and physical properties can be tuned by varying the composition³⁹¹ or the atomic ordering. The property of a bimetallic system is not only a linear combination of the property of individual metals but can also be enhanced due to synergistic effects. In catalysis,^{392,393} a bimetallic catalyst usually exhibits improved performance either with higher conversion, higher selectivity, or longer lifetime than monometallic catalyst. Bimetallic catalysts containing Au and Ni or Cu have found extensive use in the reforming of petrochemicals,^{394,395} while bimetallic Au and Pd particles are

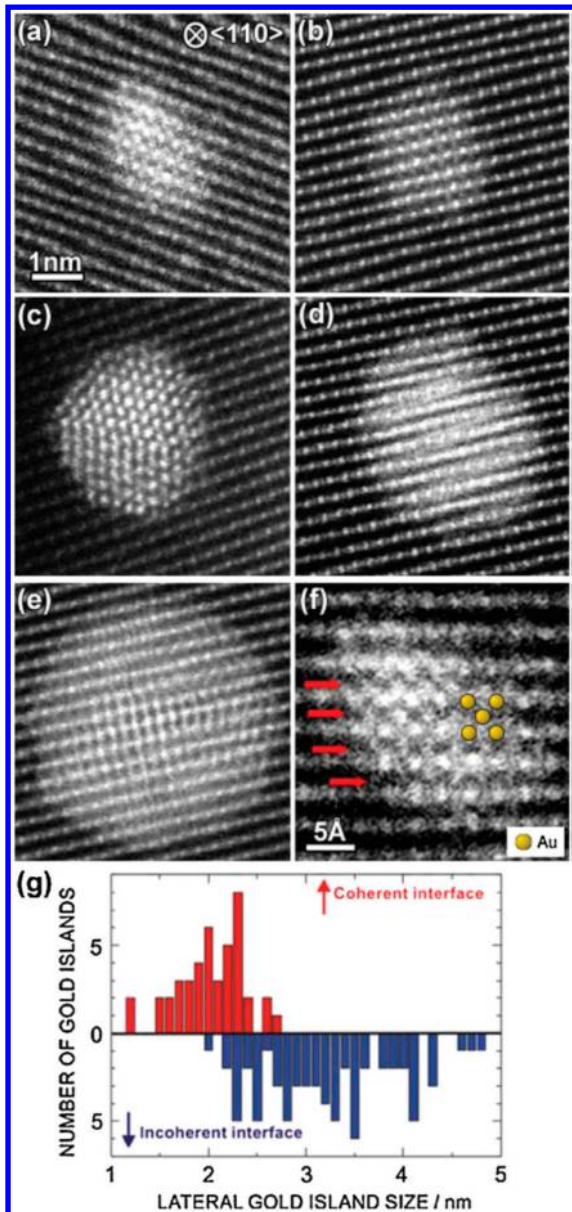


Figure 30. (a–e) HAADF-STEM images of gold nanoparticles on TiO_2 substrate. Small gold particles (a, b) exhibit a coherent, and big particles (c–e) show an incoherent interface with the TiO_2 (110) surface. (f) Enlarged image of the epitaxial Au structure of (a) showing the Au sites on top of Ti–O columns and on top of O columns (along the arrows). (g) Histogram of coherent or incoherent interfaces as a function of lateral size gold particle estimated from the HAADF-STEM images. Reprinted with permission from ref 377. Copyright 2009 American Physical Society.

of importance in liquid phase oxidation of alcohol.^{329,396–402} Bimetallic nanoparticles have a long history in the field of electroncatalysis.^{403,404} Replacing precious metals that are exclusively required for electrocatalysis and increasing the resistance to CO poison are the major driving forces for the study of noble metal-based bi- or even trimetalic systems in electrocatalysis.^{405–407} Adding transition metals to platinum catalyst is also aimed to accelerate the sluggish performance of platinum in oxygen reduction reaction.

According to their mixing patterns, bimetallic systems could have the following four (structural) types:³⁸⁷ (i) core–shell segregated nanoparticles consisting of a shell of A atoms

surrounding a core of B atoms (Figure 33a); (ii) subcluster segregated nanoparticles consisting of A and B subclusters sharing a mixed interface (Figure 33b); (iii) ordered mixing (alloy) or randomly mixed solid solution of A and B atoms (Figure 33c); (iv) multishell nanoparticle with alternating -A-B-A- shell structure (Figure 33d). These structural models are also applicable to tri- or multimetallic systems. Electron microscopy, with all its facilities mentioned above, is the most suitable tool in characterization of the structure and chemical composition of bimetallic or multimetallic systems.

For small alloying or solid solution bimetallic particles, phase contrast HR-TEM images do not contain any information on the element distribution: phase contrast image is not element specific. Due to this constraint HR-TEM of bimetallic particles is mostly used to identify the shape and to study the microstructural perfectness of bimetallic catalysts.⁴⁰⁸ For relatively large bimetallic particles, core–shell structure could be distinguished from alloy or solid solution by mass–thickness contrast.⁴⁰⁹ However, if prior information is not available, the assignment of core or shell to any element is not unique. The conventional HR-TEM and electron diffraction must be combined with EELS or EDX to determine the composition of bimetallic systems.^{329,408,410}

The HAADF-STEM imaging technique can overcome the obstacle of HR-TEM (partly) to solve the inner structure of bimetallic nanoparticles: the present different atoms have different cross-sections for large-angle Rutherford scattering of fast electrons, so the distribution of different atoms can be easily obtained for the identification of the above-mentioned structure type.^{411–413} Even with this easiness, compositional information by means of EELS/EDS should be available in tandem with structural information for an unique assignment of elements. The HAADF-STEM method is particularly useful for studying bimetallic particles where the constituent elements have similar unit cell parameters, for instance the fcc Pd–Pt, Pd–Au, and Ag–Au bimetallic system. They cannot be distinguished from single metallic particles by HR-TEM. The difference in atomic numbers is but a good reason to use HAADF-STEM.⁴¹⁴ Figure 34 shows various structure types of AuPd bimetallic nanoparticles on activated carbon and TiO_2 supports, respectively.³²⁶ Alloy structure (Figure 34a, b), Pd–core/Au-shell (Figure 34c, d), and Au–core/Pd–shell (Figure 34e, f) morphologies can be clearly identified.

Apart from imaging, other element-specific techniques, such as EFTEM, STEM-EELS, or STEM-EDX,^{121,124,415–419} are also powerful tools for clarifying the structure type of bimetallic nanoparticles. Figure 35 is a typical example how the structure and composition of a bimetallic system are accessed by a combination of STEM with EDS, element mapping (Figure 35a), and line scan (Figure 35b).²⁷³ For the studied Pd–Ga catalyst used for alkyne-selective hydrogenation, STEM-EDX analysis and elemental maps reveal a homogeneous composition of Pd and Ga of an atomic ratio of 2:1; that is, the bimetallic particle is Pd_2Ga (Figure 35a). A TEM-EDX line scan shows that the composition of Pd_2Ga particles remains unchanged after reaction (Figure 35b). This technique can also be used to distinguish alloyed or solid solution bimetallic nanoparticles from core–shell structure.⁴²⁰ Such techniques, with the help of aberration correction, allow the analysis of chemical composition down to atomic levels.

Adding a third metal atom to a bimetallic nanoparticle catalyst can modify the activity and improve the selectivity in some reactions. For instance, Ru_5Pt , $\text{Ru}_{10}\text{Pt}_2$, Ru_6Pd_6 , and

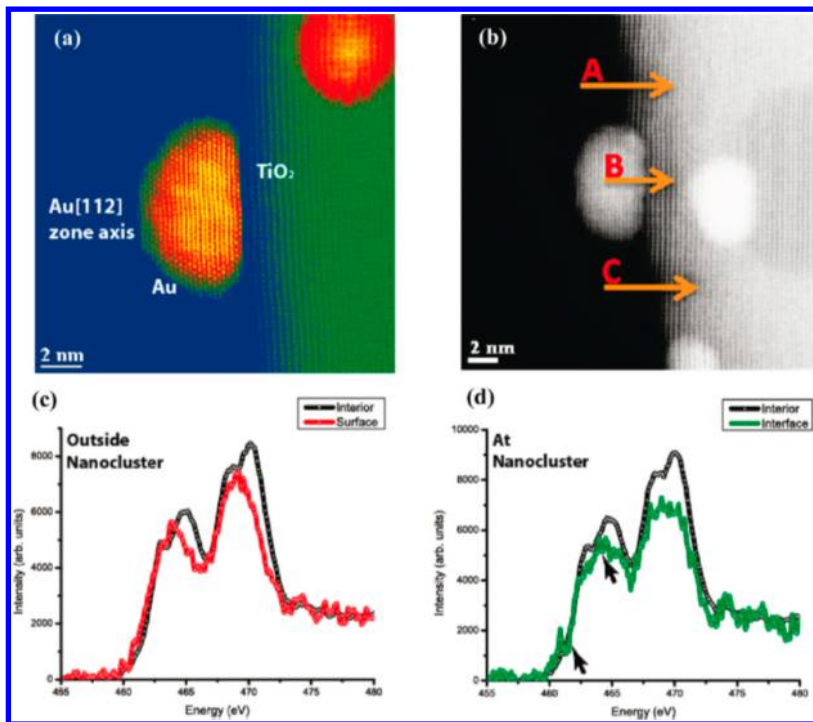


Figure 31. (a) Colored cross-sectional STEM image of Au nanoclusters on (-110) TiO₂. (b) Cross-sectional STEM image of Au nanoclusters on TiO₂ with arrows showing the position where EELS was taken. (c, d) Ti-L edge spectra for the regions (arrows) scanned in part (b). Reprinted with permission from ref 56. Copyright 2010 American Chemical Society.

Ru₁₂Cu₄ clusters catalyze the single step conversion of dimethyl terephthalate into 1,4-cyclohexanediethanol.⁴²¹ When adding tin to these systems, the trimetallic systems had better performance and Ru₃PtSn exhibits the highest activity and selectivity in this reaction. HAADF-STEM, HAADF tomography and high-spacial resolution EDX were shown to be unique techniques in evaluation of the dispersion, location, and composition of the bimetallic and trimetallic nanoparticles.^{422,423}

Also here, care must be taken to avoid any electron beam damage or induced structure modification of bimetallic particles in (S)TEM study. One specific damage for a bi- or multielement system is the selected depletion of one element when high beam current and long acquisition time are used for STEM-EDS or STEM-EELS measurement to ensure a suitable signal-to-noise ratio in the obtained spectra or mapping. If one constituent element is more sensitive to electron-beam irradiation than others, the EDX/EELS results can be deceiving. For instance, for each Ag X-ray signal detected, one Ag atom of a Au–Ag bimetallic system was lost due to sputtering and knock-on damage.²⁵⁹ A special method has been developed to retrieve the initial content of Ag by extrapolating the evaluation of the particle composition with the electron dose.²⁵⁹ The method could be extended to the analysis of electron-beam sensitive bimetallic nanoparticles of light elements and transition metals using EELS.⁴²⁴

Dynamics of Bimetallic Particles. We discussed the “static” structure of bimetallic nanoparticles and their determination using a modern TEM/STEM. The surface structure and composition of bimetallic nanoparticles prepared under specific kinetic conditions could be a function of chemical potential that very likely undergoes dynamic responses to chemical environments (in a reactant gas or an gas mixture, in solution or electrolyte), to electrical potential

applied,^{82,425} and to electron-beam irradiation, as shortly mentioned above. One future of the dynamic behavior of a bimetallic system differing from other catalysts is the depletion/leaching and/or the segregation of one constituent element and the consequence of this leaching/segregation. One other future could be the selective response of one element in an oxidative/reductive atmosphere (for instance, one element can be more easily or preferably oxidized than the other element) or the selective chemisorption of a gas molecule on one constituent element. The complexity of the solid–gas or solid–liquid interfaces under reaction conditions makes the study of the structural and chemical evolution of bimetallic particles and the understanding of corresponding catalytic mechanisms extremely challenging, as it is evidenced by numerous efforts using various *in situ* and *ex-situ* methods.⁴²⁶

Pt-based alloy nanoparticles were prepared as a possible solution to reduce the amount of platinum used in an electrode aimed for a realistic and cost-effective application of fuel cell technology and to accelerate the sluggish oxygen reduction reaction on Pt catalyst. Aberration-corrected STEM and EELS line profiles/mapping with angstrom resolution can provide details on the homogeneous or inhomogeneous distribution of added element (usually one of transition metals) and its response in electrocatalysis. One example is the compositional segregation of polyhedral Pt–Ni alloy nanoparticles (Figure 36a) and the structural behavior of these alloyed particles in voltammetric potential cycles.^{427–430} The Z-contrast STEM images (Figure 36b,c) reveal a nonuniform Ni distribution, further confirmed and quantified by EELS line profiles across the particles (Figure 36d–f). Pt and Ni metal are segregated and enriched differently: Pt atoms segregated preferentially along the edges and corners of the octahedra, while Ni atoms segregated preferentially on the {111} facet, as is colorfully illustrated in Figure 36g–i.

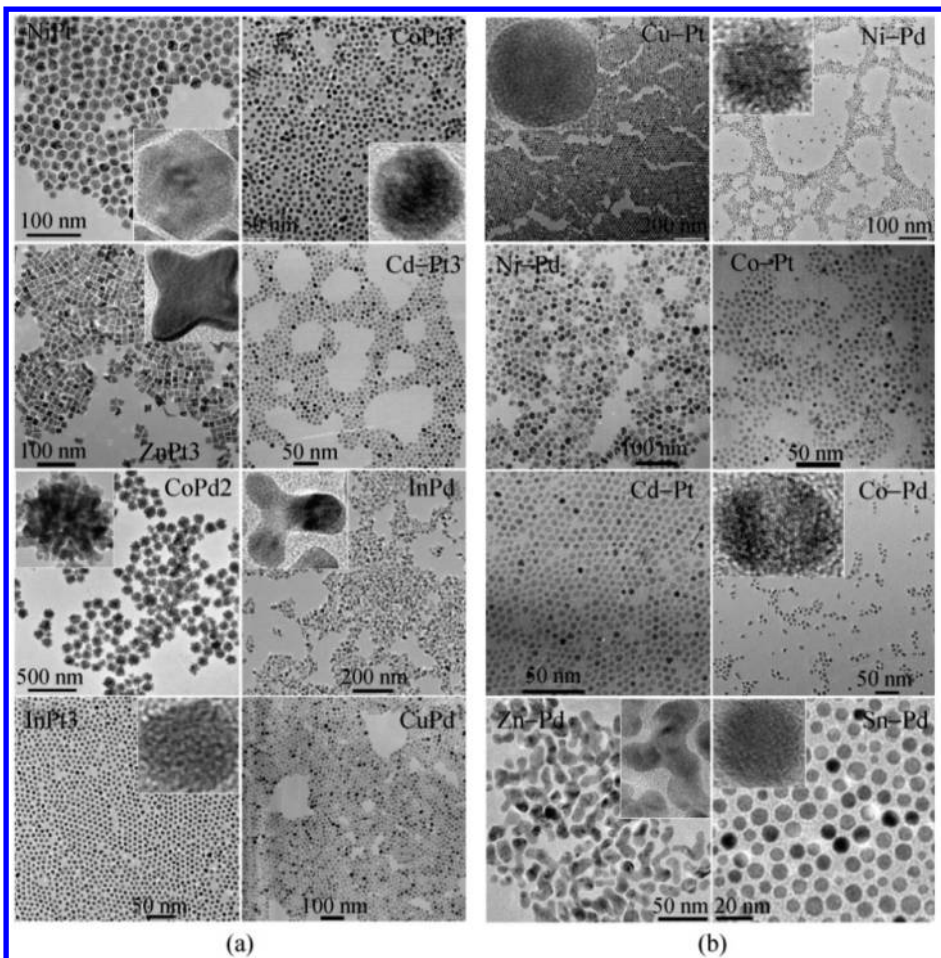


Figure 32. Representative TEM images of (a) intermetallic and (b) alloyed nanoparticles. Reprinted with permission from ref 389. Copyright 2010 Tsinghua University Press and Springer-Verlag Berlin Heidelberg.

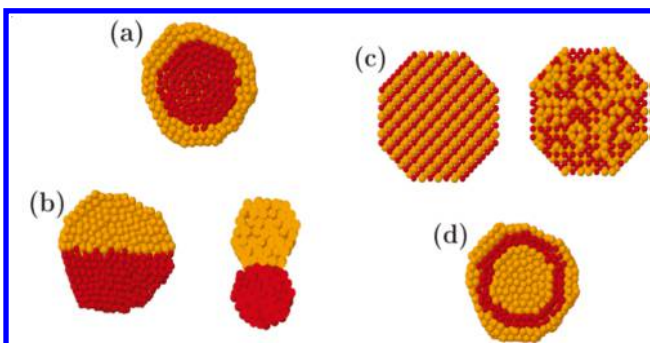


Figure 33. Schematic illustration of major structure types of a bimetallic system: core–shell (a), subcluster segregated (b), ordered or randomly mixed (c), three shell (d). Reprinted with permission from ref 387. Copyright 2008 American Chemical Society.

The complexity of the metallic particles responding to chemical potential is evidenced by characterizations after 25 voltammetric potential cycles. The depletion of Ni atoms and transformation of facets were observed depending also on the concentration of alloying elements of the prepared particles. The leaching of Ni from PtNi nanoparticles proceeds inhomogeneously: there is an area with Ni depletion (Figure 37a), but also regions with high Ni content left (Figure 37b). The leaching of Ni from $\text{Pt}_{1.5}\text{Ni}$ octahedra after 25 cycles leaves 5–12 Pt-rich surface layers. The Ni leaching in the facet centers

of Ni-rich particles ($\text{PtNi}_{1.5}$) can proceed deeply into the octahedral, leading to the formation of a concave structure (Figure 37f). The selected leaching of Ni atoms from the octahedral {111} facet is documented in the HR-TEM image of Figure 37c. The observed dealloying and collapses of the surface facets of the Pt-based bimetallic system is highly interesting for designing high performance catalysts for oxygen reduction reactions.

Apart from leaching or depletion of one constituent element from bi- and multimetallic systems during reactions, other dynamic behaviors were observed.⁴¹⁶ For instance, when physically mixed Au/AC and Pd/AC catalyst (here AC for activated carbon) is used for liquid phase oxidation of benzyl alcohol, there is a precipitation of Pd atoms onto Au nanoparticles, also observed with STEM and associated techniques.³⁹⁹ The number of precipitated Pd atoms increases with reaction time. Once bimetallic sites were formed, gold atoms can stabilize palladium atoms, preventing aggregation and leaching.³⁸⁸

Clearly, the understanding of catalytic mechanisms of bimetallic nanoparticles must be based on the correlation between surface structure and performance, especially on the structural dynamics (surface composition, active sites, oxidation states, and atomic distribution) during chemical reactions. This structure dynamics is not only governed by chemical potential (pressure P and temperature T), but also by other factors, such as how the bimetallic particles are formed and their interaction

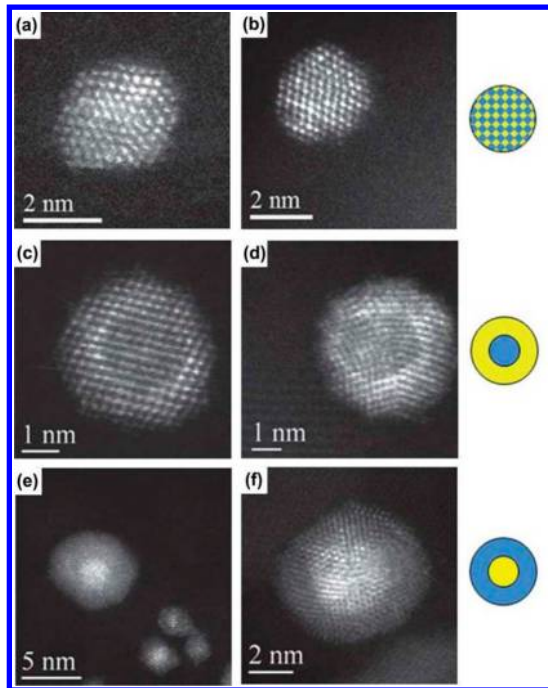


Figure 34. HAADF-STEM images of (Au+Pd) alloy (a), Au-shell/Pd-core (c), Pd-shell/Au-core (e) nanostructure on activated carbon, and (Au+Pd) alloy (b), Au-shell/Pd-core (d), Pd-shell/Au-core (f) nanostructure on TiO₂, respectively. Adapted with permission from ref 326. Copyright 2011 Royal Society of Chemistry.

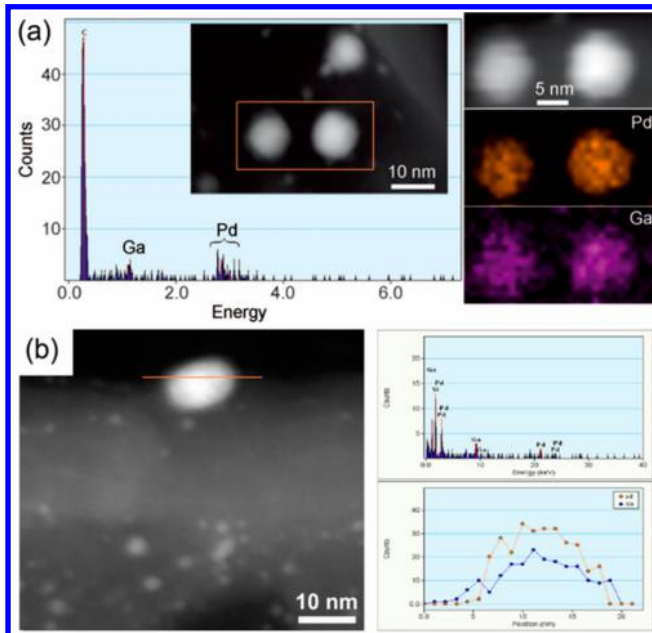


Figure 35. STEM-EDX element mapping of Pd₂Ga nanoparticles supported on a CNT (a), and STEM image, EDX spectra and line-profiles of Pd₂Ga/CNT after reaction. Adapted with permission from ref 273. Copyright 2011 WILEY-VCH Verlag GmbH & Co. KGaA, Weinheim.

with the support. Shao et al. reported that by establishing covalence interactions in intermetallics or by anchoring on localized double bonds on CNTs, Pd₂Ga intermetallic nanoparticles are stable in acetylene hydrogenation reaction and no dynamic behaviors were observed.²⁷³ How to track dynamic changes on the surface of bimetallic nanoparticles at the atomic

scale under reaction conditions, especially for gas phase reactions, is still a challenge.^{35,82}

6.7. Atomic Structure of Surface of Performance Catalyst

The surface structure of a catalyst and the structure dynamic under reaction conditions are usually studied by surface science methods on model catalysts under very demanding high-vacuum conditions. When the surface of a solid is aligned parallel to the incident electron beam and the specimen is tilted to a right zone axis, the surface structure of a catalyst can be well-studied in modern TEM/STEM, providing active centers of atomic resolution.^{85,333,364,413,431–437} The very high-resolution of such corrected TEM makes the retrieval of the atomic structure of a surface possible. The combination of aberration-corrected TEM with environmental TEM allows the imaging of the active sites on industrial catalysts with the study of surface redox dynamic under near reaction conditions at high temperature.⁴³⁸ The surface chemistry of industrial catalysts can be studied by TEM now, as demonstrated by the following examples.

Surface Oxygen in Ag Catalyst. Silver catalysts are one of the important industrial catalysts for hydrogenation of unsaturated aldehydes, oxidative coupling of methane to ethane and ethylene, partial oxidation of methanol to formaldehyde, and some other important reactions. In the 1990s, Ertl et al. found that the surface and subsurface of an Ag catalyst are not in the pure form since TPD and XPS revealed the existence of oxygen species on and in Ag catalysts.^{439,440} Three species of atomic oxygen with distinct structural and energetic properties are present in a model Ag catalyst pretreated in oxygen; α -oxygen on the outmost surface (surface oxygen), β -oxygen dissolved in the bulk with low interaction energy (bulk oxygen), and the γ -oxygen incorporated into the top surface layer of Ag with high electron density (subsurface oxygen).⁴⁴¹ The identification of surface and subsurface oxygen in Ag is of significance for understanding the reaction steps and mechanisms; even this is achieved using single crystal Ag and using the surface science method. Subsurface oxygen is a kind of strongly interacting atomic species, could cause an upshift of the surface *d*-band center of silver, and thus increases the reactivity. Ertl et al. found that γ -oxygen stabilizes the adsorption of H, C, N, O, O₂, CO, NO, C₂H₂, and C₂H₄ on Ag(111), and changes the kinetics of H₂, O₂, and NO dissociation substantially.⁴⁴² All these important findings were obtained by means of spectroscopic methods on model Ag catalyst; the location of subsurface oxygen atoms, however, remains an unanswered question. A much more important question is whether industrial silver catalysts have the same surface chemistry, or more generally, how relevant is the surface science finding to real catalysts.^{19,443}

As the surface structure of an industrial catalyst is far away from that of a single crystal, we need a tool to study the surface structure at the atomic resolution to identifying the presence of oxygen species or to detect any changes due to the presence of such species. Cs-corrected TEM allows a clear imaging of the surface structure of real catalyst. The Fresnel fringes due to the delocalization effect, usually appearing as an extension of the perimeter, are eliminated. The atomic structure of terraces, kinks, and edges that makes the surface of a real catalyst can be revealed, as is shown in Figure 38a in the case of an industrial Ag catalyst. Such a high-resolution image gives a clear local structure of the Ag catalyst, but in-depth analysis is still needed to retrieve correctly more detailed information from a simple

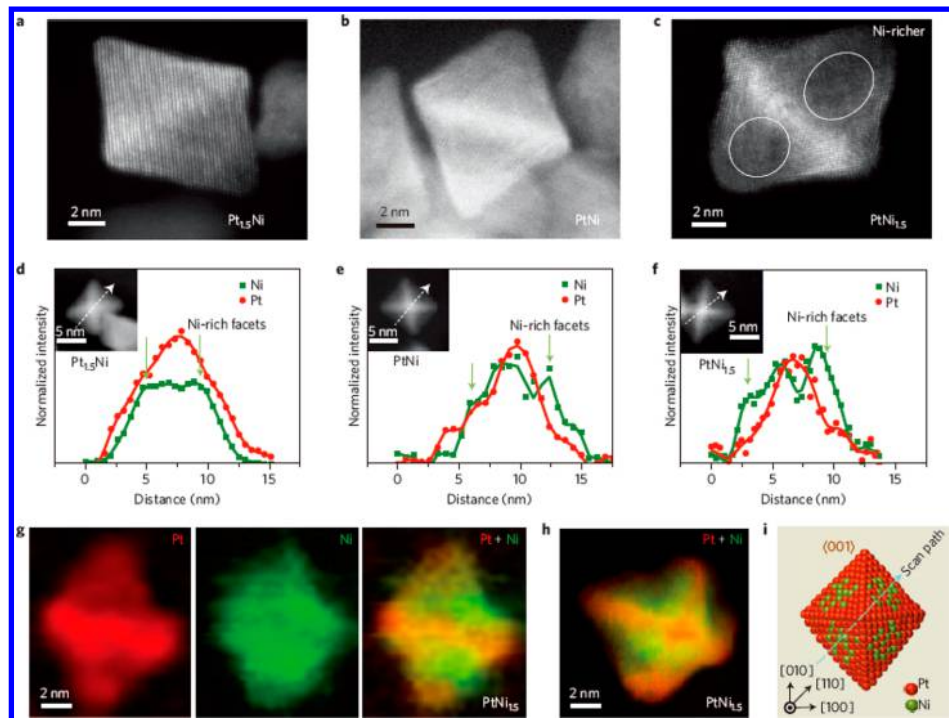


Figure 36. HAADF-STEM images and composition profile of Pt_{1.5}Ni (a,d), PtNi (b,e), PtNi_{1.5} (c,f) octahedral nanoparticles. (g) Colored EELS mapping of PtNi_{1.5} showing the segregated distribution of Pt (red) and Ni (green) taken along the [110] direction. (h) Colored element mapping taken along the [100] zone axis. (i) Structure model showing Pt-rich frame and Ni-rich faces. Reprinted with permission from ref 430. Copyright 2013 Nature Publishing Group.

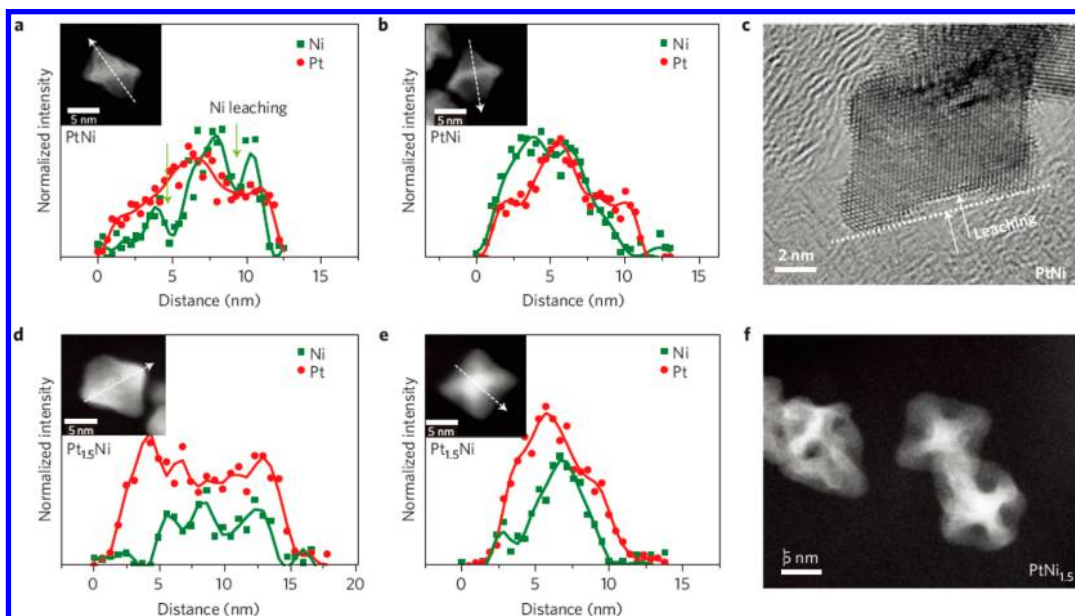


Figure 37. STEM-EELS analysis of Pt–Ni octahedra after 25 voltammetric potential cycles. (a,b) EELS line scans showing the selective leaching of Ni from the facet region on PtNi. (c) HRTEM image of PtNi showing how the selective leaching proceeds. (d,e) EELS line scans showing the thick Pt surface shell on Pt_{1.5}Ni relative to PtNi due to the cycling. (f) STEM image of PtNi_{1.5} showing the formation of a concave structure in PtNi_{1.5} due to the selective leaching of Ni from the facets. Reprinted with permission from ref 430. Copyright 2013 Nature Publishing Group.

TEM image. Su et al. analyzed the lattice distance of the atom columns of the top layers of Figure 38a and found deviations from the lattice distance of a perfect Ag structure. Based on the lattice fringes analysis and density functional theory (DFT) calculations,¹⁹ they found that the α - and γ -oxygens are positioned on the edge and steps of the surface of an industrial catalyst (Figure 38b), but it is energetically unfavorable for such

surface oxygen to exist on or under the terrace with perfect termination. Image simulations (Figure 38c) using the obtained surface structure model with oxygen (Figure 38b) confirmed this finding.

HRTEM confirmed also the subsurface carbon and a Pd–C surface phase on Pd foils used for alkyne hydrogenation formed during the reaction^{444,445} that were revealed first by the *in situ*

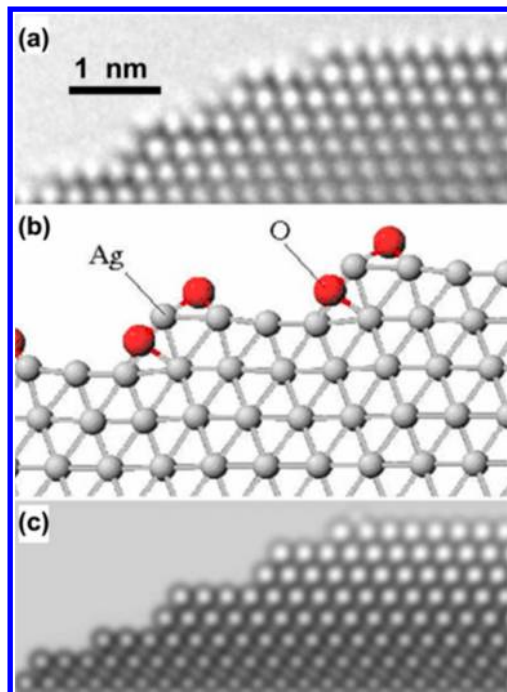


Figure 38. (a) Aberration-corrected high-resolution image of Ag catalyst viewed along the (110) direction. (b) Structural model obtained from DFT calculations showing the position of α - and γ -oxygens on the surface of Ag and (c) simulated high-resolution image using the structure of part (b). Adapted with permission from ref 19. Copyright 2008 WILEY-VCH Verlag GmbH & Co. KGaA, Weinheim.

spectroscopic method. These subsurface carbons play an important role in hydrogenation reactions, as they control the selectivity of the reaction.²⁴⁷ Rinaldi et al. reported that carbon dissolved on the subsurface of Ni nanoparticles controls the initial stages of nanocarbon growth, leading to either the formation of carbon nanotubes or disordered carbon.⁴⁴⁶

Surface Structure of Oxides. The surface structure of oxide is critical for understanding its catalytic performance. Restructuring of an oxide surface is a common phenomena and has been studied on clean oxide surfaces under ultra-high vacuum conditions with surface science methods.^{447–449} High-resolution TEM or STEM in profile-imaging mode provides not only the surface atomic configuration but also the structure under the surface and the bulk that cannot be studied with surface science methods.

MgO is a suitable model catalyst for oxidative coupling of methane. Its operation is enigmatic, as it does not exhibit any redox sites allowing exchanging electrons between oxygen and methane. The notion that Li promoters should form active radical centers was found⁴⁵⁰ to be erroneous. Rather Li restructures the catalyst⁴⁵¹ to make it exhibit under the reaction conditions a stable (111) pseudofaceted orientation. This occurs also slowly under operation conditions (Figure 39A,B) and modifies the whole bulk of the ionic crystal, revealing the power of chemical-induced restructuring. Such restructuring is not active^{452,450} for lowering the surface free energy of the terminating layer under vacuum conditions (Figure 39C). Doping with very small amounts of redox-active iron ions⁴⁵² leads to a shallow bed of dopants beneath the surface, as can be seen from the STEM image (Figure 39D). With no other method would the localization of such small amounts of

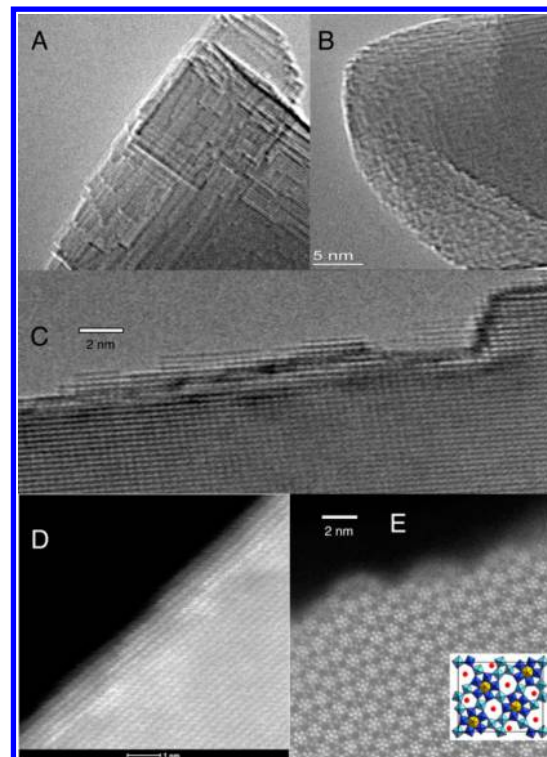


Figure 39. MgO as catalyst for oxidative coupling of methane. The most active fresh catalyst exhibits after 6 times on stream (TOS) (1073 K, CH₄/O₂/N₂: 3/1/1) multiple (100) surface steps (A). After 230 h TOS (B) the whole MgO crystal is restructured under the influence of water and CO₂ from unwanted combustion of methane and exhibits now microsteps along (111).⁴⁵³ This orientation is stable for long times but less productive per unit surface area. In (C) and (D) the perfect termination of (100) steps without any restructuring can be seen in TEM and STEM modes.⁴⁵² The contrast changes in the STEM image (D) subsurface arise from a deliberate doing with 0.05 wt % Fe atoms residing in a shallow region beneath the surface. Complex oxides as a MoVO_x system can lower their surface energy by formation of a termination layer of different composition than the bulk exhibiting structural dynamics (E). Adapted with permission from refs 452 and 453. (Ref 452: Copyright 2013 WILEY-VCH Verlag GmbH & Co. KGaA, Weinheim. Ref 453 Copyright 2014 WILEY-VCH Verlag GmbH & Co. KGaA, Weinheim.).

dopants detectable in integral form by optical and electron paramagnetic resonance (EPR) spectroscopy be possible.

The termination without detectable restructuring with respect to the bulk structure (Figure 39C) is typical for binary oxides with considerable ionic bonding character. In complex oxides the substantial free energy arising from cutting the crystal structure with its many metal–oxygen bonds may become effectively lowered by segregating a binary component to the surface that is capable of forming a layered structure as termination layer. In Figure 39E such an example is shown where a V_xO_y layer segregates⁴⁵⁴ on top of the complex M1 structure formed in this particular sample only from Mo and V cations (see also section 6.8).

Reconstruction can occur on reduced oxides as the stoichiometry and oxidation state of cations change. Aberration-corrected STEM reveals that reconstructed titanium atoms at the outmost surface occupy the interstitial site of the TiO₂ bulk structure (Figure 40).⁴⁵⁵ Images from two orthogonal directions (in the exemplified case [001] and [1–10] directions) are needed with corresponding image simulations

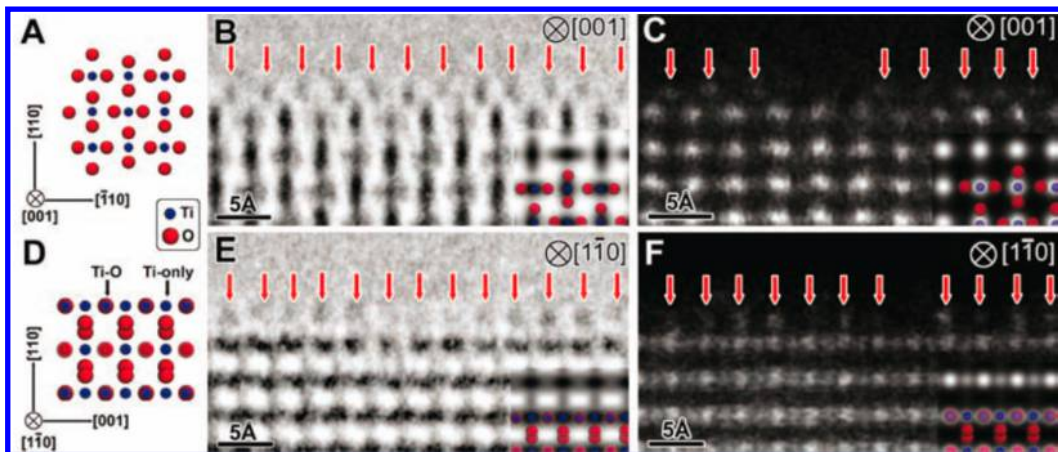


Figure 40. (A and D) Schematic illustrations of a rutile TiO_2 structure viewed along the [001] and [1–10] directions, respectively. (B–F) Atomic-resolution TEM (B, E) and HAADF-STEM (C, F) images of a TiO_2 (110) surface observed from the [001] and [1–10] directions. In parts (B and E), the dark image contrast corresponds to the position of atomic columns. In parts (C and F), bright contrast corresponds to the position of Ti-containing atomic columns. Reprinted with permission from ref 455. Copyright 2008 The American Association for the Advancement of Science.

to determine the 3D position of the Ti interstitials at atomic scales. This work allows verification of the two reconstruction models^{456,457} proposed earlier with different oxygen stoichiometries.⁴⁵⁵

The atomic surface structure of oxide under chemical conditions is a long-pending issue and involved in many applications including oxidation catalysts.⁴⁵⁸ That the surface of an oxide catalyst may suffer dynamic changes with the creating of active sites is expected, but its visualization under reaction conditions remains a challenge. Many efforts have been made to study the surface dynamics under environmental conditions as a function of the oxygen pressure p and temperature T defining the oxygen chemical potential. For instance, spin-density functional theory predicted two distinct domains on the $\alpha\text{-Fe}_2\text{O}_3$ (0001) surface.⁴⁵⁹ One is terminated by iron and the other by oxygen, depending on the oxygen chemical potential. This is confirmed by scanning tunneling microscopy revealing the coexistence of the two domains on single crystalline $\alpha\text{-Fe}_2\text{O}_3$ (0001) films prepared in high oxygen pressures.⁴⁵⁹ In a partial reduction–reoxidation cycle, Barbier et al. observed surface dynamics in the sequence from oxygen-, to ferryl-, and again to oxygen-terminations that were also predicted by recent DFT studies.⁴⁶⁰

The dynamic behavior of an oxide surface in a reducing atmosphere remains mostly unknown, but it could be highly relevant for understanding the fundamental aspects of oxide catalyst.⁴⁶¹ Ceria is an interesting oxide in catalysis, finding applications in solid state fuel cells, in catalytic converters, and as cocatalyst in many gas phase reactions. Under reducing conditions, a large amount of oxygen vacancies can be formed within the crystals and ceria (VI) oxide can be reduced to ceria (III) oxides. *In-situ* ETEM study revealed that ceria underwent a reversible phase transformation from a fluorite structure to a cubic superstructure with a periodicity of about twice the parent lattice at 730 °C in hydrogen atmosphere.⁴⁶² In hydrogen atmosphere, the ceria (110) surface has a sawtooth structure constructed by the low energy (111) nanofacets (Figure 41a). This sawtooth structure transforms to a smooth profile viewed by TEM after heating for 30 min at 730 °C (Figure 41b). A change in morphology of this smooth surface structure was not observed upon reoxidation. After 2 h when the sample was cooled to 600 °C (Figure 41c), the surface flattens to a very

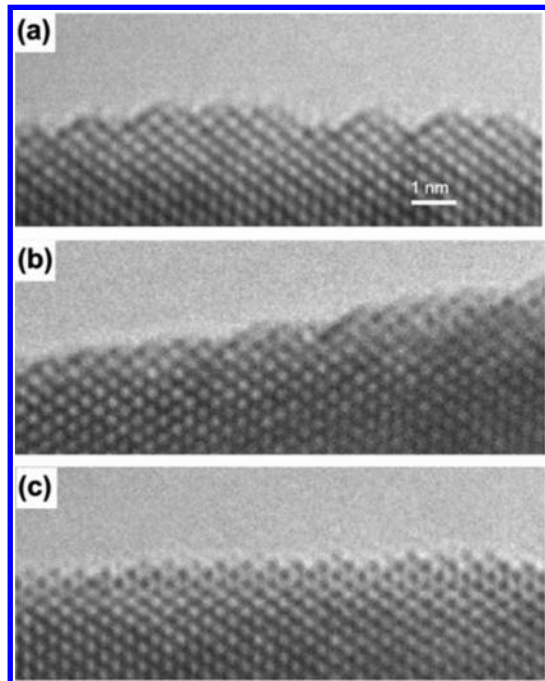


Figure 41. High resolution images showing the evolution of the ceria (110) surface dynamic of an identical region during heating in 0.5 Torr of H_2 recorded at (a) 270 °C, (b) 730 °C, and (c) 600 °C. Reprinted with permission from ref 462. Copyright 2008 Elsevier.

smooth terrace composed of (110) terraces with few (111) components remaining (Figure 41c).⁴⁶² The observation of this structural transformation on the surface of ceria in an environmental TEM is very important, since the reduction and oxidation of molecules or cocatalysts occur on its surface. More important is to know the oxidation state of the top surface layer of the cerium atoms and the degree of oxygen vacancies that may drive the observed structure transformation.

The surface science method is powerful to study the (plan) surface structure and less sensitive to the subsurface, but it provides no information about the bulk that the surface terminates. The previous examples show that the subsurface is equally important as the surface in determining the selectivity of a working catalyst. The dynamic of the bulk is of the same

relation, since any “surface” or “surface dynamic” is only a space cutoff of a bulk. The fact that TEM can provide the structural information on surface, subsurface, and bulk simultaneously is the unique advantage of TEM compared with other methods in catalysis science.

6.8. Structure of Complex Oxide Catalyst

Complex oxide catalysts usually have a complicated structure consisting of several subunits with different atomic occupations. Full information on surface, subsurface, and bulk can be obtained in one image acquired in aberration-corrected STEM when a complex oxide is oriented with one of its main axes parallel to the electron beam.

Selective oxidation reactions, for instance, three propane oxidations to acrylic acid or propane ammoxidation to acrylonitrile, involve multiple electron transfers and selective multiple bond breaking/formation to target molecules.⁴⁶⁴ Complex oxides are usually needed, as each element introduces different reaction steps either controlling the reaction rate or the selectivity. Mo–V–W–O, Mo–V–Nb–Sb–O, as well as the Mo–V–Nb–Te–O complex have been identified as the promising catalysts for the mentioned reactions.⁴⁶⁵ The later one is the most promising catalyst and is a two phase system referred to as the M1/M2 system. The M1 phase has the chemical form of $(\text{TeO})_{0.94}(\text{Mo}_{7.8}\text{V}_{12}\text{Nb})\text{O}_{28}$ and has a very large unit cell ($a = 21.134 \text{ \AA}$, $b = 26.658 \text{ \AA}$, $c = 4.015 \text{ \AA}$). The structure complex projected along the (001) zone axis is given in Figure 42a.⁴⁶³ This kind of oxide has been investigated to establish preparation–morphology–performance correlations.^{68,466,467} The imaging of such a large unit cell is even possible on uncorrected TEM (LaB₆ cathode, Cs = 1.35 mm), when going far away from Scherzer focus as is shown by the contrast transfer functions (CTF) in Figure 42b. The border

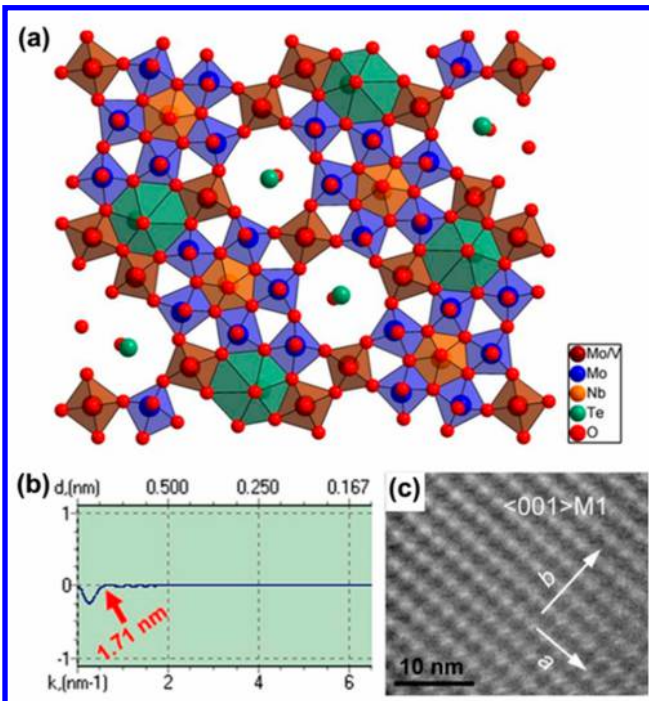


Figure 42. (a) Structural model of the M1 phase viewed along the [001] zone axis. (b) Contrast transfer function at $\Delta f = 70 \text{ nm}$. (c) HRTEM image of the M1 phase along the [001] direction far away from Scherzer focus. Adapted with permission from ref 463. Copyright 2010 WILEY-VCH Verlag GmbH & Co. KGaA, Weinheim.

lines of the $2.1 \text{ nm} \times 2.6 \text{ nm}$ basic structural units of the M1 phase along <001> represent the locations of transition metal oxygen polyhedra (Figure 42c).⁴⁶³

The atomic positions of such complex oxides were usually revolved with the Rietvelds method of refinement of X-ray powder diffractograms.⁴⁶⁸ However, up to 200 adjustable parameters are needed for the structure refinements. A converging refinement is only achievable upon using a very high-quality diffraction pattern and a suitable starting model with imposed constraints.⁵⁷ Buttrey et al. recently showed that Cs-corrected STEM could be used to determine the structure of the unit cell of M1 with very good accuracy.⁴⁶⁹ The starting model (and thus the adjustable parameters) can be significantly improved by analyzing a sub-angstrom resolution STEM image, selected area diffraction pattern, and EDS data before starting the Rietveld analysis. The extent of “trial-and-error” iterations is then reduced. The atomic coordinates x , y extracted directly from HAADF images are in good agreement with those from the Rietveld refinement of high-resolution X-ray and neutron powder diffraction data, revealing the potential of aberration-corrected STEM in structural determination of complex oxide. The discrepancies in atomic positions are less than 0.03 nm. However, using STEM-HAADF has the additional advantage to determine the atomic occupancy: the Z-contrast of HAADF allows a comparison of the expected contrast ratio of the refined M1 phase model with that of HAADF-STEM images and therefore the determination of the site occupancies (Figure 43).⁴⁶⁹

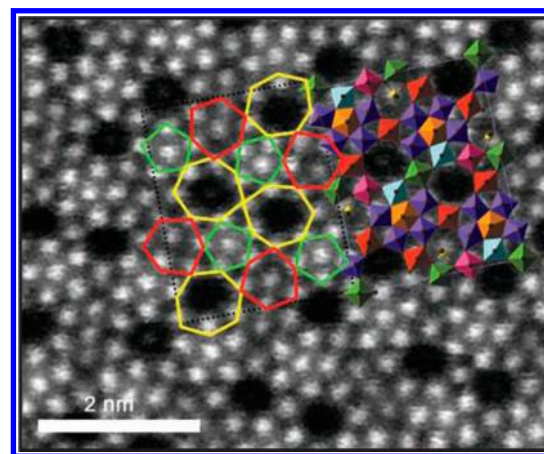


Figure 43. Aberration-corrected HAADF-STEM images showing the [001] projection of the M1 phase superimposed with a scaled unit-cell model. Reprinted with permission from ref 469. Copyright 2008 WILEY-VCH Verlag GmbH & Co. KGaA, Weinheim.

The unequilibrium during the crystal growth or phase transition may cause derivation from the parent phase in complex oxide catalyst. It is HAADF-STEM that revealed the presence of structurally distinct intergrowth phases in the Mo–V–O complex.⁴⁷⁰ For instance, a trigonal Mo–V–O phase is found coherently grown between the orthorhombic M1-type phases. A piece of Mo–V–Nb–Te–O with a domain of M1-T-M1 intergrowth is shown in Figure 44A with the corresponding high-resolution image in Figure 44B and C. The two M1-type intergrowths are separated by a trigonal band with a width of 18 heptagonal triplet units. The structure model in Figure 44E illustrates that the intergrowth proceeds without the formation of the excess trigonal unit cells. Figure 44F summarizes the

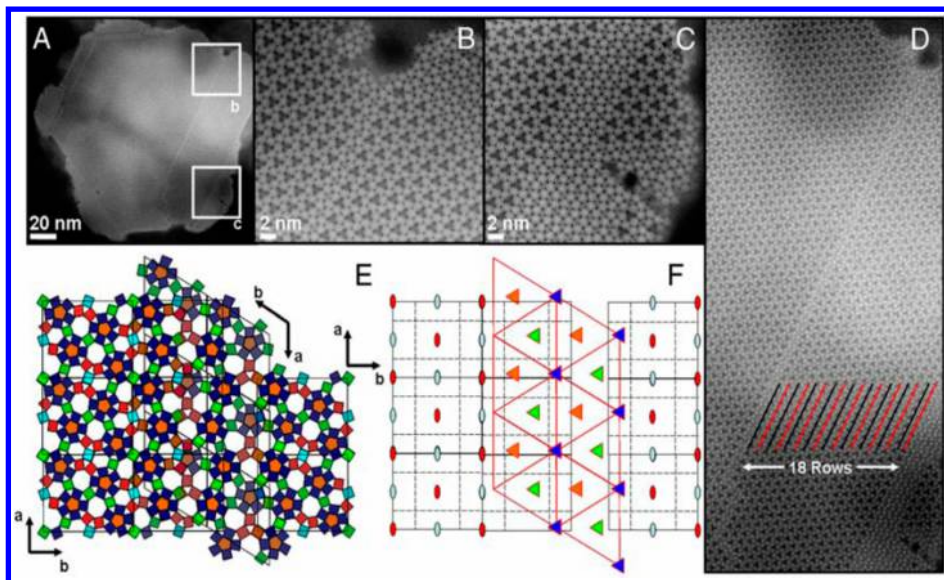


Figure 44. (A) HAADF image of a particle with M1-type intergrowths. (B and C) High-resolution HAADF images of the M1-domain labeled “b” and “c” in part (A), respectively. (D) HAADF image showing a trigonal intergrowth with a width of 18 heptagonal triplets separating the two M1-type domains. (E) Simplified representation of the M1-T-M1 phase intergrowth using M1-type and trigonal unit cells. (F) Reconstruction of the intergrowth using the plane group symmetry operators. Reprinted with permission from ref 470. Copyright 2010 National Academy of Sciences.

symmetry relationship between the trigonal domain and neighboring M1 phase: six staggered columns of 3-fold rotational operators separate the two M1-type domains. Other phase intergrowths (for instance, T-M1-T_{rot}, T-M1-T, M1-T-M1_{rot}), defect structures, and grain boundaries have also been identified. This shows the advantage of using imaging techniques with high-resolution to study the local structure against diffraction or spectroscopic methods, providing global information on the studied samples. The intergrowth is a unique phenomenon of lattice registry in the complex oxide family. To what extent such intergrowth and boundaries may have catalytic significance remains to be discovered.

So far the power of electron microscopy was used to elucidate details of the real structure of the bulk of the catalyst. Its function occurs, however, on the surface that is not analyzed. The origin is the dynamical nature of the system terminating under reaction conditions in a surface-terminating layer with different chemical composition than the bulk phase. This was found⁴⁵⁴ by near ambient pressure XPS, a surface sensitive method⁴⁷¹ capable of identifying the composition and electronic structure of the surface under working conditions. The overlayer that was imaged by STEM^{463,466} (see also Figure 39) takes away the pronounced structural anisotropy of the oxide system. The data in Figure 44 reveal that the relevant active site configuration exists only on the (100) prismatic face of the needle-shaped crystals. The vastly abundant faces would be inactive^{471,472} without this terminating layer. The relation of the complex real structural analysis of the M1 phase presented in this section to the catalytic function that does not directly profit from a surface structure seen by electron microscopy lies in the fact that the defect structure of the bulk decides the local details of the termination. The composition of the structure is given by a sequence of the clusters around the pentagonal bipyramids in the structure (rosette feature in the EM images). Their local chemical composition is given by the strength of the metal oxygen bonds. This strength is given by the nature of the central cation in each of the octahedra forming the perimeter of the rosette feature. The variable cation distribution⁴⁷³ that gives

an ordered form rise to the features of Figure 44 occurs without long-range order in each of the rosettes and determines in this way if Mo–O or V–O is the terminating surface species. It was found⁴⁷¹ that the working catalyst is enriched in V_xO_y species relative to the bulk concentration within the standard unit cell: the structural origin is the more facile breaking of less-stable VO₆ structures than MoO₆ structures. In this way it determines the cation ordering that is generated during the early stages of the synthesis⁴⁷⁴ what is the likely surface termination and thus what is the catalytic activity being generated by V_xO_y clusters supported on Mo enriched subsurface rosette units. The dynamics of the process occurs as the partial pressure of water⁴⁷¹ regulates the stability of the V_xO_y species with respect to rediffusion into defect sites in the subsurface regime when insufficient partial pressures of water (OH groups) are present. Without the detailed real structural information and the termination structure visualization by various techniques of electron microscopy, this rather involved scenario of the mode of operation would have been impossible to deduce.

6.9. Defects and Nonstoichiometry of Graphene and CNT

Carbon exists in catalysis everywhere: as catalyst, catalyst support, absorbent, and deposited species (coke formation). The possibility to form *sp*, *sp*², and *sp*³ hybridization opens the door for a multitude of carbon materials: a number of carbon nanostructure have been synthesized and tested for many applications. Among them, the most famous examples are fullerene, carbon nanotube, and graphene, being the key materials in nanoscience and nanotechnology.^{476–480} It is the EM and associated techniques that reveal the existence of various morphologies of nanocarbons.^{38,481}

Hashimoto et al. investigated the graphite network in single-walled CNTs (SWCNTs) by TEM, as shown in Figure 45.⁴⁷⁵ In a perfect SWCNT (Figure 45a, b), two regular hexagons can be identified by Fourier transformation (Figure 45b inset), one from the upper and one from the lower tube walls. The chiral indices of SWCNTs can be determined by measuring the angles that these hexagons make with the equatorial line and the tube diameter. In the example shown in Figure 45, the indices were

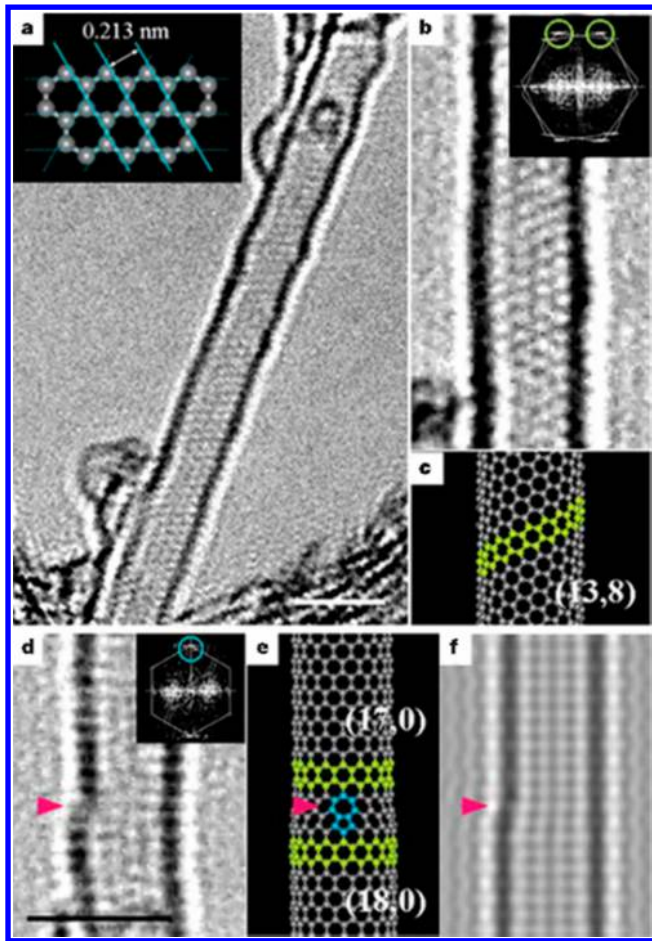


Figure 45. (a) HRTEM image of a SWCNT together with a zigzag chain model (inset). (b) Moire pattern and the corresponding optical diffraction (inset). (c) Structure model of SWCNT with chiral index (13, 8). (d) Cross-sectional view of a topological defect at the side of a SWCNT. (e) Pentagon–heptagon pair in SWCNT that generates a serial junction of two zigzag nanotubes (17, 0) and (18, 0). (f) Simulated image of the SWCNT in part (e) rotated by 90°. Scale bar, 2 nm. Reprinted with permission from ref 475. Copyright 2004 Nature Publishing Group.

determined to be (13, 8). Defects can also be deliberately introduced into SWCNTs by electron bombardment. Figure 45d shows a junction between two tubes with slightly different diameters that was produced in this way. Based on the analysis of the transform, the indices (17, 0) to the upper tube and (18, 0) to the lower tube can be assigned. It is interesting to see that this junction created *in situ* consists of a semiconducting (17, 0) SWNT and a metallic (18, 0) SWNT generating a nano-diode.⁴⁷⁵

Defect is a most important feature of nanocarbon that can control the electronic, chemical, mechanical, and magnetic properties of nanocarbon materials. The defects can be classified into structural defects (e.g., point defect, cluster defects and edges), topological defects (e.g., bond rotations), linear defects (i.e., grain boundaries), or doping induced defects (substitution of carbon atoms by heteroatoms), non-sp² carbon defects in sp² carbon, high-strain folding of graphene sheets.^{245,482–488}

The edge configuration of graphene of limited size is of particular interest, since it determines its electronic properties. The motion of carbon atoms or the dynamics of edges is

therefore an interesting phenomenon. Using Cs-corrected TEM, Zettl and co-workers studied the evaluation of a suspended graphene hole by recording movies with frames of less 1 s. The dynamics of carbon atoms on the edges of a hole could be observed. Two frames of snapshots are shown in Figure 46A and B.⁴⁸⁹ A high degree of “armchair” and “zigzag”

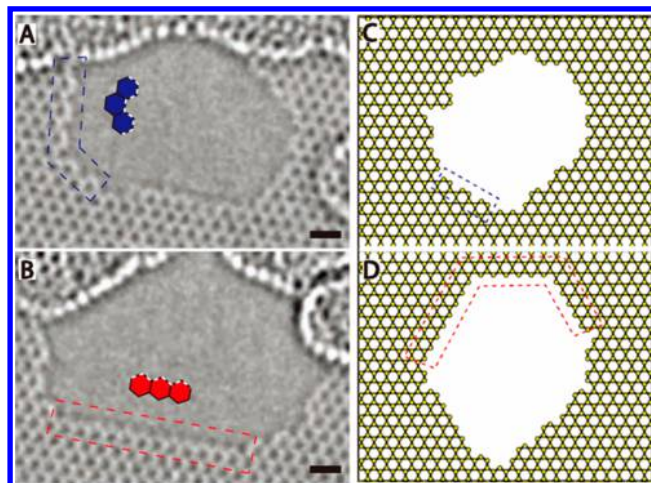


Figure 46. Aberration-corrected TEM image of (A) an armchair and (B) zigzag configuration of carbon atoms at the edge of a hole in graphene. An armchair (upper panel) and zigzag (lower panel) arrangement are inset in the respective image. Examples of the emergence of long-range order in the simulation of hole growth are (C) with a 7-hexagon armchair segment at the edge of the simulated hole and (D) with an extremely long (19 hexagon) zigzag edge interrupted by two 60° turns. Reprinted with permission from ref 489. Copyright 2009 The American Association for the Advancement of Science.

ordered edge configuration of long-range (spans about 12 hexagons) is observed (the outlined region of the hole in Figure 46A and B). The image indicates that those configurations are stable. The kinetic Monte Carlo simulation of the evaluation of a hole in a suspended graphene sheet confirmed the existence of such a long-range ordered armchair and zigzag edge, as shown in Figure 46C and D. Edges of up to 7-hexagon armchair and 19-hexagon zigzag configuration are stable. The complex behaviors of carbon atoms at a boundary can thus be followed by analysis of recorded images and kinetic Monte-Carlo simulations.

It is noteworthy to mention that the images in Figures 45 and 46 were obtained at operating voltage below the critical energy of beam damage. Carbon materials are irradiation-sensitive and could suffer from severe knock-on effects.

6.10. Real Structure of Molecular Sieve

Molecular sieves are materials of crystalline metal aluminosilicates with micro-, meso-, and macropores. The micropores can be precise and uniform in size of some molecules. Molecular sieves are often used in the petroleum industry (e.g., for the purification of gas streams, for separating compounds, and for drying reaction starting materials) or some other fields (e.g., in the filtration of air supplies for breathing apparatus).^{60,490–493} Molecular sieves are also solid catalysts for, for instance, fluid catalytic cracking (FCC).

The structure and properties of a molecular sieve are usually determined by diffraction (X-ray, for instance) or spectroscopic (solid state NMR, for instance) methods. The major

contributions of (S)TEM to the investigation of molecular sieve or zeolite materials are the exploring of local singularity or faults of a crystal of molecular sieve, including structural intergrowth or stacking faults. The readers may refer to numerous published reviews.^{54,494–496} Molecular sieves, unfortunately, belong to the most electron-beam sensitive materials and can suffer damage upon electron irradiation. It is rather difficult to image point defects, single metal atoms, or clusters in the pores.⁴⁹⁷ However, under optimum conditions and operating in suitable modes, the atomic structure of a molecular sieve can also be read off by means of high-resolution (S)TEM, but also relying on postsophisticated image analysis.

One strategy to study molecular sieve or zeolite materials in a TEM is the low-dose imaging technique that can significantly reduce the effects of electron beam damage.^{497,498} The specimen is not screened off in image mode (a certain amount of electron is needed to see the specimen that may already cause beam damage), but rather in diffraction mode (using defocused condenser lenses) until a crystallite oriented with a main zone axis parallel to electron beam is located. The TEM is then switched to image mode and goes to the magnifications needed for high resolution, but without refocusing condenser lenses. If the beam passing various lenses and correctors is perfectly aligned and the TEM is in a very stable environment, a TEM image of molecular sieve can be obtained after long acquisition time. Figure 47a–c show a HRTEM of MCM-48

of the interested area at high magnification with a high electron dose as the consequence. In a STEM, the rastered probe can reduce the beam damage to a certain degree.⁴⁹⁷ In addition, HAADF-STEM images contain very minimal diffraction contrast. This is particularly useful for porous materials with high crystalline structure suffering from diffraction contrast effects in TEM images.⁴⁹⁷ Not to forget are the signals of X-ray, Auger, and inelastically and backscattered electrons that can be collected simultaneously in STEM mode.⁵⁰ All those features make STEM especially useful to study high atomic number metal catalysts dispersed within the pores.^{500–502}

One important contribution of the HAADF-STEM technique to the investigation of the zeolite-supported metal catalyst is the identification of isolated metal atoms. Figure 48b and c show the isolated iridium atoms anchored in dealuminated HY zeolite crystal with a simulated image of [011] projection in Figure 48a.⁵⁰⁰ By comparing the simulated images given in Figure 48g–i with the structure model in Figure 48d–f, the sites anchoring the isolated iridium atoms can be determined.

7. IN SITU AND ENVIRONMENTAL ELECTRON MICROSCOPY

7.1. In Situ Electron Microscopy of Catalysts

Electron microscopy is not only a diagnostic method of materials with excellent resolution, it has also been used for *in situ* experiments by heating, controlled electron beam irradiation of the specimens,^{72,503–508} or manipulation using a specially built specimen holder. The later one has been used in nanoscience and nanotechnology, for instance, for the measurement of electrical conductivity or field emission of nanoobjects by applying a potential that otherwise cannot be studied individually. The readers are referred to the numerous reviews on the topics.^{509,510}

Catalysts are mostly small nanoparticles. The large percentage of surface atoms renders many of them with different properties from the bulk. TEM is a unique tool in which the sample temperature could be cooled down to liquid helium temperature or heated to 1200 °C. This large span of temperature allows the study of temperature-induced phase transformation and chemical evolution of nanoparticles.^{30,31} For instance, the stability and dynamic behaviors of Pt nanoparticles with various shape, synthesized by changing the ratio of polyacrylate to that of Pt²⁺ ions reduced by H₂ from K₂PtCl₆ at room temperature, have been studied *in situ* in TEM by heating the specimen up to 610 °C.^{509,511} The shape of particles does not change until about 350 °C, and a dramatic change of the polyhedral particles to spherical-form occurs (the melting temperature of bulk Pt is 1773 °C) at temperatures higher than 500 °C. While how the shape change proceeds at atomic scale remains to be studied, this observation gives an indication about the thermal stability of Pt nanocatalysts at elevated temperature, though this stability is certainly size-dependent.

More valuable information on the thermal stability of oxide could also be obtained by *in situ* TEM experiments.⁵¹² Reduction and phase transformation are phenomena observed on many multivalent oxides when used as catalyst. We studied thermal behaviors of vanadium pentoxide (V₂O₅) in a TEM specimen chamber by *in situ* heating up to 600 °C.⁵¹² By following the evaluation of V L ELNES as a function of temperature (Figure 49), we found a sequence of transformations from V₂O₅ via VO₂ to V₂O₃, but not to VO. The

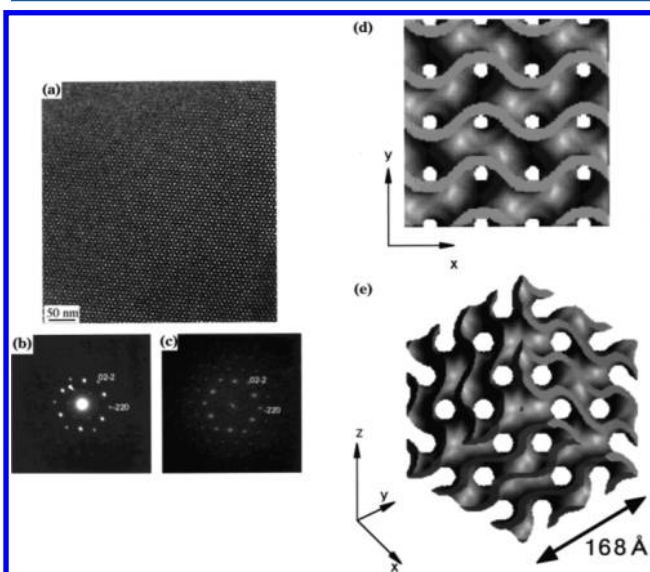


Figure 47. (a) HR-TEM of MCM-48 along the [111] direction; (b) the corresponding electron diffraction pattern and Fourier diffractogram of (a); (c) structure of MCM-48 projected along the [100] direction; (e) 3D representation of MCM-48 along the [111] direction. Reprinted with permission from ref 50. Copyright 2001 American Chemical Society.

taken along the [111] zone axis together with the corresponding electron diffraction pattern and Fourier diffractogram.⁵⁰ The obtained 3D model of the 2 × 2 × 2 unit cells of the mesoporous silica structure reveals that the walls between the pores have a gyroid morphology of minimal surface (Figure 47d–e).^{50,499}

Compared with TEM mode, STEM may have some advantages regarding the characterization of molecular sieves. If not working with the above-mentioned strategy of low-dosing, HRTEM imaging needs continuous static illumination

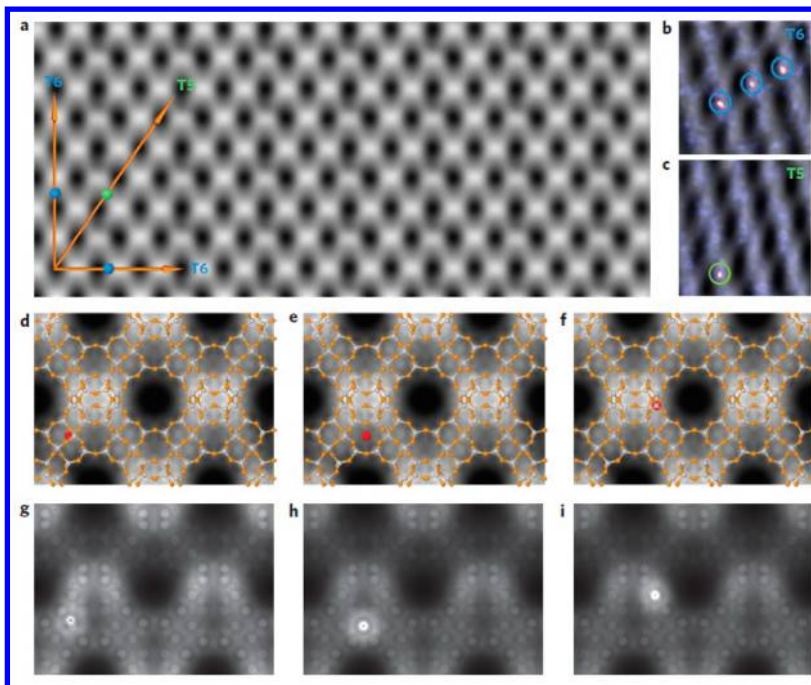


Figure 48. Identification of isolated atoms in porous materials. (a) Simulated HAADF-STEM image of the faujasite crystal along the [011] direction. (b, c) Experimental images for six-ring sites (T6) and for three-hollow positions next to the aluminum center (T5), respectively. (d–f) Simulated images of the faujasite along the [011] orientation superimposed on the faujasite unit cell with a single iridium atom (red colored) attached to a T5 site (d) and to two different T6 sites (e,f), respectively. (g–i) Simulated images of the structures shown in d (g), e (h), and f (i), respectively. The bright intensity features are iridium atoms. Reprinted with permission from ref 500. Copy 2010 Nature Publishing Group.

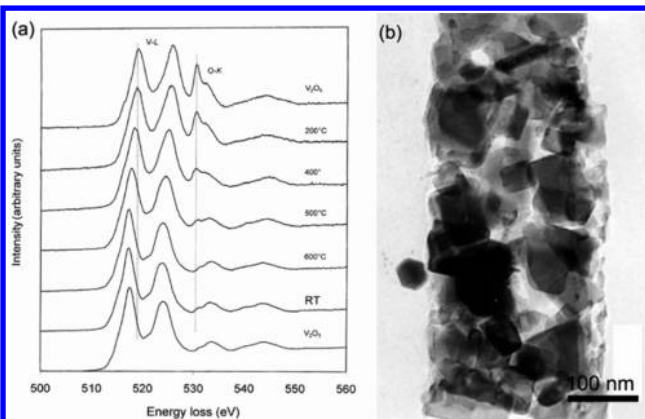


Figure 49. (a) V-L and O-K edge spectra taken on a V_2O_5 crystal heated in TEM to various temperatures and after cooling down to room temperature (RT). A reference spectrum from V_2O_3 is included. (b) Nanostructured V_2O_3 obtained by *in situ* heating of a V_2O_5 crystal in TEM. Adapted with permission from ref 512. Copyright 2002 Springer.

phase transformation does not proceed topotactically but rather via a combination of diffusion, coalescence, and stabilization processes. This temperature-induced phase transformation (in TEM vacuum) differs from that induced by mechanical treatment, for instance, ball-milling.^{75,106} V_2O_5 crystallizes in a highly anisotropic structure. EELS, combined with band structure calculations, has also been successfully used to study the anisotropy of the micro- and electronic structure.^{131,179,513}

Apart from *in situ* heating in a TEM, controlled electron beam irradiation has also been used to study the redox properties of metal oxides and phase transformation of nano materials.^{514,515} For instance, a single V_2O_5 crystal could be

reduced to monoxide VO (V in V^{2+} state) of defective crystalline structure by electron beam irradiation.⁵¹⁶ This low oxidation state of vanadium cannot be reached by *in situ* heating.⁵¹² However, when the specimen was cooled down to 4.2 K by liquid helium in TEM, the effect of electron beam irradiation is weakened to a certain degree: the electron beam can induce only a reduction of V^{5+} to V^{4+} , but not deeper, accompanied by an amorphization of the irradiated area.⁷² This is a clear indication that, at the very low temperature, the lattice collapses when sufficient V and O atoms are knocked-off by electron bombardment, with no phase transformation occurring. The diffusion of oxygen and vanadium atoms is too slow to allow any rearrangement of atoms left for recrystallization. The “mild” effect of the electron beam radiation (vanadium reduced V^{5+} to V^{4+} but not to V^{2+}) explains why cryo-TEM should be used for the investigation of electron beam sensitive materials to keep the electron beam damage as low as possible, as is already a good practice in biology. Controlled electron beam irradiation has also been used to study phase transformation of nanodiamond to nano onion^{517,518} or onion-like carbon to nanodiamond structure,^{519,520} and to probe the redox behavior of vanadium oxide catalyst supported on $\text{TiO}_2/\text{SBA}-15$.³²⁷

Electron beam irradiation can be used to stimulate some chemical processes at nanoscale that are otherwise difficult to follow. One example is the metal–cluster formation from a metal–organic complex simulated by an electron beam that can be simultaneously observed and recorded thanks to the aberration-correction technique and a high-speed camera. The formation of an Ir-cluster from $([\text{Ir}(\text{C}_2\text{H}_4)_2])$ on MgO support stimulated by an electron beam was studied by sequential STEM imaging of iridium species (Figure 50).²⁹⁵ The frames of HAADF-STEM movies (Figure 50b) show that iridium species

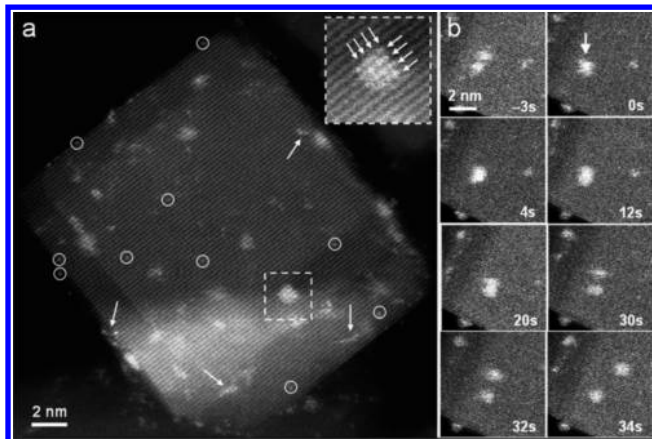


Figure 50. (a) Aberration-corrected HAADF-STEM image taken after 30 s of electron-beam irradiation of a sample prepared by adsorption of $[\text{Ir}(\text{C}_2\text{H}_4)_2(\text{acac})]$ on MgO. Isolated Ir atoms are circled; aligned Ir atoms on the way to cluster formation are indicated by arrows. The inset is an enlarged image of a square (4×4) atom face of an iridium cluster. (b) Sequences of HAADF-STEM images showing that iridium clusters do not coalesce but bounce off each other on MgO. Reprinted with permission from ref 295. Copyright 2013 WILEY-VCH Verlag GmbH & Co. KGaA, Weinheim.

were mobile on the support. Electron beam irradiation drives the isolated Ir atoms aligning at first before aggregating together forming clusters (Figure 50a). The initial process upon irradiation is fast, but the aggregation stopped once the iridium species reached approximately 1 nm in diameter. An interesting phenomenon is that the formed Ir nanoclusters do not coalesce but bounce off each other (Figure 50b). This stimulated process may provide some clues how these isolated species may

behave at high temperature when thermal energy instead of energy from fast electrons is transferred to them.

In addition, the HRTEM imaging technique enables direct tracking of the dynamic process of the heteroatoms catalyst in 2D graphene stimulated by an electron beam.⁵⁰⁶ Figures 51a–b show the morphology of graphene with SiO_2 nanoparticles, the cluster impurities, and the perfect atomic structure of graphene. The silicon substitutional defects were also identified in this sample. They can act as the catalyst tailoring the single graphene layer at atomic level under beam irradiation, as shown in Figure 51c. By adjusting the electron beam, the pore size can be optimally controlled. The first-principles calculations demonstrate that the doped silicon atom could lower the binding energy of adjacent carbon atoms and remove them easily aided from the beam irradiation. Figure 51d shows the trajectory of catalyzing process, by which the pore size and chiseling rates were quantified (see Figure 51e). The nanoscale fabrication provides the insights that the nanostructure in 2D materials can be *in situ* monitored and tailored at the atomic level, which may open new possibilities toward engineering 2D electronic devices.

7.2. Environmental Electron Microscopy of Catalytic Reactions

Heterogeneous catalysis is a dynamic process of several time and dimension scales; the reactions occur at the atomic level. Direct observation of the microstructural, compositional evolution, and active site information of a catalyst under dynamic reaction conditions is highly desired to understand the reaction mechanism and for catalyst design.^{521–529} This approach is useful both for atomic-resolution information discussed below and for mesoscopic surface transformations. The example shown in Figure 52 and the associated video

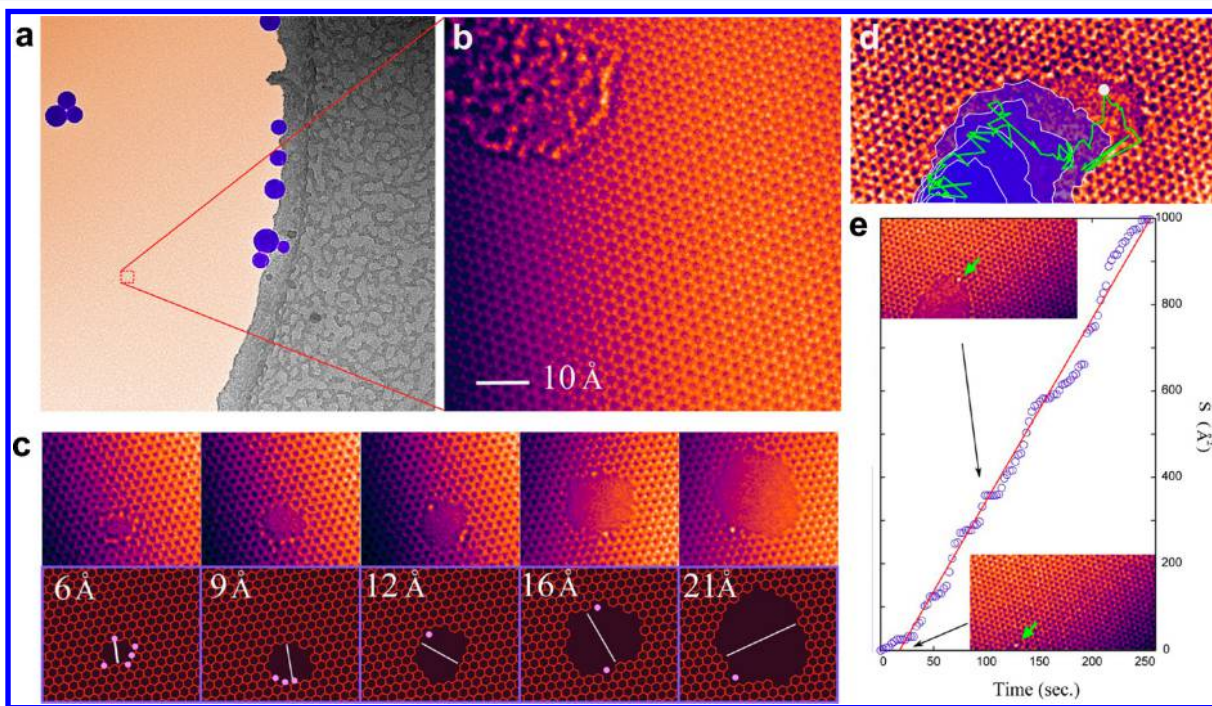


Figure 51. (a) Low-magnification TEM image of 2D graphene (light-orange color) decorated with SiO_2 nanoparticles (deep-blue color) loaded on a TEM grid. (b) HRTEM image of graphene; the left-top is the impurity aggregation. (c) *In-situ* HRTEM images of a small pore opening process, with the silicon atoms on the pore edges. The lower part is the schematic illustration of the corresponding pore opening process (above). (d) Process of a silicon atom catalyzing the pore in a graphene layer; the green line is the trajectory of the mobile silicon atom. (e) Area of the small-pore drawn as a function of open-pore time. Adapted with permission from ref 506. Copyright 2014 American Chemical Society.

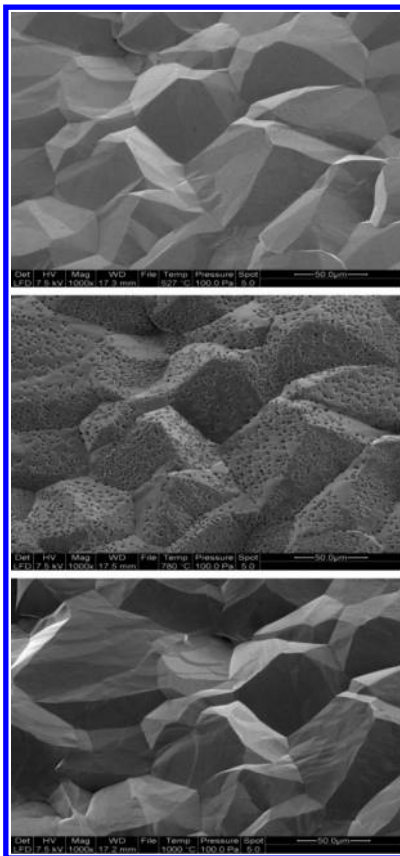


Figure 52. Snapshots of the transformation of a polycrystalline Cu foil during hydrogen treatment at elevated temperatures between 560 and 1000 °C. A pressure of 100 Pa H₂ was applied in a modified ESEM instrument utilizing a laser-beam heating stage housed in a FEI Quanta instrument equipped with a high-pressure electron detector. Reprinted with permission from ref 536. Copyright 2014 Kloster Seeon.

movie reveal the surface dynamics of Cu that still contain some subsurface dissolved residual oxygen. The sample is by X-ray inspection pure copper metal with a 0.1% enlarged lattice constant highlighting a few lattice defects. In the images one can see that hydrogen causes the residual oxygen to segregate to the surface via newly generated dislocation defects and not only via grain boundary defects. When all oxygen is removed, the surface termination collapses as the stabilizing residual adsorbed oxygen^{530–536} is finally removed and the expected low-indexed termination occurs through substantial restructuring of the whole surface and subsurface regime of the sample, being facilitated by the temperature being substantially higher than the Tammann temperature for Cu (ca. 650 °C). The example illustrates the extent to which segregation of bulk-dissolved traces of reactive gases can restructure bulk metals below the melting point and indicates the potential of *in situ* environmental scanning electron microscopy (ESEM) in observation of mesoscopic surface transformations,⁵³⁷ and in this example in detecting the gas impurities by their restructuring action. It is obvious that *ex-situ* studies would not have revealed the drastic structural changes associated with the cleaning of the metal bulk. For the atomically resolved dimension, the same approach can be taken.

Environmental TEM (ETEM) needs the introduction of gas at the level of the specimen in the TEM during observations. However, the very small mean free path of electrons in any gas under ambient pressure or even high pressure and the high-

vacuum requirement of the electron gun have ruled out, for a long time, TEM/STEM and the associated techniques for the investigation of solids and their surfaces in reacting gases or immersed in liquid under typical industrial catalytic conditions. The ambition has, however, never been given up. In the past decade, significant progresses in spectroscopic and image techniques has been made to probe or to observe directly the dynamics of catalytic gas–solid or liquid–solid reactions under industry-relevant conditions.^{35,54,328,436,438,538–551} Currently there are two well-established methods for environmental electron microscopy investigation: using windowed specimen holder (also called environmental cell, E-cell) or introducing differential pumping system: gas in- and outlet in the TEM column.

Heider designed in 1962 a windows holder for biological applications, which was used later by Baker to study the reshaping of catalyst particles in various gas environments.⁵⁵² An E-cell system is the modification of a common TEM holder to a cell with two copper discs with holes in the middle, but precovered with very thin amorphous carbon films or silicon nitride for electron beam transmission (Figure 10). The cell is sealed toward the vacuum of the TEM by Viton O-rings. The working temperature, controlled by a thermal couple, could be increased from room temperature to 350 °C at a maximum pressure of 10 mbar.²²³ This system allows atomic lattice imaging, can be adapted on any TEM and is not expensive. Giorgio et al. studied the oxido-reduction behavior of the supported Au and Pd particles at 350 °C with the resolution of (111) lattice fringes. Contaminated Au particles became cleaned in H₂, and reach the equilibrium shape of the fcc crystals with facets during annealing. The E-cell system has been recently developed for electrochemistry purposes when a potential is applied, and a refined E-cell can afford ever higher temperature and pressure than the mentioned one.

The concept of in-column ETEM was introduced by Doole and Parkinson by modifying a JEOL 4000 EX TEM introducing differential pumping apertures,⁵⁵³ which was realized a few years later by Boyes and Gai,^{210,554} and Sharma and Crozier⁵⁵⁵ on Philips microscopes. The specimen stage is modified to a gas reaction cell with gas in- and outlet, and is differentially pumped to avoid escape of a gas molecule to the high vacuum environment of the electron gun. Reducing gases such as H₂, hydrocarbons, carbon monoxide (CO), oxidizing gases (such as O₂), or H₂/water or He/water vapor can be used to study the response of catalyst upon exposure to the reaction gas at high temperature. The Topsøe laboratory has used an extensively built ETEM to study Cu clusters on ZnO during oxido-reduction cycles in an H₂/H₂O environment at a total pressure of 1.5 mbar.²¹⁹

ETEM has provided much important information on the active sites or reaction mechanism, even on industrial catalyst, that otherwise cannot be accessed by other (*in situ*) methods. One example is the identification of the active site of vanadium–phosphorus-oxide catalysts in selective oxidation of *n*-butane to maleic anhydride.⁵⁵⁶ This reaction is already industrialized, and the best active phase is identified as vanadyl pyrophosphate, (VO)₂P₂O₇ (hereafter referred to as VPO). Gai and co-workers could introduce *n*-butane to one of the earlier developed ETEM. By comparing and analyzing the atomic resolution images and electron diffraction patterns taken at room temperature and at the operating temperature (~390 °C) in *n*-butane, they revealed that only anions in the (201) plane of VPO, between vanadyl octahedral and phosphate tetrahedral,

are involved in the *n*-butane oxidation reaction, not those on all other planes in the crystal structure. They also proposed a glide shear mechanism to explain how the anion vacancies are accommodated in VPO without collapsing the catalyst bulk structure that allows oxide catalysts to continue to operate in the reaction.⁵⁵⁶

Atomic level ETEM allows the investigation of many basic physical or chemical processes on nanometer scale.^{211,213,219,557–567} Reduction in hydrogen or carbon monoxide is an important process in catalysis as to reduce precursors to metallic particles or to activate the catalyst before reactions. By evaluating the reduction of nickel nitrate and copper nitrate on titanium dioxide in hydrogen at 300 °C in an *in situ* ETEM, Crozier and co-workers made some interesting observations: (i) in some stage, the diffusion species for the growing of NiCu bimetallic particles are not metallic atoms, but oxide species; (ii) copper may reduce faster than nickel; (iii) the first formed metallic Cu enhances the reducibility of the Ni species. In addition, they confirmed that the growth of NiCu takes place via Ostwald ripening or short-range particle–particle coalescence. One important finding of this *in situ* reduction study in ETEM is that, for the given reduction conditions, the structure of the bimetallic particles was controlled by kinetics rather than by thermodynamics.⁵⁶⁸ With this work, Crozier et al. also demonstrated that EELS in an ETEM is an excellent tool to study the structural homogeneity of metallic nanoparticles and their growth mechanism.

The first step of a gas–solid catalytic reaction is the adsorption of gas molecules on the surface. The interaction of gas molecules with a surface has been a long-term interest in catalysis, mostly studied through surface science methods on a well-defined flat surface of model catalysts. How a surface responds upon the adsorption under reaction conditions is of prominent interest. As mentioned above, small gold particles supported on oxides with reducible metal cations are active for CO oxidation. Takeda and coworkers used aberration-corrected ETEM to study what happens once CO molecules adsorb on gold particles on ceria.⁵⁶⁹ Supported by ab initio calculations and image simulations, they show that adsorption of CO molecules induces a reconstruction of a {100} surface facet of gold nanoparticles to a {100}-hex facet. No reconstruction of {111} facets was observed (Figure 53). Tensile stress and high surface energy of the (100) surface are assigned as the driving force for the reconstruction upon interaction with CO molecules. The affinity of CO molecules for the reconstructed (100) surface that sustains the adsorption may indicate a differentiated reaction oxidation rate of CO on different surfaces of gold particles. This work, based on the atomic-scale visualization of gas molecules on the surface of a catalyst in an aberration-corrected ETEM, provides a different view of CO oxidation on supported gold nanoparticles.⁵⁶⁹ However, how this observation can be related or correlated to the reported activation of oxygen molecules at the perimeters or to charge-transfer between gold particles and support to give an unified mechanism of gold catalyzed CO oxidation remains to be answered.

Oxidation of metal is an important issue in materials science and catalysis. While the oxidation phenomena have been studied for a long time, how the oxidation of a metal starts and proceeds at the atomic level remains an open question. Using an ETEM, Yang et al. followed the initial stage of oxidation of a Cu film and visualized how the oxidation proceeds from a two-

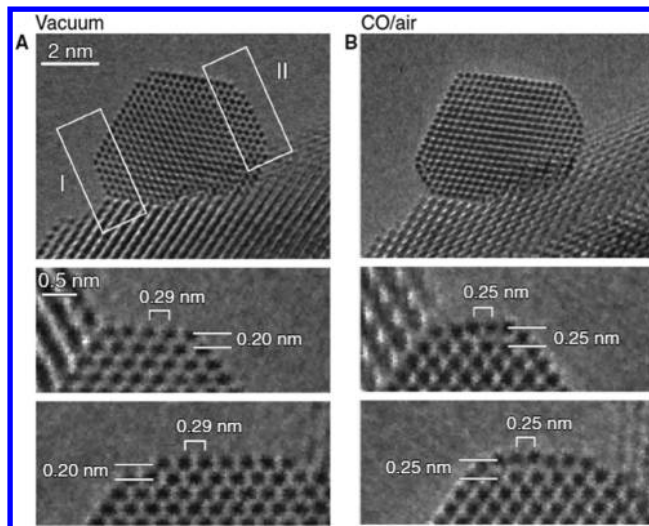


Figure 53. Au surface response to CO adsorption. Au nanoparticle supported on CeO_2 in (A) a vacuum and (B) a reaction environment (1 volume % CO in air gas mixture at 45 Pa at room temperature). Two {100} facets are marked in rectangular regions indicated by I and II in (A). The enlarged images of these regions in vacuum and in the CO/air gas mixture are shown at the bottom of (A) and (B), respectively. The change in atom position upon CO adsorption as shown in the micrographs indicates a Au{100}-hex reconstruction. Reprinted with permission from ref 569. Copyright 2012 The American Association for the Advancement of Science.

dimensional double layer to a three-dimensional island.⁵⁷⁰ The observation was followed by ETEM under the oxidation conditions ($p\text{O}_2 = 5 \times 10^{-3}$ Torr, $T = 350$ °C) on a (100) surface of a Cu film in cross-sectional view (Figure 54). The

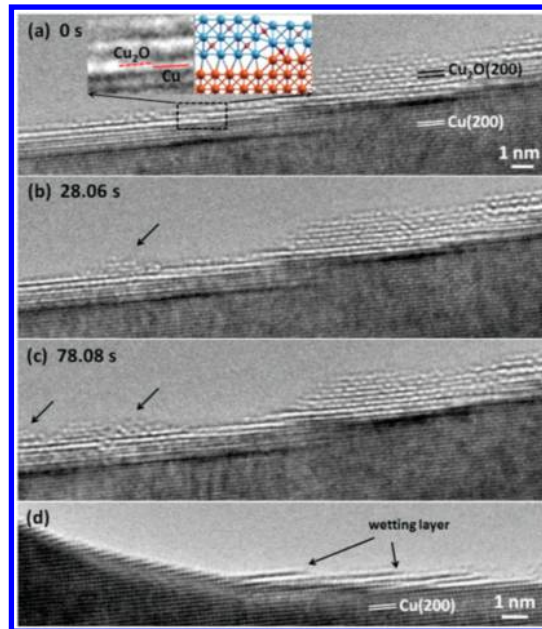


Figure 54. (a–c) Series of TEM images showing the evaluation of a Cu_2O island on the oxide wetting layer during oxidation of Cu(100) at 350 °C and $p\text{O}_2 = 5 \times 10^{-3}$ Torr. The inset in (a) shows the disconnection at the buried Cu– Cu_2O interface due to the atomic Cu surface step. (d) TEM image revealing that the oxide wetting layers initiate at Cu surface steps. Reprinted with permission from ref 570. Copyright 2013 Royal Society of Chemistry.

oxidation starts with the nucleation of an oxides wetting layer of cuprous oxide, Cu_2O , on surface defect sites such as steps. The enlarged dashed box in Figure S4a shows a $\text{Cu}_2\text{O}-\text{Cu}$ interface at a Cu step on Cu film. Figure S4b–c recorded the evaluation of the nucleated Cu_2O double layers to a 3D Cu_2O island in the course of the oxidation. This study reveals that the very initial oxidation of the surface occurs via the formation of oxide islands on the defects sites of the surface (Figure S4d). This could be the initial stage of a oxidation process that was not included in the classical theory in which the metal oxidation is a uniform, layer-by-layer process forming a continuous oxide film.⁵⁷⁰

Additionally, the structural rearrangement of bimetallic nanocatalysts in oxidation and reduction environments was uncovered by *in situ* techniques. This will facilitate further exploring the structure–performance relationship in Fischer–Tropsch synthesis or fuel cells. The example shown in Figure S5 is the dynamic process of oxidation and reduction of

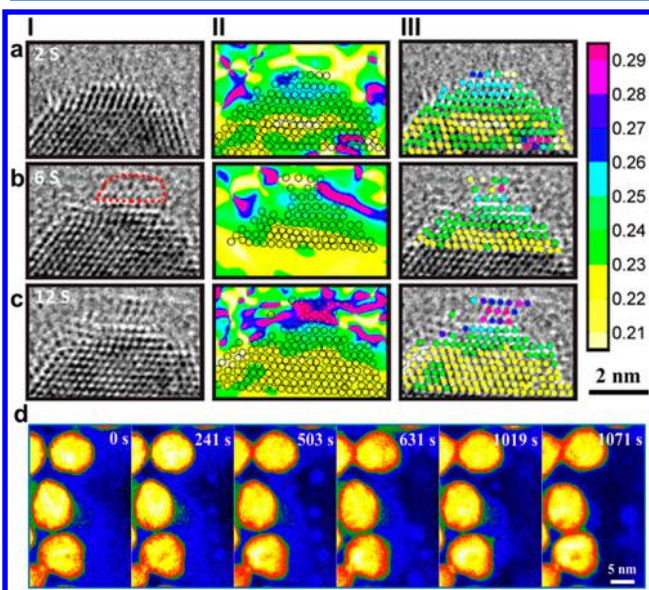


Figure S5. (a–c) show the dynamic changes of cobalt segregation in a $\text{Pt}_{0.5}\text{Co}_{0.5}$ nanoparticle during oxidation atmosphere in 0.1 mbar O_2 at 250 °C. I: the original HRTEM images acquired at 2, 6, and 12 s, respectively; II–III: the atomic displacement maps. (d) shows the dynamic changes of the reduction of oxidized Pt–Co nanoparticles (CoO: blue color, metallic core: yellow color). Adapted with permission from ref 571. Copyright 2014 American Chemical Society.

$\text{Pt}_{0.5}\text{Co}_{0.5}$ bimetallic nanoparticles.⁵⁷¹ The snapshots acquired from the oxidation process reveal that two stages occurred on the Pt–Co nanoparticles: conformal coating and island growth (Figure S5a–c). By using the geometric phase analysis method, the strain field and lattice changes in $\text{Pt}_{0.5}\text{Co}_{0.5}$ nanoparticles were quantified, which display the process of CoO formation on the surface of Pt–Co nanoparticle within a few seconds (see column II–III in Figures S5a–c). The low-angle annular dark-field STEM images show the reduction process of oxidized Pt–Co alloy nanoparticles (Figure S5d). CoO on the surface of Pt–Co nanoparticles is reduced first, and then Co atoms reconstruct into a platinum-rich lattice to form a bimetallic alloy. The study of these redox processes of Pt–Co nanoparticles opens the door to understand and identify the reaction pathways of catalysis.

Apart from the gas-phase reaction, *in situ* observation in liquid phase can only be made with a liquid environmental cell in TEM now. Electrolyte or solution can be introduced to the cell by a capillary effect that must be sealed with epoxy. With this technique, many colloidal processes such as nucleation, growth of nanoparticles, and their motion in solution can be studied.^{572–574} The nucleation and growth process under electrochemical conditions can also be studied *in situ* using this kind of E-cell when a potential can be applied.^{575–577}

One important work using liquid E-cells is the observation of the formation process of nanoarchitecture from preformed nano building blocks.⁵⁷⁸ The formation of colloidal particles is to a large extent understood as additions of monomers onto or as coalescences of small particles into relaxed spherical nanoparticles with minimum surface energy. By recording images with atomic resolution, Zheng et al. studied the formation of Pt_3Fe nanorods, one kind of nanoarchitecture, in solution. The formation of a nanorod starts with the formation of a chain (dimer) when two nanoparticles meet another. Due to some kinetic reasons, the chain does not relax to a sphere; rather, a chain consisting of three nanoparticles forms with another particle connecting the dimer end. An end-to-end attachment generates a nanoparticle chain. A mass redistribution and orientation correction must follow to straighten the long chain into a rod. Figure S6 shows snapshots

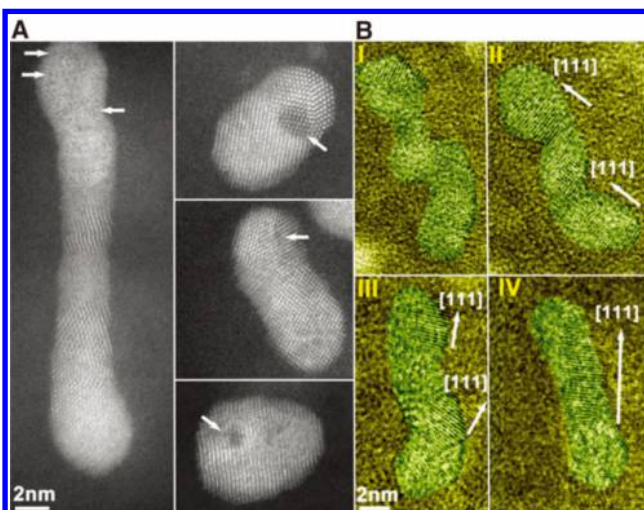


Figure S6. Formation and dynamic changes of the shape and orientation of Pt_3Fe nanorods during structural relaxation in liquid. (A) HAADF-STEM image of a polycrystalline Pt_3Fe nanorod, dimers, and nanoparticles obtained in a liquid cell. The dark regions marked by arrows are iron-rich. (B) Series of HR-TEM images (I–IV) showing that the orientation and shape of crystals changes during the straightening of a twisted nanoparticle chain. Reprinted with permission from ref 578. Copyright 2012 The American Association for the Advancement of Science.

of such a process. The HR-STEM image reveals how the structure of a polycrystalline Pt_3Fe nanorod is relaxed. To form a rod shape from a chain, the diffusion and mass redistribution must proceed through the bulk of the rod, not only on the surface. Iron-rich regions found in the Pt_3Fe nanorod are the indication of such a mass redistribution (Figure S6A). Figure S6B shows how a single crystal nanorod is born from a chain of three connected nanoparticles. The formation follows via lattice rotation, mass redistribution, and straightening.⁵⁷⁹ This observation reveals the difference between the formation of

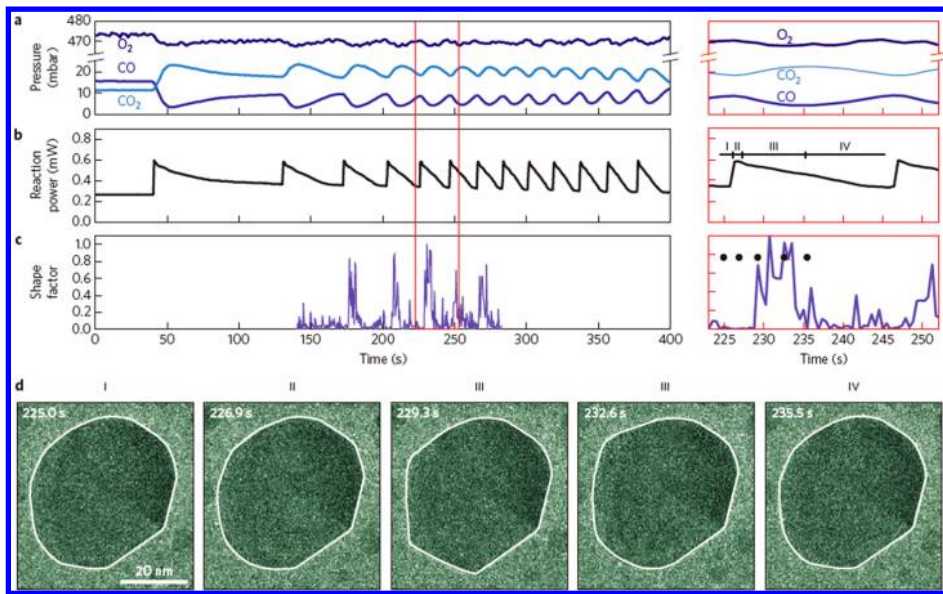


Figure 57. (a–c) show the mass spectrometry of the CO, O₂, and CO₂ pressures, the reaction power, and shape factor for the single platinum nanoparticle in (d) as a function of time under gas atmosphere at 659 K (the pressure of gas entering the reaction zone is 1.0 bar, CO:O₂:He = 3%:42%:55%). (d) A series of TEM images showing the *in situ* dynamic changes of a Pt nanoparticle corresponding to stages I–IV in part b. The shape factors from 0 to 1 represent the evolution of the particle shape from spherical to faceted shapes. The upper-right column is the enlargement of the red part in parts a–c. Reprinted with permission from ref 580. Copyright 2014 Nature Publishing Group.

colloidal particles and nanoarchitecture in liquid phase that is controlled by the kinetics rather than thermodynamics. It remains interesting work to find kinetic parameters and formation mechanisms of other nanoarchitectures, for instance, a tree-shaped structure.

Most ETEM investigations focus on the dynamic structure changes in the gas or liquid environment. However, it is still a challenge to obtain the structure dynamics and catalytic data synchronously under real reaction surroundings. Recently, Vendelbo et al. studied the structure–activity relationship of Pt nanocatalysts during oscillatory CO oxidation by using a gas-flow nanoreactor in a FEI-Titan 80-300 ETEM system equipped with mass spectrometry and calorimetry.⁵⁸⁰ Figure 57 shows the concurrently dynamic changes of Pt nanoparticles between spherical and faceted shape corresponding to the oscillatory CO oxidation. The time-resolved and low-dose HRTEM images combined with DFT and mass transport calculations reveal the catalysis mechanism in the oscillatory reaction. Owing to the site-dependency of the CO adsorption energy and oxidation rate, the spherical shape of Pt nanoparticles matched with lower CO conversion and refaceted to the particles with high index stepped terminations when the CO conversion increased, which is periodic in the oscillatory reaction. Such a method can be used to directly detect and unravel the dynamic structure of the gas–solid interface correlation with the activity in the catalytic reactions.

The above-mentioned examples show how important *in situ* or environmental EM is in studying some physical or chemical process at atomic scale, delivering details or information that cannot be accessed by other methods. However, we must keep in mind that TEM is a tool providing very local or localized information. Care must be taken to scale up the TEM finding to a macroscopic process. In addition, a catalytic reaction always has a desired direction or product. So monitoring the reactants and products is necessary to ensure that the reaction proceeds with desired selectivity. The conversion in such a designed E-cell or E-column could be secondary. The recently

developed “operando TEM” technique allows the simultaneous monitoring of the catalyst activity during the reaction while making the nanostructural characterization of the catalyst possible.^{66,580} Mass spectrometry (example in Figure 57) or EELS could be used for this purpose. This is one step further to studying structure–reactivity relationships in catalysis reactions on an Cs-corrected environmental (S)TEM, an excellent example that (S)TEM is transforming from a characterization method to a research toolbox.

8. ELECTRON MICROSCOPY FOR CATALYSIS: ELECTRON-BEAM DAMAGE AND OTHER SIDE-EFFECTS

8.1. Electron-Beam Damage

Electron–matter interactions, either elastic or inelastic, are the physical basis of imaging and spectroscopy in electron microscopy. This interaction is stronger than the interaction of X-ray with matter: we recall the short time to record a diffraction pattern compared with that of an X-ray diffractometer. Unfortunately, this (strong) electron–matter interaction can induce a destructive effect on the structure of the irradiated part, and the effect is called electron-beam damage that is a major obstacle to applications of TEM/STEM operating at any voltage.⁵⁸¹ When this strong interaction is used in a controlled way without spattering of atoms, it can be used to stimulate the phase transition (one well-known example is the diamond-graphitic carbon^{517,518} or graphitic species–diamond transformation^{519,520} induced by insensitive electron beam irradiation) or redox property of a metal oxide.^{72,515,582} Other examples to use an electron-beam to stimulate some *in situ* experiments have been discussed in section 7.1.

Three physical processes can induce electron-beam damage when an electron beam passes through a specimen in TEM.¹⁰⁰ The electron–nuclei collision can displace atoms from equilibrium sites and create point defects. The left vacancy and interstitial are called a Frenkel pair. This damage is also

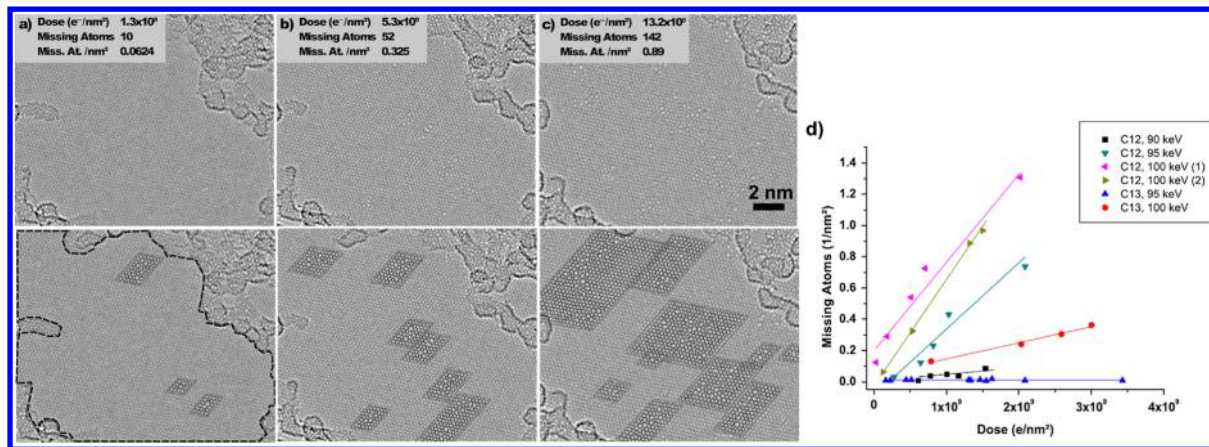


Figure 58. (a–c) HRTEM images of ¹²C graphene with increasing electron dose at 100 keV showing that the beam damage induced multivacancy defects. The lower panels in parts a–c show the same images with the atomic configuration overlay. (d) The missing atoms as a function of electron dose under the different accelerating voltages. The slope denotes the dose rate. Adapted with permission from ref 587. Copyright 2012 American Physical Society.

termed as knock-on displacement. The incident electrons can also transfer energy to atomic electrons. When the transferred energy exceeds a certain threshold (for instance the binding energy of a core electron), local electronic excitation occurs. Ionization can take place. The electron–electron interaction is inelastic, and the phenomenon is called radiolysis. The electrostatic charging of isolating materials induced by the incident electron beam can also cause beam damage.⁵⁸³ We must keep in mind once a specimen is exposed to an electron beam, the above mentioned interaction takes place and the specimen suffers already from electron irradiation. In the case of radiolysis, displacement of atoms occurs above a specific energy threshold. When the transferred energies are smaller than this critical displacement energy, sample atoms vibrate in their equilibrium site and dissipate energy as phonons⁵⁸⁴ with a local temperature increase (heating).

A (S)TEM with field-emission gun operating at 200 kV can produce a sub-nanometer electron probe with a current density of about 10^5 A/cm². When the electron probe is corrected for spherical-aberration, the current density can approach 10^6 A/cm² or even higher.⁵⁸¹ A solid catalyst that will not suffer from any structural or electronic changes under such electron-beam radiation may also be not active in any catalytic reaction: recalling here that a solid catalyst should have the function and ability to undergo in catalytic reaction structural changes: forming an active phase and creating active sites, under a condition that might be milder than the strong electron-beam irradiation, although the chemical potential is rather different. In this sense, electron-beam damage or an electron-beam induced effect is common in the electron microscopic investigation of solid catalysts. The question is only knowing the behaviors of the studied samples in a (S)TEM and minimizing the damage or side-effects in a controlled way to get information that maximally reflects the true nature or property of a solid catalyst.⁵⁸⁵

Electron-Beam Damage in Conventional TEM. We consider in this subsection the electron-beam damage of solid catalyst in high vacuum at room temperature without the presence of gas or liquid in an E-cell. The effects can be summarized as the following:

1. Creating defects, destroying the long-rang ordering of a crystalline catalyst to a disordered or, in the severe case, to an amorphous structure. The well-known examples are molecular

sieve or zeolite (see section 6.10) or transition metal oxides with cations in the highest oxidation state (divanadium pentoxide^{72,516} or molybdenum sesquioxide, for instance).

2. Creating ordered structure from a disordered or amorphous structure. One example is the graphitization of activated carbon under electron beam irradiation. Also the carbon supporting film, which is usually a very thin amorphous carbon, could be graphitized. Although the electron beam induces a well-ordered structure, it is a kind of beam damage.

3. Reducing maximal valence transition metal atoms in a higher oxidation state to a lower state, or even to metal, with the corresponding structure transformation. A dedicated study⁵⁸² reveals that V₂O₅ and MoO₃ more easily undergo a reduction under an electron beam than anatase TiO₂. Orthorhombic V₂O₅ transforms to cubic VO and the orthorhombic MoO₃ can be reduced to a face centered cubic phase with an oxidation state less than that in MoO₂. The observed different response to an electron beam is explained by the difference in bond strength and lattice structure that determines the atom diffusion rate for the reorganization of the lattice.

4. Oxidizing metal oxide to a higher oxidation state. This could happen on a specimen consisting of two oxides or more (both support and catalyst are oxide). Zhang et al. reported that an electron beam can induce the oxidation of vanadia from an amorphous lower-oxidation-state to V₂O₅ at the expense of oxygen from TiO₂ support which is reduced.³²⁷

5. Fluctuating the structure of supported nanoparticles. High-resolution (S)TEM is mostly used to study the atomic structure of nanoparticles. However, many metal particles are unstable under electrons. The shape, orientation, and internal structure, as is well-documented in Figure 21 for a gold nanoparticle of about 2 nm, suffer from electron beam induced fluctuations. Wrong conclusions could be drawn if any such snapshots shown in Figure 21 were used to identify the structure of the as-prepared nanoparticle. This phenomenon has been known for a long time and well followed already in the 1980s.⁵⁸⁶ The state of “ultrafine particles”, a nomenclature used in the 1980s to name all particles that are very small in size before the prefix “nano” was widely used, that undergo high frequency structure fluctuation under an electron beam is proposed to be a so-called “quasi solid state”, neither solid nor liquid.⁵⁸⁶ Even

particles large than 5 nm can undergo phase transitions under an electron beam.⁷⁴

6. Driving the migration of the atom off the supported nanoparticles. In the recently frequently reported HAADF-STEM image of single atoms it must be verified that the single atoms are not migrated from the surface of a nanocatalyst upon electron beam irradiation via either knock-on effect or radiolysis. This phenomenon can cause for bi- or multimetallic particles a wrong interpretation of chemical composition if constituent atoms respond differently to the electron beam that some atoms are already lost before chemical analysis is performed.

7. Changing the size distribution of supported catalyst. Highly energetic electrons can also drive the motion of small particles. When they coalesce to large particles, the particle size distribution deviates from that as prepared. Also Ostwald-ripening can take place when atoms of small particles migrate to the large one, drawn by the electron beam.

8. Eliminating the active species. A supported single metal complex or oxide cluster can be easily knocked out or reduced to a metallic species by a highly energetic electron beam.

It is clear that to explore the full potential of a (S)TEM an experiment must be carefully planned.⁵⁸⁵ Two things are very important to be ready to take a image/diffraction/spectrum from the sample. First, the TEM specimen must be very clean; any contaminations, especially adsorbed hydrocarbon or water, can accelerate beam damage. Bake-off at allowable temperature and plasma cleaning are suggested here. Second, to access the response of the specimen beam to the electron beam, if the specimen is prone to be beam sensitivity, a low-dose condition or low (in some case high) accelerating voltage could be a good choice.

Figure 58 shows an example of how an electron beam creates defects in carbon materials in TEM observation. With the increasing electron dose, displacements of ¹²C atoms in graphene were induced by an electron beam under 100 keV. This leads to the formation of multivacancy defects, such as pentagons and heptagons. The missing atoms can be accurately measured under the different accelerating voltage and dose rates (see Figure 58d). The comparison of ¹²C and ¹³C has been made, showing that the knock-on damage is correlated with the species of the isotope composition as well as the accelerating voltage. This effect can be reduced to the minimum by adjusting the accelerating voltage lower than the knock-on threshold of carbon materials so that the original structure can be recorded.⁵⁸⁷

Lowering accelerating voltage is a recent tendency to reduce electron beam radiation damage. The loss of resolution due to the relatively longer wavelength of low energy electrons can be compensated by aberration correction. Carbon materials should be stable, as the threshold of beam damage is about 86 keV. However, care still be taken when carbon materials are functionalized or doped. Susi et al. reported that incorporation of nitrogen atoms into the *sp*² network can result in a noticeable knock-on damage even at an acceleration voltage of 80 keV, but essentially no damage is created in nondoped structures under the same conditions, as shown in Figure 59.¹⁷⁶ This work suggested that electron-beam induced structural changes depend on many other factors and cannot be neglected even at low-acceleration voltage. The behavior of a single metal complex or oxide cluster under low energy beam irradiation remains to be studied. They can be very easily reduced⁵⁸⁸ or knocked out by an electron beam. Lowering acceleration

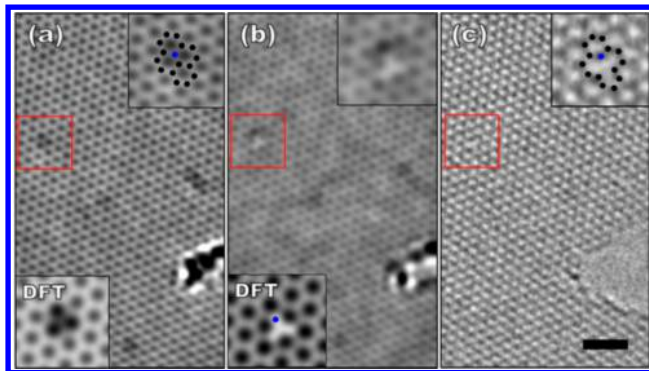


Figure 59. High resolution images of an N-doped graphene recorded at 80 keV. The top right insets show an enlarged view of the red marked area in each panel (Blue colored is N atom; black circles are carbon atoms). (a) Area of undamaged N-graphene. The position of substitutional N dopant is assigned to the three darker bonds around a central atom. The bottom left inset shows the simulated image. (b) Same area of a, but after a cumulative electron dose of $1.9 \times 10^7 \text{ e}^-/\text{\AA}^2$. Beam damage is noticeable on the contrast change due to missing atom displaced by fast electron. The bottom left inset is the simulated image of a single pyridinic vacancy defect. (c) Image of the same area recorded at the Scherzer defocus. The atomic structure of graphene and a 5–9 vacancy next to a nitrogen atom are clearly imaged, allowing a direct interpretation. For more details on experimental conditions and DFT simulation, please read ref 176. The scale bar is 1 nm. Reprinted with permission from ref 176. Copyright 2012 American Chemical Society.

voltage can certainly reduce the knock-on effect, but not necessarily the radiolysis. The structural change under the electron beam can also be evaluated by image simulation when radiation damage dynamics can be included in the computational methodology.⁵⁸⁹

In addition to electron-beam irradiation damage, hydrocarbon molecules condensed from the vacuum of the microscope or adsorbed on the specimen surface can form a contamination layer by electron-beam irradiation and cross-linking.⁵⁹⁰ This artifact is more serious when the electron beam is stationary for EDS or core-level EELS (microanalysis), or when the electron beam is finely focused to a probe for scanning or microdiffraction. Unfortunately, liquid-nitrogen-cooled anticontamination blades or coldfingers in the specimen chamber cannot eliminate or reduce this contamination satisfactorily. Washing the specimen cartridge and the specimen in methyl alcohol is the simplest way of eliminating the contamination. Further improvements can be obtained by plasma-cleaning or specimen heating.⁵⁹¹

Electron-Beam Damage in Environmental TEM.

Electron-beam induced damage or structural modification becomes more complicated when the specimen is in gas atmosphere or in a liquid cell, and in many cases also at elevated temperature. A dedicated ETEM with differential pumping vacuum systems or TEM with a gas E-cell allows gas pressures up to 20 mbar in the sample area.^{29,567,592} Although the catalyst to be studied is the specimen, the system under ETEM observation, however, consists of a catalyst and gas (or liquid, in the case of a liquid E-Cell, is used) molecules.

1. *Electron-beam damage in the presence of gas.* There is no systematic study on the electron-beam damage in the presence of gas in an ETEM. In general, it can be supposed that the most electron-beam damage or electron-beam induced structural changes listed in the previous subsection will be

worse or enhanced in the presence of gas molecules. For instance, nanoparticles may become more active when interacted with gas molecules. However, some processes such as electron beam induced reduction and phase transformation may be become slower or even be stopped in an oxidative atmosphere. It is therefore important to access the response of the catalyst to an electron beam in the presence of gas to find out the optimized working conditions to ensure that the study is on a real reaction in ETEM rather than on an artifact.

Kuwauchi et al. demonstrated that artifact produced on Au/TiO₂ catalysts under electron irradiation is a multiple function of electron current density, electron dose, gas, and pressure at room temperature.^{28,593} TiO₂ support can decorate and encapsulate the gold nanoparticles in the presence of oxygen or CO. The effects as a function of pressure and electron dose in vacuum, in the presence of oxygen and CO, respectively, are summarized in Figure 60. In regions of low current density and

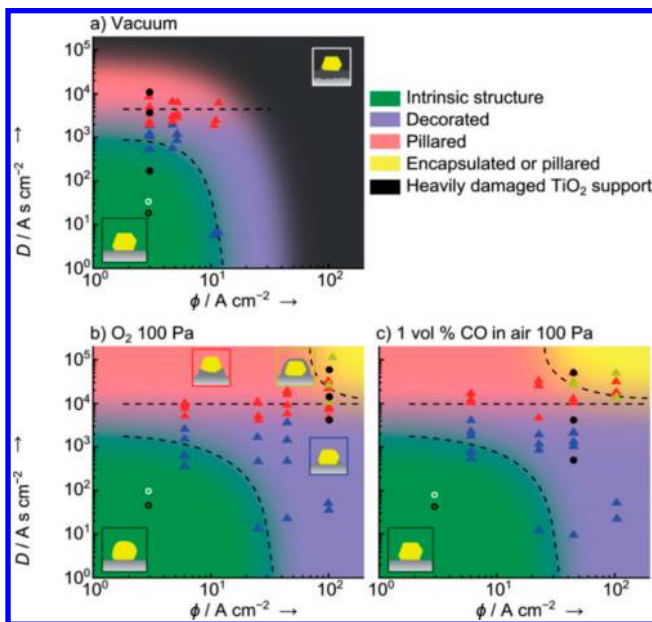


Figure 60. Structure evolution diagrams of Au/TiO₂ catalysts under electron irradiation as a function of electron current density, ϕ , and dose, D , in (a) vacuum, (b) O₂ (100 Pa), and (c) 1 vol % CO in air (100 Pa) at room temperature. Electron beam irradiation with conditions in green regions will not induce artifact, while decorations and pillars on gold nanoparticles could be observed in the blue and red regions, respectively. In the yellow regions, gold nanoparticle either with pillars or being encapsulated could be observed. Reprinted with permission from ref 593. Copyright 2012 WILEY-VCH Verlag GmbH & Co. KGaA, Weinheim.

low electron dose (green in Figure 60), morphological changes of Au/TiO₂ were not noticeable within the spatial resolution available in the ETEM. By extrapolating the structure at $\phi = 0$ and $D = 0$ in Figure 60, the intrinsic structure of catalysts under reaction conditions without interference of an electron beam can be deduced.²⁸ This is a good example how important it is to know the limitations of ETEM and how the intrinsic structures and/or intrinsic phenomena of various chemical reactions explored in ETEM can be deduced.

2. Electron-beam damage at elevated temperature. Some chemical reactions take place at high temperature, and the observation in an ETEM requires heating of the specimen. The thermal energy transferred to the specimen will enhance the

frequency and amplitude of the atomic vibration. Electron-beam damage due to radiolysis will be accelerated; the same could be true for the knock-on effect since the diffusion rate of displaced atoms and vacancies will increase, thus speeding up the collapse of the ordered structure. To our knowledge there is no systematic study on the electron-beam damage or induced structure modification of metal or oxide in a TEM as a function of heating temperature.

Su and co-workers explored the role of sample temperature in electron beam induced reduction of divanadium pentoxide in an opposite experiment. By exposing V₂O₅ crystallite to an electron beam at liquid helium temperature (4.2 K) for a prolonged time, they observed that V⁵⁺ of V₂O₅ is reduced to V⁴⁺ and the orthorhombic structure is transformed to an amorphous phase.⁷² However, for the same experiment at the room temperature, V₂O₅ crystallite is further reduced to a stable cubic VO with the vanadium atom in the V²⁺ state.⁵¹⁶ This is an indirect indication that elevated temperature will increase the diffusion rate of oxygen and displaced atoms. An elevated temperature is beneficial for the rearrangement of atoms to a structure that is also stable under electron beam irradiation.

3. Electron–gas interaction and the associated effects. In an ETEM, the studied object is a system of specimens with its surroundings and the reactions of this system (without the influence of the electron beam). However, this system must be irradiated by high-energy electrons for retrieval of the reaction details by means of imaging and spectroscopy. High-energy electrons transfer their energy and momentum to the system and induce different elemental excitations (for instance, ionization or plasmon oscillation). For a closed system (gas or liquid phase E-Cell with sealed windows), the electron beam irradiation may be induced gradually but irreversible changes with increasing of the electron dose so that the system will never return to the initial state. This may remain a major disadvantage of E-cell ETEM.

The impact of electron irradiation on the gas and on the chemical processes must be minimized or eliminated by using appropriate experimental conditions. Otherwise, any observation or conclusion from an ETEM experiment is rather questionable or even wrong. Using very low electron beam currents, avoiding the accumulation of high dose, and blanking the beam during the temperature ramp are “MUST”s for such an experiment. The effect of the response of the studied system to an electron beam and thus searching for an optimum condition to perform the experiment should be checked or done in a parallel “blank” experiment, with the beam switched off and the sample exposed to the beam only to record the final state of the catalysts. Under carefully simulated conditions close to those in real catalytic reactors, data from *in situ* ETEM can be directly related to structure–property relationships in catalysis.^{53,216,594}

8.2. Other Side-Effects

Differing from semiconducting or other bulk materials, most catalysts, although prefixed with solid, are fine nanoparticles that allow the transmission of an electron beam. Complicated sample preparations such as polishing followed by ion-milling are saved. For most TEM investigations, the fine catalysts are dispersed, in solution or dying, on ultrathin amorphous carbon film mounted on a Cu grid. A carbon nanotube network, graphene, and a silicon monoxide film are occasionally used as support: there are also grids made of Ni, Mo, or Au available. The use of grids covered with supporting film is under the

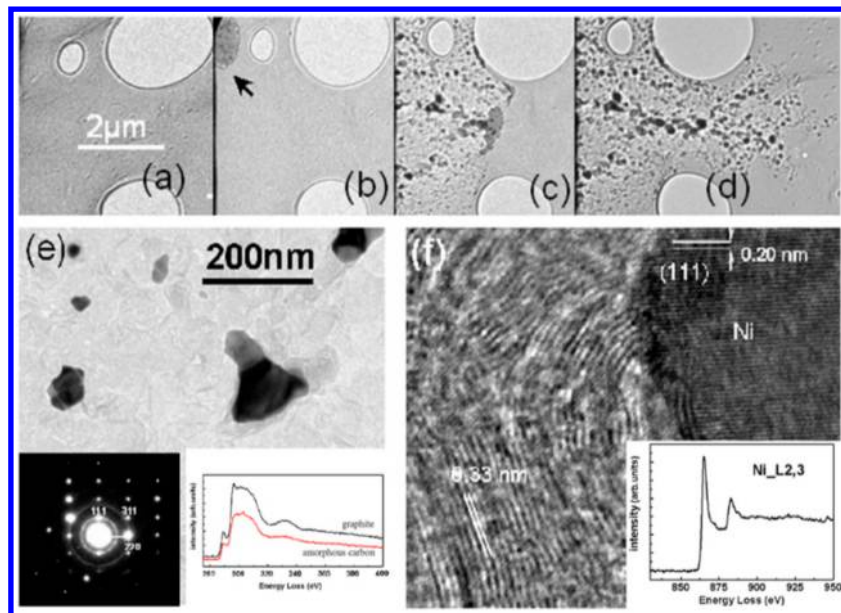


Figure 61. Series of images (a–d) showing the formation of Ni particles on amorphous carbon film supported on a Ni grid during consecutively *in situ* heating. Panel (e) displays the enlarged bright-field image, electron diffraction pattern, and EELS spectra recorded from the C film, respectively. Panel (f) displays a HRTEM image of Ni particles wrapped by graphite layers and a Ni core-loss spectrum. Reprinted with permission from ref 595. Copyright 2009 Elsevier.

assumption that they are stable under electron beam irradiation, at elevated temperature and in reactive gas.

However, a detailed study revealed quite a mixed behavior of supporting films and grids at elevated temperature in vacuum of a TEM.⁵⁹⁵ Zhang et al. studied the stability of Ni, Cu, Mo and Au TEM-grids coated with ultrathin α -C or silicon monoxide film is examined by *in situ* heating up to 500–850 °C in a TEM. Up temperature of 600 °C, Cu and Ni grid covered with amorphous carbon film are not suitable for *in situ* TEM, generating nanoparticles respectively on the supporting film. The generated Ni nanoparticles induce also the graphitization of amorphous carbon (Figure 61). In contrast, Mo and Au grid covered with amorphous carbon film exhibit relatively good stability at elevated temperature under a TEM vacuum condition up to 680 and 850 °C, respectively. Silicon monoxide supporting film on a Cu grid is stable in vacuum up to 550 °C, but silicon nanocrystals appear under intensive electron beam.⁵⁹⁵ A systematic study on the stability of various grids in combination with different supporting film at high temperature at the presence of gas is still missing, however, such preknowledge is essential for a careful planning of *in situ* environmental study in a ETEM.

The instability of the TEM grid or supporting film generates artifacts and thus complicates *in situ* studies of dynamic behaviors of nanomaterials at high temperature. For example, in a study of the stability of confined Pt nanoparticles in CNT, Zhang et al. found that Cu atoms from the grid diffuse into the Pt-filled CNT through the open cap during annealing at 600 °C for a prolonged time. The observed nanorod in Figure 62 is a Pt–Cu alloy, but not coalesced from the Pt nanoparticles confined in the tube before heating.⁵⁹⁵

9. A WORKED EXAMPLE: CU/ZNO

The role of electron microscopy is illustrated in the endeavor to understand the mode of operation of the technical Cu/Zn. This catalyst is used in methanol synthesis, one of the largest technical chemical processes. In addition it has enormous

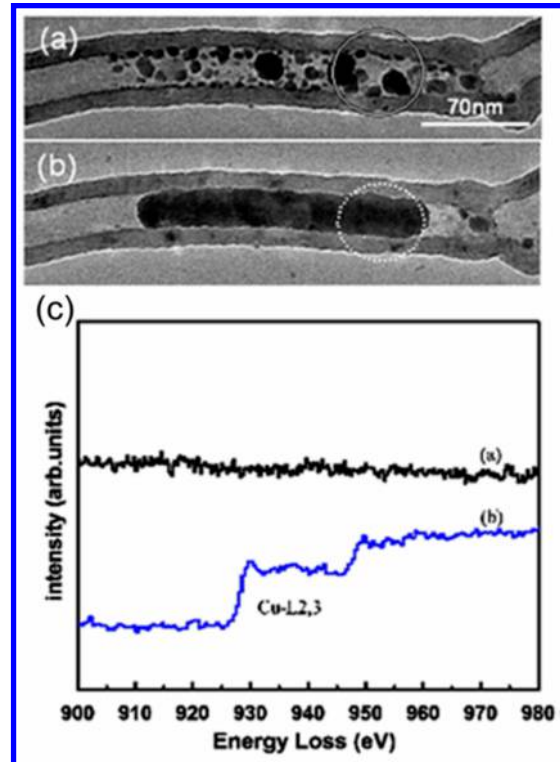


Figure 62. Artifact generated due to the instability of the Cu grid in an *in situ* experiment in a TEM: (a) and (b) show TEM images of a CNT containing Pt particles before and after heating at 600 °C for a prolonged time, respectively. The nanorod in (b) containing Cu atoms migrated into CNT, confirmed by the EELS spectrum in (c). Reprinted with permission from ref 595. Copyright 2009 Elsevier.

potential for the energy challenge, as methanol would be an excellent chemical storage medium for electrical energy and could contribute significantly to the mitigation of CO₂ emission.⁵⁹⁶ The catalyst is synthesized in a complex sequence

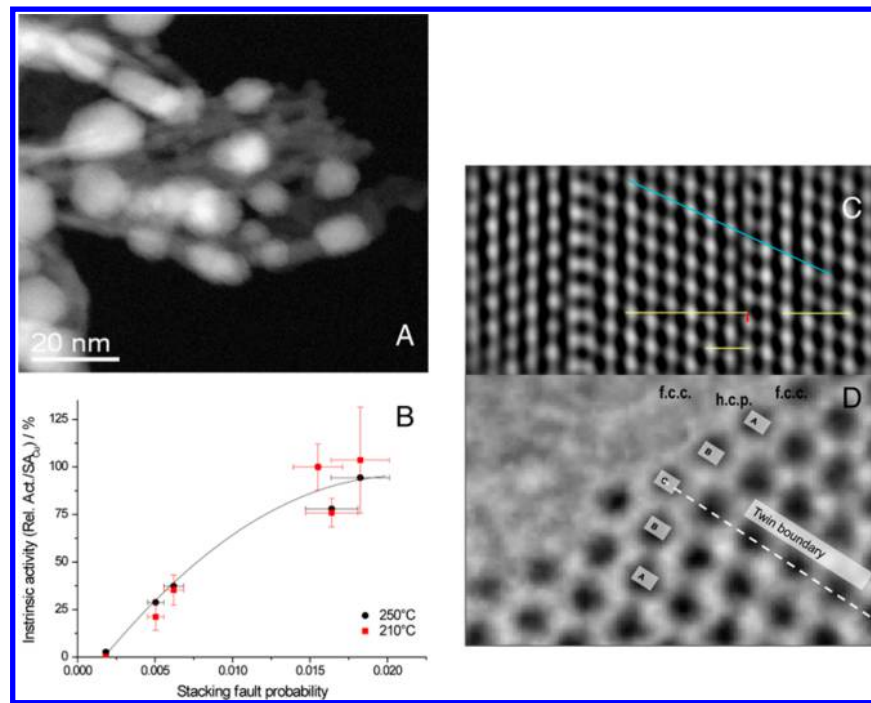


Figure 63. Cu/ZnO a synergistic complex catalyst. STEM shows (A) the disposition of Cu nanoparticles on needle-shaped ZnO stemming from the nanowires of its carbonate precursor. Close inspection shows a contrast of a core–shell structure. *In-situ* neutron-diffraction and Warren analysis (B) of the line profiles reveals for a series of catalysts a structure–function correlation between surface catalysis and bulk stacking defect density. The TEM image in (C) exemplifies two stacking defects in one Cu nanoparticle with the red vector illustrating the displacement of one column of atoms arising from the stacking disorder.⁶⁰⁰ This column terminates with an “extra” row of atoms at the surface generating a surface step that acts as a high-energy site and thus an active site for methanol synthesis (D).⁶⁰¹ Adapted with permission from refs 600 and 601. (ref 600: Copyright 2013 WILEY-VCH Verlag GmbH & Co. KGaA, Weinheim. Ref 601: Copyright 2012 The American Association for the Advancement of Science.).

of steps involving two oxidic precursors that are finally reduced to a Cu metal/ZnO nanocomposite with a peculiar pore structure allowing the gas phase to access a maximum fraction of the nanostructured internal surface without compromising the stability of the system operating for several years under rather severe conditions.

The precursors are essential to generate the nanostructure. During optimized precipitation a mixed metal malachite phase (zincian malachite) is formed. This adopts the form of “nanowires” defining in their diameter the size of the final Cu particles (ca. 5–10 nm). A series of topochemical solid–gas phase interfacial reactions^{597–599} transforms the system into a mixture of round Cu nanoparticles with spacers of ZnO in between. For a shape analysis of the interfaces, see Figure 29.

Figure 63A gives an impression how a network of ZnO nanowires supports the Cu particles in the activated catalyst. The pore network can be clearly seen in the STEM image. The Cu particles are not of equilibrium Wulff shape but exhibit a rather rounded shape and a contrast as if they were core–shell structures. Having synthesized a series of such catalysts with the same chemical composition but different real structures,^{601,602} it was possible to obtain the structure–function relation shown in Figure 63B. It is clear that the relative catalytic activity scales with the stacking order defect density, as revealed by *in situ* high pressure neutron diffraction⁶⁰⁰ and quantitative electron microscopy⁶⁰³ providing input for the data analysis.

10. CONCLUDING REMARKS AND PERSPECTIVES

In this review, we have described the progress of advanced electron microscopy techniques to characterize solid catalysts. First and foremost it should be stated that the family of

techniques available in EM has evolved into an indispensable toolbox for advancing our understanding of catalytic materials and is likely to even further enhance its relevance for the science of catalysis. The EM has evolved from a magnifying instrument toward a versatile and powerful nanolaboratory for characterizing morphological, crystallographic, compositional, and electronic properties of solid catalysts. The observation potential in the EM unfolded from a strictly 2-D projection to tomographic reconstructions of 3-dimensional information. The nanolaboratory EM can simultaneously and with excellent spatial control give information in real space, in reciprocal space, and in the energy domain using EELS. It is the purpose of this concluding section to give the possible application potentials of EM in catalysis some perspectives. They are based upon the notion that the largest potential of EM lies in the analysis of the structural complexity of performance catalysts. Here the largest benefit for the whole field of catalysis may be generated also in view of the often-questioned relation between cost and value of EM in practical catalysis. This does not preclude the evolution of cutting edge application of EM in model catalysis studies. For this rather limited field, however, modifications of instrumentation and application procedures will remain isolated and local solutions that can hardly be discussed from a general viewpoint.

The advancing possibilities of ultrafast time-resolved EM studies will have to develop their potential for catalytic applications. Here we are mainly concerned with multiple time-dependent phenomena occurring however on long time scales with respect to the making and breaking of chemical bonds; this is given by the transport dynamics of reactants and energy initiating chemical transformations. The ultrafast time

domain is relevant for model studies elucidating the charge carrier dynamics of materials and adsorbates. Such studies will rarely be done on performance catalysts forming the focus of this work.

The dynamic *in situ* ETEM and low-voltage EM open new opportunities to explore a wider variety of solid catalysts under working conditions. Avoiding beam-induced artifact formation, beam damage, and the necessity to completely remove volatile components such as crystal water from the specimen are limitations when molecular solids, carbon systems, or acid–base catalysts based upon hydroxides or organic structures are the relevant samples.

In catalysis the by far most important application of TEM techniques concerns the quantitative determination of morphology and size distributions of nanostructures. These comprise in supported or agglomerated forms all performance catalysts. Quantitative information is needed for any relation of catalytic performance with structural details. Often microanalytical information on STEM, EDX, or EFTEM most usefully complements the quantitative information. In the future such studies are made much more facile (time-saving) with modern instrumentation. The routine application of STEM observation will benefit enormously when the analysis software is brought up to the standards used, e.g. in semiconductor science. The presently critical limit of statistical significance in many reports should be improved by better software allowing using machine-learning strategies and advanced methods of description of structural features beyond spherical projections. Such improvements would make the application of TEM in catalysis much more attractive and error-proof and would not require specific high-end microscopy hardware. With such improvements the power of EM to elucidate descriptors of structural features and their variance as complement to the integrating techniques of diffraction and gas-adsorption would allow searching for the elusive active sites representing only a minor fraction of the active mass of a catalyst with more success than with the at present necessary structural averaging concepts.

High demands on the microscopy hardware arise from the desire to use the TEM for nanocrystallography and to detect local structures in complex matrices or determine the atomic structure of “defects”. Such applications are very important, complementing the standard averaging “phase” analysis of catalysts with XRD and EXAFS. As we know that active sites are high energy locations in the usually periodic matrix structure, the potential of TEM methods to elucidate local structure in geometric chemical and electronic dimensions would be most important. Here the reviewers state that in many cases the application potential of the TEM may be underused due to a lack of specialized knowledge about the analysis power of TEM at the originator of the analysis request complemented by the lack of knowledge of the TEM operator about the relevance for irregularities in catalysis over the beauty of translational structures. More topical interdisciplinary exchange of information can still greatly enhance the beneficial use of TEM in catalysis for “seeing” possible structures for active sites.

The advent of complex nanostructures from self-organization and nanochemistry has greatly enhanced the need for nanoanalytics for chemical and electronic structures. The availability of dedicated STEM analysis instruments and the enormous improvements of all spectroscopic methods in the EM allow in the future much more precise information about

the distribution and local nature of nanocatalysts. The detailed nature of segregated or dealloyed nanometals and the quantification of the composition of core–shell structures are examples for TEM analytics allowing better control synthesis and performance of advanced catalyst systems.

The use of the nanolaboratory TEM for performing catalysis experiments and to observe the kinetics and dynamics of the catalyst–reactant interaction is the most challenging domain of TEM application in catalysis. Despite the enormous potential and the significant progress made in the field of “*in-situ*” (operando) TEM, there is still much to do both in hardware development and in application method definition and verification. The present review gives an overview over the approaches. At the time of its completion, the novel techniques of *in situ* MEMS devices are coming to the field. It is too early to compare the advantages and disadvantages of ETEM and MEMS-TEM. The reviewers state that both techniques have specific application profiles that are not identical, calling thus for a coexistence of the two methods. It is clear, however, that all the imaging and analytical power of the nanolaboratory must be used to rationalize the dynamic and kinetic observation. Only then can a clear distinction of adventitious and artifact-induced observations be eliminated from the enormous amount of information gathered with such experiments. Even the data analysis and mining capabilities of EM are challenged by the flux of simultaneous observation enriched by the chemical data from the performance observation. Here we see a bottleneck limiting the use of the method: only very few simultaneous observations of catalysis and EM were possible in the past. The enormous technical challenges with observing conversions from nanogram samples in differential operation conditions are not yet adequately solved. This also includes the knowledge about interferences of the “EM chemistry” induced by materials, the atmosphere, and the electron beam present during observation. To advance here, much work has still to be done. At present these issues exclude a facile and widespread application much desirable from catalysis science as a type of standard methodology. Only if the hardware development can make substantial progress in terms of process automatization, of safety in chemical terms, and of the operability of such *in situ* instruments, then the full potential could be used for a wide community of catalysis science. These advances need critically the robust understanding of the scientific issues addressed above. Only then meaningful interpretations can give guidance in the understanding of dynamics and kinetics of catalyst transformation during their operation. In the foreseeable future thus only few centers of dedicated electron microscopy will be able to handle all the challenges associated with *in situ* microscopy.

The present work documented that many kinds of heterogeneous catalysts can be studied with a suite of techniques referred to as “electron microscopy”. Detailed structural and compositional information and a correlation of local electronic and geometric structure at the microscopic as well as at the mesoscopic level are possible. However, we must also keep in mind that the dynamical character of catalysts requires utmost attention in sample preparation, location of site for in-depth analysis, and beam artifact detection. To many catalysts the “atmosphere” inside a working TEM is also a sort of reaction environment of unknown properties to materials that are designed to respond to monolayer adsorption. The advent of aberration-corrected microscopy allows now imaging the outer surface of solids where the catalytic action takes place.

From the bad experiences of surface analysis made about 40 years ago, we know that the definition of the solid–vacuum interface in terms of chemical reactivity is critical for observing relevant structures and not for seeing the relaxation of the active structure induced by the “TEM chemistry”. All this is possible albeit time-consuming and poorly documented in the manifold of publications dealing with electron microscopy and catalysis.

One conclusion from this work would be that future publications document the phenomena of artifact formation on their samples in Supporting Information as well as refrain from using the term “typical average location”. A gallery of morphological situations including temporal evolutions is today facile to document and should serve as an illustration as to what location was chosen for in-depth analysis.

The complexity of catalysts in geometric and electronic structure is enormous when studied with techniques not relying on translational symmetry but providing atomic resolution. This lets us ask how many relevant structural details are in such systems. If we accept that from average turnover frequency measurements only a fraction of the surface exposed is active for conversion, then we have to answer the question about the relevance of the limited observations by TEM. Is it possible that we see too many details and cannot discover the relevant structures?

Our answer is clearly no. Accepting that heterogeneous performance catalysts are dynamical solids that undergo reactions with their substrates to form the active sites means that in an electron microscope we do not see the active form of the catalyst but merely the residue of it after removing it from the reaction. Here it must be considered that the majority of publications describe TEM experiments on as-synthesized forms of catalysts and thus cannot expect to see active sites, as the catalysts were never activated in the reaction feed.

The information gathered nonetheless holds many clues for understanding the reactivity of precatalytic solids that allow the formation of active sites. Reconstructions, segregations, and mobility phenomena on a support are such typical issues that need full understanding not only to describe the deactivation of the system but more importantly to understand the chemical concepts standing behind the activation of the precatalyst. This most critical but most hidden episode in the life of a catalyst requires a driving force and a suitable kinetics. Nanostructuring and storing chemical energy in metastable forms of the material are the means for providing this driving force. The capacity of EM methods to observe in real space and without translational order makes EM the technique of choice to analyze the driving force and so to understand the process leading from the precatalyst to the active form. Electron microscopy can indicate the reaction pathways that such a metastable high-energy functional material may take to minimize its energy. In the view of the authors EM has here a leading role bridging the still isolated worlds of model materials with observable transformations but very limited performance to that of performance systems where good activity arises from transient and largely unknown structural transformations.

One desire in this context is to study such phenomena by using IL TEM combined with multiple techniques of identifying the structure and bonding of one and the same object group in a catalyst. The sample may then be subject to reaction conditions without the electron beam present and without any pressure gap, both affecting the course of a kinetically controlled relaxation of a high-energy structure. This

can be done best outside the TEM instrument to verify the correct performance of the specimen. In such an experiment the observed changes in performance with time indicate activation and later deactivation when successive cycles of observation and operation are put together. The time scales of activation processes can be hundreds of hours, preventing facile direct *in situ* observation. Interrupted experiments with back-transfer to the microscope can give invaluable information on the dynamics of the active material.

Such time-consuming studies may be equally useful as ETEM experiments where the dynamics of systems can be studied with better resolution in time and possibly in space but where presently no proven link to catalytic performance is possible. In all cases where structural dynamics of a nanomaterial without link to catalytic reactivity is the target of investigation, the ETEM is the instrument of choice. The limitations coming with the technique were discussed above. Thus, for the special case of determination structure–function relations in catalysis it seems a bit over-rated to deduce these from ETEM blindly without functional verification (measuring the catalytic performance during observation) given the multiple reactions that metastable systems can undergo and the only single pathway leading to a performance catalyst.

The reviewers state in the literature a certain fixation of electron microscopy on atomic resolution. Catalysis is a phenomenon where transport in multiple dimensions of space and time affects the performance in equal relevance to the molecular details of the active sites. The over-rating of a local molecular view as the “sole relevant factor of catalysis” with respect to the necessity in a catalytic reaction to exchange atoms and molecules as well as thermal energy and charge carriers over molecular and supramolecular dimensions leads to an “obsession” for atomic resolution. It is a great value to observe local structure in real space without having to refer to models and spectroscopic interpretation: but it should be kept in mind that despite all achievements in resolution we have never seen an active site in operation. Thus, we cannot be sure that any observed local structure is the relevant one. As interesting and inspiring is the real-space observation of molecular morphologies, one must avoid its suggestive effect. In addition, we cannot see nonregular adsorbates or reaction products or the relaxation of heavy-atomic structures during catalytic operation.

We can, however, see very well the features of a catalyst at the mesoscopic level. This is done today in the highly detailed studies upon metal particle mobility on supports. Very little analysis on the ability of the solid interface between active phase and support for transport properties can be found in the literature, with the prominent exception of mesoporous and microporous silicates, where such questions are discussed explicitly in the context of the concept of an “inner surface”.

A combination of imaging at several scales of dimensions with the respective simulation of transport in the boundary layer between solid catalyst and fluid reactants would open a new dimension of addressing structure–function relations. The recent progress in using secondary electron imaging in TEM (with high brightness sources) and in ESEM (also with field emission sources) allows compensating for the strictly two-dimensional projection image in the conventional TEM, rendering a reconstruction of the interacting morphology in real space a nontrivial task. Such instrumentation can be combined with advanced tomographic methods and then give a complete picture about the shape and chemical diversity of the

boundary between solid and fluid phase comprising the very nature of “heterogeneous” catalysis.

At the end of this review the authors state that the progress in catalysis science on a rational design basis will be very difficult without widespread use of the comprehensive set of techniques available in the nanolaboratory “electron microscope”. We advocate the reorientation of the development focus from performance in resolution, imaging potential, and spectroscopic capabilities toward controlling the application environment. For the case of catalysis, we suggest to develop the “chemical electron microscope” that has the capabilities of a high-end material science instrument plus features allowing handling specimens in controlled environments of chemical potential. This review gives multiple insights into what it takes to arrive at such a “chemical electron microscope”. It is most relevant to carry forward this evolution such that statistically meaningful observations can be made by a multitude of users interested in the subject. Only then will the information move from cutting edge “curiosity” to chemical usefulness in the hands of application-oriented users.

AUTHOR INFORMATION

Corresponding Author

* E-mail: dssu@imr.ac.cn, dangsheng@fhi-berlin.mpg.de (D.S.S.).

Notes

The authors declare no competing financial interest.

Biographies



Dang Sheng Su completed his Ph.D. at the Technical University of Vienna (Vienna, Austria) in 1991, and then moved to the Fritz Haber Institute (FHI) of the Max Planck Society in Berlin, Germany, as a postdoctoral fellow in the Department of Electron Microscopy. After a short stay at the Hahn Meitner Institut GmbH and the Humboldt Universität zu Berlin (Berlin, Germany), he rejoined the FHI in 1999, where he worked on electron microscopy and nanomaterials in heterogeneous catalysis and energy storage until 2011. He is now a Professor and Head of the Catalysis and Materials Division of the Shenyang National Laboratory for Materials Science, Institute of Metal Research, Chinese Academy of Sciences, Shenyang, PR China. His research interests are nanomaterials and nanocatalysis, energy storage and conversion, electron microscopy, and electron energy-loss spectroscopy.



Bingsen Zhang completed his Ph.D. at the Northeastern University (China) in 2009, and then went to the Fritz Haber Institute of the Max Planck Society in Berlin (Germany) as a postdoctoral fellow in the Department of Inorganic Chemistry. In 2011, he received an IMR SYNL-T.S. Ké Research Fellowship founded by the Shenyang National Laboratory for Materials Science (SYNL) and joined the Institute of Metal Research (IMR), Chinese Academy of Sciences (CAS). Now he is a professor of SYNL, IMR CAS. His current main research interest is the advanced transmission electron microscopy investigation of carbon, catalyst, and energy conversion and storage materials.



Robert Schlögl studied chemistry and completed his Ph.D. on graphite intercalation compounds at the Ludwig Maximilians University in Munich (1982). After postdoctoral stays at Cambridge and Basle, he carried out his habilitation under the supervision of Professor Ertl (Nobel Laureate) at the Fritz Haber Institute in Berlin (1989). Later he accepted the call for a Full Professorship of Inorganic Chemistry at Frankfurt University. In 1994 he was appointed his current position as Director at the Fritz Haber Institute of the Max Planck Society in Berlin. In addition, in 2011 he was appointed Founding Director at the new Max Planck Institute for Chemical Energy Conversion in Mülheim a.d. Ruhr. He is an Honorary Professor at Technical University Berlin, at Humboldt University Berlin, and at University Duisburg-Essen. Robert Schlögl's research focuses primarily on the investigation of heterogeneous catalysts, with the aim to combine scientific with technical applicability as well as on the development of nanochemically optimized materials for energy storage. The application of knowledge-based heterogeneous catalysis for large-scale chemical energy conversion summarizes his current research focus.

ACKNOWLEDGMENTS

D.S.S. and B.S.Z. acknowledge the financial support from NSFC of China (21133010, 21203215, 51221264,

21261160487), MOST (2011CBA00504), and “Strategic Priority Research Program” of the Chinese Academy of Sciences (Grant No. XDA09030103). D.S.S. thanks the members of the electron microscopy group at the Fritz Haber Institute, where he acted as group leader for more than ten years, especially the former members Di Wang, Thomas Hansen, Jacob Wagner, Zaoli Zhang, Wei Zhang, and Lide Yao, and former Ph.D. students in the group Jens-Oliver Mueller, Marc Willinger, and Manfrend Schuster. R.S. wishes to thank the many members of the past and present electron microscopy group. The present team is led by M. Willinger and Th. Lunkenbein, who both shall be acknowledged for their multiple discussion contributions and for their dedicated practical work. A. Klein-Hoffmann, G. Weinberg, W. Franzen, and N. Pfänder are the technical support team who operate the microscopes and perform the diligent tasks of specimen preparation. They all contributed much practical insight supporting the critical analysis of the work discussed.

ABBREVIATIONS

| | |
|--------|---|
| EM | electron microscopy |
| TEM | transmission electron microscopy |
| STEM | scanning transmission electron microscopy |
| EDX | energy dispersion X-ray spectroscopy |
| EELS | electron energy loss spectroscopy |
| ET | electron tomography |
| XRD | X-ray diffraction |
| XRF | X-ray fluorescence |
| NEXAFS | near edge X-ray absorption fine structure |
| STM | scanning tunneling microscope |
| AFM | atomic force microscope |
| GC-MS | gas chromatography–mass spectrometry |
| SAED | selected area electron diffraction |
| HRTEM | high-resolution TEM |
| HRSTEM | high-resolution STEM |
| CBED | convergent-beam electron diffraction |
| HAADF | high-angle annular dark-field |
| EFTEM | energy-filtering TEM |
| CNT | carbon nanotube |
| ELNES | electron energy loss near edge structure |
| CCD | charge-coupled device |
| FEG | field emission gun |
| 2D | two-dimension |
| 3D | three-dimension |
| 4D | four-dimension |
| ETEM | environmental TEM |
| SEM | scanning electron microscopy |
| ESEM | environmental SEM |
| IL-TEM | identical locations TEM |
| PED | precession electron diffraction |
| EST | equally sloped tomography |
| PSD | particle size distribution |
| AC | aberration corrected |
| SMSI | strong metal–support interaction |
| HVEM | high voltage EM |
| DFT | density functional theory |
| CTF | contrast transfer functions |
| GNP | gold nanoparticle |
| BF | bright field |
| EPR | electron paramagnetic resonance |
| TOS | time on stream |

REFERENCES

- Smith, D. J. Development of aberration-corrected electron microscopy. *Microsc. Microanal.* **2008**, *14*, 2–15.
- Urban, K. W. Is science prepared for atomic-resolution electron microscopy? *Nat. Mater.* **2009**, *8*, 260–262.
- Kisielowski, C.; Freitag, B.; Bischoff, M.; van Lin, H.; Lazar, S.; Knippels, G.; Tiemeijer, P.; van der Stam, M.; von Harrach, S.; Stekelenburg, M.; Haider, M.; Uhlemann, S.; Muller, H.; Hartel, P.; Kabius, B.; Miller, D.; Petrov, I.; Olson, E. A.; Donchev, T.; Kenik, E. A.; Lupini, A. R.; Bentley, J.; Pennycook, S. J.; Anderson, I. M.; Minor, A. M.; Schmid, A. K.; Duden, T.; Radmilovic, V.; Ramasse, Q. M.; Watanabe, M.; Erni, R.; Stach, E. A.; Denes, P.; Dahmen, U. Detection of single atoms and buried defects in three dimensions by aberration-corrected electron microscope with 0.5-angstrom information limit. *Microsc. Microanal.* **2008**, *14*, 469–477.
- Sawada, H.; Hosokawai, F.; Kaneyama, T.; Ishizawa, T.; Terao, M.; Kawazoe, M.; Sannomiya, T.; Tomita, T.; Kondo, Y.; Tanaka, T.; Oshima, Y.; Tanishiro, Y.; Yamamoto, N.; Takayanagi, K. Achieving 63 pm resolution in scanning transmission electron microscope with spherical aberration corrector. *Jpn. J. Appl. Phys.* **2007**, *46*, L568–L570.
- Uhlemann, S.; Müller, H.; Hartel, P.; Zach, J.; Haider, M. Thermal Magnetic Field Noise Limits Resolution in Transmission Electron Microscopy. *Phys. Rev. Lett.* **2013**, *111*, 046101.
- Reich, E. S. Imaging hits noise barrier. *Nature* **2013**, *499*, 135–136.
- Muller, D. A.; Kourkoutis, L. F.; Murfitt, M.; Song, J. H.; Hwang, H. Y.; Silcox, J.; Dellby, N.; Krivanek, O. L. Atomic-scale chemical imaging of composition and bonding by aberration-corrected microscopy. *Science* **2008**, *319*, 1073–1076.
- Muller, D. A. Structure and bonding at the atomic scale by scanning transmission electron microscopy. *Nat. Mater.* **2009**, *8*, 263–270.
- Zhou, W.; Oxley, M. P.; Lupini, A. R.; Krivanek, O. L.; Pennycook, S. J.; Idrobo, J. C. Single Atom Microscopy. *Microsc. Microanal.* **2012**, *18*, 1342–1354.
- Colliex, C.; Gloter, A.; March, K.; Mory, C.; Stephan, O.; Suenaga, K.; Tence, M. Capturing the signature of single atoms with the tiny probe of a STEM. *Ultramicroscopy* **2012**, *123*, 80–89.
- Suenaga, K.; Iizumi, Y.; Okazaki, T. Single atom spectroscopy with reduced delocalization effect using a 30 kV-STEM. *Eur. Phys. J.—Appl. Phys.* **2011**, *54*, 33508.
- Suenaga, K.; Sato, Y.; Liu, Z.; Kataura, H.; Okazaki, T.; Kimoto, K.; Sawada, H.; Sasaki, T.; Omoto, K.; Tomita, T.; Kaneyama, T.; Kondo, Y. Visualizing and identifying single atoms using electron energy-loss spectroscopy with low accelerating voltage. *Nat. Chem.* **2009**, *1*, 415–418.
- Pennycook, S. J.; Rafferty, B.; Nellist, P. D. Z-contrast imaging in an aberration-corrected scanning transmission electron microscope. *Microsc. Microanal.* **2000**, *6*, 343–352.
- Sohlberg, K.; Rashkeev, S.; Borisovich, A. Y.; Pennycook, S. J.; Pantelides, S. T. Origin of anomalous Pt-Pt distances in the Pt/alumina catalytic system. *ChemPhysChem* **2004**, *5*, 1893–1897.
- Qiao, B. T.; Wang, A. Q.; Yang, X. F.; Allard, L. F.; Jiang, Z.; Cui, Y. T.; Liu, J. Y.; Li, J.; Zhang, T. Single-atom catalysis of CO oxidation using Pt1/FeOx. *Nat. Chem.* **2011**, *3*, 634–641.
- Lin, J.; Qiao, B. T.; Liu, J. Y.; Huang, Y. Q.; Wang, A. Q.; Li, L.; Zhang, W. S.; Allard, L. F.; Wang, X. D.; Zhang, T. Design of a Highly Active Ir/Fe(OH)x Catalyst: Versatile Application of Pt-Group Metals for the Preferential Oxidation of Carbon Monoxide. *Angew. Chem., Int. Ed.* **2012**, *51*, 2920–2924.
- Zhou, W.; Ross-Medgaarden, E. I.; Knowles, W. V.; Wong, M. S.; Wachs, I. E.; Kiely, C. J. Identification of active Zr-WOx clusters on a ZrO₂ support for solid acid catalysts. *Nat. Chem.* **2009**, *1*, 722–728.
- Herzing, A. A.; Kiely, C. J.; Carley, A. F.; Landon, P.; Hutchings, G. J. Identification of active gold nanoclusters on iron oxide supports for CO oxidation. *Science* **2008**, *321*, 1331–1335.
- Su, D. S.; Jacob, T.; Hansen, T. W.; Wang, D.; Schlogl, R.; Freitag, B.; Kujawa, S. Surface chemistry of Ag particles: Identification

- of oxide species by aberration-corrected TEM and by DFT calculations. *Angew. Chem., Int. Ed.* **2008**, *47*, 5005–5008.
- (20) Gontard, L. C.; Chang, L. Y.; Hetherington, C. J. D.; Kirkland, A. I.; Ozkaya, D.; Dunin-Borkowski, R. E. Aberration-corrected imaging of active sites on industrial catalyst nanoparticles. *Angew. Chem., Int. Ed.* **2007**, *46*, 3683–3685.
- (21) Akita, T.; Kohyama, M.; Haruta, M. Electron microscopy study of gold nanoparticles deposited on transition metal oxides. *Acc. Chem. Res.* **2013**, *46*, 1773–1782.
- (22) Su, D. S.; Hebert, C.; Willinger, M.; Schlogl, R. Anisotropy and collection angle dependence of the oxygen K ELNES in V₂O₅: a band-structure calculation study. *Micron* **2003**, *34*, 227–233.
- (23) Midgley, P. A.; Dunin-Borkowski, R. E. Electron tomography and holography in materials science. *Nat. Mater.* **2009**, *8*, 271–280.
- (24) Thomas, J. M.; Simpson, E. T.; Kasama, T.; Dunin-Borkowski, R. E. Electron holography for the study of magnetic nanomaterials. *Acc. Chem. Res.* **2008**, *41*, 665–674.
- (25) Friedrich, H.; de Jongh, P. E.; Verkleij, A. J.; de Jong, K. P. Electron Tomography for Heterogeneous Catalysts and Related Nanostructured Materials. *Chem. Rev.* **2009**, *109*, 1613–1629.
- (26) Leary, R.; Midgley, P. A.; Thomas, J. M. Recent Advances in the Application of Electron Tomography to Materials Chemistry. *Acc. Chem. Res.* **2012**, *45*, 1782–1791.
- (27) Bals, S.; Goris, B.; Altantzis, T.; Heidari, H.; Van Aert, S.; Van Tendeloo, G. Seeing and measuring in 3D with electrons. *C. R. Phys.* **2014**, *15*, 140–150.
- (28) Takeda, S.; Yoshida, H. Atomic-resolution environmental TEM for quantitative in-situ microscopy in materials science. *J. Electron Microsc.* **2013**, *62*, 193–203.
- (29) Jinschek, J. R. Use of an Environmental Transmission Electron Microscope for Dynamic in situ Studies of Nano-Structured Materials at the Atomic Scale. *Am. Lab.* **2013**, *45*, 12–16.
- (30) Jinschek, J. R.; Helveg, S. Image resolution and sensitivity in an environmental transmission electron microscope. *Micron* **2012**, *43*, 1156–1168.
- (31) Jinschek, J. R. Atomic scale structure-function relationship of heterogeneous catalysts: investigation of gas-solid interactions by ETEM. *Microsc. Anal.* **2012**, *26*, S5–S10.
- (32) Boyes, E. D.; Gai, P. L. Visualising reacting single atoms under controlled conditions: Advances in atomic resolution in situ Environmental (Scanning) Transmission Electron Microscopy (E(S)-TEM). *C. R. Phys.* **2014**, *15*, 200–213.
- (33) Jinschek, J. R. Advances in the environmental transmission electron microscope (ETEM) for nanoscale in situ studies of gas-solid interactions. *Chem. Commun.* **2014**, *50*, 2696–2706.
- (34) Hansen, T. W.; Wagner, J. B. Catalysts under Controlled Atmospheres in the Transmission Electron Microscope. *ACS Catal.* **2014**, *4*, 1673–1685.
- (35) Tao, F.; Salmeron, M. In Situ Studies of Chemistry and Structure of Materials in Reactive Environments. *Science* **2011**, *331*, 171–174.
- (36) Liu, J.; Cao, G. Z.; Yang, Z. G.; Wang, D. H.; Dubois, D.; Zhou, X. D.; Graff, G. L.; Pederson, L. R.; Zhang, J. G. Oriented Nanostructures for Energy Conversion and Storage. *ChemSusChem* **2008**, *1*, 676–697.
- (37) Schlogl, R. The Role of Chemistry in the Energy Challenge. *ChemSusChem* **2010**, *3*, 209–222.
- (38) Zhang, B.; Su, D. S. Transmission Electron Microscopy and the Science of Carbon Nanomaterials. *Small* **2014**, *10*, 222–229.
- (39) Su, D. S. Special Issue: Advanced Electron Microscopy for Catalysis. *ChemCatChem* **2013**, *5*, 2543–2545.
- (40) Su, D. S. Special Issue: Advanced Electron Microscopy for Catalysis. *ChemCatChem* **2011**, *3*, 919–920.
- (41) Colliex, C. Seeing and measuring with electrons: Transmission electron microscopy today and tomorrow—An introduction. *C. R. Phys.* **2014**, *15*, 101–109.
- (42) Zhang, B.; Su, D. S. Using electron beams to investigate catalytic materials. *C. R. Phys.* **2014**, *15*, 258–268.
- (43) Sohlberg, K.; Pennycook, T. J.; Zhou, W.; Pennycook, S. J. Insights into the physical chemistry of materials from advances in HAADF-STEM. *Phys. Chem. Chem. Phys.* **2015**, *17*, 3982–4006.
- (44) Liu, J. Y. Advanced electron microscopy characterization of nanostructured heterogeneous catalysts. *Microsc. Microanal.* **2004**, *10*, 55–76.
- (45) Liu, J. Y. Advanced Electron Microscopy of Metal-Support Interactions in Supported Metal Catalysts. *ChemCatChem* **2011**, *3*, 934–948.
- (46) Zhang, S. R.; Nguyen, L.; Zhu, Y.; Zhan, S. H.; Tsung, C. K.; Tao, F. In-Situ Studies of Nanocatalysis. *Acc. Chem. Res.* **2013**, *46*, 1731–1739.
- (47) Grunwaldt, J. D.; Wagner, J. B.; Dunin-Borkowski, R. E. Imaging Catalysts at Work: A Hierarchical Approach from the Macro- to the Meso- and Nano-scale. *ChemCatChem* **2013**, *5*, 62–80.
- (48) Thomas, J. M.; Leary, R.; Midgley, P. A.; Holland, D. J. A new approach to the investigation of nanoparticles: Electron tomography with compressed sensing. *J. Colloid Interface Sci.* **2013**, *392*, 7–14.
- (49) Bernal, S.; Baker, R. T.; Burrows, A.; Calvino, J. J.; Kiely, C. J.; Lopez-Cartes, C.; Perez-Omil, J. A.; Rodriguez-Izquierdo, J. M. Structure of highly dispersed metals and oxides: exploring the capabilities of high-resolution electron microscopy. *Surf. Interface Anal.* **2000**, *29*, 411–421.
- (50) Thomas, J. M.; Terasaki, O.; Gai, P. L.; Zhou, W. Z.; Gonzalez-Calbet, J. Structural elucidation of microporous and mesoporous catalysts and molecular sieves by high-resolution electron microscopy. *Acc. Chem. Res.* **2001**, *34*, 583–594.
- (51) Gai, P. L. Developments of electron microscopy methods in the study of catalysts. *Curr. Opin. Solid State Mater. Sci.* **2001**, *5*, 371–380.
- (52) Datye, A. K. Electron microscopy of catalysts: recent achievements and future prospects. *J. Catal.* **2003**, *216*, 144–154.
- (53) Gai, P. L.; Calvino, J. J. Electron Microscopy in the Catalysis of Alkane Oxidation, Environmental Control, And Alternative Energy Sources. *Annu. Rev. Mater. Res.* **2005**, *35*, 465–504.
- (54) Thomas, J. M.; Gal, P. L. In *Advances in Catalysis*; Gates, B. C., Knoblinger, H., Eds.; 2004; Vol. 48, pp 171–227.
- (55) Liu, J. Y. Scanning transmission electron microscopy and its application to the study of nanoparticles and nanoparticle systems. *J. Electron Microsc.* **2005**, *54*, 251–278.
- (56) Sanchez, S. I.; Small, M. W.; Sivaramakrishnan, S.; Wen, J. G.; Zuo, J. M.; Nuzzo, R. G. Visualizing Materials Chemistry at Atomic Resolution. *Anal. Chem.* **2010**, *82*, 2599–2607.
- (57) Thomas, J. M.; Midgley, P. A. The Merits of Static and Dynamic High-Resolution Electron Microscopy (HREM) for the Study of Solid Catalysts. *ChemCatChem* **2010**, *2*, 783–798.
- (58) Zhou, W.; Wachs, I. E.; Kiely, C. J. Nanostructural and chemical characterization of supported metal oxide catalysts by aberration corrected analytical electron microscopy. *Curr. Opin. Solid State Mater. Sci.* **2012**, *16*, 10–22.
- (59) Yang, J. C.; Small, M. W.; Grieshaber, R. V.; Nuzzo, R. G. Recent developments and applications of electron microscopy to heterogeneous catalysis. *Chem. Soc. Rev.* **2012**, *41*, 8179–8194.
- (60) Thomas, J. M.; Ducati, C.; Leary, R.; Midgley, P. A. Some Turning Points in the Chemical Electron Microscopic Study of Heterogeneous Catalysts. *ChemCatChem* **2013**, *5*, 2560–2579.
- (61) Hansen, T. W.; DeLaRiva, A. T.; Challa, S. R.; Datye, A. K. Sintering of Catalytic Nanoparticles: Particle Migration or Ostwald Ripening? *Acc. Chem. Res.* **2013**, *46*, 1720–1730.
- (62) Schlogl, R. In *Advances in Catalysis*; Gates, B. C., Knoblinger, H., Eds.; Elsevier Academic Press Inc.: San Diego, 2009; Vol. 52, p 273–338.
- (63) Lee, A. F.; Prabhakaran, V.; Wilson, K. Surface X-ray studies of catalytic clean technologies. *Chem. Commun.* **2010**, *46*, 3827–3842.
- (64) Bottger, I.; Schedel-Niedrig, T.; Timpe, O.; Gottschall, R.; Havecker, M.; Ressler, T.; Schlogl, R. Catalytic methanol oxidation over copper: Observation of reaction-induced nanoscale restructuring by means of in situ time-resolved X-ray absorption spectroscopy. *Chem.—Eur. J.* **2000**, *6*, 1870–1876.

- (65) Uchida, Y.; Bao, X.; Weiss, K.; Schlogl, R. Oxygen-induced restructuring of Au(111) observed by reflection electron microscopy. *Surf. Sci.* **1998**, *401*, 469–475.
- (66) Chenna, S.; Crozier, P. A. Operando Transmission Electron Microscopy: A Technique for Detection of Catalysis Using Electron Energy-Loss Spectroscopy in the Transmission Electron Microscope. *ACS Catal.* **2012**, *2*, 2395–2402.
- (67) Beale, A. M.; Jacques, S. D. M.; Weckhuysen, B. M. Chemical imaging of catalytic solids with synchrotron radiation. *Chem. Soc. Rev.* **2010**, *39*, 4656–4672.
- (68) Wagner, J. B.; Su, D. S.; Schunk, S. A.; Hibst, H.; Petzoldt, J.; Schlogl, R. Structural characterization of high-performance catalysts for partial oxidation—the high-resolution and analytical electron microscopy approach. *J. Catal.* **2004**, *224*, 28–35.
- (69) Ueda, W.; Vitry, D.; Kato, T.; Watanabe, N. Structural organization of catalytic functions in Mo-based oxides for propane selective oxidation. *Abstr. Pap. Am. Chem. Soc.* **2003**, *226*, U392–U392.
- (70) Ovsitser, O.; Uchida, Y.; Mestl, G.; Weinberg, G.; Blume, A.; Jager, J.; Dieterle, M.; Hibst, H.; Schlogl, R. Molybdenum oxide based partial oxidation catalyst—Part 3. Structural changes of a MoVV mixed oxide catalyst during activation and relation to catalytic performance in acrolein oxidation. *J. Mol. Catal. A—Chem.* **2002**, *185*, 291–303.
- (71) Uchida, Y.; Mestl, G.; Ovsitser, O.; Jager, J.; Blume, A.; Schlogl, R. Molybdenum oxide based partial oxidation catalyst 4. TEM identification of a new oxygen-reduced phase formed during acrolein partial oxidation under reducing conditions. *J. Mol. Catal. A—Chem.* **2002**, *187*, 247–257.
- (72) Wieske, M.; Su, D. S.; Beckmann, F.; Schlogl, R. Electron-beam-induced structural variations of divanadium pentoxide (V₂O₅) at liquid helium temperature. *Catal. Lett.* **2002**, *81*, 43–47.
- (73) Pinna, N.; Willinger, M.; Weiss, K.; Urban, J.; Schlogl, R. Local structure of nanoscopic materials: V₂O₅ nanorods and nanowires. *Nano Lett.* **2003**, *3*, 1131–1134.
- (74) Wagner, J. B.; Willinger, M. G.; Muller, J. O.; Su, D. S.; Schlogl, R. Surface-charge-induced reversible phase transitions of Bi nanoparticles. *Small* **2006**, *2*, 230–234.
- (75) Ayub, I.; Su, D. S.; Willinger, M.; Kharlamov, A.; Ushkalov, L.; Zazhigalov, V. A.; Kirillova, N.; Schlogl, R. Tribomechanical modification of Bi promoted vanadyl phosphate systems 1: An improved catalyst and insight into structure-function relationship. *Phys. Chem. Chem. Phys.* **2003**, *5*, 970–978.
- (76) Ertl, G.; Knoeziinger, H.; Schueth, F.; Weitkamp, J. *Handbook of heterogeneous catalysis*; Wiley-VCH: Weinheim, 2008.
- (77) Mestl, G.; Srinivasan, T. K. K. Raman Spectroscopy of Monolayer-Type Catalysts: Supported Molybdenum Oxides. *Catal. Rev.* **1998**, *40*, 451–570.
- (78) Mestl, G.; Knizlinger, H.; Ertl, G.; Knizlinger, H.; Weitkamp, J. *Vibrational Spectroscopies*; VCH-Verlag: Weinheim, 1997; pp 539–574.
- (79) Wachs, I. E. Recent conceptual advances in the catalysis science of mixed metal oxide catalytic materials. *Catal. Today* **2005**, *100*, 79–94.
- (80) Knop-Gericke, A.; Kleimenov, E.; Havecker, M.; Blume, R.; Teschner, D.; Zafeiratos, S.; Schlogl, R.; Bukhtiyarov, V. I.; Kaichev, V. V.; Prosvirin, I. P.; Nizovskii, A. I.; Bluhm, H.; Barinov, A.; Dudin, P.; Kiskinova, M. In *Advances in Catalysis*; Gates, B. C., Knozinger, H., Eds.; Elsevier Academic Press Inc.: San Diego, 2009; Vol. 52, pp 213–272.
- (81) Havecker, M.; Cavalleri, M.; Herbert, R.; Follath, R.; Knop-Gericke, A.; Hess, C.; Hermann, K.; Schlogl, R. Methodology for the structural characterisation of V_xO_y species supported on silica under reaction conditions by means of in situ O K-edge X-ray absorption spectroscopy. *Phys. Status Solidi B* **2009**, *246*, 1459–1469.
- (82) Tao, F.; Zhang, S. R.; Nguyen, L.; Zhang, X. Q. Action of bimetallic nanocatalysts under reaction conditions and during catalysis: evolution of chemistry from high vacuum conditions to reaction conditions. *Chem. Soc. Rev.* **2012**, *41*, 7980–7993.
- (83) Amri, A.; Jiang, Z. T.; Bahri, P. A.; Yin, C. Y.; Zhao, X. L.; Xie, Z. H.; Duan, X. F.; Widjaja, H.; Rahman, M. M.; Pryor, T. Surface Electronic Structure and Mechanical Characteristics of Copper-Cobalt Oxide Thin Film Coatings: Soft X-ray Synchrotron Radiation Spectroscopic Analyses and Modeling. *J. Phys. Chem. C* **2013**, *117*, 16457–16467.
- (84) Datye, A. K.; Xu, Q.; Kharas, K. C.; McCarty, J. M. Particle size distributions in heterogeneous catalysts: What do they tell us about the sintering mechanism? *Catal. Today* **2006**, *111*, 59–67.
- (85) Wang, D.; Villa, A.; Su, D.; Prati, L.; Schlogl, R. Carbon-Supported Gold Nanocatalysts: Shape Effect in the Selective Glycerol Oxidation. *ChemCatChem* **2013**, *5*, 2717–2723.
- (86) Gan, L.; Rudi, S.; Cui, C.; Strasser, P. Ni-Catalyzed Growth of Graphene Layers during Thermal Annealing: Implications for the Synthesis of Carbon-Supported Pt Ni Fuel-Cell Catalysts. *ChemCatChem* **2013**, *5*, 2691–2694.
- (87) Zhang, W.; Chen, M.; Theil Kuhn, L.; Bowen, J. R.; Bentzen, J. J. Electrochemistry Unlocks Wettability: Epitaxial Growth of Oxide Nanoparticles on Rough Metallic Surfaces. *ChemElectroChem* **2014**, *1*, 520–523.
- (88) Su, D. S.; Xiao-Wei, C.; Hamid, S. B. A.; Schlogl, R. The morphology, porosity and productivity control of carbon nanofibers or nanotubes on modified activated carbon. *Carbon* **2007**, *45*, 895–898.
- (89) Miiller, J. O.; Su, D. S.; Wild, U.; Schlogl, R. Bulk and surface structural investigations of diesel engine soot and carbon black. *Phys. Chem. Chem. Phys.* **2007**, *9*, 4018–4025.
- (90) Su, D. S.; Zhu, Z. P.; Liu, X.; Weinberg, G.; Wang, N.; Schlogl, R. Assembly of carbon tube-in-tube nanostructures. *AIP Conf. Proc.* **2005**, *296*–300.
- (91) Su, D. S.; Zhu, Z. P.; Lu, Y.; Schlogl, R.; Weinberg, G.; Liu, Z. Y. In *Electronic Properties of Synthetic Nanostructures*; Kuzmany, H., Fink, J., Mehring, M., Roth, S., Eds.; 2004; Vol. 723, pp 32–35.
- (92) Marks, L. D. Experimental Studies of Small-Particle Structures. *Rep. Prog. Phys.* **1994**, *57*, 603–649.
- (93) Smith, D. J. The realization of atomic resolution with the electron microscope. *Rep. Prog. Phys.* **1997**, *60*, 1513–1580.
- (94) Zhang, B.; Zhang, W.; Shao, L.; Su, D. S. High-Resolution TEM Analysis of Supported Metal Nanoparticles Combining with Image Simulation. *Microsc. Microanal.* **2013**, *19*, 1556–1557.
- (95) Yacaman, M. J.; Heinemann, K.; Poppa, H. The Determination of the Habit Planes of Nanometer-Size Single-Crystal Gold Particles. *CRC Crit. Rev. Sol. State* **1981**, *10*, 243–260.
- (96) Marks, L. D. Inhomogeneous Strains in Small Particles. *Surf. Sci.* **1985**, *150*, 302–318.
- (97) José-Yacamán, M.; Avalos-Borja, M. Electron Microscopy of Metallic Nano Particles Using High- and Medium-Resolution Techniques. *Catal. Rev.* **1992**, *34*, 55–127.
- (98) Velazquez-Palenzuela, A.; Brillas, E.; Arias, C.; Centellas, F.; Garrido, J. A.; Rodriguez, R. M.; Cabot, P. L. Structural Characterization of Ru-Modified Carbon-Supported Pt Nanoparticles Using Spontaneous Deposition with CO Oxidation Activity. *J. Phys. Chem. C* **2012**, *116*, 18469–18478.
- (99) Alden, L. R.; Han, D. K.; Matsumoto, F.; Abruna, H. D.; DiSalvo, F. J. Intermetallic PtPb nanoparticles prepared by sodium naphthalide reduction of metal-organic precursors: Electrocatalytic oxidation of formic acid. *Chem. Mater.* **2006**, *18*, 5591–5596.
- (100) Williams, D. B.; Carter, C. B. *Transmission electron microscopy: a textbook for materials science*; Springer: 2009.
- (101) Su, D. S.; Schloegl, R.; Kujawa, S.; Freitag, B. Interface Study of Silver Nano-particles Using an Image Cs-corrected TEM. *Microscopy and microanalysis* **2005**, *11* (Suppl 2), 1550–1551.
- (102) Kornelak, P.; Su, D. S.; Thomas, C.; Camra, J.; Weselucha-Birczynska, A.; Toba, M.; Najbar, M. Surface species structure and activity in NO decomposition of an anatase-supported V-O-Mo catalyst. *Catal. Today* **2008**, *137*, 273–277.
- (103) Kornelak, P.; Borzecka-Prokop, B.; Litynska-Dobrzynska, L.; Wagner, J.; Su, D. S.; Camra, J.; Weselucha-Birczynska, A. The physicochemical properties of rutile-supported V-O-Mo catalyst. *Catal. Today* **2007**, *119*, 204–208.

- (104) Gajovic, A.; Djerdj, I.; Furic, K.; Schloegl, R.; Su, D. S. Preparation of nanostructured ZrTiO₄ by solid state reaction in equimolar mixture of TiO₂ and ZrO₂. *Cryst. Res. Technol.* **2006**, *41*, 1076–1081.
- (105) Dong, W. S.; Bartley, J. K.; Dummer, N. F.; Girgsdies, F.; Su, D. S.; Schlogl, R.; Volta, J. C.; Hutchings, G. J. Reaction of vanadium phosphates with alcohols at elevated temperature and pressure. *J. Mater. Chem.* **2005**, *15*, 3214–3220.
- (106) Su, D. S.; Roddatis, V.; Willinger, M.; Weinberg, G.; Kitzelmann, E.; Schlogl, R.; Knozinger, H. Tribocochemical modification of the microstructure of V₂O₅. *Catal. Lett.* **2001**, *74*, 169–175.
- (107) Zhang, W.; Kuhn, L. T.; Jorgensen, P. S.; Sudireddy, B. R.; Bentzen, J. J.; Bernuy-Lopez, C.; Veltze, S.; Ramos, T. Instability and growth of nanoscale Ce_{0.8}Gd_{0.2}O_{1.9}/NiO infiltrate in Sr_{0.94}Ti_{0.9}Nb_{0.1}O₃-Zr_{0.84}Y_{0.16}O_{1.92} anodes for solid oxide fuel cells. *J. Power Sources* **2014**, *258*, 297–304.
- (108) Su, D. S.; Neumann, W.; Giersig, M.; Zeitler, E. *Electron microscopy of I-III-V-2 semiconductor compounds: Ordering behaviour of cations in CuInS₂* **1998**, 415–416.
- (109) Su, D. S.; Neumann, W.; Hunger, R.; Giersig, M. Defect structure of In-rich (Cu,In)-S₂ epitaxial films. *Eur. J. Cell Biol.* **1997**, *74*, S2–S2.
- (110) Ni, X.; Zhang, B.; Li, C.; Pang, M.; Su, D.; Williams, C. T.; Liang, C. Microwave-assisted green synthesis of uniform Ru nanoparticles supported on non-functional carbon nanotubes for cinnamaldehyde hydrogenation. *Catal. Commun.* **2012**, *24*, 65–69.
- (111) Zhang, B. S.; Yi, Y. J.; Zhang, W.; Liang, C. H.; Su, D. S. Electron microscopy investigation of the microstructure of unsupported Ni-Mo-W sulfide. *Mater. Charact.* **2011**, *62*, 684–690.
- (112) Zhao, Y.; Chen, P.; Zhang, B.; Su, D. S.; Zhang, S.; Tian, L.; Lu, J.; Li, Z.; Cao, X.; Wang, B.; Wei, M.; Evans, D. G.; Duan, X. Highly Dispersed TiO₆ Units in a Layered Double Hydroxide for Water Splitting. *Chem.—Eur. J.* **2012**, *18*, 11949–11958.
- (113) Yi, Y.; Zhang, B.; Jin, X.; Wang, L.; Williams, C. T.; Xiong, G.; Su, D.; Liang, C. Unsupported NiMoW sulfide catalysts for hydrodesulfurization of dibenzothiophene by thermal decomposition of thiosalts. *J. Mol. Catal. A—Chem.* **2011**, *351*, 120–127.
- (114) Zhang, B.; Shao, L.; Zhang, W.; Sun, X.; Pan, X.; Su, D. S. Interaction between Palladium Nanoparticles and Surface-Modified Carbon Nanotubes: Role of Surface Functionalities. *ChemCatChem* **2014**, *6*, 2607–2612.
- (115) Wang, L.; Zhang, B.; Zhang, W.; Zhang, J.; Gao, X.; Meng, X.; Su, D. S.; Xiao, F.-S. Positively charged bulk Au particles as an efficient catalyst for oxidation of styrene with molecular oxygen. *Chem. Commun.* **2013**, *49*, 3449–3451.
- (116) Wang, L.; Zhang, B.; Meng, X.; Su, D. S.; Xiao, F.-S. Hydrogenation of Biofuels with Formic Acid over a Palladium-Based Ternary Catalyst with Two Types of Active Sites. *ChemSusChem* **2014**, *7*, 1537–1541.
- (117) Egerton, R. F. *Electron energy-loss spectroscopy in the electron microscope*; Springer: 2011.
- (118) Wang, R.; Sun, X.; Zhang, B.; Sun, X.; Su, D. Hybrid Nanocarbon as a Catalyst for Direct Dehydrogenation of Propane: Formation of an Active and Selective Core-Shell sp(2)/sp(3) Nanocomposite Structure. *Chem.—Eur. J.* **2014**, *20*, 6324–6331.
- (119) Tian, G.-L.; Zhang, Q.; Zhang, B.; Jin, Y.-G.; Huang, J.-Q.; Su, D. S.; Wei, F. Toward Full Exposure of "Active Sites": Nanocarbon Electrocatalyst with Surface Enriched Nitrogen for Superior Oxygen Reduction and Evolution Reactivity. *Adv. Funct. Mater.* **2014**, *24*, 5956–5961.
- (120) Sun, X.; Wang, R.; Zhang, B.; Huang, R.; Huang, X.; Su, D. S.; Chen, T.; Miao, C.; Yang, W. Evolution and Reactivity of Active Oxygen Species on sp(2)@sp(3) Core-Shell Carbon for the Oxidative Dehydrogenation Reaction. *ChemCatChem* **2014**, *6*, 2270–2275.
- (121) Jeyabharathi, C.; Hodnik, N.; Baldizzone, C.; Meier, J. C.; Heggen, M.; Phani, K. L. N.; Bele, M.; Zorko, M.; Hocevar, S.; Mayrhofer, K. J. J. Time Evolution of the Stability and Oxygen Reduction Reaction Activity of PtCu/C Nanoparticles. *ChemCatChem* **2013**, *5*, 2627–2635.
- (122) Zhang, B.; Zhang, W.; Shao, L.; Su, D. S. Optimum Energy-Dispersive X-Ray Spectroscopy Elemental Mapping for Advanced Catalytic Materials. *ChemCatChem* **2013**, *5*, 2586–2590.
- (123) Florea, I.; Liu, Y.; Ersen, O.; Meny, C.; Pham-Huu, C. Microstructural Analysis and Energy-Filtered TEM Imaging to Investigate the Structure–Activity Relationship in Fischer–Tropsch Catalysts. *ChemCatChem* **2013**, *5*, 2610–2620.
- (124) Johns, T. R.; Gaudet, J. R.; Peterson, E. J.; Miller, J. T.; Stach, E. A.; Kim, C. H.; Balogh, M. P.; Datye, A. K. Microstructure of Bimetallic Pt/Pd Catalysts under Oxidizing Conditions. *ChemCatChem* **2013**, *5*, 2636–2645.
- (125) Wang, X.; Choi, J.; Mitchell, D. R. G.; Truong, Y. B.; Kyratzis, I. L.; Caruso, R. A. Enhanced Photocatalytic Activity: Macroporous Electrospun Mats of Mesoporous Au/TiO₂ Nanofibers. *ChemCatChem* **2013**, *5*, 2646–2654.
- (126) Shi, Q.; Peng, F.; Liao, S.; Wang, H.; Yu, H.; Liu, Z.; Zhang, B.; Su, D. Sulfur and nitrogen co-doped carbon nanotubes for enhancing electrochemical oxygen reduction activity in acidic and alkaline media. *J. Mater. Chem. A* **2013**, *1*, 14853–14857.
- (127) Egerton, R. F. Application of electron energy-loss spectroscopy to the study of solid catalysts. *Top. Catal.* **2002**, *21*, 185–190.
- (128) Su, D. S. Analytical TEM characterisation of catalytic materials. *Low-Dimensional Systems: Theory, Preparation, and Some Applications*; NATO Science Series; 2003; Vol. 91, pp 241–252.
- (129) Liskowski, A.; Su, D. S.; Schlogl, R.; Lopez-Sanchez, J.; Bartley, J. K.; Hutchings, G. J. Microstructural differences between the catalyst and the standard V⁵⁺ phases of VPO. *Microsc. Microanal.* **2003**, *9*, 316–317.
- (130) Willinger, M. G.; Su, D. S.; Schlogl, R. Electronic structure of beta-VOPO₄. *Phys. Rev. B* **2005**, *71*, 155118.
- (131) Hebert, C.; Willinger, M.; Su, D. S.; Pongratz, P.; Schattschneider, P.; Schlogl, R. Oxygen K-edge in vanadium oxides: simulations and experiments. *Eur. Phys. J. B* **2002**, *28*, 407–414.
- (132) Muller, J. O.; Su, D. S.; Schlogl, R. Fullerene black in soot: morphology vs. electronic structure. *Microsc. Microanal.* **2003**, *9*, 186–187.
- (133) Su, D. S.; Zeitler, E. Influence of collection aperture and specimen thickness on quantitative EELS analysis. *Electron Microscopy International Congress*; 1994; pp 651652.
- (134) Su, D. S.; Swoboda, M.; Zeitler, E. Single-Electron Excitation of Amorphous-Carbon Observed with Energy Filter. *Ultramicroscopy* **1994**, *53*, 97–100.
- (135) Su, D. S.; Schattschneider, P.; Zeitler, E. Determination of the Position Maximum for Electron Compton-Scattering in Electron-Microscopy. *Phys. Rev. B* **1994**, *49*, 8552–8555.
- (136) Su, D. S.; Schattschneider, P. Numerical Aspects of the Deconvolution of Angle-Integrated Electron Energy-Loss Spectra. *J. Microsc.-Oxford* **1992**, *167*, 63–75.
- (137) Schattschneider, P.; Su, D. S. Hyperquadratic Plasmon Dispersion in Indium. *J. Electron Spectrosc. Relat. Phenom.* **1992**, *58*, R13–R18.
- (138) Su, D. S.; Schattschneider, P. Multiple-Scattering Correction by a Direct Convolution Method. *Ultramicroscopy* **1991**, *36*, 385–386.
- (139) Hebert, C.; Schoene, W. D.; Su, D. S. Experimental and theoretical determination of low electron energy loss spectra of Ag and Ru. *Ultramicroscopy* **2006**, *106*, 1115–1119.
- (140) Egerton, R. F. Electron energy-loss spectroscopy in the TEM. *Rep. Prog. Phys.* **2009**, *72*.
- (141) Zhang, B. S.; Ni, X. J.; Zhang, W.; Shao, L. D.; Zhang, Q.; Girgsdies, F.; Liang, C. H.; Schlogl, R.; Su, D. S. Structural rearrangements of Ru nanoparticles supported on carbon nanotubes under microwave irradiation. *Chem. Commun.* **2011**, *47*, 10716–10718.
- (142) Zewail, A. H.; Thomas, J. M. *4D Electron Microscopy Imaging in Space and Time*; Imperial College Press: 2010.
- (143) Zhang, B. S.; Su, D. S. Electron Tomography: Three-Dimensional Imaging of Real Crystal Structures at Atomic Resolution. *Angew. Chem., Int. Ed.* **2013**, *52*, 8504–8506.
- (144) López-Haro, M.; Delgado, J. J.; Hernández-Garrido, J. C.; López-Castro, J. d. D.; Mira, C.; Trasobares, S.; Hungría, A. B.; Pérez-

- Omil, J. A.; Calvino, J. J. *Handbook of Nanoscopy*; Wiley-VCH Verlag GmbH & Co. KGaA: 2012; pp 877–960.
- (145) Yang, X. F.; Wang, A. Q.; Qiao, B. T.; Li, J.; Liu, J. Y.; Zhang, T. Single-Atom Catalysts: A New Frontier in Heterogeneous Catalysis. *Acc. Chem. Res.* **2013**, *46*, 1740–1748.
- (146) Lin, J.; Wang, A.; Qiao, B.; Liu, X.; Yang, X.; Wang, X.; Liang, J.; Li, J.; Liu, J.; Zhang, T. Remarkable Performance of Ir₁/FeO_x Single-Atom Catalyst in Water Gas Shift Reaction. *J. Am. Chem. Soc.* **2013**, *135*, 15314–15317.
- (147) Surnev, S.; Ramsey, M. G.; Netzer, F. P. Synchrotron radiation applied to the study of heterogeneous model catalyst surfaces. *J. Phys.-Condens. Mater.* **2001**, *13*, 11305–11332.
- (148) Wang, J.; Li, Q.; Ronning, C.; Stichtenoth, D.; Muller, S.; Tang, D. Nanomaterial electronic structure investigation by valence electron energy loss spectroscopy—An example of doped ZnO nanowires. *Micron* **2008**, *39*, 703–708.
- (149) Browning, N. D.; Campbell, G. H.; Evans, J. E.; LaGrange, T. B.; Jungjohann, K. L.; Kim, J. S.; Masiel, D. J.; Reed, B. W. *Handbook of Nanoscopy*; Wiley-VCH Verlag GmbH & Co. KGaA: 2012; pp 309–343.
- (150) Tichelaar, F. D.; van Huis, M. A.; Zandbergen, H. W. *Handbook of Nanoscopy*; Wiley-VCH Verlag GmbH & Co. KGaA: 2012; pp 345–374.
- (151) Scherzer, O. Über einige Fehler von Elektronenlinsen. *Z. Phys. A* **1936**, *101*, 593–603.
- (152) Batson, P. E.; Dellby, N.; Krivanek, O. L. Sub-angstrom resolution using aberration corrected electron optics. *Nature* **2002**, *418*, 617–620.
- (153) Haider, M.; Uhlemann, S.; Schwan, E.; Rose, H.; Kabius, B.; Urban, K. Electron microscopy image enhanced. *Nature* **1998**, *392*, 768–769.
- (154) Jia, C. L.; Lentzen, M.; Urban, K. High-resolution transmission electron microscopy using negative spherical aberration. *Microsc. Microanal.* **2004**, *10*, 174–184.
- (155) Lentzen, M. Progress in aberration-corrected high-resolution transmission electron microscopy using hardware aberration correction. *Microsc. Microanal.* **2006**, *12*, 191–205.
- (156) Gu, L.; Zhu, C.; Li, H.; Yu, Y.; Li, C.; Tsukimoto, S.; Maier, J.; Ikuhara, Y. Direct Observation of Lithium Staging in Partially Delithiated LiFePO₄ at Atomic Resolution. *J. Am. Chem. Soc.* **2011**, *133*, 4661–4663.
- (157) Sun, Y.; Zhao, L.; Pan, H.; Lu, X.; Gu, L.; Hu, Y.-S.; Li, H.; Armand, M.; Ikuhara, Y.; Chen, L.; Huang, X. Direct atomic-scale confirmation of three-phase storage mechanism in Li₄Ti₅O₁₂ anodes for room-temperature sodium-ion batteries. *Nat. Commun.* **2013**, *4*, 1870.
- (158) Lu, X.; Zhao, L.; He, X.; Xiao, R.; Gu, L.; Hu, Y.-S.; Li, H.; Wang, Z.; Duan, X.; Chen, L.; Maier, J.; Ikuhara, Y. Lithium Storage in Li₄Ti₅O₁₂ Spinel: The Full Static Picture from Electron Microscopy. *Adv. Mater.* **2012**, *24*, 3233–3238.
- (159) Yu, X.; Lyu, Y.; Gu, L.; Wu, H.; Bak, S.-M.; Zhou, Y.; Amine, K.; Ehrlich, S. N.; Li, H.; Nam, K.-W.; Yang, X.-Q. Understanding the Rate Capability of High-Energy-Density Li-Rich Layered Li_{1.2}Ni_{0.15}Co_{0.1}Mn_{0.55}O₂ Cathode Materials. *Adv. Energy Mater.* **2014**, *4*, 1300950.
- (160) Lu, X.; Sun, Y.; Jian, Z.; He, X.; Gu, L.; Hu, Y.-S.; Li, H.; Wang, Z.; Chen, W.; Duan, X.; Chen, L.; Maier, J.; Tsukimoto, S.; Ikuhara, Y. New Insight into the Atomic Structure of Electrochemically Delithiated O₃-Li_(1-x)CoO₂ (0 ≤ x ≤ 0.5) Nanoparticles. *Nano Lett.* **2012**, *12*, 6192–6197.
- (161) Jia, C. L.; Lentzen, M.; Urban, K. Atomic-resolution imaging of oxygen in perovskite ceramics. *Science* **2003**, *299*, 870–873.
- (162) Jia, C. L.; Urban, K. Atomic-resolution measurement of oxygen concentration in oxide materials. *Science* **2004**, *303*, 2001–2004.
- (163) Urban, K. W.; Jia, C. L.; Houben, L.; Lentzen, M.; Mi, S. B.; Tillmann, K. Negative spherical aberration ultrahigh-resolution imaging in corrected transmission electron microscopy. *Philos. Trans. R. Soc. A* **2009**, *367*, 3735–3753.
- (164) Houben, L.; Thust, A.; Urban, K. Atomic-precision determination of the reconstruction of a 90 degrees tilt boundary in YBa₂Cu₃O₇-delta by aberration corrected HRTEM. *Ultramicroscopy* **2006**, *106*, 200–214.
- (165) Krivanek, O. L.; Dellby, N.; Lupini, A. R. Towards sub-angstrom electron beams. *Ultramicroscopy* **1999**, *78*, 1–11.
- (166) Krivanek, O. L.; Nellist, P. D.; Dellby, N.; Murfitt, M. F.; Szilagyi, Z. Towards sub-0.5 angstrom electron beams. *Ultramicroscopy* **2003**, *96*, 229–237.
- (167) Krivanek, O. L.; Corbin, G. J.; Dellby, N.; Elston, B. F.; Keyse, R. J.; Murfitt, M. F.; Own, C. S.; Szilagyi, Z. S.; Woodruff, J. W. An electron microscope for the aberration-corrected era. *Ultramicroscopy* **2008**, *108*, 179–195.
- (168) Tiemeijer, P. C.; Bischoff, M.; Freitag, B.; Kisielowski, C. Using a monochromator to improve the resolution in TEM to below 0.5 angstrom. Part I: Creating highly coherent monochromated illumination. *Ultramicroscopy* **2012**, *114*, 72–81.
- (169) Freitag, B.; Kujawa, S.; Mul, P. M.; Ringnalda, J.; Tiemeijer, P. C. Breaking the spherical and chromatic aberration barrier in transmission electron microscopy. *Ultramicroscopy* **2005**, *102*, 209–214.
- (170) Zach, J. Chromatic correction: a revolution in electron microscopy? *Philos. Trans. R. Soc. A* **2009**, *367*, 3699–3707.
- (171) Tiemeijer, P. C. In *Electron Microscopy and Analysis*; Kiely, C. J., Ed.; IOP Publishing Ltd: Bristol, 1999; pp 191–194.
- (172) Rose, H. Properties of Spherically Corrected Achromatic Electron-Lenses. *Optik* **1971**, *33*, 1.
- (173) Tiemeijer, P. C.; Bischoff, M.; Freitag, B.; Kisielowski, C. Using a monochromator to improve the resolution in TEM to below 0.5 angstrom. Part II: Application to focal series reconstruction. *Ultramicroscopy* **2012**, *118*, 35–43.
- (174) Colliex, C.; Manoubi, T.; Ortiz, C. Electron-Energy-Loss-Spectroscopy Near-Edge Fine-Structures in the Iron-Oxygen System. *Phys. Rev. B* **1991**, *44*, 11402–11411.
- (175) Chen, C.; Zhang, J.; Zhang, B.; Yu, C.; Peng, F.; Su, D. Revealing the enhanced catalytic activity of nitrogen-doped carbon nanotubes for oxidative dehydrogenation of propane. *Chem. Commun.* **2013**, *49*, 8151–8153.
- (176) Susi, T.; Kotakoski, J.; Arenal, R.; Kurash, S.; Jiang, H.; Skakalova, V.; Stephan, O.; Krasheninnikov, A. V.; Kauppinen, E. I.; Kaiser, U.; Meyer, J. C. Atomistic Description of Electron Beam Damage in Nitrogen-Doped Graphene and Single-Walled Carbon Nanotubes. *ACS Nano* **2012**, *6*, 8837–8846.
- (177) Nicholls, R. J.; Murdock, A. T.; Tsang, J.; Britton, J.; Pennycook, T. J.; Koós, A.; Nellist, P. D.; Grobert, N.; Yates, J. R. Probing the Bonding in Nitrogen-Doped Graphene Using Electron Energy Loss Spectroscopy. *ACS Nano* **2013**, *7*, 7145–7150.
- (178) Habel, D.; Gorke, O.; Tovar, M.; Willinger, M.; Ziermann, M.; Schwarz, O.; Schomacker, R.; Schubert, H. Microstraining in titania-, alumina- and silica-supported V₂O₅-catalysts. *J. Eur. Ceram. Soc.* **2009**, *29*, 1093–1099.
- (179) Willinger, M.; Pinna, N.; Su, D. S.; Schlogl, R. Geometric and electronic structure of gamma-V₂O₅: Comparison between alpha-V₂O₅ and gamma-V₂O₅. *Phys. Rev. B* **2004**, *69*, 155114.
- (180) Mitterbauer, C.; Kothleitner, G.; Grogger, W.; Zandbergen, H.; Freitag, B.; Tiemeijer, P.; Hofer, F. Electron energy-loss near-edge structures of 3d transition metal oxides recorded at high-energy resolution. *Ultramicroscopy* **2003**, *96*, 469–480.
- (181) Genc, A.; Kovarik, L.; Gu, M.; Cheng, H.; Plachinda, P.; Pullan, L.; Freitag, B.; Wang, C. XEDS STEM tomography for 3D chemical characterization of nanoscale particles. *Ultramicroscopy* **2013**, *131*, 24–32.
- (182) Derosier, D. J.; Klug, A. Reconstruction of 3 Dimensional Structures from Electron Micrographs. *Nature* **1968**, *217*, 130–134.
- (183) Hart, R. G. Electron Microscopy of Unstained Biological Material—Polytropic Montage. *Science* **1968**, *159*, 1464–1467.
- (184) Hoppe, W.; Langer, R.; Knesch, G.; Poppe, C. Protein Crystal Structure Analysis with Electron Rays. *Naturwissenschaften* **1968**, *55*, 333–336.

- (185) Midgley, P. A.; Weyland, M.; Thomas, J. M.; Johnson, B. F. G. Z-Contrast tomography: a technique in three-dimensional nanostructural analysis based on Rutherford scattering. *Chem. Commun.* **2001**, 907–908.
- (186) Mobus, G.; Inkson, B. J. Nanoscale tomography in materials science. *Mater. Today* **2007**, 10, 18–25.
- (187) Van Tendeloo, G.; Bals, S.; Van Aert, S.; Verbeeck, J.; Van Dyck, D. Advanced Electron Microscopy for Advanced Materials. *Adv. Mater.* **2012**, 24, 5655–5675.
- (188) Nan, F.; Song, C.; Zhang, J.; Hui, R.; Chen, J.; Fairbridge, C.; Botton, G. A. STEM HAADF Tomography of Molybdenum Disulfide with Mesoporous Structure. *ChemCatChem* **2011**, 3, 999–1003.
- (189) Gonzalez, J. C.; Hernandez, J. C.; Lopez-Haro, M.; del Rio, E.; Delgado, J. J.; Hungria, A. B.; Trasobares, S.; Bernal, S.; Midgley, P. A.; Calvino, J. J. 3D Characterization of Gold Nanoparticles Supported on Heavy Metal Oxide Catalysts by HAADF-STEM Electron Tomography. *Angew. Chem., Int. Ed.* **2009**, 48, 5313–5315.
- (190) Arslan, I.; Walmsley, J. C.; Rytter, E.; Bergene, E.; Midgley, P. A. Toward three-dimensional nanoengineering of heterogeneous catalysts. *J. Am. Chem. Soc.* **2008**, 130, 5716–5719.
- (191) Midgley, P. A.; Ward, E. P. W.; Hungria, A. B.; Thomas, J. M. Nanotomography in the chemical, biological and materials sciences. *Chem. Soc. Rev.* **2007**, 36, 1477–1494.
- (192) Leary, R.; Saghi, Z.; Midgley, P. A.; Holland, D. J. Compressed sensing electron tomography. *Ultramicroscopy* **2013**, 131, 70–91.
- (193) Bethge, H.; Keller, K. W.; Ziegler, E. Molecular processes during crystal growth from the vapour phase. *J. Cryst. Growth* **1968**, 3–4, 184–187.
- (194) Evans, E. L.; Griffith, R.; Thomas, J. M. Kinetics of Single-Layer Graphite Oxidation—Evaluation by Electron Microscopy. *Science* **1971**, 171, 174–175.
- (195) Thomas, J. M.; Evans, E. L.; Williams, J. O. Microscopic Studies of enhanced Reactivity at Structural Faults in Solids. *Proc. R. Soc. London A Mater.* **1972**, 331, 417–427.
- (196) Gabor, D. Microscopy by Reconstructed Wave-Fronts. *Proc. R. Soc. London Ser. A—Math. Phys. Sci.* **1949**, 197, 454–454.
- (197) Lichte, H.; Formanek, P.; Lenk, A.; Linck, M.; Matzeck, C.; Lehmann, M.; Simon, P. *Annu. Rev. Mater. Res.* **2007**, 37, 539–588.
- (198) McCartney, M. R. Introduction to Electron Holography. *Proc. Ann. Meet. MSA* **1994**, 396–397.
- (199) Volkl, E.; Allard, L. F.; Joy, D. C. *Introduction to Electron Holography*; Plenum: 1998; pp 271–280.
- (200) Kwon, O. H.; Zewail, A. H. 4D Electron Tomography. *Science* **2010**, 328, 1668–1673.
- (201) Zewail, A. H. Four-Dimensional Electron Microscopy. *Science* **2010**, 328, 187–193.
- (202) Su, D. S. Electron Tomography: From 3D Statics to 4D Dynamics. *Angew. Chem., Int. Ed.* **2010**, 49, 9569–9571.
- (203) Flannigan, D. J.; Zewail, A. H. 4D electron microscopy: principles and applications. *Acc. Chem. Res.* **2012**, 45, 1828–1839.
- (204) van der Veen, R. M.; Kwon, O.-H.; Tissot, A.; Hauser, A.; Zewail, A. H. Single-nanoparticle phase transitions visualized by four-dimensional electron microscopy. *Nat. Chem.* **2013**, 5, 395–402.
- (205) Shorokhov, D.; Zewail, A. H. 4D electron imaging: principles and perspectives. *Phys. Chem. Chem. Phys.* **2008**, 10, 2879–2893.
- (206) Spencer Baskin, J.; Zewail, A. H. Seeing in 4D with electrons: Development of ultrafast electron microscopy at Caltech. *C. R. Phys.* **2014**, 15, 176–189.
- (207) Zewail, A. H.; Thomas, J. M. *4D Electron Microscopy*; Imperial College Press: 2009.
- (208) Gai, P. L.; Boyes, E. D.; Helveg, S.; Hansen, P. L.; Giorgio, S.; Henry, C. R. Atomic-resolution environmental transmission electron microscopy for probing gas-solid reactions in heterogeneous catalysis. *MRS Bull.* **2007**, 32, 1044–1050.
- (209) Gai, P. L.; Kourtakis, K. Solid-State Defect Mechanism in Vanadyl Pyrophosphate Catalysts—Implications for Selective Oxidation. *Science* **1995**, 267, 661–663.
- (210) Boyes, E. D.; Gai, P. L. Environmental high resolution electron microscopy and applications to chemical science. *Ultramicroscopy* **1997**, 67, 219–232.
- (211) Benavidez, A. D.; Kovarik, L.; Genc, A.; Agrawal, N.; Larsson, E. M.; Hansen, T. W.; Karim, A. M.; Datye, A. K. Environmental Transmission Electron Microscopy Study of the Origins of Anomalous Particle Size Distributions in Supported Metal Catalysts. *ACS Catal.* **2012**, 2, 2349–2356.
- (212) Cavalca, F.; Laursen, A. B.; Kardynal, B. E.; Dunin-Borkowski, R. E.; Dahl, S.; Wagner, J. B.; Hansen, T. W. In situ transmission electron microscopy of light-induced photocatalytic reactions. *Nanotechnology* **2012**, 23, 075705.
- (213) Banerjee, R.; Crozier, P. A. In Situ Synthesis and Nanoscale Evolution of Model Supported Metal Catalysts: Ni on Silica. *J. Phys. Chem. C* **2012**, 116, 11486–11495.
- (214) Sharma, V.; Crozier, P. A.; Sharma, R.; Adams, J. B. Direct observation of hydrogen spillover in Ni-loaded Pr-doped ceria. *Catal. Today* **2012**, 180, 2–8.
- (215) Raabe, S.; Mierwaldt, D.; Ciston, J.; Uijttewaal, M.; Stein, H.; Hoffmann, J.; Zhu, Y.; Blöchl, P.; Jooss, C. In Situ Electrochemical Electron Microscopy Study of Oxygen Evolution Activity of Doped Manganite Perovskites. *Adv. Funct. Mater.* **2012**, 22, 3378–3388.
- (216) Chenna, S.; Crozier, P. A. In situ environmental transmission electron microscopy to determine transformation pathways in supported Ni nanoparticles. *Micron* **2012**, 43, 1188–1194.
- (217) Crozier, P. A.; Sharma, R.; Datye, A. K. Oxidation and reduction of small palladium particles on silica. *Microsc. Microanal.* **1998**, 4, 278–285.
- (218) Sharma, R.; Weiss, K. Development of a TEM to study in situ structural and chemical changes at an atomic level during gas-solid interactions at elevated temperatures. *Microsc. Res. Technol.* **1998**, 42, 270–280.
- (219) Hansen, P. L.; Wagner, J. B.; Helveg, S.; Rostrup-Nielsen, J. R.; Clausen, B. S.; Topsoe, H. Atom-resolved imaging of dynamic shape changes in supported copper nanocrystals. *Science* **2002**, 295, 2053–2055.
- (220) Hansen, T. W.; Wagner, J. B. Environmental transmission electron microscopy in an aberration-corrected environment. *Microsc. Microanal.* **2012**, 18, 684.
- (221) Wagner, J. B.; Cavalca, F.; Damsgaard, C. D.; Duchstein, L. D.; Hansen, T. W. Exploring the environmental transmission electron microscope. *Micron* **2012**, 43, 1169.
- (222) Yokosawa, T.; Alan, T.; Pandraud, G.; Dam, B.; Zandbergen, H. In-situ TEM on (de) hydrogenation of Pd at 0.5–4.5 bar hydrogen pressure and 20–400° C. *Ultramicroscopy* **2012**, 112, 47–52.
- (223) Giorgio, S.; Joao, S. S.; Nitsche, S.; Chaudanson, D.; Sitja, G.; Henry, C. R. Environmental electron microscopy (ETEM) for catalysts with a closed E-cell with carbon windows. *Ultramicroscopy* **2006**, 106, 503–507.
- (224) Yaguchi, T.; Suzuki, M.; Watabe, A.; Nagakubo, Y.; Ueda, K.; Kamino, T. Development of a high temperature-atmospheric pressure environmental cell for high-resolution TEM. *J. Electron Microsc.* **2011**, 60, 217–225.
- (225) van Tendeloo, G., van Dyck, D., Pennycook, S. J., Eds. *Handbook of Nanoscopy*; Wiley: 2012; Vol. 1.
- (226) de Jonge, N.; Ross, F. M. Electron microscopy of specimens in liquid. *Nat. Nanotechnol.* **2011**, 6, 695–704.
- (227) Donald, A. M. The use of environmental scanning electron microscopy for imaging wet and insulating materials. *Nat. Mater.* **2003**, 2, 511–516.
- (228) Yang, D.-S.; Mohammed, O. F.; Zewail, A. H. Environmental Scanning Ultrafast Electron Microscopy: Structural Dynamics of Solvation at Interfaces. *Angew. Chem., Int. Ed.* **2013**, 52, 2897–2901.
- (229) Stokes, D. J. Recent advances in electron imaging, image interpretation and applications: environmental scanning electron microscopy. *Philos. Trans. R. Soc. London Ser. A—Math. Phys. Eng. Sci.* **2003**, 361, 2771–2787.

- (230) Gwinnett, A. J. Chemically Conditioned Dentin—A Comparison of Conventional and Environmental Scanning Electron-Microscopy Findings. *Dent. Mater.* **1994**, *10*, 150–155.
- (231) Rossi, M. P.; Ye, H. H.; Gogotsi, Y.; Babu, S.; Ndungu, P.; Bradley, J. C. Environmental scanning electron microscopy study of water in carbon nanopipes. *Nano Lett.* **2004**, *4*, 989–993.
- (232) Danilatos, G. D. Foundations of Environmental Scanning Electron-Microscopy. *Adv. Electron. Electron Phys.* **1988**, *71*, 109–250.
- (233) Meier, J. C.; Katsounaros, I.; Galeano, C.; Bongard, H. J.; Topalov, A. A.; Kostka, A.; Karschin, A.; Schuth, F.; Mayrhofer, K. J. J. Stability investigations of electrocatalysts on the nanoscale. *Energy Environ. Sci.* **2012**, *5*, 9319–9330.
- (234) Mayrhofer, K. J. J.; Ashton, S. J.; Meier, J. C.; Wiberg, G. K. H.; Hanzlik, M.; Arenz, M. Non-destructive transmission electron microscopy study of catalyst degradation under electrochemical treatment. *J. Power Sources* **2008**, *185*, 734–739.
- (235) Schlogl, K.; Mayrhofer, K. J. J.; Hanzlik, M.; Arenz, M. Identical-location TEM investigations of Pt/C electrocatalyst degradation at elevated temperatures. *J. Electroanal. Chem.* **2011**, *662*, 355–360.
- (236) Mayrhofer, K. J. J.; Meier, J. C.; Ashton, S. J.; Wiberg, G. K. H.; Kraus, F.; Hanzlik, M.; Arenz, M. Fuel cell catalyst degradation on the nanoscale. *Electrochim. Commun.* **2008**, *10*, 1144–1147.
- (237) Meier, J. C.; Galeano, C.; Katsounaros, I.; Topalov, A. A.; Kostka, A.; Schuth, F.; Mayrhofer, K. J. J. Degradation Mechanisms of Pt/C Fuel Cell Catalysts under Simulated Start-Stop Conditions. *ACS Catal.* **2012**, *2*, 832–843.
- (238) Nikkuni, F. R.; Ticianelli, E. A.; Dubau, L.; Chatenet, M. Identical-Location Transmission Electron Microscopy Study of Pt/C and Pt-Co/C Nanostructured Electrocatalyst Aging: Effects of Morphological and Compositional Changes on the Oxygen Reduction Reaction Activity. *Electrocatalysis* **2013**, *4*, 104–116.
- (239) Zana, A.; Speder, J.; Roefzaad, M.; Altmann, L.; Baumer, M.; Arenz, M. Probing Degradation by IL-TEM: The Influence of Stress Test Conditions on the Degradation Mechanism. *J. Electrochem. Soc.* **2013**, *160*, F608–F615.
- (240) Meyer, J. C.; Chuvalin, A.; Algara-Siller, G.; Biskupek, J.; Kaiser, U. Selective Sputtering and Atomic Resolution Imaging of Atomically Thin Boron Nitride Membranes. *Nano Lett.* **2009**, *9*, 2683–2689.
- (241) Zobelli, A.; Gloter, A.; Ewels, C. P.; Seifert, G.; Colliex, C. Electron knock-on cross section of carbon and boron nitride nanotubes. *Phys. Rev. B* **2007**, *75*, 245402.
- (242) Kaiser, U.; Biskupek, J.; Meyer, J. C.; Leschner, J.; Lechner, L.; Rose, H.; Stoger-Pollach, M.; Khlobystov, A. N.; Hartel, P.; Muller, H.; Haider, M.; Eyhusen, S.; Benner, G. Transmission electron microscopy at 20 kV for imaging and spectroscopy. *Ultramicroscopy* **2011**, *111*, 1239–1246.
- (243) Bell, D. C.; Russo, C. J.; Kolmykov, D. V. 40 keV atomic resolution TEM. *Ultramicroscopy* **2012**, *114*, 31–37.
- (244) Krivanek, O. L.; Dellby, N.; Murfitt, M. F.; Chisholm, M. F.; Pennycook, T. J.; Suenaga, K.; Nicolosi, V. Gentle STEM: ADF imaging and EELS at low primary energies. *Ultramicroscopy* **2010**, *110*, 935–945.
- (245) Meyer, J. C.; Kurasch, S.; Park, H. J.; Skakalova, V.; Kunzel, D.; Gross, A.; Chuvalin, A.; Algara-Siller, G.; Roth, S.; Iwasaki, T.; Starke, U.; Smet, J. H.; Kaiser, U. Experimental analysis of charge redistribution due to chemical bonding by high-resolution transmission electron microscopy. *Nat. Mater.* **2011**, *10*, 209–215.
- (246) Tessonner, J. P.; Becker, M.; Xia, W.; Grgsdes, F.; Blume, R.; Yao, L. D.; Su, D. S.; Muhler, M.; Schlogl, R. Spinel-Type Cobalt-Manganese-Based Mixed Oxide as Sacrificial Catalyst for the High-Yield Production of Homogeneous Carbon Nanotubes. *ChemCatChem* **2010**, *2*, 1559–1561.
- (247) Teschner, D.; Borsodi, J.; Woitsch, A.; Revay, Z.; Havecker, M.; Knop-Gericke, A.; Jackson, S. D.; Schlogl, R. The roles of subsurface carbon and hydrogen in palladium-catalyzed alkyne hydrogenation. *Science* **2008**, *320*, 86–89.
- (248) Vincent, R.; Midgley, P. A. Double Conical Beam-Rocking System for Measurement of Integrated Electron-Diffraction Intensities. *Ultramicroscopy* **1994**, *53*, 271–282.
- (249) Own, C. S.-Y. *System design and verification of the precession electron diffraction technique*. Ph.D. Thesis; Northwestern University: Evanston, IL, 2005.
- (250) Barnard, J.; Eggeman, A.; Sharp, J.; White, T.; Midgley, P. Dislocation electron tomography and precession electron diffraction—minimising the effects of dynamical interactions in real and reciprocal space. *Philos. Mag.* **2010**, *90*, 4711–4730.
- (251) Dorset, D. L.; Gilmore, C. J.; Jorda, J. L.; Nicolopoulos, S. Direct electron crystallographic determination of zeolite zonal structures. *Ultramicroscopy* **2007**, *107*, 462–473.
- (252) Jiang, J. X.; Jorda, J. L.; Yu, J. H.; Baumes, L. A.; Mugnaioli, E.; Diaz-Cabanias, M. J.; Kolb, U.; Corma, A. Synthesis and Structure Determination of the Hierarchical Meso-Microporous Zeolite ITQ-43. *Science* **2011**, *333*, 1131–1134.
- (253) Deng, H. X.; Gruner, S.; Cordova, K. E.; Valente, C.; Furukawa, H.; Hmaedeh, M.; Gandara, F.; Whalley, A. C.; Liu, Z.; Asahina, S.; Kazumori, H.; O'Keeffe, M.; Terasaki, O.; Stoddart, J. F.; Yaghi, O. M. Large-Pore Apertures in a Series of Metal-Organic Frameworks. *Science* **2012**, *336*, 1018–1023.
- (254) Denysenko, D.; Grzywa, M.; Tonigold, M.; Streppel, B.; Krkljus, I.; Hirscher, M.; Mugnaioli, E.; Kolb, U.; Hanss, J.; Volkmer, D. Elucidating Gating Effects for Hydrogen Sorption in MFU-4-Type Triazolate-Based Metal-Organic Frameworks Featuring Different Pore Sizes. *Chem.—Eur. J.* **2011**, *17*, 1837–1848.
- (255) Yu, X. Z.; Onose, Y.; Kanazawa, N.; Park, J. H.; Han, J. H.; Matsui, Y.; Nagaosa, N.; Tokura, Y. Real-space observation of a two-dimensional skyrmion crystal. *Nature* **2010**, *465*, 901–904.
- (256) Westenfelder, B.; Meyer, J. C.; Biskupek, J.; Kurasch, S.; Scholz, F.; Krill, C. E.; Kaiser, U. Transformations of Carbon Adsorbates on Graphene Substrates under Extreme Heat. *Nano Lett.* **2011**, *11*, 5123–5127.
- (257) Krivanek, O. L.; Chisholm, M. F.; Nicolosi, V.; Pennycook, T. J.; Corbin, G. J.; Dellby, N.; Murfitt, M. F.; Own, C. S.; Szilagyi, Z. S.; Oxley, M. P.; Pantelides, S. T.; Pennycook, S. J. Atom-by-atom structural and chemical analysis by annular dark-field electron microscopy. *Nature* **2010**, *464*, 571–574.
- (258) Tsen, S. C. Y.; Crozier, P. A.; Liu, J. Lattice measurement and alloy compositions in metal and bimetallic nanoparticles. *Ultramicroscopy* **2003**, *98*, 63–72.
- (259) Braidy, N.; Jakubek, Z. J.; Simard, B.; Botton, G. A. Quantitative energy dispersive X-ray microanalysis of electron beam-sensitive alloyed nanoparticles. *Microsc. Microanal.* **2008**, *14*, 166–175.
- (260) Findlay, S. D.; Shibata, N.; Sawada, H.; Okunishi, E.; Kondo, Y.; Yamamoto, T.; Ikuhara, Y. Robust atomic resolution imaging of light elements using scanning transmission electron microscopy. *Appl. Phys. Lett.* **2009**, *95*, 191913.
- (261) Masiel, D. J.; Reed, B. W.; LaGrange, T. B.; Campbell, G. H.; Guo, T.; Browning, N. D. Time-Resolved Annular Dark Field Imaging of Catalyst Nanoparticles. *ChemPhysChem* **2010**, *11*, 2088–2090.
- (262) William, D. B.; Carter, C. B. *Transmission electron microscopy: a textbook for materials science*; Plenum Press: New York & London, 1996.
- (263) De Graef, M. In *Handbook of Nanoscopy*; Wiley-VCH Verlag GmbH & Co. KGaA: 2012; pp 9–44.
- (264) Urban, K. W.; Barthel, J.; Houben, L.; Jia, C.-L.; Lentzen, M.; Thust, A.; Tillmann, K. In *Handbook of Nanoscopy*; Wiley-VCH Verlag GmbH & Co. KGaA: 2012; pp 81–107.
- (265) Krause, F. F.; Muller, K.; Zillmann, D.; Jansen, J.; Schowalter, M.; Rosenauer, A. Comparison of intensity and absolute contrast of simulated and experimental high-resolution transmission electron microscopy images for different multislice simulation methods. *Ultramicroscopy* **2013**, *134*, 94–101.
- (266) Stadelmann, P. A. EMS—A Software Package for Electron-Diffraction Analysis and HREM Image Simulation in Materials Science. *Ultramicroscopy* **1987**, *21*, 131–145.

- (267) Pennycook, S. J.; Lupini, A. R.; Borisevich, A. Y.; Oxley, M. P. *Handbook of Nanoscopy*; Wiley-VCH Verlag GmbH & Co. KGaA: 2012; pp 109–152.
- (268) Gai, P. L.; Boyes, E. D. *Handbook of Nanoscopy*; Wiley-VCH Verlag GmbH & Co. KGaA: 2012; pp 375–403.
- (269) Uzun, A.; Ortalan, V.; Browning, N. D.; Gates, B. C. Site-isolated iridium complexes on MgO powder: individual Ir atoms imaged by scanning transmission electron microscopy. *Chem. Commun.* **2009**, 4657–4659.
- (270) He, S.; Li, C.; Chen, H.; Su, D.; Zhang, B.; Cao, X.; Wang, B.; Wei, M.; Evans, D. G.; Duan, X. A Surface Defect-Promoted Ni Nanocatalyst with Simultaneously Enhanced Activity and Stability. *Chem. Mater.* **2013**, 25, 1040–1046.
- (271) Sanfiz, A. C.; Hansen, T. W.; Sakthivel, A.; Trunschke, A.; Schlogl, R.; Knoester, A.; Brongersma, H. H.; Looi, M. H.; Hamid, S. B. A. How important is the (001) plane of M1 for selective oxidation of propane to acrylic acid? *J. Catal.* **2008**, 258, 35–43.
- (272) Zhang, B. S.; Wang, D.; Zhang, W.; Su, D. S.; Schlogl, R. Structural Dynamics of Low-Symmetry Au Nanoparticles Stimulated by Electron Irradiation. *Chem.—Eur. J.* **2011**, 17, 12877–12881.
- (273) Shao, L. D.; Zhang, W.; Armbruster, M.; Teschner, D.; Girgsdies, F.; Zhang, B. S.; Timpe, O.; Friedrich, M.; Schlogl, R.; Su, D. S. Nanosizing Intermetallic Compounds Onto Carbon Nanotubes: Active and Selective Hydrogenation Catalysts. *Angew. Chem., Int. Ed.* **2011**, 50, 10231–10235.
- (274) Ertl, G.; Freund, H. J. Catalysis and surface science. *Phys. Today* **1999**, 52, 32–38.
- (275) Thomas, J. M.; Raja, R. The advantages and future potential of single-site heterogeneous catalysts. *Top. Catal.* **2006**, 40, 3–17.
- (276) Taylor, H. S. Catalysis in chemical industry. *Nature* **1920**, 104, 94–95.
- (277) Boyes, E. D.; Ward, M. R.; Lari, L.; Gai, P. L. ESTEM imaging of single atoms under controlled temperature and gas environment conditions in catalyst reaction studies. *Ann. Phys.-Berlin* **2013**, 525, 423–429.
- (278) Crewe, A. V.; Wall, J.; Langmore, J. Visibility of Single Atoms. *Science* **1970**, 168, 1338–1340.
- (279) Nellist, P. D.; Pennycook, S. J. Direct imaging of the atomic configuration of ultradispersed catalysts. *Science* **1996**, 274, 413–415.
- (280) Thomas, J. M.; Raja, R.; Lewis, D. W. Single-site heterogeneous catalysts. *Angew. Chem., Int. Ed.* **2005**, 44, 6456–6482.
- (281) Ranocchiai, M.; Lothschutz, C.; Grolimund, D.; van Bokhoven, J. A. Single-atom active sites on metal-organic frameworks. *Proc. R. Soc. A: Math., Phys. Eng. Sci.* **2012**, 468, 1985–1999.
- (282) Zhang, L.; Wang, A.; Miller, J. T.; Liu, X.; Yang, X.; Wang, W.; Li, L.; Huang, Y.; Mou, C.-Y.; Zhang, T. Efficient and Durable Au Alloyed Pd Single-Atom Catalyst for the Ullmann Reaction of Aryl Chlorides in Water. *ACS Catal.* **2014**, 4, 1546–1553.
- (283) Wei, H.; Liu, X.; Wang, A.; Zhang, L.; Qiao, B.; Yang, X.; Huang, Y.; Miao, S.; Liu, J.; Zhang, T. FeOx-supported platinum single-atom and pseudo-single-atom catalysts for chemoselective hydrogenation of functionalized nitroarenes. *Nat. Commun.* **2014**, 5, 5634.
- (284) Chen, M. S.; Goodman, D. W. The structure of catalytically active gold on titania. *Science* **2004**, 306, 252–255.
- (285) Valden, M.; Lai, X.; Goodman, D. W. Onset of catalytic activity of gold clusters on titania with the appearance of nonmetallic properties. *Science* **1998**, 281, 1647–1650.
- (286) Freund, H.-J.; Meijer, G.; Scheffler, M.; Schlogl, R.; Wolf, M. CO Oxidation as a Prototypical Reaction for Heterogeneous Processes. *Angew. Chem., Int. Ed.* **2011**, 50, 10064–10094.
- (287) Hlatky, G. G. Heterogeneous single-site catalysts for olefin polymerization. *Chem. Rev.* **2000**, 100, 1347–1376.
- (288) Uzun, A.; Ortalan, V.; Browning, N. D.; Gates, B. C. A site-isolated mononuclear iridium complex catalyst supported on MgO: Characterization by spectroscopy and aberration-corrected scanning transmission electron microscopy. *J. Catal.* **2010**, 269, 318–328.
- (289) Ortalan, V.; Uzun, A.; Gates, B. C.; Browning, N. D. Towards full-structure determination of bimetallic nanoparticles with an aberration-corrected electron microscope. *Nat. Nanotechnol.* **2010**, 5, 843–847.
- (290) Oukaci, R.; Singleton, A. H.; Goodwin, J. G. Comparison of patented CoF-T catalysts using fixed-bed and slurry bubble column reactors. *Appl. Catal. A-Gen.* **1999**, 186, 129–144.
- (291) Shannon, M. D.; Lok, C. M.; Casci, J. L. Imaging promoter atoms in Fischer–Tropsch cobalt catalysts by aberration-corrected scanning transmission electron microscopy. *J. Catal.* **2007**, 249, 41–51.
- (292) Hino, M.; Arata, K. Synthesis of Solid Superacid of Tungsten-Oxide Supported on Zirconia and Its Catalytic Action for Reactions of Butane and Pentane. *J. Chem. Soc., Chem. Commun.* **1988**, 1259–1260.
- (293) Santiesteban, J. G.; Vartuli, J. C.; Han, S.; Bastian, R. D.; Chang, C. D. Influence of the preparative method on the activity of highly acidic WO_x/ZrO₂ and the relative acid activity compared with zeolites. *J. Catal.* **1997**, 168, 431–441.
- (294) Weckhuysen, B. M. HETEROGENEOUS CATALYSIS Catch me if you can! *Nat. Chem.* **2009**, 1, 690–692.
- (295) Browning, N. D.; Aydin, C.; Lu, J.; Kulkarni, A.; Okamoto, N. L.; Ortalan, V.; Reed, B. W.; Uzun, A.; Gates, B. C. Quantitative Z-Contrast Imaging of Supported Metal Complexes and Clusters—A Gateway to Understanding Catalysis on the Atomic Scale. *ChemCatChem* **2013**, 5, 2673–2683.
- (296) Iijima, S. Electron-Microscopy of Small Particles. *J. Electron Microsc.* **1985**, 34, 249–265.
- (297) Altenhein, C.; Giorgio, S.; Urban, J.; Weiss, K. Structure of Supported Palladium, Silver and Gold Clusters. *Z. Phys. D Atom. Mol. Cl.* **1991**, 19, 303–306.
- (298) Buffat, P. A. Electron diffraction and HRTEM studies of multiply-twinned structures and dynamical events in metal nanoparticles: facts and artefacts. *Mater. Chem. Phys.* **2003**, 81, 368–375.
- (299) Li, Z. Y.; Young, N. P.; Di Vece, M.; Palomba, S.; Palmer, R. E.; Bleloch, A. L.; Curley, B. C.; Johnston, R. L.; Jiang, J.; Yuan, J. Three-dimensional atomic-scale structure of size-selected gold nanoclusters. *Nature* **2008**, 451, 46–U42.
- (300) López-Haro, M.; Pérez-Omil, J. A.; Hernández-Garrido, J. C.; Trasobares, S.; Hungría, A. B.; Cíes, J. M.; Midgley, P. A.; Bayle-Guillemaud, P.; Martínez-Arias, A.; Bernal, S.; Delgado, J. J.; Calvino, J. J. Advanced Electron Microscopy Investigation of Ceria–Zirconia-Based Catalysts. *ChemCatChem* **2011**, 3, 1015–1027.
- (301) Liu, L.; Yao, Z.; Deng, Y.; Gao, F.; Liu, B.; Dong, L. Morphology and Crystal-Plane Effects of Nanoscale Ceria on the Activity of CuO/CeO₂ for NO Reduction by CO. *ChemCatChem* **2011**, 3, 978–989.
- (302) Howie, A. New Strategies for e-Beam Characterization of Catalysts. *ChemCatChem* **2011**, 3, 961–964.
- (303) Hondow, N. S.; Chou, Y.-H.; Sader, K.; Douthwaite, R. E.; Brydson, R. Electron Microscopy of Cocatalyst Nanostructures on Semiconductor Photocatalysts. *ChemCatChem* **2011**, 3, 990–998.
- (304) Li, L.; Zhang, B.; Kunkes, E.; Foettinger, K.; Armbruester, M.; Su, D. S.; Wei, W.; Schloegl, R.; Behrens, M. Ga-Pd/Ga₂O₃ Catalysts: The Role of Gallia Polymorphs, Intermetallic Compounds, and Pretreatment Conditions on Selectivity and Stability in Different Reactions. *ChemCatChem* **2012**, 4, 1764–1775.
- (305) Ino, S. Epitaxial Growth of Metals on Rocksalt Faces Cleaved in Vacuum 0.2. Orientation and Structure of Gold Particles Formed in Ultrahigh Vacuum. *J. Phys. Soc. Jpn.* **1966**, 21, 346–362.
- (306) Ino, S.; Ogawa, S. Multiply Twinned Particles at Earlier Stages of Gold Film Formation on Alkalihalide Crystals. *J. Phys. Soc. Jpn.* **1967**, 22, 1365–1374.
- (307) Jefferson, D. A.; Thomas, J. M.; Millward, G. R.; Tsuno, K.; Harriman, A.; Brydson, R. D. Atomic-Structure of Ultrafine Catalyst Particles Resolved with a 200-KeV Transmission Electron-Microscope. *Nature* **1986**, 323, 428–431.
- (308) Giorgio, S.; Nihoul, G.; Urban, J.; Sackkongehl, H. Structures and Defects of Au Particles (1–3 nm) by HREM. *Z. Phys. D Atom. Mol. Cl.* **1992**, 24, 395–400.

- (309) Urban, J.; Sackkongehl, H.; Weiss, K. Computer-Simulations of HREM Images of Metal-Clusters. *Z. Phys. D Atom. Mol. Cl.* **1993**, *28*, 247–255.
- (310) Bernal, S.; Botana, F. J.; Calvino, J. J.; Lopez-Cartes, C.; Perez-Omil, J. A.; Rodriguez-Izquierdo, J. M. The interpretation of HREM images of supported metal catalysts using image simulation: profile view images. *Ultramicroscopy* **1998**, *72*, 135–164.
- (311) Lopez-Sanchez, J. A.; Dimitratos, N.; Hammond, C.; Brett, G. L.; Kesavan, L.; White, S.; Miedziak, P.; Tiruvalam, R.; Jenkins, R. L.; Carley, A. F.; Knight, D.; Kiely, C. J.; Hutchings, G. J. Facile removal of stabilizer-ligands from supported gold nanoparticles. *Nat. Chem.* **2011**, *3*, 551–556.
- (312) Tian, N.; Zhou, Z. Y.; Sun, S. G.; Ding, Y.; Wang, Z. L. Synthesis of tetrahedrahedral platinum nanocrystals with high-index facets and high electro-oxidation activity. *Science* **2007**, *316*, 732–735.
- (313) Tian, N.; Zhou, Z. Y.; Sun, S. G. Platinum Metal Catalysts of High-Index Surfaces: From Single-Crystal Planes to Electrochemically Shape-Controlled Nanoparticles. *J. Phys. Chem. C* **2008**, *112*, 19801–19817.
- (314) Tian, N.; Zhou, Z. Y.; Sun, S. G. Electrochemical preparation of Pd nanorods with high-index facets. *Chem. Commun.* **2009**, 1502–1504.
- (315) Tian, N.; Zhou, Z. Y.; Yu, N. F.; Wang, L. Y.; Sun, S. G. Direct Electrodeposition of Tetrahedrahedral Pd Nanocrystals with High-Index Facets and High Catalytic Activity for Ethanol Electrooxidation. *J. Am. Chem. Soc.* **2010**, *132*, 7580–7581.
- (316) Zhou, Z. Y.; Tian, N.; Li, J. T.; Broadwell, I.; Sun, S. G. Nanomaterials of high surface energy with exceptional properties in catalysis and energy storage. *Chem. Soc. Rev.* **2011**, *40*, 4167–4185.
- (317) Tian, N.; Xiao, J.; Zhou, Z. Y.; Liu, H. X.; Deng, Y. J.; Huang, L.; Xu, B. B.; Sun, S. G. Pt-group bimetallic nanocrystals with high-index facets as high performance electrocatalysts. *Faraday Discuss.* **2013**, *162*, 77–89.
- (318) Wei, L.; Zhou, Z. Y.; Chen, S. P.; Xu, C. D.; Su, D. S.; Schuster, M. E.; Sun, S. G. Electrochemically shape-controlled synthesis in deep eutectic solvents: triambic icosahedral platinum nanocrystals with high-index facets and their enhanced catalytic activity. *Chem. Commun.* **2013**, *49*, 11152–11154.
- (319) Chen, C.-C.; Zhu, C.; White, E. R.; Chiu, C.-Y.; Scott, M. C.; Regan, B. C.; Marks, L. D.; Huang, Y.; Miao, J. Three-dimensional imaging of dislocations in a nanoparticle at atomic resolution. *Nature* **2013**, *496*, 74–77.
- (320) Scott, M. C.; Chen, C. C.; Mecklenburg, M.; Zhu, C.; Xu, R.; Ercius, P.; Dahmen, U.; Regan, B. C.; Miao, J. W. Electron tomography at 2.4 angstrom resolution. *Nature* **2012**, *483*, 444–U491.
- (321) Goris, B.; Bals, S.; Van den Broek, W.; Carbo-Argibay, E.; Gomez-Grana, S.; Liz-Marzan, L. M.; Van Tendeloo, G. Atomic-scale determination of surface facets in gold nanorods. *Nat. Mater.* **2012**, *11*, 930–935.
- (322) Bals, S.; Casavola, M.; van Huis, M. A.; Van Aert, S.; Batenburg, K. J.; Van Tendeloo, G.; Vanmaekelbergh, D. Three-Dimensional Atomic Imaging of Colloidal Core-Shell Nanocrystals. *Nano Lett.* **2011**, *11*, 3420–3424.
- (323) Van Aert, S.; Batenburg, K. J.; Rossell, M. D.; Erni, R.; Van Tendeloo, G. Three-dimensional atomic imaging of crystalline nanoparticles. *Nature* **2011**, *470*, 374–377.
- (324) Wagner, J. B.; Hansen, P. L.; Molenbroek, A. M.; Topsoe, H.; Clausen, B. S.; Helveg, S. In situ electron energy loss spectroscopy studies of gas-dependent metal-support interactions in Cu/ZnO catalysts. *J. Phys. Chem. B* **2003**, *107*, 7753–7758.
- (325) Kasatkin, I.; Kurr, P.; Kniep, B.; Trunschke, A.; Schlogl, R. Role of lattice strain and defects in copper particles on the activity of Cu/ZnO/Al₂O₃ catalysts for methanol synthesis. *Angew. Chem., Int. Ed.* **2007**, *46*, 7324–7327.
- (326) Tiruvalam, R. C.; Pritchard, J. C.; Dimitratos, N.; Lopez-Sanchez, J. A.; Edwards, J. K.; Carley, A. F.; Hutchings, G. J.; Kiely, C. J. Aberration corrected analytical electron microscopy studies of sol-immobilized Au plus Pd, Au{Pd} and Pd{Au} catalysts used for benzyl alcohol oxidation and hydrogen peroxide production. *Faraday Discuss.* **2011**, *152*, 63–86.
- (327) Zhang, W.; Zhang, B. S.; Wolfram, T.; Shao, L. D.; Schlogl, R.; Su, D. S. Probing a Redox Behavior of TiO₂/SBA-15 Supported VxOy Catalyst Using an Electron Beam in a 200 kV Transmission Electron Microscope. *J. Phys. Chem. C* **2011**, *115*, 20550–20554.
- (328) Simonsen, S. B.; Chorkendorff, I.; Dahl, S.; Skoglundh, M.; Sehested, J.; Helveg, S. Direct Observations of Oxygen-induced Platinum Nanoparticle Ripening Studied by In Situ TEM. *J. Am. Chem. Soc.* **2010**, *132*, 7968–7975.
- (329) Wang, D.; Villa, A.; Porta, F.; Su, D. S.; Prati, L. Single-phase bimetallic system for the selective oxidation of glycerol to glycerate. *Chem. Commun.* **2006**, 1956–1958.
- (330) Bock, C.; Paquet, C.; Couillard, M.; Botton, G. A.; MacDougall, B. R. Size-selected synthesis of PtRu nano-catalysts: Reaction and size control mechanism. *J. Am. Chem. Soc.* **2004**, *126*, 8028–8037.
- (331) Xu, Q.; Kharas, K. C.; Croley, B. J.; Datye, A. K. The Sintering of Supported Pd Automotive Catalysts. *ChemCatChem* **2011**, *3*, 1004–1014.
- (332) Sobal, N. S.; Ebels, U.; Mohwald, H.; Giersig, M. Synthesis of core-shell PtCo nanocrystals. *J. Phys. Chem. B* **2003**, *107*, 7351–7354.
- (333) Datye, A. K.; Smith, D. J. The Study of Heterogeneous Catalysts by High-Resolution Transmission Electron-Microscopy. *Catal. Rev.* **1992**, *34*, 129–178.
- (334) Heinemann, K.; Soria, F. On the Detection and Size Classification of Nanometer-Size Metal Particles on Amorphous Substrates. *Ultramicroscopy* **1986**, *20*, 1–14.
- (335) Zhang, B. S.; Zhang, W.; Su, D. S. Towards a More Accurate Particle Size Distribution of Supported Catalyst by using HAADF-STEM. *ChemCatChem* **2011**, *3*, 965–968.
- (336) Sun, K.; Liu, J.; Nag, N. K.; Browning, N. D. Atomic scale characterization of supported Pd-Cu/gamma-Al₂O₃ bimetallic catalysts. *J. Phys. Chem. B* **2002**, *106*, 12239–12246.
- (337) Karim, A.; Conant, T.; Datye, A. The role of PdZn alloy formation and particle size on the selectivity for steam reforming of methanol. *J. Catal.* **2006**, *243*, 420–427.
- (338) Pan, X.; Zhang, B.; Zhong, B.; Wang, J.; Su, D. S. Towards a highly dispersed and more thermally stable Ru/OCNT catalyst. *Chem. Commun.* **2014**, *50*, 3856–3858.
- (339) Okamoto, N.; Mehraeen, S.; Kulkarni, A.; Nemana, S.; Gates, B.; Browning, N. Determination of Nanocluster Size Distributions From HAADF-STEM images. *Microsc. Microanal.* **2007**, *13*, 546–547.
- (340) Okamoto, N. L.; Reed, B. W.; Mehraeen, S.; Kulkarni, A.; Morgan, D. G.; Gates, B. C.; Browning, N. D. Determination of nanocluster sizes from dark-field scanning transmission electron microscopy images. *J. Phys. Chem. C* **2008**, *112*, 1759–1763.
- (341) Mitchell, D. R. G.; Wang, X. D.; Caruso, R. A. Plasmon imaging: An efficient TEM-based method for locating noble metal particles dispersed on oxide catalysts at very low densities. *Micron* **2008**, *39*, 344–347.
- (342) Cervera Gontard, L.; Ozkaya, D.; Dunin-Borkowski, R. E. A simple algorithm for measuring particle size distributions on an uneven background from TEM images. *Ultramicroscopy* **2011**, *111*, 101–106.
- (343) Arve, K.; Kannisto, H.; Ingelsten, H. H.; Eranen, K.; Skoglundh, M.; Murzin, D. Y. Did Chemisorption Become an Obsolete Method With Advent of Tem? Comparison of Mean Particle Size and Distribution of Silver on Alumina. *Catal. Lett.* **2011**, *141*, 665–669.
- (344) Su, D. S.; Perathoner, S.; Centi, G. Nanocarbons for the development of advanced catalysts. *Chem. Rev.* **2013**, *113*, 5782–5816.
- (345) Pan, X. L.; Fan, Z. L.; Chen, W.; Ding, Y. J.; Luo, H. Y.; Bao, X. H. Enhanced ethanol production inside carbon-nanotube reactors containing catalytic particles. *Nat. Mater.* **2007**, *6*, 507–511.
- (346) Serp, P.; Castillejos, E. Catalysis in Carbon Nanotubes. *ChemCatChem* **2010**, *2*, 41–47.
- (347) Tessonner, J. P.; Ersen, O.; Weinberg, G.; Pham-Huu, C.; Su, D. S.; Schlogl, R. Selective Deposition of Metal Nanoparticles Inside or

- Outside Multiwalled Carbon Nanotubes. *ACS Nano* **2009**, *3*, 2081–2089.
- (348) Zheng, W. Q.; Zhang, J.; Zhu, B.; Blume, R.; Zhang, Y. L.; Schlichte, K.; Schlogl, R.; Schuth, F.; Su, D. S. Structure-Function Correlations for Ru/CNT in the Catalytic Decomposition of Ammonia. *ChemSusChem* **2010**, *3*, 226–230.
- (349) Zhang, J.; Muller, J. O.; Zheng, W. Q.; Wang, D.; Su, D. S.; Schlogl, R. Individual Fe-Co alloy nanoparticles on carbon nanotubes: Structural and catalytic properties. *Nano Lett.* **2008**, *8*, 2738–2743.
- (350) Wang, X.; Li, N.; Pfefferle, L. D.; Haller, G. L. Metal nanoparticles inside multi-walled carbon nanotubes: A simple method of preparation and of microscopic image analysis. *Microporous Mesoporous Mater.* **2013**, *176*, 139–144.
- (351) Ward, E. P. W.; Yates, T. J. V.; Fernandez, J. J.; Vaughan, D. E. W.; Midgley, P. A. Three-dimensional nanoparticle distribution and local curvature of heterogeneous catalysts revealed by electron tomography. *J. Phys. Chem. C* **2007**, *111*, 11501–11505.
- (352) Hernandez-Garrido, J. C.; Yoshida, K.; Gai, P. L.; Boyes, E. D.; Christensen, C. H.; Midgley, P. A. The location of gold nanoparticles on titania: A study by high resolution aberration-corrected electron microscopy and 3D electron tomography. *Catal. Today* **2011**, *160*, 165–169.
- (353) Ziese, U.; de Jong, K. P.; Koster, A. J. Electron tomography: a tool for 3D structural probing of heterogeneous catalysts at the nanometer scale. *Appl. Catal. A—Gen.* **2004**, *260*, 71–74.
- (354) Ersen, O.; Werckmann, J.; Houlle, M.; Ledoux, M. J.; Pham-Huu, C. 3D electron microscopy study of metal particles inside multiwalled carbon nanotubes. *Nano Lett.* **2007**, *7*, 1898–1907.
- (355) Laursen, A. B.; Hojholz, K. T.; Lundsgaard, L. F.; Simonsen, S. B.; Helveg, S.; Schuth, F.; Paul, M.; Grunwaldt, J. D.; Kegnoes, S.; Christensen, C. H.; Egeblad, K. Substrate Size-Selective Catalysis with Zeolite-Encapsulated Gold Nanoparticles. *Angew. Chem., Int. Ed.* **2010**, *49*, 3504–3507.
- (356) Tauster, S. J.; Fung, S. C.; Garten, R. L. Strong Metal-Support Interactions—Group-8 Noble-Metals Supported on TiO₂. *J. Am. Chem. Soc.* **1978**, *100*, 170–175.
- (357) Tauster, S. J. Strong Metal-Support Interactions. *Acc. Chem. Res.* **1987**, *20*, 389–394.
- (358) Haller, G. L.; Resasco, D. E. Metal Support—Group-VIII Metals and Reducible Oxides. *Adv. Catal.* **1989**, *36*, 173–235.
- (359) Wang, D.; Penner, S.; Su, D. S.; Rupprechter, G.; Hayek, K.; Schlogl, R. Pt/SiO₂ model catalyst: metal support interaction studied by TEM and EELS. *Microsc. Microanal.* **2003**, *9*, 200–201.
- (360) d'Alnoncourt, R. N.; Friedrich, M.; Kunkes, E.; Rosenthal, D.; Girgsdies, F.; Zhang, B.; Shao, L.; Schuster, M.; Behrens, M.; Schloegl, R. Strong metal-support interactions between palladium and iron oxide and their effect on CO oxidation. *J. Catal.* **2014**, *317*, 220–228.
- (361) Bernal, S.; Calvino, J. J.; Cauqui, M. A.; Gatica, J. M.; Larese, C.; Omil, J. A. P.; Pintado, J. M. Some recent results on metal/support interaction effects in NM/CeO₂ (NM: noble metal) catalysts. *Catal. Today* **1999**, *50*, 175–206.
- (362) Baker, R. T.; Bernal, S.; Calvino, J. J.; Perez-Omil, J. A.; Lopez-Cartes, C. *Nano-scale characterisation of supported phases in catalytic materials by high resolution transmission electron microscopy*; Kluwer Academic/Plenum Publ: New York, 2004; pp 403–426.
- (363) Cargnello, M.; Doan-Nguyen, V. V. T.; Gordon, T. R.; Diaz, R. E.; Stach, E. A.; Gorte, R. J.; Fornasiero, P.; Murray, C. B. Control of Metal Nanocrystal Size Reveals Metal-Support Interface Role for Ceria Catalysts. *Science* **2013**, *341*, 771–773.
- (364) Zhou, W. Z.; Thomas, J. M. HRTEM surface profile imaging of solids. *Curr. Opin. Solid State Mater.* **2001**, *5*, 75–83.
- (365) Shao, L.; Zhang, B.; Zhang, W.; Hong, S. Y.; Schloegl, R.; Su, D. S. The Role of Palladium Dynamics in the Surface Catalysis of Coupling Reactions. *Angew. Chem., Int. Ed.* **2013**, *52*, 2114–2117.
- (366) Zhou, B.; Hermans, S.; Somorjai, G. A. *Nanotechnology in Catalysis Vols. 1 and 2*; Kluwer Academic/Plenum Publishers: New York, 2003.
- (367) Bernal, S.; Calvino, J. J.; Gatica, J. M.; Cartes, C. L.; Pintado, J. M. Chemical and nanostructural aspects of the preparation and characterisation of ceria and ceria-based mixed oxide-supported metal catalysts. *Catalysis by Ceria and Related Materials* **2002**, *2*, 85–168.
- (368) Gatica, J. M.; Baker, R. T.; Fornasiero, P.; Bernal, S.; Blanco, G.; Kaspar, J. Rhodium dispersion in a Rh/Ce_{0.68}Zr_{0.32}O₂ catalyst investigated by HRTEM and H₂ chemisorption. *J. Phys. Chem. B* **2000**, *104*, 4667–4672.
- (369) Bernal, S.; Botana, F. J.; Calvino, J. J.; Cifredo, G. A.; Perezomil, J. A. HREM Study of the Behavior of a Rh/CeO₂ Catalyst under High-Temperature Reducing and Oxidizing Conditions. *Catal. Today* **1995**, *23*, 219–250.
- (370) Rupprechter, G.; Hayek, K.; Rendon, L.; Joseyacaman, M. Epitaxially Grown Model Catalyst Particles of Platinum, Rhodium, Iridium, Palladium and Rhenium Studied by Electron-Microscopy. *Thin Solid Films* **1995**, *260*, 148–155.
- (371) Wang, D.; Penner, S.; Su, D. S.; Rupprechter, G.; Hayek, K.; Schlogl, R. Silicide formation on a Pt/SiO₂ model catalyst studied by TEM, EELS, and EDXS. *J. Catal.* **2003**, *219*, 434–441.
- (372) Willinger, M. G.; Zhang, W.; Bondarchuk, O.; Shaikhutdinov, S.; Freund, H.-J.; Schlogl, R. A Case of Strong Metal–Support Interactions: Combining Advanced Microscopy and Model Systems to Elucidate the Atomic Structure of Interfaces. *Angew. Chem., Int. Ed.* **2014**, *53*, 5998–6001.
- (373) Qin, Z. H.; Lewandowski, M.; Sun, Y. N.; Shaikhutdinov, S.; Freund, H. J. Encapsulation of Pt nanoparticles as a result of strong metal-support interaction with Fe(3)O(4) (111). *J. Phys. Chem. C* **2008**, *112*, 10209–10213.
- (374) Kandemir, T.; Kasatkin, I.; Girgsdies, F.; Zander, S.; Kuehl, S.; Tovar, M.; Schloegl, R.; Behrens, M. Microstructural and Defect Analysis of Metal Nanoparticles in Functional Catalysts by Diffraction and Electron Microscopy: The Cu/ZnO Catalyst for Methanol Synthesis. *Top. Catal.* **2014**, *57*, 188–206.
- (375) Fichtl, M. B.; Schumann, J.; Kasatkin, I.; Jacobsen, N.; Behrens, M.; Schloegl, R.; Muhler, M.; Hinrichsen, O. Counting of Oxygen Defects versus Metal Surface Sites in Methanol Synthesis Catalysts by Different Probe Molecules. *Angew. Chem., Int. Ed.* **2014**, *53*, 7043–7047.
- (376) Kasatkin, I.; Kniep, B.; Ressler, T. Cu/ZnO and Cu/ZrO₂ interactions studied by contact angle measurement with TEM. *Phys. Chem. Chem. Phys.* **2007**, *9*, 878–883.
- (377) Shibata, N.; Goto, A.; Matsunaga, K.; Mizoguchi, T.; Findlay, S. D.; Yamamoto, T.; Ikuhara, Y. Interface Structures of Gold Nanoparticles on TiO₂ (110). *Phys. Rev. Lett.* **2009**, *102*, 136105.
- (378) Ichikawa, S.; Akita, T.; Okumura, M.; Haruta, M.; Tanaka, K.; Kohyama, M. Electron holographic 3-D nano-analysis of Au/TiO₂ catalyst at interface. *J. Electron Microsc.* **2003**, *52*, 21–26.
- (379) Ichikawa, S.; Akita, T.; Okumura, M.; Haruta, M.; Tanaka, K. In *Nanostructured Interfaces*; Plitzko, J. M., Duscher, G., Zhu, Y., Ichinose, H., Eds.; Materials Research Society: Warrendale, 2002; Vol. 727, pp 11–16.
- (380) Ichikawa, S.; Akita, T.; Okumura, M.; Kohyama, M.; Tanaka, K. Electron holographic analysis of nanostructured gold catalyst. *JEOL News* **2003**, *38*, 6–9.
- (381) Oyama, S. T.; Gaudet, J.; Zhang, W.; Su, D. S.; Bando, K. K. Platinum-Like Catalytic Behavior of Au⁺. *ChemCatChem* **2010**, *2*, 1582–1586.
- (382) Guzman, J.; Gates, B. C. Structure and reactivity of a mononuclear gold-complex catalyst supported on magnesium oxide. *Angew. Chem., Int. Ed.* **2003**, *42*, 690–693.
- (383) Fu, Q.; Saltsburg, H.; Flytzani-Stephanopoulos, M. Active nonmetallic Au and Pt species on ceria-based water-gas shift catalysts. *Science* **2003**, *301*, 935–938.
- (384) Manzoli, M.; Chiorino, A.; Bocuzzi, F. FTIR study of nanosized gold on ZrO₂ and TiO₂. *Surf. Sci.* **2003**, *532*, 377–382.
- (385) Socaciu, L. D.; Hagen, J.; Bernhardt, T. M.; Woste, L.; Heiz, U.; Hakkinen, H.; Landman, U. Catalytic CO oxidation by free Au^{2(–)}: Experiment and theory. *J. Am. Chem. Soc.* **2003**, *125*, 10437–10445.
- (386) Meyer, R.; Lemire, C.; Shaikhutdinov, S. K.; Freund, H. Surface chemistry of catalysis by gold. *Gold Bull.* **2004**, *37*, 72–124.

- (387) Ferrando, R.; Jellinek, J.; Johnston, R. L. Nanoalloys: From theory to applications of alloy clusters and nanoparticles. *Chem. Rev.* **2008**, *108*, 845–910.
- (388) Villa, A.; Wang, D.; Su, D. S.; Prati, L. New challenges in gold catalysis: bimetallic systems. *Catal. Sci. Technol.* **2014**, *5*, 55–68.
- (389) Wang, D. S.; Peng, Q.; Li, Y. D. Nanocrystalline Intermetallics and Alloys. *Nano Res.* **2010**, *3*, 574–580.
- (390) Wang, D. S.; Li, Y. D. Bimetallic Nanocrystals: Liquid-Phase Synthesis and Catalytic Applications. *Adv. Mater.* **2011**, *23*, 1044–1060.
- (391) Park, J. Y.; Zhang, Y.; Grass, M.; Zhang, T.; Somorjai, G. A. Tuning of catalytic CO oxidation by changing composition of Rh-Pt bimetallic nanoparticles. *Nano Lett.* **2008**, *8*, 673–677.
- (392) Schmid, G.; Lehnert, A.; Malm, J. O.; Bovin, J. O. Ligand-Stabilized Bimetallic Colloids Identified by HRTEM and EDX. *Angew. Chem., Int. Ed.* **1991**, *30*, 874–876.
- (393) Bracey, C. L.; Ellis, P. R.; Hutchings, G. J. Application of copper-gold alloys in catalysis: current status and future perspectives. *Chem. Soc. Rev.* **2009**, *38*, 2231–2243.
- (394) Hongjing, W.; La Parola, V.; Pantaleo, G.; Puleo, F.; Venezia, A. M.; Liotta, L. F. Ni-based catalysts for low temperature methane steam reforming: Recent results on Ni-Au and comparison with other bi-metallic systems. *Catalysts* **2013**, *3*, 563–583.
- (395) Pojanavaraphan, C.; Luengnaruemitchai, A.; Gulari, E. Effect of catalyst preparation on Au/Ce_{1-x}Zr_xO₂ and Au-Cu/Ce_{1-x}Zr_xO₂ for steam reforming of methanol. *Int. J. Hydrogen Energy* **2013**, *38*, 1348–1362.
- (396) Prati, L.; Villa, A.; Su, D. S.; Wang, D.; Krpetic, Z.; Porta, F. In Scientific Bases for the Preparation of Heterogeneous Catalysts. *Proceedings of the 9th International Symposium*; Gaigneaux, E. M., Devillers, M., De Vos, D. E., Hermans, S., Jacobs, P. A., Martens, J. A., Ruiz, P., Eds.; Elsevier Science Bv: Amsterdam, 2006; Vol. 162, pp 553–560.
- (397) Dimitratos, N.; Villa, A.; Wang, D.; Porta, F.; Su, D. S.; Prati, L. Pd and Pt catalysts modified by alloying with Au in the selective oxidation of alcohols. *J. Catal.* **2006**, *244*, 113–121.
- (398) Prati, L.; Villa, A.; Porta, F.; Wang, D.; Su, D. S. Single-phase gold/palladium catalyst: The nature of synergistic effect. *Catal. Today* **2007**, *122*, 386–390.
- (399) Wang, D.; Villa, A.; Porta, F.; Prati, L.; Su, D. S. Bimetallic gold/palladium catalysts: Correlation between nanostructure and synergistic effects. *J. Phys. Chem. C* **2008**, *112*, 8617–8622.
- (400) Villa, A.; Janjic, N.; Spontoni, P.; Wang, D.; Su, D. S.; Prati, L. Au-Pd/AC as catalysts for alcohol oxidation: Effect of reaction parameters on catalytic activity and selectivity. *Appl. Catal. A—Gen.* **2009**, *364*, 221–228.
- (401) Villa, A.; Wang, D.; Spontoni, P.; Arrigo, R.; Su, D. S.; Prati, L. Nitrogen functionalized carbon nanostructures supported Pd and Au-Pd NPs as catalyst for alcohols oxidation. *Catal. Today* **2010**, *157*, 89–93.
- (402) Villa, A.; Wang, D.; Su, D. S.; Veith, G. M.; Prati, L. Using supported Au nanoparticles as starting material for preparing uniform Au/Pd bimetallic catalysts. *Phys. Chem. Chem. Phys.* **2010**, *12*, 2183–2189.
- (403) Kunz, H. R.; Gruver, G. A. Catalytic Activity of Platinum Supported on Carbon for Electrochemical Oxygen Reduction in Phosphoric-Acid. *J. Electrochem. Soc.* **1975**, *122*, 1279–1287.
- (404) Stonehart, P. Development of Alloy Electrocatalysts for Phosphoric-Acid Fuel-Cells (Pafc). *J. Appl. Electrochem.* **1992**, *22*, 995–1001.
- (405) Russell, A. E.; Rose, A. X-ray absorption Spectroscopy of low temperature fuel cell catalysts. *Chem. Rev.* **2004**, *104*, 4613–4635.
- (406) Ji, X. L.; Lee, K. T.; Holden, R.; Zhang, L.; Zhang, J. J.; Botton, G. A.; Couillard, M.; Nazar, L. F. Nanocrystalline intermetallics on mesoporous carbon for direct formic acid fuel cell anodes. *Nat. Chem.* **2010**, *2*, 286–293.
- (407) Chen, C.; Kang, Y. J.; Huo, Z. Y.; Zhu, Z. W.; Huang, W. Y.; Xin, H. L. L.; Snyder, J. D.; Li, D. G.; Herron, J. A.; Mavrikakis, M.; Chi, M. F.; More, K. L.; Li, Y. D.; Markovic, N. M.; Somorjai, G. A.; Yang, P. D.; Stamenkovic, V. R. Highly Crystalline Multimetallic Nanoframes with Three-Dimensional Electrocatalytic Surfaces. *Science* **2014**, *343*, 1339–1343.
- (408) Pal, U.; Ramirez, J. F. S.; Liu, H. B.; Medina, A.; Ascencio, J. A. Synthesis and structure determination of bimetallic Au/Cu nanoparticles. *Appl. Phys. A—Mater.* **2004**, *79*, 79–84.
- (409) Harpness, R.; Gedanken, A. Microwave synthesis of core-shell gold/palladium bimetallic nanoparticles. *Langmuir* **2004**, *20*, 3431–3434.
- (410) Sobal, N. S.; Hilgendorff, M.; Mohwald, H.; Giersig, M.; Spasova, M.; Radetic, T.; Farle, M. Synthesis and structure of colloidal bimetallic nanocrystals: The non-alloying system Ag/Co. *Nano Lett.* **2002**, *2*, 621–624.
- (411) Voyles, P. M.; Muller, D. A.; Grazul, J. L.; Citrin, P. H.; Gossmann, H. J. L. Atomic-scale imaging of individual dopant atoms and clusters in highly n-type bulk Si. *Nature* **2002**, *416*, 826–829.
- (412) Kiely, C. ELECTRON MICROSCOPY New views of catalysts. *Nat. Mater.* **2010**, *9*, 296–297.
- (413) Leary, R.; de la Peña, F.; Barnard, J. S.; Luo, Y.; Armbrüster, M.; Meurig Thomas, J.; Midgley, P. A. Revealing the Atomic Structure of Intermetallic GaPd₂ Nanocatalysts by using Aberration-Corrected Scanning Transmission Electron Microscopy. *ChemCatChem* **2013**, *5*, 2599–2609.
- (414) Mejia-Rosales, S. J.; Fernandez-Navarro, C.; Perez-Tijerina, E.; Blom, D. A.; Allard, L. F.; Jose-Yacaman, M. On the structure of Au/Pd bimetallic nanoparticles. *J. Phys. Chem. C* **2007**, *111*, 1256–1260.
- (415) Cazayous, M.; Langlois, C.; Oikawa, T.; Ricolleau, C.; Sacuto, A. Cu-Ag core-shell nanoparticles: A direct correlation between micro-Raman and electron microscopy. *Phys. Rev. B* **2006**, *73*, 113402.
- (416) Wang, D.; Villa, A.; Spontoni, P.; Su, D. S.; Prati, L. In Situ Formation of Au-Pd Bimetallic Active Sites Promoting the Physically Mixed Monometallic Catalysts in the Liquid-Phase Oxidation of Alcohols. *Chem.—Eur. J.* **2010**, *16*, 10007–10013.
- (417) Lyman, C. E.; Lakis, R. E.; Stenger, H. G.; Totdal, B.; Prestvik, R. Analysis of alloy nanoparticles. *Mikrochim. Acta* **2000**, *132*, 301–308.
- (418) Hannemann, S.; Grunwaldt, J. D.; Lienemann, P.; Gunther, D.; Krumeich, F.; Pratsinis, S. E.; Baiker, A. Combination of flame synthesis and high-throughput experimentation: The preparation of alumina-supported noble metal particles and their application in the partial oxidation of methane. *Appl. Catal. A—Gen.* **2007**, *316*, 226–239.
- (419) Shi, L.; Wang, A.; Zhang, T.; Zhang, B.; Su, D.; Li, H.; Song, Y. One-Step Synthesis of Au-Pd Alloy Nanodendrites and Their Catalytic Activity. *J. Phys. Chem. C* **2013**, *117*, 12526–12536.
- (420) Alayoglu, S.; Eichhorn, B. Rh-Pt Bimetallic Catalysts: Synthesis, Characterization, and Catalysis of Core-Shell, Alloy, and Monometallic Nanoparticles. *J. Am. Chem. Soc.* **2008**, *130*, 17479–17486.
- (421) Yang, H.; Gao, H. R.; Angelici, R. J. Hydrogenation of arenes under mild conditions using rhodium pyridylphosphine and bipyridyl complexes tethered to a silica-supported palladium heterogeneous catalyst. *Organometallics* **2000**, *19*, 622–629.
- (422) Rodriguez-Gonzalez, B.; Burrows, A.; Watanabe, M.; Kiely, C. J.; Liz-Marzan, L. M. Multishell bimetallic AuAg nanoparticles: synthesis, structure and optical properties. *J. Mater. Chem.* **2005**, *15*, 1755–1759.
- (423) Hungria, A. B.; Raja, R.; Adams, R. D.; Captain, B.; Thomas, J. M.; Midgley, P. A.; Golovko, V.; Johnson, B. F. G. Single-step conversion of dimethyl terephthalate into cyclohexanediethanol with Ru₅Pt₂Sn, a trimetallic nanoparticle catalyst. *Angew. Chem., Int. Ed.* **2006**, *45*, 4782–4785.
- (424) Zhou, W.; Doura, K. F.; Watanabe, M.; Herzing, A. A.; Okunishi, E.; Ross-Medgaarden, E. I.; Wachs, I. E.; Kiely, C. J. Aberration-corrected Analytical Microscopy Characterization of Double-Supported WO₃/TiO₂/SiO₂ Solid Acid Catalysts. *ChemCatChem* **2011**, *3*, 1045–1050.

- (425) Sankar, M.; Dimitratos, N.; Miedziak, P. J.; Wells, P. P.; Kiely, C. J.; Hutchings, G. J. Designing bimetallic catalysts for a green and sustainable future. *Chem. Soc. Rev.* **2012**, *41*, 8099–8139.
- (426) Tao, F. Synthesis, catalysis, surface chemistry and structure of bimetallic nanocatalysts. *Chem. Soc. Rev.* **2012**, *41*, 7977–7979.
- (427) Gan, L.; Heggen, M.; Rudi, S.; Strasser, P. Core-Shell Compositional Fine Structures of Dealloyed Pt_xNi_{1-x} Nanoparticles and Their Impact on Oxygen Reduction Catalysis. *Nano Lett.* **2012**, *12*, 5423–5430.
- (428) Gan, L.; Heggen, M.; O’Malley, R.; Theobald, B.; Strasser, P. Understanding and Controlling Nanoporosity Formation for Improving the Stability of Bimetallic Fuel Cell Catalysts. *Nano Lett.* **2013**, *13*, 1131–1138.
- (429) Oezaslan, M.; Heggen, M.; Strasser, P. Size-Dependent Morphology of Dealloyed Bimetallic Catalysts: Linking the Nano to the Macro Scale. *J. Am. Chem. Soc.* **2012**, *134*, 514–524.
- (430) Cui, C.; Gan, L.; Heggen, M.; Rudi, S.; Strasser, P. Compositional segregation in shaped Pt alloy nanoparticles and their structural behaviour during electrocatalysis. *Nat. Mater.* **2013**, *12*, 765–771.
- (431) Lee, S. W.; Chen, S. O.; Sheng, W. C.; Yabuuchi, N.; Kim, Y. T.; Mitani, T.; Vescovo, E.; Shao-Horn, Y. Roles of Surface Steps on Pt Nanoparticles in Electro-oxidation of Carbon Monoxide and Methanol. *J. Am. Chem. Soc.* **2009**, *131*, 15669–15677.
- (432) Zavyalova, U.; Geske, M.; Horn, R.; Weinberg, G.; Frandsen, W.; Schuster, M.; Schlögl, R. Morphology and Microstructure of Li/MgO Catalysts for the Oxidative Coupling of Methane. *ChemCatChem* **2011**, *3*, 949–959.
- (433) Specht, P.; Gulotty, R. J.; Barton, D.; Cieslinski, R.; Rozeveld, S.; Kang, J. H.; Dubon, O. D.; Kisielowski, C. Quantitative Contrast Evaluation of an Industry-Style Rhodium Nanocatalyst with Single Atom Sensitivity. *ChemCatChem* **2011**, *3*, 1034–1037.
- (434) Asahina, S.; Takami, S.; Otsuka, T.; Adschari, T.; Terasaki, O. Exploitation of Surface-Sensitive Electrons in Scanning Electron Microscopy Reveals the Formation Mechanism of New Cubic and Truncated Octahedral CeO₂ Nanoparticles. *ChemCatChem* **2011**, *3*, 1038–1044.
- (435) Rozita, Y.; Brydson, R.; Comyn, T. P.; Scott, A. J.; Hammond, C.; Brown, A.; Chauruka, S.; Hassanpour, A.; Young, N. P.; Kirkland, A. I.; Sawada, H.; Smith, R. I. A Study of Commercial Nanoparticulate γ -Al₂O₃ Catalyst Supports. *ChemCatChem* **2013**, *5*, 2695–2706.
- (436) Delannoy, L.; Giorgio, S.; Mattei, J. G.; Henry, C. R.; El Kollil, N.; Méthivier, C.; Louis, C. Surface Segregation of Pd from TiO₂-Supported AuPd Nanoalloys under CO Oxidation Conditions Observed In situ by ETEM and DRIFTS. *ChemCatChem* **2013**, *5*, 2707–2716.
- (437) Chan, M. C. Y.; Chen, L.; Nan, F. H.; Britten, J. F.; Bock, C.; Botton, G. A. Structure, ordering, and surfaces of Pt-Fe alloy catalytic nanoparticles from quantitative electron microscopy and X-ray diffraction. *Nanoscale* **2012**, *4*, 7273–7279.
- (438) Ward, M. R.; Boyes, E. D.; Gai, P. L. In Situ Aberration-Corrected Environmental TEM: Reduction of Model Co₃O₄ in H₂ at the Atomic Level. *ChemCatChem* **2013**, *5*, 2655–2661.
- (439) Bao, X.; Muhler, M.; Pettinger, B.; Schlögl, R.; Ertl, G. On the Nature of the Active State of Silver During Catalytic-Oxidation of Methanol. *Catal. Lett.* **1993**, *22*, 215–225.
- (440) Bao, X.; Muhler, M.; Schlögl, R.; Ertl, G. Oxidative Coupling of Methane on Silver Catalysts. *Catal. Lett.* **1995**, *32*, 185–194.
- (441) Schubert, H.; Tegtmeyer, U.; Herein, D.; Bao, X.; Muhler, M.; Schlögl, R. On the Relation between Catalytic Performance and Microstructure of Polycrystalline Silver in the Partial Oxidation of Methanol. *Catal. Lett.* **1995**, *33*, 305–319.
- (442) Xu, Y.; Greeley, J.; Mavrikakis, M. Effect of subsurface oxygen on the reactivity of the Ag(111) surface. *J. Am. Chem. Soc.* **2005**, *127*, 12823–12827.
- (443) Claus, P.; Hofmeister, H. Electron microscopy and catalytic study of silver catalysts: Structure sensitivity of the hydrogenation of crotonaldehyde. *J. Phys. Chem. B* **1999**, *103*, 2766–2775.
- (444) Teschner, D.; Pestryakov, A.; Kleimenov, E.; Havecker, M.; Bluhm, H.; Sauer, H.; Knop-Gericke, A.; Schlögl, R. High-pressure X-ray photoelectron spectroscopy of palladium model hydrogenation catalysts. Part 2: Hydrogenation of trans-2-pentene on palladium. *J. Catal.* **2005**, *230*, 195–203.
- (445) Teschner, D.; Vass, E.; Havecker, M.; Zafeiratos, S.; Schnorch, P.; Sauer, H.; Knop-Gericke, A.; Schlögl, R.; Chamam, M.; Woitsch, A.; Canning, A. S.; Gamman, J. J.; Jackson, S. D.; McGregor, J.; Gladden, L. F. Alkyne hydrogenation over Pd catalysts: A new paradigm. *J. Catal.* **2006**, *242*, 26–37.
- (446) Rinaldi, A.; Tessonner, J. P.; Schuster, M. E.; Blume, R.; Girgsdies, F.; Zhang, Q.; Jacob, T.; Hamid, S. B. A.; Su, D. S.; Schlögl, R. Dissolved Carbon Controls the Initial Stages of Nanocarbon Growth. *Angew. Chem., Int. Ed.* **2011**, *50*, 3313–3317.
- (447) Kuhlenbeck, H.; Shaikhutdinov, S.; Freund, H. J. Well-Ordered Transition Metal Oxide Layers in Model Catalysis—A Series of Case Studies. *Chem. Rev.* **2013**, *113*, 3986–4034.
- (448) Pacchioni, G.; Freund, H. Electron Transfer at Oxide Surfaces. The MgO Paradigm: from Defects to Ultrathin Films. *Chem. Rev.* **2013**, *113*, 4035–4072.
- (449) Ertl, G. Molecules at Surfaces: 100 Years of Physical Chemistry in Berlin-Dahlem. *Angew. Chem., Int. Ed.* **2013**, *52*, 52–60.
- (450) Myrach, P.; Nilius, N.; Levchenko, S. V.; Gonchar, A.; Rissee, T.; Dinse, K. P.; Boatner, L. A.; Frandsen, W.; Horn, R.; Freund, H. J.; Schlögl, R.; Scheffler, M. Temperature-Dependent Morphology, Magnetic and Optical Properties of Li-Doped MgO. *ChemCatChem* **2010**, *2*, 854–862.
- (451) Zavyalova, U.; Weinberg, G.; Frandsen, W.; Girgsdies, F.; Rissee, T.; Dinse, K. P.; Schlögl, R.; Horn, R. Lithium as a Modifier for Morphology and Defect Structure of Porous Magnesium Oxide Materials Prepared by Gel Combustion Synthesis. *ChemCatChem* **2011**, *3*, 1779–1788.
- (452) Schwach, P.; Willinger, M. G.; Trunschke, A.; Schlögl, R. Methane Coupling over Magnesium Oxide: How Doping Can Work. *Angew. Chem., Int. Ed.* **2013**, *52*, 11381–11384.
- (453) Kwapien, K.; Paier, J.; Sauer, J.; Geske, M.; Zavyalova, U.; Horn, R.; Schwach, P.; Trunschke, A.; Schlögl, R. Sites for Methane Activation on Lithium-Doped Magnesium Oxide Surfaces. *Angew. Chem., Int. Ed.* **2014**, 8774–8778.
- (454) Sanfiz, A. C.; Hansen, T. W.; Teschner, D.; Schnoerich, P.; Girgsdies, F.; Trunschke, A.; Schlögl, R.; Looi, M. H.; Hamid, S. B. A. Dynamics of the MoVTeNb Oxide M1 Phase in Propane Oxidation. *J. Phys. Chem. C* **2010**, *114*, 1912–1921.
- (455) Shibata, N.; Goto, A.; Choi, S. Y.; Mizoguchi, T.; Findlay, S. D.; Yamamoto, T.; Ikuhara, Y. Direct imaging of reconstructed atoms on TiO₂(110) surfaces. *Science* **2008**, *322*, 570–573.
- (456) Park, K.; Pan, M.; Meunier, V.; Plummer, E. Surface reconstructions of TiO₂(110) driven by suboxides. *Phys. Rev. Lett.* **2006**, *96*.
- (457) Elliott, S. D.; Bates, S. P. Energetically accessible reconstructions along interstitial rows on the rutile (110) surface. *Phys. Chem. Chem. Phys.* **2001**, *3*, 1954–1957.
- (458) Weiss, W.; Zscherpel, D.; Schlögl, R. On the nature of the active site for the ethylbenzene dehydrogenation over iron oxide catalysts. *Catal. Lett.* **1998**, *52*, 215–220.
- (459) Wang, X. G.; Weiss, W.; Shaikhutdinov, S. K.; Ritter, M.; Petersen, M.; Wagner, F.; Schlögl, R.; Scheffler, M. The hematite (α -Fe₂O₃) (0001) surface: Evidence for domains of distinct chemistry. *Phys. Rev. Lett.* **1998**, *81*, 1038–1041.
- (460) Barbier, A.; Stierle, A.; Kasper, N.; Guittet, M. J.; Jupille, J. Surface termination of hematite at environmental oxygen pressures: Experimental surface phase diagram. *Phys. Rev. B* **2007**, *75*, 233406.
- (461) Wang, R.; Crozier, P. A.; Sharma, R. Structural Transformation in Ceria Nanoparticles during Redox Processes. *J. Phys. Chem. C* **2009**, *113*, 5700–5704.
- (462) Crozier, P. A.; Wang, R. G.; Sharma, R. In situ environmental TEM studies of dynamic changes in cerium-based oxides nanoparticles during redox processes. *Ultramicroscopy* **2008**, *108*, 1432–1440.

- (463) Zhang, W.; Trunschke, A.; Schlogl, R.; Su, D. S. Real-Space Observation of Surface Termination of a Complex Metal Oxide Catalyst. *Angew. Chem., Int. Ed.* **2010**, *49*, 6084–6089.
- (464) Grasselli, R. K.; Buttrey, D. J.; Burrington, J. D.; Andersson, A.; Holmberg, J.; Ueda, W.; Kubo, J.; Lugmair, C. G.; Volpe, A. F. Active centers, catalytic behavior, symbiosis and redox properties of MoV(Nb,Ta)TeO ammoxidation catalysts. *Top. Catal.* **2006**, *38*, 7–16.
- (465) Watanabe, N.; Ueda, W. Comparative study on the catalytic performance of single-phase Mo-V-O-based metal oxide catalysts in propane ammoxidation to acrylonitrile. *Ind. Eng. Chem. Res.* **2006**, *45*, 607–614.
- (466) Wagner, J. B.; Timpe, O.; Hamid, F. A.; Trunschke, A.; Wild, U.; Su, D. S.; Widi, R. K.; Abd Hamid, S. B.; Schlogl, R. Surface texturing of Mo-V-Te-Nb-O-x selective oxidation catalysts. *Top. Catal.* **2006**, *38*, 51–58.
- (467) Blom, D. A.; Li, X.; Mitra, S.; Vogt, T.; Buttrey, D. J. STEM HAADF Image Simulation of the Orthorhombic M1 Phase in the Mo-V-Nb-Te-O Propane Oxidation Catalyst. *ChemCatChem* **2011**, *3*, 1028–1033.
- (468) DeSanto, P.; Buttrey, D. J.; Grasselli, R. K.; Lugmair, C. G.; Volpe, A. F.; Toby, B. H.; Vogt, T. Structural aspects of the M1 and M2 phases in MoVNbTeO propane ammoxidation catalysts. *Z. Kristallogr.—Cryst. Mater.* **2004**, *219*, 152–165.
- (469) Pyrz, W. D.; Blom, D. A.; Vogt, T.; Buttrey, D. J. Direct imaging of the MoVTeNbO M1 phase using an aberration-corrected high-resolution scanning transmission electron microscope. *Angew. Chem., Int. Ed.* **2008**, *47*, 2788–2791.
- (470) Pyrz, W. D.; Blom, D. A.; Sadakane, M.; Kodato, K.; Ueda, W.; Vogt, T.; Buttrey, D. J. Atomic-level imaging of Mo-V-O complex oxide phase intergrowth, grain boundaries, and defects using HAADF-STEM. *Proc. Natl. Acad. Sci. U.S.A.* **2010**, *107*, 6152–6157.
- (471) Havecker, M.; Wrabetz, S.; Krohnert, J.; Csepei, L. I.; d'Alnoncourt, R. N.; Kolen'ko, Y. V.; Girgisdies, F.; Schlogl, R.; Trunschke, A. Surface chemistry of phase-pure M1MoVTeNb oxide during operation in selective oxidation of propane to acrylic acid. *J. Catal.* **2012**, *285*, 48–60.
- (472) Kolen'ko, Y. V.; Zhang, W.; d'Alnoncourt, R. N.; Girgisdies, F.; Hansen, T. W.; Wolfram, T.; Schloegl, R.; Trunschke, A. Synthesis of MoVTeNb Oxide Catalysts with Tunable Particle Dimensions. *ChemCatChem* **2011**, *3*, 1597–1606.
- (473) Zenkovets, G. A.; Kryukova, G. N.; Gavrilov, V. Y.; Tsybulya, S. V.; Anufrienko, V. A.; Larina, T. A.; Khabibulin, D. F.; Lapina, O. B.; Roedel, E.; Trunschke, A.; Ressler, T.; Schloegl, R. The structural genesis of a complex(MoVW)(5)O-14 oxide during thermal treatments and its redox behavior at elevated temperatures. *Mater. Chem. Phys.* **2007**, *103*, 295–304.
- (474) Sanchez, M. S.; Girgisdies, F.; Jastak, M.; Kube, P.; Schloegl, R.; Trunschke, A. Aiding the Self-Assembly of Supramolecular Polyoxometalates under Hydrothermal Conditions To Give Precursors of Complex Functional Oxides. *Angew. Chem., Int. Ed.* **2012**, *51*, 7194–7197.
- (475) Hashimoto, A.; Suenaga, K.; Gloter, A.; Urata, K.; Iijima, S. Direct evidence for atomic defects in graphene layers. *Nature* **2004**, *430*, 870–873.
- (476) Iijima, S. Helical Microtubules of Graphitic Carbon. *Nature* **1991**, *354*, 56–58.
- (477) Oberlin, A.; Endo, M.; Koyama, T. Filamentous Growth of Carbon Through Benzene Decomposition. *J. Cryst. Growth* **1976**, *32*, 335–349.
- (478) Iijima, S.; Ichihashi, T. Single-Shell Carbon Nanotubes of 1-nm Diameter. *Nature* **1993**, *363*, 603–605.
- (479) Krishnan, A.; Dujardin, E.; Treacy, M. M. J.; Hugdahl, J.; Lynum, S.; Ebbesen, T. W. Graphitic cones and the nucleation of curved carbon surfaces. *Nature* **1997**, *388*, 451–454.
- (480) Iijima, S.; Yudasaka, M.; Yamada, R.; Bandow, S.; Suenaga, K.; Kokai, F.; Takahashi, K. Nano-aggregates of single-walled graphitic carbon nano-horns. *Chem. Phys. Lett.* **1999**, *309*, 165–170.
- (481) Suenaga, K. Elemental analysis down to the single atom with electron beams. *C. R. Phys.* **2014**, *15*, 151–157.
- (482) Terrones, M.; Botello-Mendez, A. R.; Campos-Delgado, J.; Lopez-Urias, F.; Vega-Cantu, Y. L.; Rodriguez-Macias, F. J.; Elias, A. L.; Munoz-Sandoval, E.; Cano-Marquez, A. G.; Charlier, J. C.; Terrones, H. Graphene and graphite nanoribbons: Morphology, properties, synthesis, defects and applications. *Nano Today* **2010**, *5*, 351–372.
- (483) Araujo, P. T.; Terrones, M.; Dresselhaus, M. S. Defects and impurities in graphene-like materials. *Mater. Today* **2012**, *15*, 98–109.
- (484) Panchakarla, L. S.; Govindaraj, A.; Rao, C. N. R. Boron- and nitrogen-doped carbon nanotubes and graphene. *Inorg. Chim. Acta* **2010**, *363*, 4163–4174.
- (485) Kurasch, S.; Kotakoski, J.; Lehtinen, O.; Skakalova, V.; Smet, J.; Krill, C. E.; Krasheninnikov, A. V.; Kaiser, U. Atom-by-Atom Observation of Grain Boundary Migration in Graphene. *Nano Lett.* **2012**, *12*, 3168–3173.
- (486) Jin, C.; Suenaga, K.; Iijima, S. Vacancy migrations in carbon nanotubes. *Nano Lett.* **2008**, *8*, 1127–1130.
- (487) Jin, C.; Suenaga, K.; Iijima, S. Plumbing carbon nanotubes. *Nat. Nanotechnol.* **2008**, *3*, 17–21.
- (488) Jin, C.; Lan, H.; Peng, L.; Suenaga, K.; Iijima, S. Deriving Carbon Atomic Chains from Graphene. *Phys. Rev. Lett.* **2009**, *102*.
- (489) Girit, C. O.; Meyer, J. C.; Erni, R.; Rossell, M. D.; Kisielowski, C.; Yang, L.; Park, C. H.; Crommie, M. F.; Cohen, M. L.; Louie, S. G.; Zettl, A. Graphene at the Edge: Stability and Dynamics. *Science* **2009**, *323*, 1705–1708.
- (490) Kresge, C. T.; Roth, W. J. The discovery of mesoporous molecular sieves from the twenty year perspective. *Chem. Soc. Rev.* **2013**, *42*, 3663–3670.
- (491) Thomas, J. M.; Raja, R. Exploiting nanospace for asymmetric catalysis: Confinement of immobilized, single-site chiral catalysts enhances enantioselectivity. *Acc. Chem. Res.* **2008**, *41*, 708–720.
- (492) Suib, S. L. Porous manganese oxide octahedral molecular sieves and octahedral layered materials. *Acc. Chem. Res.* **2008**, *41*, 479–487.
- (493) Thomas, J. M. The societal significance of catalysis and the growing practical importance of single-site heterogeneous catalysts. *P. R. Soc. A—Math. Phys.* **2012**, *468*, 1884–1903.
- (494) Pan, M. High resolution electron microscopy of zeolites. *Micron* **1996**, *27*, 219–238.
- (495) Nicolopoulos, S.; GonzalezCalbet, J. M.; ValletRegi, M.; Cambor, M. A.; Corell, C.; Corma, A.; DiazCabanias, M. J. Use of electron microscopy and microdiffraction for zeolite framework comparison. *J. Am. Chem. Soc.* **1997**, *119*, 11000–11005.
- (496) Thomas, J. M.; Terasaki, O. The electron microscope is an indispensable instrument for the characterisation of catalysts. *Top. Catal.* **2002**, *21*, 155–159.
- (497) Chester, A. W.; Derouane, E. G. *Zeolite characterization and catalysis*; Springer: New York, 2009.
- (498) Williams, R. C.; Fisher, H. W. Electron microscopy of tobacco mosaic virus under conditions of minimal beam exposure. *J. Mol. Biol.* **1970**, *52*, 121–123.
- (499) Carlsson, A.; Kaneda, M.; Sakamoto, Y.; Terasaki, O.; Ryoo, R.; Joo, S. H. The structure of MCM-48 determined by electron crystallography. *J. Electron Microsc.* **1999**, *48*, 795–798.
- (500) Ortalan, V.; Uzun, A.; Gates, B. C.; Browning, N. D. Direct imaging of single metal atoms and clusters in the pores of dealuminated HY zeolite. *Nat. Nanotechnol.* **2010**, *5*, 506–510.
- (501) Yoshida, K.; Toyoura, K.; Matsunaga, K.; Nakahira, A.; Kurata, H.; Ikuhara, Y. H.; Sasaki, Y. Atomic sites and stability of Cs+ captured within zeolitic nanocavities. *Sci. Rep.* **2013**, *3*, 2457.
- (502) Mayoral, A.; Coronas, J.; Casado, C.; Tellez, C.; Diaz, I. Atomic Resolution Analysis of Microporous Titanosilicate ETS-10 through Aberration Corrected STEM Imaging. *ChemCatChem* **2013**, *5*, 2595–2598.
- (503) Zhang, W.; Theil Kuhn, L. Strong Metal–Support Interaction: Growth of Individual Carbon Nanofibers from Amorphous Carbon Interacting with an Electron Beam. *ChemCatChem* **2013**, *5*, 2591–2594.

- (504) Zhang, B.; Shao, L.; Zhang, W.; Su, D. S. Clothing Carbon Nanotubes with Palladium Rings: Constructing Carbon Metal Hybrid Nanostructures under Electron-Beam Irradiation. *ChemCatChem* **2013**, *5*, 2581–2585.
- (505) Baumgardner, W. J.; Yu, Y.; Hovden, R.; Honrao, S.; Hennig, R. G.; Abruna, H. D.; Muller, D.; Hanrath, T. Nanoparticle Metamorphosis: An in Situ High-Temperature Transmission Electron Microscopy Study of the Structural Evolution of Heterogeneous Au:Fe₂O₃ Nanoparticles. *ACS Nano* **2014**, *8*, 5315–5322.
- (506) Wang, W. L.; Santos, E. J. G.; Jiang, B.; Cubuk, E. D.; Ophus, C.; Centeno, A.; Pesquera, A.; Zurutuza, A.; Ciston, J.; Westervelt, R.; Kaxiras, E. Direct Observation of a Long-Lived Single-Atom Catalyst Chiseling Atomic Structures in Graphene. *Nano Lett.* **2014**, *14*, 450–455.
- (507) Pan, X.; Zhang, B.; Zhong, B.; Wang, J.; Su, D. S. Towards a highly dispersed and more thermally stable Ru/OCNT catalyst. *Chem. Commun.* **2014**, *50*, 3856–3858.
- (508) Liu, Z.; Lin, Y.-C.; Lu, C.-C.; Yeh, C.-H.; Chiu, P.-W.; Iijima, S.; Suenaga, K. In situ observation of step-edge in-plane growth of graphene in a STEM. *Nat. Commun.* **2014**, *5*, 4055–4055.
- (509) Wang, Z. L. New developments in transmission electron microscopy for nanotechnology. *Adv. Mater.* **2003**, *15*, 1497–1514.
- (510) Wang, Z. L. *Electron Microscopy of Nanotubes*; Kluwer Academic Publisher: New York, 2003.
- (511) Ahmadi, T. S.; Wang, Z. L.; Green, T. C.; Henglein, A.; ElSayed, M. A. Shape-controlled synthesis of colloidal platinum nanoparticles. *Science* **1996**, *272*, 1924–1926.
- (512) Su, D. S.; Schlögl, R. Thermal decomposition of divanadium pentoxide V₂O₅: Towards a nanocrystalline V₂O₃ phase. *Catal. Lett.* **2002**, *83*, 115–119.
- (513) Su, D. S.; Zandbergen, H. W.; Tiemeijer, P. C.; Kothleitner, G.; Havecker, M.; Hebert, C.; Knop-Gericke, A.; Freitag, B. H.; Hofer, F.; Schlögl, R. High resolution EELS using monochromator and high performance spectrometer: comparison of V₂O₅ ELNES with NEXAFS and band structure calculations. *Micron* **2003**, *34*, 235–238.
- (514) Roddatis, V. V.; Su, D. S.; Jentoft, F. C.; Schlögl, R. Temperature- and electron-beam-induced crystallization of zirconia thin films deposited from an aqueous medium: a transmission electron microscopy study. *Philos. Mag. A* **2002**, *82*, 2825–2839.
- (515) Wang, D.; Su, D. S.; Schlögl, R. Electron beam induced transformation of MoO₃ to MoO₂ and a new phase MoO. *Z. Anorg. Allg. Chem.* **2004**, *630*, 1007–1014.
- (516) Su, D. S.; Wieske, M.; Beckmann, E.; Blume, A.; Mestl, G.; Schlögl, R. Electron beam induced reduction Of V₂O₅ studied by analytical electron microscopy. *Catal. Lett.* **2001**, *75*, 81–86.
- (517) Qin, L. C.; Iijima, S. Onion-like graphitic particles produced from diamond. *Chem. Phys. Lett.* **1996**, *262*, 252–258.
- (518) Roddatis, V. V.; Kuznetsov, V. L.; Butenko, Y. V.; Su, D. S.; Schlögl, R. Transformation of diamond nanoparticles into carbon onions under electron irradiation. *Phys. Chem. Chem. Phys.* **2002**, *4*, 1964–1967.
- (519) Banhart, F. The transformation of graphitic onions to diamond under electron irradiation. *J. Appl. Phys.* **1997**, *81*, 3440–3445.
- (520) Banhart, F.; Ajayan, P. M. Carbon onions as nanoscopic pressure cells for diamond formation. *Nature* **1996**, *382*, 433–435.
- (521) Liao, H. G.; Zherebetsky, D.; Xin, H.; Czarnik, C.; Ercius, P.; Elmlund, H.; Pan, M.; Wang, L. W.; Zheng, H. Nanoparticle growth. Facet development during platinum nanocube growth. *Science* **2014**, *345*, 916–919.
- (522) Fujita, T.; Guan, P.; McKenna, K.; Lang, X.; Hirata, A.; Zhang, L.; Tokunaga, T.; Arai, S.; Yamamoto, Y.; Tanaka, N.; Ishikawa, Y.; Asao, N.; Yamamoto, Y.; Erlebacher, J.; Chen, M. Atomic origins of the high catalytic activity of nanoporous gold. *Nat. Mater.* **2012**, *11*, 775–780.
- (523) Gamalski, A. D.; Voorhees, P. W.; Ducati, C.; Sharma, R.; Hofmann, S. Twin plane re-entrant mechanism for catalytic nanowire growth. *Nano Lett.* **2014**, *14*, 1288–1292.
- (524) Zhang, L.; Miller, B. K.; Crozier, P. A. Atomic level in situ observation of surface amorphization in anatase nanocrystals during light irradiation in water vapor. *Nano Lett.* **2013**, *13*, 679–684.
- (525) Ta, N.; Liu, J.; Chennai, S.; Crozier, P. A.; Li, Y.; Chen, A.; Shen, W. Stabilized Gold Nanoparticles on Ceria Nanorods by Strong Interfacial Anchoring. *J. Am. Chem. Soc.* **2012**, *134*, 20585–20588.
- (526) Yoshida, K.; Bright, A. N.; Ward, M. R.; Lari, L.; Zhang, X.; Hiroyama, T.; Boyes, E. D.; Gai, P. L. Dynamic wet-ETEM observation of Pt/C electrode catalysts in a moisturized cathode atmosphere. *Nanotechnology* **2014**, *25*, 425702.
- (527) Fujita, T.; Tokunaga, T.; Zhang, L.; Li, D.; Chen, L.; Arai, S.; Yamamoto, Y.; Hirata, A.; Tanaka, N.; Ding, Y.; Chen, M. Atomic observation of catalysis-induced nanopore coarsening of nanoporous gold. *Nano Lett.* **2014**, *14*, 1172–1177.
- (528) Yoshida, H.; Takeda, S. Elucidation of the origin of grown-in defects in carbon nanotubes. *Carbon* **2014**, *70*, 266–272.
- (529) Picher, M.; Lin, P. A.; Gomez-Ballesteros, J. L.; Balbuena, P. B.; Sharma, R. Nucleation of graphene and its conversion to single-walled carbon nanotubes. *Nano Lett.* **2014**, *14*, 6104–6108.
- (530) Werner, H.; Herein, D.; Schulz, G.; Wild, U.; Schlögl, R. Reaction Pathways in Methanol Oxidation: Kinetic Oscillations in the Copper/Oxygen System. *Catal. Lett.* **1997**, *49*, 109–119.
- (531) Schedel-Niedrig, T.; Neisius, T.; Böttger, I.; Kitzelmann, E.; Weinberg, G.; Demuth, D.; Schlögl, R. Copper (Sub)Oxide Formation: A Surface Sensitive Characterization of Model Catalysts. *Phys. Chem. Chem. Phys.* **2000**, *2*, 2407–2417.
- (532) Schedel-Niedrig, T.; Bao, X.; Mühler, M.; Schlögl, R. Surface-Embedded Oxygen: Electronic Structure of Ag(111) and Cu(poly) Oxidised at Atmospheric Pressure. *Ber. Bunsen-Ges. Phys. Chem.* **1997**, *101*, 994–1006.
- (533) Sanders, P. G.; Eastman, J. A.; Weertman, J. R. Elastic and tensile behavior of nanocrystalline copper and palladium. *Acta Mater.* **1997**, *45*, 4019–4025.
- (534) Günther, W.; Pfänder, N.; Weinberg, G.; Liedtke, R.; Nissen, J.; Schlögl, R. Morphology and Texture of Nanocrystalline Copper Prepared Electrochemically from Oxides. *J. Mater. Sci.* **2000**, *35*, 3963–3975.
- (535) Böttger, I.; Pettinger, B.; Schedel-Niedrig, T.; Knop-Gericke, A.; Schlögl, R.; Froment, G. F.; Waugh, G. C. *Self Sustained Oscillations Over Copper in the Catalytic Oxidation of Methanol*; Elsevier Science: Amsterdam, 2001; p 57–70.
- (536) Wang, Z.-J.; Weinberg, G.; Schlögl, R.; Willinger, M. G. In *The 3rd International Symposium on Advanced Electron Microscopy for Catalysis*; Su, D. S., Ed.; Kloster Seeon: Germany, 2014.
- (537) Wang, Z.-J.; Weinberg, G.; Zhang, Q.; Lunkenbein, T.; Klein-Hoffmann, A.; Kurnatowska, M.; Plodinec, M.; Li, Q.; Chi, L.; Schloegl, R.; Willinger, M.-G. Direct Observation of Graphene Growth and Associated Copper Substrate Dynamics by in Situ Scanning Electron Microscopy. *ACS Nano* **2015**, DOI: 10.1021/nn5059826.
- (538) Kuwauchi, Y.; Yoshida, H.; Akita, T.; Haruta, M.; Takeda, S. Intrinsic Catalytic Structure of Gold Nanoparticles Supported on TiO₂. *Angew. Chem., Int. Ed.* **2012**, *51*, 7729–7733.
- (539) Xin, H. L.; Pach, E. A.; Diaz, R. E.; Stach, E. A.; Salmeron, M.; Zheng, H. Revealing Correlation of Valence State with Nanoporous Structure in Cobalt Catalyst Nanoparticles by In Situ Environmental TEM. *ACS Nano* **2012**, *6*, 4241–4247.
- (540) Challa, S. R.; Delariva, A. T.; Hansen, T. W.; Helveg, S.; Sehested, J.; Hansen, P. L.; Garzon, F.; Datye, A. K. Relating Rates of Catalyst Sintering to the Disappearance of Individual Nanoparticles during Ostwald Ripening. *J. Am. Chem. Soc.* **2011**, *133*, 20672–20675.
- (541) Yoshida, H.; Matsuura, K.; Kuwauchi, Y.; Kohno, H.; Shimada, S.; Haruta, M.; Takeda, S. Temperature-dependent change in shape of platinum nanoparticles supported on CeO₂ during catalytic reactions. *Appl. Phys. Express* **2011**, *4*, 065001.
- (542) Dehghan, R.; Hansen, T.; Wagner, J.; Holmen, A.; Ryttner, E.; Borg, Ø.; Walmsley, J. In-Situ Reduction of Promoted Cobalt Oxide Supported on Alumina by Environmental Transmission Electron Microscopy. *Catal. Lett.* **2011**, *141*, 754–761.

- (543) Janbroers, S.; Crozier, P. A.; Zandbergen, H. W.; Kooyman, P. J. A model study on the carburization process of iron-based Fischer–Tropsch catalysts using *in situ* TEM–EELS. *Appl. Catal., B* **2011**, *102*, 521–527.
- (544) Ciston, J.; Si, R.; Rodriguez, J. A.; Hanson, J. C.; Martínez-Arias, A.; Fernandez-García, M.; Zhu, Y. Morphological and Structural Changes during the Reduction and Reoxidation of CuO/CeO₂ and Ce_{1-x} Cu_x O₂ Nanocatalysts: In Situ Studies with Environmental TEM, XRD, and XAS. *J. Phys. Chem. C* **2011**, *115*, 13851–13859.
- (545) Chenna, S.; Banerjee, R.; Crozier, P. A. Atomic-Scale Observation of the Ni Activation Process for Partial Oxidation of Methane Using *In Situ* Environmental TEM. *ChemCatChem* **2011**, *3*, 1051–1059.
- (546) Crozier, P. A.; Chenna, S. *In situ* analysis of gas composition by electron energy-loss spectroscopy for environmental transmission electron microscopy. *Ultramicroscopy* **2011**, *111*, 177–185.
- (547) Sharma, R.; Chee, S.-W.; Herzing, A.; Miranda, R.; Rez, P. Evaluation of the Role of Au in Improving Catalytic Activity of Ni Nanoparticles for the Formation of One-Dimensional Carbon Nanostructures. *Nano Lett.* **2011**, *11*, 2464–2471.
- (548) Simonsen, S. B.; Chorkendorff, I.; Dahl, S.; Skoglundh, M.; Sehested, J.; Helveg, S. Ostwald ripening in a Pt/SiO₂ model catalyst studied by *in situ* TEM. *J. Catal.* **2011**, *281*, 147–155.
- (549) Wang, R.; Crozier, P. A.; Sharma, R. Structural Transformation in Ceria Nanoparticles during Redox Processes. *J. Phys. Chem. C* **2009**, *113*, 5700–5704.
- (550) Topsøe, H. Developments in *operando* studies and *in situ* characterization of heterogeneous catalysts. *J. Catal.* **2003**, *216*, 155–164.
- (551) Cavalca, F.; Laursen, A. B.; Wagner, J. B.; Damsgaard, C. D.; Chorkendorff, I.; Hansen, T. W. Light-Induced Reduction of Cuprous Oxide in an Environmental Transmission Electron Microscope. *ChemCatChem* **2013**, *5*, 2667–2672.
- (552) Baker, R. T. K. A review of *in-situ* electron microscopy studies of metal/metal oxide-graphite interactions. *J. Adhes.* **1995**, *52*, 13–40.
- (553) Doole, R.; Parkinson, G.; Stead, J. Institute of Physics Conference Series; 1991; pp 157–160.
- (554) Boyes, E. D.; Gai, P. L.; Hanna, L. G. Controlled environment ECELL TEM for dynamic *in-situ* reaction studies with HREM lattice imaging. *In Situ Electron and Tunneling Microscopy of Dynamic Processes Symposium* **1995**, 53–60.
- (555) Crozier, P. A.; Sharma, R. *In situ* oxidation and reduction of Pd particles. In *Electron Microscopy 1998: Proceedings; Volume 3: Materials Science 2*; Benavides, H. A. C., Yacaman, M. J., Ed.; IOP Publishing Ltd.: Bristol, UK, 1998; Vol. 3, pp 499–500.
- (556) Gai, P. L.; Kourtakis, K.; Coulson, D. R.; Sonnichsen, G. C. HREM microstructural studies on the effect of steam exposure and cation promoters on vanadium phosphorus oxides: New correlations with n-butane oxidation reaction chemistry. *J. Phys. Chem. B* **1997**, *101*, 9916–9925.
- (557) Peng, Z.; Somodi, F.; Helveg, S.; Kisielowski, C.; Specht, P.; Bell, A. T. High-resolution *in situ* and *ex situ* TEM studies on graphene formation and growth on Pt nanoparticles. *J. Catal.* **2012**, *286*, 22–29.
- (558) Uchiyama, T.; Yoshida, H.; Kuwauchi, Y.; Ichikawa, S.; Shimada, S.; Haruta, M.; Takeda, S. Systematic Morphology Changes of Gold Nanoparticles Supported on CeO₂ during CO Oxidation. *Angew. Chem., Int. Ed.* **2011**, *50*, 10157–10160.
- (559) Hansen, T. W.; Wagner, J. B.; Dunin-Borkowski, R. E. Aberration corrected and monochromated environmental transmission electron microscopy: challenges and prospects for materials science. *Mater. Sci. Technol.* **2010**, *26*, 1338–1344.
- (560) Helveg, S.; Hansen, P. L. Atomic-scale studies of metallic nanocluster catalysts by *in situ* high-resolution transmission electron microscopy. *Catal. Today* **2006**, *111*, 68–73.
- (561) Hansen, P. L.; Helveg, S.; Datye, A. K. In *Advances in Catalysis*; Bruce, C. G., Helmut, K., Eds.; Academic Press: 2006; Vol. 50, pp 77–95.
- (562) Li, P.; Liu, J.; Nag, N.; Crozier, P. A. Atomic-Scale Study of *in Situ* Metal Nanoparticle Synthesis in a Ni/TiO₂ System. *J. Phys. Chem. B* **2005**, *109*, 13883–13890.
- (563) Helveg, S.; Lopez-Cartes, C.; Sehested, J.; Hansen, P. L.; Clausen, B. S.; Rostrup-Nielsen, J. R.; Abild-Pedersen, F.; Norskov, J. K. Atomic-scale imaging of carbon nanofibre growth. *Nature* **2004**, *427*, 426–429.
- (564) Hansen, T. W.; Wagner, J. B.; Hansen, P. L.; Dahl, S.; Topsøe, H.; Jacobsen, C. J. H. Atomic-Resolution *In Situ* Transmission Electron Microscopy of a Promoter of a Heterogeneous Catalyst. *Science* **2001**, *294*, 1508–1510.
- (565) Kuwauchi, Y.; Takeda, S.; Yoshida, H.; Sun, K.; Haruta, M.; Kohno, H. Stepwise Displacement of Catalytically Active Gold Nanoparticles on Cerium Oxide. *Nano Lett.* **2013**, *13*, 3073–3077.
- (566) Zhang, S.; Shan, J.-j.; Zhu, Y.; Frenkel, A. I.; Patlolla, A.; Huang, W.; Yoon, S. J.; Wang, L.; Yoshida, H.; Takeda, S.; Tao, F. WGS Catalysis and *In Situ* Studies of CoO_{1-x}PtCo_n/C_{0.3}O₄ and Pt_mCo_m/CoO_{1-x} Nanorod Catalysts. *J. Am. Chem. Soc.* **2013**, *135*, 8283–8293.
- (567) Bright, A. N.; Yoshida, K.; Tanaka, N. Influence of total beam current on HRTEM image resolution in differentially pumped ETEM with nitrogen gas. *Ultramicroscopy* **2013**, *124*, 46–51.
- (568) Li, P.; Liu, J.; Nag, N.; Crozier, P. A. *In situ* preparation of Ni-Cu/TiO₂ bimetallic catalysts. *J. Catal.* **2009**, *262*, 73–82.
- (569) Yoshida, H.; Kuwauchi, Y.; Jinschek, J. R.; Sun, K. J.; Tanaka, S.; Kohyama, M.; Shimada, S.; Haruta, M.; Takeda, S. Visualizing Gas Molecules Interacting with Supported Nanoparticulate Catalysts at Reaction Conditions. *Science* **2012**, *335*, 317–319.
- (570) Zhou, G.; Luo, L.; Li, L.; Ciston, J.; Stach, E. A.; Saidi, W. A.; Yang, J. C. *In situ* atomic-scale visualization of oxide islanding during oxidation of Cu surfaces. *Chem. Commun.* **2013**, *49*, 10862–10864.
- (571) Xin, H. L.; Alayoglu, S.; Tao, R.; Genc, A.; Wang, C. M.; Kovarik, L.; Stach, E. A.; Wang, L. W.; Salmeron, M.; Somorjai, G. A.; Zheng, H. Revealing the atomic restructuring of Pt-Co nanoparticles. *Nano Lett.* **2014**, *14*, 3203–3207.
- (572) Zheng, H. Using molecular tweezers to move and image nanoparticles. *Nanoscale* **2013**, *5*, 4070–4078.
- (573) De Clercq, A.; Dachraoui, W.; Margeat, O.; Pelzer, K.; Henry, C. R.; Giorgio, S. Growth of Pt-Pd Nanoparticles Studied *In Situ* by HRTEM in a Liquid Cell. *J. Phys. Chem. Lett.* **2014**, *5*, 2126–2130.
- (574) Proetto, M. T.; Rush, A. M.; Chien, M.-P.; Baeza, P. A.; Patterson, J. P.; Thompson, M. P.; Olson, N. H.; Moore, C. E.; Rheingold, A. L.; Andolina, C.; Millstone, J.; Howell, S. B.; Browning, N. D.; Evans, J. E.; Gianneschi, N. C. Dynamics of Soft Nanomaterials Captured by Transmission Electron Microscopy in Liquid Water. *J. Am. Chem. Soc.* **2014**, *136*, 1162–1165.
- (575) Radisic, A.; Vereecken, P. M.; Hannon, J. B.; Searson, P. C.; Ross, F. M. Quantifying electrochemical nucleation and growth of nanoscale clusters using real-time kinetic data. *Nano Lett.* **2006**, *6*, 238–242.
- (576) Radisic, A.; Ross, F. M.; Searson, P. C. *In situ* study of the growth kinetics of individual island electrodeposition of copper. *J. Phys. Chem. B* **2006**, *110*, 7862–7868.
- (577) Williamson, M. J.; Tromp, R. M.; Vereecken, P. M.; Hull, R.; Ross, F. M. Dynamic microscopy of nanoscale cluster growth at the solid-liquid interface. *Nat. Mater.* **2003**, *2*, 532–536.
- (578) Liao, H. G.; Cui, L. K.; Whitelam, S.; Zheng, H. M. Real-Time Imaging of Pt3Fe Nanorod Growth in Solution. *Science* **2012**, *336*, 1011–1014.
- (579) Jungjohann, K.; Bliznakov, S.; Sutter, P.; Stach, E. A.; Sutter, E. In-Situ Liquid Cell Electron Microscopy of the Solution Growth of Au-Pd Core-Shell Nanostructures. *Nano Lett.* **2013**, *17*, 2964–2970.
- (580) Vendelbo, S. B.; Elkjaer, C. F.; Falsig, H.; Puspitasari, I.; Dona, P.; Mele, L.; Morana, B.; Nelissen, B. J.; van Rijn, R.; Creemer, J. F.; Kooyman, P. J.; Helveg, S. Visualization of oscillatory behaviour of Pt nanoparticles catalysing CO oxidation. *Nat. Mater.* **2014**, *13*, 884–890.
- (581) Egerton, R. F.; Wang, F.; Crozier, P. A. Beam-induced damage to thin specimens in an intense electron probe. *Microsc. Microanal.* **2006**, *12*, 65–71.

- (582) Su, D. S. Electron beam induced changes in transition metal oxides. *Anal. Bioanal. Chem.* **2002**, *374*, 732–735.
- (583) Jiang, N.; Spence, J. C. H. On the dose-rate threshold of beam damage in TEM. *Ultramicroscopy* **2012**, *113*, 77–82.
- (584) Reyes-Gasga, J.; Garcia-Garcia, R.; Bres, E. Electron beam interaction, damage and reconstruction of hydroxyapatite. *Physica B* **2009**, *404*, 1867–1873.
- (585) Hobbs, L. W. Electron-beam sensitivity in inorganic specimens. *Ultramicroscopy* **1987**, *23*, 339–344.
- (586) Iijima, S.; Ichihashi, T. Structural Instability of Ultrafine Particles of Metals. *Phys. Rev. Lett.* **1986**, *56*, 616–619.
- (587) Meyer, J. C.; Eder, F.; Kurasch, S.; Skakalova, V.; Kotakoski, J.; Park, H. J.; Roth, S.; Chuvilin, A.; Eyhusen, S.; Benner, G.; Krasheninnikov, A. V.; Kaiser, U. Accurate Measurement of Electron Beam Induced Displacement Cross Sections for Single-Layer Graphene. *Phys. Rev. Lett.* **2012**, *108*.
- (588) Schwank, J.; Allard, L. F.; Deeba, M.; Gates, B. C. Alumina-Supported Triosmium Clusters and Ensembles - Characterization by High-Resolution Transmission Electron-Microscopy. *J. Catal.* **1983**, *84*, 27–37.
- (589) Santana, A.; Zobelli, A.; Kotakoski, J.; Chuvilin, A.; Bichoutskaia, E. Inclusion of radiation damage dynamics in high-resolution transmission electron microscopy image simulations: The example of graphene. *Phys. Rev. B* **2013**, *87*, 094110.
- (590) In *Transmission Electron Microscopy*; Springer: New York, 2008; Vol. 36, pp 456–487.
- (591) Reimer, L.; Kohl, H. *Transmission electron microscopy: physics of image formation*; Springer Verlag: New York, 2008.
- (592) Sharma, R. An environmental transmission electron microscope for in situ synthesis and characterization of nanomaterials. *J. Mater. Res.* **2005**, *20*, 1695–1707.
- (593) Kuwauchi, Y.; Yoshida, H.; Akita, T.; Haruta, M.; Takeda, S. Intrinsic Catalytic Structure of Gold Nanoparticles Supported on TiO₂. *Angew. Chem., Int. Ed.* **2012**, *51*, 7729–7733.
- (594) Gai, P. L. Developments in in situ environmental cell high-resolution electron microscopy and applications to catalysis. *Top. Catal.* **2002**, *21*, 161–173.
- (595) Zhang, Z. L.; Su, D. S. Behaviour of TEM metal grids during in-situ heating experiments. *Ultramicroscopy* **2009**, *109*, 766–774.
- (596) Rihko-Struckmann, L. K.; Peschel, A.; Hanke-Rauschenbach, R.; Sundmacher, K. Assessment of Methanol Synthesis Utilizing Exhaust CO₂ for Chemical Storage of Electrical Energy. *Ind. Eng. Chem. Res.* **2010**, *49*, 11073–11078.
- (597) Miao, S.; Naumann d'Alnoncourt, R.; Reinecke, T.; Kasatkin, I.; Behrens, M.; Schlögl, R.; Muhler, M. A Study of the Influence of Composition on the Microstructural Properties of ZnO/Al₂O₃ Mixed Oxides. *Eur. J. Inorg. Chem.* **2009**, *2009*, 910–921.
- (598) Behrens, M.; Girgsdies, F.; Trunschke, A.; Schlögl, R. Minerals as model compounds for Cu/ZnO catalyst precursors: Structural and thermal properties and IR spectra of mineral and synthetic (zincian) malachite, rosasite and aurichalcite and a catalyst precursor. *Eur. J. Inorg. Chem.* **2009**, *2009*, 1347–1357.
- (599) Behrens, M.; Brennecke, D.; Girgsdies, F.; Kißner, S.; Trunschke, A.; Nasrudin, N.; Zakaria, S.; Idris, N. F.; Abd Hamid, S. B.; Kniep, B.; Fischer, R.; Busser, W.; Muhler, M.; Schlögl, R. Understanding the complexity of a catalyst synthesis: Co-precipitation of mixed Cu,Zn,Al hydroxycarbonate precursors for Cu/ZnO/Al₂O₃ catalysts investigated by titration experiments. *Appl. Catal. A: General* **2011**, *392*, 93–102.
- (600) Kandemir, T.; Girgsdies, F.; Hansen, T. C.; Liss, K.-D.; Kasatkin, I.; Kunkes, E. L.; Wowsnick, G.; Jacobsen, N.; Schlögl, R.; Behrens, M. In Situ Study of Catalytic Processes: Neutron Diffraction of a Methanol Synthesis Catalyst at Industrially Relevant Pressure. *Angew. Chem., Int. Ed.* **2013**, *52*, 5166–5170.
- (601) Behrens, M.; Studt, F.; Kasatkin, I.; Kühl, S.; Hävecker, M.; Abild-Pedersen, F.; Zander, S.; Girgsdies, F.; Kurr, P.; Kniep, B.-L.; Tovar, M.; Fischer, R. W.; Nørskov, J. K.; Schlögl, R. The Active Site of Methanol Synthesis over Cu/ZnO/Al₂O₃ Industrial Catalysts. *Science* **2012**, *336*, 893–897.
- (602) Zander, S.; Kunkes, E. L.; Schuster, M. E.; Schumann, J.; Weinberg, G.; Teschner, D.; Jacobsen, N.; Schlögl, R.; Behrens, M. The Role of the Oxide Component in the Development of Copper Composite Catalysts for Methanol Synthesis. *Angew. Chem., Int. Ed.* **2013**, *52*, 6536–6540.
- (603) Ressler, T.; Kniep, B. L.; Kassatkine, I.; Schlögl, R. The Microstructure of Copper Zinc Oxide Catalysts—Bridging the Materials Gap. *Angew. Chem., Int. Ed.* **2005**, *44*, 4704–4707.